Steam reforming and WGS reactions improved by CO2 capture for the production of an H2-rich syngas

Arno Lalaut

Université de Strasbourg
École Doctorale
des Sciences Chimiques (ED 222)

Università degli Studi dell'Aquila
Dipartimento di Ingegneria Industriale
e dell'Informazione e d'Economia

THESIS

Presented by
Arno LALAUT

to obtain the degree of

Docteur
de l'Univesité de Strasbourg
en Chimie
Spécialité : Catalyse hétérogène

Dottore di ricerca
dell'Università degli Studi dell'Aquila
in Ingegneria industriale e dell'informazione e
d'economia, XXXIV ciclo

Steam reforming and WGS reactions improved by CO_2 capture for the production of an H_2-rich syngas.

16/12/2021

THÈSE dirigée par :
Dr COURSON Claire — MCF, université de Strasbourg
Dr GALLUCCI Katia — Associate Professor, università dell'Aquila

RAPPORTEURS :
Pr TAGLIERI Giuliana — Qualified Full Professor, università dell'Aquila
Pr TAOUK Bechara — PR, INSA Rouen Normandie

AUTRES MEMBRES DU JURY :
Dr MATERAZZI Massimiliano — Senior Research Associate, university Collège London
Dr LOUIS Benoît — Directeur de recherche, university de Strasbourg

Université de Strasbourg

École Doctorale
des Sciences Chimiques (ED 222)

Università degli Studi dell'Aquila

Dipartimento di Ingegneria Industriale
e dell'Informazione e d'Economia

THESIS

Presented by

Arno LALAUT

to obtain the degree of

Docteur
de l'Univesité de Strasbourg
en Chimie
Spécialité : Catalyse hétérogène

Dottore di ricerca
dell'Università degli Studi dell'Aquila
in Ingegneria industriale e dell'informazione e
d'economia, XXXIV ciclo

Steam reforming and WGS reactions improved by CO_2 capture for the production of an H_2-rich syngas.

Supervisor
Dr. Claire COURSON

UMR 7515 - ICPEES
Institut de Chimie et Procédés pour l'Energie,
l'Environnement et la Santé
Equipe ECED : *Energie et carburants pour un Environnement Durable*

Director of the ICPEES
Prof. Guy SCHLATTER

Supervisor
Dr. Katia GALLUCCI

Laboratorio di Reattori Chimici a Fluidodinamica
DIIIE : *Dipartimento di Ingegneria Industriale e dell'Infomazione e di Economia*

Responsabile di IC5
Prof. Andrea Di Carlo

Academic year 2020/2021

CONTENTS

GENERAL INTRODUCTION

Major joint innovations from industry and academic research must be implemented to combat climate change. The development of processes to produce sustainable fuels from non-fossil sources with low CO_2 emissions has become an international priority. The optimization of the biomass gasification process to obtain synthesis gas (H_2, CO) contributes to the possible solutions; on the one hand by valorizing organic waste and on the other hand by producing a carbon-neutral fuel for numerous applications in chemistry and in the energy field. The use of biomass for the production of syngas generates the presence of impurities such as tars (heavy hydrocarbons) which are added to the gas mixture, causing fouling and harmfulness. The elimination of these tars is then experimented in this thesis by syngas reforming.

The SESR (Sorption Enhanced Steam Reforming) reaction allows the conversion of impurities into hydrogen and carbon oxide with the help of a catalyst in the presence of water. The reaction is enhanced by the presence of a CO_2 absorbent to increase the H_2 content of the final product. To carry out this reaction, a hybrid material includes catalytic sites active in reforming and CO_2 absorbing sites at high temperature. The innovative character of this project lies in the development of these bi-functional materials in addition to the water gas shift reaction. The concrete experiments performed during this 3 year thesis – synthesis, characterization and catalytic reactivity of the sorbent-catalysts – are made to demonstrate the viability of the bi-functional material operating in a single reactor and this for transposable results on a larger scale.

More in detail, the project includes the optimization of the synthesis of CO2 absorbents in a first step without active phase in reforming. The formation by co-precipitation of hydrotalcite, double lamellar structures (LDH). The physical and chemical properties of these magnesium and aluminum hydroxycarbonates vary according to the synthesis pH, the composition, and the precipitation agent.

In oxidized form after calcination (LDO) they form porous structures, which make available CO_2 absorption sites, and are used as adsorbents or catalyst precursors. The substitution of a part of the magnesium by calcium in the composition of the materials is an important parameter to allow the capacity of CO2 absorption at higher temperatures than magnesium oxide. Indeed, a temperature of 500°C is necessary to reach the constraints of a catalytic activity in reforming simultaneously with the absorption. The study will therefore focus on increasing this capacity and maintaining the optimized structure and porosity of LDO. After complete characterizations, especially by measuring their CO_2 absorption capacity, a new series of synthesis are undertaken to form catalysts with optimized synthesis conditions and the addition of iron or nickel metal phase for reforming activity. The mass percentage of metal as well as some parameters previously mortified allow to optimize the desired characteristics of the bi-functional material. The measurements of CO_2 absorption capacity are compared between catalysts and between free-metal LDO equivalents. The measurements of the CO2 absorption capacity of the materials required the implementation of a specific set up.

The second part of the thesis was devoted to the reactivity of catalysts in steam reforming. A very restrictive selection of catalysts was made before starting this step. The tests were carried out at Aquila with a reactor involving several grams of catalyst to obtain results in the perspective of a scale up in pilot plant. The conditions of temperature, gaseous input, quantity of water and tar have been studied. Tests operating cyclic phases of reforming then desorption allowed to evaluate the stability of the activity and the capacity of absorption.

The experimental parts of the work end with post-catalytic test characterizations to observe the deterioration of morphology, absorption capacity and porosity. The results of all the analyses are compiled and processed for comparisons according to each parameter.

ABSTRACT IN FRENCH

1. Contexte

La recherche sur la production d'énergie durable et la synthèse de composés chimiques à partir de la biomasse est un enjeu majeur pour la communauté scientifique et l'industrie. La valorisation de la biomasse permet de décarboner la source d'énergie et de produits chimiques. En tant que matière première, la biomasse peut relocaliser la production pour plus d'autonomie. L'optimisation des procédés de traitements de la biomasse est également importante pour la résilience écologique et la gazéification fait partie des traitements thermochimiques prometteurs en essor ces dernières décennies avec les énergies renouvelables.

La gazéification permet la conversion de la biomasse en gaz combustible (H_2, CO, CO_2 et CH_4) [1-2] en présence d'un agent oxydant (air, O_2 ou H_2O) avec une production élevée de gaz et une faible quantité de charbon et de composés condensables (goudrons). Le gaz de synthèse (CO et H_2) ainsi produit peut ensuite être transformé en biocarburant par méthanation, synthèse Fischer-Tropsch, synthèse du méthanol ou du diméthyl éther. Afin d'améliorer la conversion de cette biomasse et de réduire les coûts globaux, le projet de recherche est de développer un processus combiné innovant de traitement du gaz de synthèse. La réaction de vaporeformage (SR) convertit les impuretés d'hydrocarbures (CH_4 et goudrons) en CO_2 et H_2 et la conversion de gaz à l'eau (Water Gas Shift (WGS) : $CO + H_2O \Leftrightarrow CO_2 + H_2$) permet d'optimiser la teneur en H_2 et d'ajuster le rapport CO/H_2 suivant l'utilisation ultérieure du gaz de synthèse [3]. Basée sur la performance des réactions simultanées, la capture de CO_2 (pour une valorisation ultérieure) conduit au déplacement de l'équilibre du WGS vers la production d'H_2 pour en enrichir le mélange de gaz. Au-delà d'un vecteur d'énergie, l'hydrogène est utilisé notamment pour la production d'ammoniac. Il est également utilisé pour l'hydrogénation de produits chimiques et en particulier le raffinage du pétrole mais il est actuellement produit en grande majorité à partir de ressources fossiles.

Le caractère novateur de ce projet se situe au niveau du développement d'un matériau hybride, à la fois absorbant de CO_2 et catalyseur du WGS et du SR. Pour cela, des composés naturels de structure hydrotalcite double lamellaire (LDH – Fig. 0.1) seront étudiés en tant que base du matériau hybride. Ces composés sont des hydroxycarbonates de magnésium et d'aluminium ayant pour formule $[Mg_{(1-x)}Al_x(OH)_2]$ $[CO_{3x/2}]_ZH_2O$. Sous forme oxydées après calcination (LDO), elles sont largement utilisées en tant que catalyseurs, adsorbants ou précurseurs et ont de nombreux avantages pour cette étude [4].

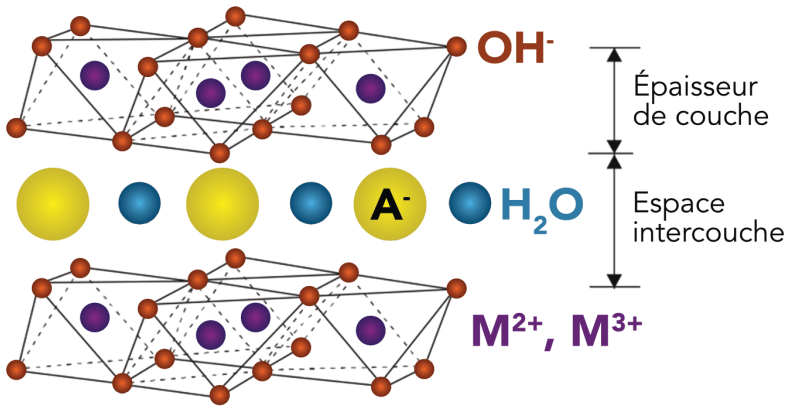

Figure 0.1: Illustration d'une structure LDH. La neutralité des charges est respectée entre les ions hydroxydes, les anions inter-couches et les charges métalliques.

Cette structure poreuse peut être maintenue malgré un échange d'anions et/ou de cations [5]. Un anion plus volumineux que le carbonate (oxalate ou stéarate) augmente l'espace inter-couche et donc l'accessibilité à la phase absorbante pour optimiser la capacité d'absorption et la phase métallique active en catalyse. La substitution partielle de Mg par Ca permet l'absorption de CO_2 à une température adaptée au SR catalysé par Ni ou Fe. En effet, en présence de CO_2, l'oxyde de magnésium se carbonate mais la désorption de CO_2 à lieu dès 400°C alors que le carbonate de calcium se décompose au-delà de 600°C.

2. Conditions de synthèse

Les absorbants ont été synthétisés par co-précipitation [6]. D'autres méthodes comme la synthèse hydrothermale [7] ou par hydrolyse de l'urée [8] sont possibles mais ne permettent pas de modifier aussi aisément la composition, l'anion et le pH. La co-précipitation est aussi une méthode facilement transposable à plus grande échelle.

Le rapport (Mg+Ca)/Al est fixé à 3, typique des valeurs retrouvées dans les hydrotalcites naturelles [9]. Ca substitue Mg et Ni ou Fe substituent Al (5, 10 ou 20_{wt}%). Différentes techniques de caractérisation telles que la diffraction des rayons X (DRX), la microscopie électonique à balayage (MEB), l'analyse thermo-gravimétrique (ATG) la physisorption de N_2 et l'analyse élémentaire ont permis d'identifier la structure, la morphologie, la porosité et la composition réelle de matériaux hybrides. Des bâtis spécifiques ont également été utilisés pour mesurer la capacité d'absorption de CO_2 des absorbants et matériaux hybrides et la réactivité ainsi que la stabilité en reformage des matériaux hybrides. Pour le développement des absorbants de CO_2, l'influence du ratio Mg/Ca = [3/0 ; 2/1 ; 1/1 ; 1/2 ; 0/3] a été étudiée (Tab.1). Le pH a aussi été varié de 8 à 10 et la taille de l'anion a été modifiée en utilisant différents sels de sodium (agent de précipitation) tels que le carbonate, l'oxalate et le stéarate.

Les catalyseurs sont synthétisés soit par co-précipitation (one-pot : OP) en substituant une partie de l'aluminium par du fer ou du nickel ; soit par impregnation (IMP) de nitrate de fer ou de nickel sur l'adsorbant qui sert de support. Les variations de paramètres de synthèse se réduisent au ratio 1.5/1.5 et 1/2 et aux anions carbonate et oxalate. Le pH est maintenu à 8 ou 10 quand le carbonate est employé et à 10 uniquement pour l'oxalate. Les quantités de métaux ajoutés sont calculées pour respecter un poucentage massique de Ni^0 ou Fe^0 de 5, 10 ou 20_{wt}%.

La nomenclature des absorbents sous la forme $Mg/Ca/Al_{A^-\cdot pH}$ et des catalyseurs sous la forme ${}_{Méthode}M_{wt\%}Mg/Ca_{A^-\cdot pH}$ indique la méthode de synthèse (IMP ou OP), le métal et son pourcentage massique (M_{wt}%), le ratio Mg/Ca/Al ou simplement Mg/Ca pour les catalyseurs, l'anion A^- utilisé (CO_3 : carbonate ; Ox : oxalate ; St : stéarate) et le pH de synthèse.

Mg/Ca/Al	pH	CO_3^{2-}	Ox^{2-}	St^-
3/0/1	8	v	v	v
	10	v	v	v
2/1/1	8	v	v	v
	10	v	v	v
1.5/1.5/1	8	v	-	v
	10	v	v	v
1/2/1	8	v	-	v
	10	v	v	-
0/3/1	8	-	-	-
	10	v	-	-

Méthode		Fer			Nickel		
Mg/Ca A-	**pH**	**wt%**	**IMP**	**OP**	**wt%**	**IMP**	**OP**
1.5/1.5 CO_3^{2-}	8	**10**	v	v	**5**	v	v
		20	v	v	**10**	v	v
	10	**10**	-	v	**5**	-	-
		20	-	-	**10**	-	v
1.5/1.5 Ox^{2-}	10	**10**	v	v	**5**	v	v
		20	v	v	**10**	v	v
1/2 CO_3^{2-}	8	**10**	v	v	**5**	v	v
		20	v	v	**10**	v	v
	10	**10**	-	v	**5**	-	v
		20	-	v	**10**	v	v
1/2 Ox^{2-}	10	**10**	v	v	**5**	v	v
		20	v	v	**10**	v	v

Tableau 0.1 : absorbants (gauche) et catalyseurs (droite) synthétisés en fonction des conditions et compositions.

3. Charactérisation des absorbants

La structure hydrotalcite est présente sur les échantillons ayant un ratio Mg/Ca/Al de 3/0/1. Dans les autres échantillons, une part du calcium entraine la formation d'aragonite ($CaCO_3$) avec le carbonate et la formation de whewellite ($Ca_2C_4H_{2.57}0_{10}$) avec l'oxalate. La calcination à 400°C oxyde cette dernière phase en carbonate de magnésium et calcium. Du periclase (MgO) est aussi faiblement visible car nettement moins cristallisé. Enfin, à 650°C, se forme de l'oxyde de calcium CaO. Par analyse élémentaire, les rapports Mg/Ca et (Mg+Ca)/Al ont été vérifiés sur des échantillons représentatifs des différentes conditions et sont très proches des valeurs attendues. Les matériaux calcinés gardent une morphologie en *roses des sables* (Fig. 0.2) qui s'effondre avec l'augmentation de la teneur en calcium. Avec des conditions de pH = 8 et l'anion carbonate et à pH = 10 pour l'oxalate, ces *roses des sables* se forment même pour le ratio Mg/Ca = 1/2. Pour les échantillons aux ratios Mg/Ca de 1,5/1,5 et 1/2, la capacité d'absorption (39 $g_{CO2}/100g_{sorbant}$) et l'accessibilité au site CaO (71 $g_{CO2}/100g_{CaO}$) sont les

meilleures (Tab. 0.2), au-delà du CaO pur (49 g_{CO2}/100g) à 600°C. Ainsi ces absorbants contenant un mélange de calcium et de magnésium, présentent une meilleure accessibilité des sites CaO et des valeurs d'absorption de CO_2 plus prometteuses. L'utilisation de l'oxalate à la place du carbonate améliore l'accessibilité des sites CaO et la stabilité au cours des cycles adsorption/désorption. Ainsi, la capacité d'absorption et l'accessibilité au sites CaO est principalement influencée par la taille de l'anion, puis la composition associée au parametre Mg/Ca et enfin le pH.

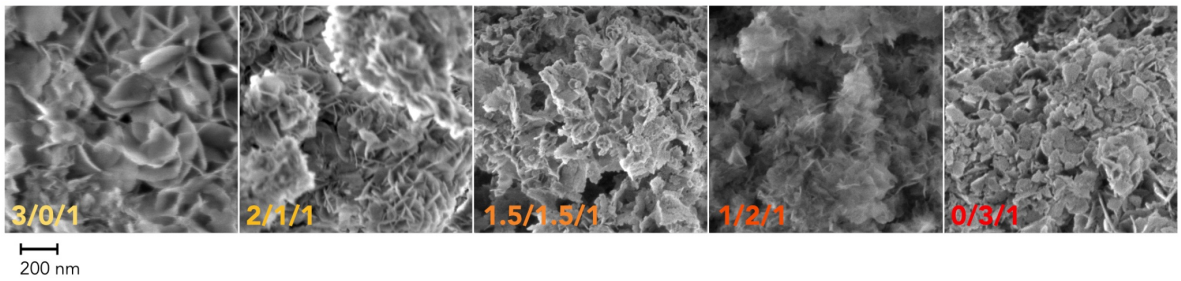

Figure 0.2 : images de MEB des échantillons synthétisés à partir de carbonate à pH10 en fonction du ratio Mg/Ca calcinés à 500°C.

Mg/Ca/Al	Anion	pH	Capacité d'absorption $gCO_2/100g$ **d'absorbant**	Accessibilité des sites CaO $gCO_2/100g$ **de CaO**
3/0/1 0*	Ox	10	1.0	-
2/1/1 23*	CO_3^{2-}	10	20.2	67.6
	CO_3^{2-}	8	9.2	30.9
	Ox	10	22.2	74.4
	Ox	8	9.7	32.5
	St	10	12.5	41.7
	St	8	6.5	21.7
1.5/1.5/1 34*	CO_3^{2-}	10	20.7	48.1
	CO_3^{2-}	8	11.4	26.4
	Ox	10	31.1	69.7
	St	10	15.6	36.4
	St	8	10.7	24.8
1/2/1 43*	CO_3^{2-}	10	37.2	67.5
	CO_3^{2-}	8	39.2	71.1
	Ox	10	31.2	56.6
	St	8	20.7	37.6
0/3/1 60*	CO_3^{2-}	10	32.8	42.7
CaO	Références		49.3	49.3
MgO			1.3	-

* Capacité d'absorption théorique (gCO_2/100 g sorbent).

Tableau 0.2 : capacité d'absorption de CO_2 et accessibilité des sites CaO des différents échantillons en fonction du ratio Mg/Ca, de l'anion et du pH.

4. Charactérisation des catalyseurs

Les structures des absorbants observées par DRX se retrouvent en présence de nickel ou de fer. Des phases intermédiaires apparaissent de façon transitoire pendant la calcination et une phase métallique s'ajoute au CaO à la fin de la calcination à 650°C. L'analyse élémentaire révèle des valeurs expérimentales de ratios Mg/Ca et (Mg+Ca)/Al similaires à celles attendues. En revanche, les fractions massiques métalliques sont en deçà des quantités introduites en particulier pour le nickel. La morphologie n'est pas perturbée par l'addition de métal par co-précipitation (OP). En plus des *roses des sables*, des phases particulièrement denses s'y mélangent et sont probablement à l'origine de la perte modérée de surface spécifique. En revanche, les échantillons imprégnés perdent les morphologie en *roses des sables* et voient leur porosité diminuer d'autant plus pour le fer à 20_{wt}% et dans une moindre mesure pour le nickel à 10_{wt}%. Les capacités d'absorption de CO_2 sont réduites par l'imprégnation de Fe ou Ni par rapport aux absorbants sans phase active et aussi par rapport aux échantillons synthétisés par co-précipitation (one-pot). La capacité d'absorption est maintenue pour les catalyseurs synthétisés par co-précipitation, au nickel en particulier et l'accessibilité aux sites CaO s'améliore même. Les plus hautes valeurs sont ainsi atteintes avec les conditions Ni_{5wt}% 1/2 oxalate pH 10 (Fig. 0.3) à 35,8 $g_{CO2}/100g_{sorbent}$ et 65,4 $g_{CO2}/100g_{CaO}$ et $Ni_{5wt\%}$ 1,5/1,5 CO_3^{2-} pH 8 à 32,9 $g_{CO2}/100g_{sorbent}$ et 76,9 $g_{CO2}/100g_{CaO}$.

Lors des cycles d'absorption/désorption, les catalyseurs sont plus stables que les absorbants correspondants mais ont une capacité d'absorption généralement plus faible : la perte de capacité est moindre et la capacité se stabilise notamment avec les catalyseurs produits par co-précipitation au fer après 7 cycles ou moins selon le catalyseurs.

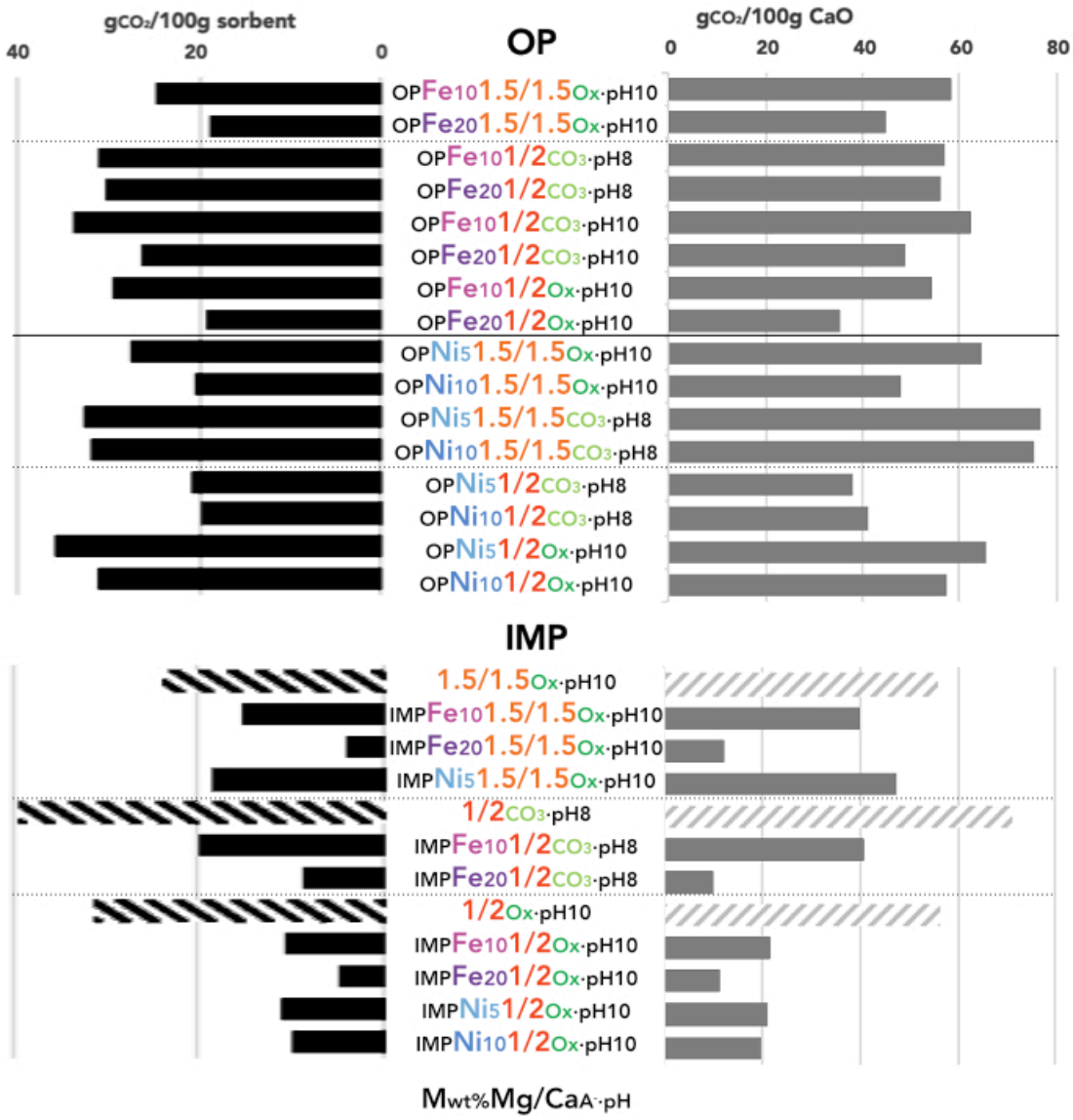

Figure 0.3 : capacité d'absorption de CO_2 et accessibilité des sites CaO des différents catalyseurs en fonction du ratio Mg/Ca, de l'anion, du pH, du métal, de son pourcentage massique et de la méthode de synthèse.

5. Réactivité catalytique

L'approche développée pour la catalyse est de simuler les impuretés de type hydrocarbures présents dans le gaz de synthèse issu de la gazéification de la biomasse et de mesurer leurs conversions en hydrogène à l'aide des catalyseurs. Pour cela un mélange $73/27_{wt}$% de toluène/naphtalène est utilisé comme mélange de goudrons de référence à faible concentration. La capacité de capture de CO_2 produit

in situ sera aussi évaluée. Le réacteur, la masse de catalyseur et les flux de gaz correspondent à un montage semi-pilote. L'activité catalytique a été étudiée en vaporeformage en variant la température de 600°C à 750°C et le ratio S/C (vapeur/carbone) de 3,5 à 6 pour les catalyseurs les plus prometteurs selon deux méthodes : les tests de réactivité et les tests de stabilité sur 10 cycles reformage/désorption. Une pré-réduction au-delà de la tempertarure de réaction est nécessaire d'après les TPR-H_2 et ce jusqu'à 800°C. De plus, elle permet, comme lors des tests de mesure de capacité d'absorption, de désorber le CO_2 accumulé lors du stockage des échantillons à l'air.

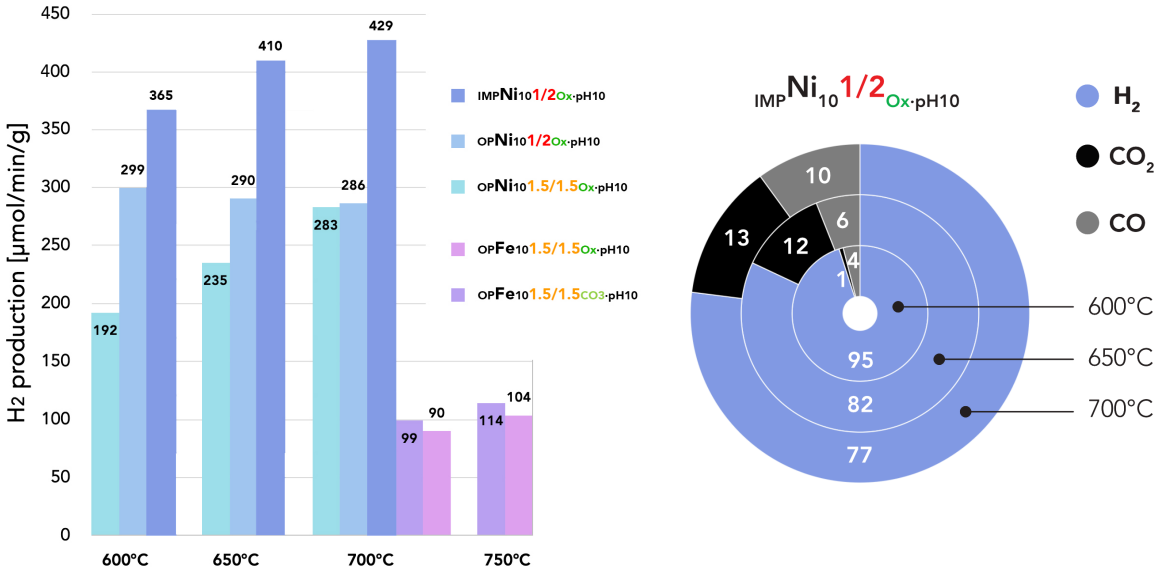

Figure 0.4 : à gauche la productivié en H_2 en fonction de la température des catalyseurs au nickel et au fer pour un ratio S/C de 6 ; à droite le ratio $H_2/CO_2/CO$ dans le gaz sortant du test de vaporeformage amélioré par l'adsorption (SESR) avec le catalyseur $_{IMP}Ni_{10}1/2_{Ox\cdot pH10}$ en fonction de la température.

Avec une faible productivité (Fig. 0.4), les catalyseurs au fer nécessitent une température plus élevée pour être actifs alors que ceux au nickel donnent de meilleurs résultats à 700°C. Les meilleurs productivités en H_2 atteignent 429 µmol/min/g à 700°C et 365 µmol/min/g à 600°C avec un ratio S/C = 6 pour le même catalyseur $_{IMP}Ni_{10}1/2_{Ox\cdot pH10}$. Le catalyseur équivalent synthétisé par coprécipitation se démarque également des autres. Les ratios $H_2/CO_2/CO$ sont aussi améliorés aux températures plus basses

(Fig. 0.4). La productivité et la sélectivité en H_2 sont d'autant plus grandes que l'eau est en excès, c'est-à-dire pour un ratio S/C élevé.

Enfin, les tests de stabilité montrent une rapide rupture de productivité indiquant la saturation du matériau absorbant qui à lieu de plus en plus tard de cycles en cycles. La production d'hydrogène après saturation reste stable d'un cycle à l'autre et cela jusqu'au dixième cycle de reformage/désorption avec des pertes de productivité de 5% à 30% selon le catalyseur. Sur ces tests cycliques à 600°C, le ratio S/C a été maintenu à 6 et offre de meilleurs résultats avec des valeurs de pré-rupture atteignant 540 µmol/min/g au premier cycle et se maintenant jusqu'à 416 µmol/min/g en phase post-rupture après 10 cycles. La sélectivité représentée par le ratio $H_2/CO_2/CO$ varie progressivement de 82/12/6 au mieux pour le catalyseur $_{OP}Ni_{10}1/2_{Ox\cdot pH10}$ juqu'à 72/22/6 au 10^{e} cycle pour les trois catalyseurs testés dans les même conditions.

Les analyses post-tests des catalyseurs ont montrés une perte de porosité et de capacité d'absorption mais aucun changement de phase des matériaux hybrides.

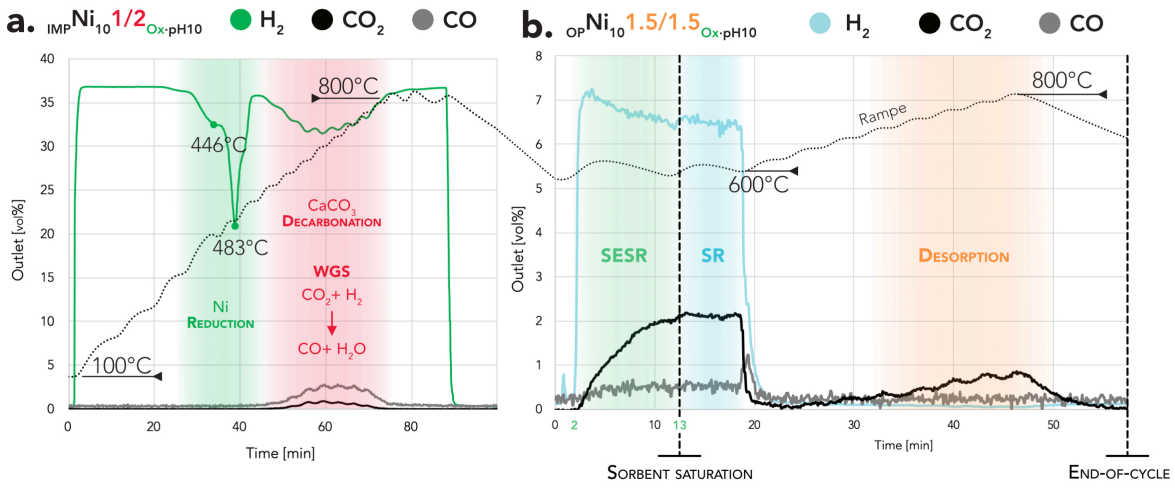

Figure 0.6: profil de test SESR cyclique: composition du flux sortant (H_2, CO_2 et CO [$_{vol}$%]) a) pendant l'étape de pre-réduction avec $_{IMP}Ni_{10}1/2_{Ox\cdot pH10}$; b) 8^{e} cycle pendant le test SESR cyclique de $_{OP}Ni_{10}1.5/1.5_{Ox\cdot pH10}$.

6. Conclusion générale

Les paramètres de synthèse (anion, pH, composition en Ca, en Fe ou Ni) montrent une différence notoire de comportement entre les composés sans et avec calcium. Une dégradation progressive des propriétés de porosité et de morphologie souhaitées s'accentuent globalement avec la hausse de calcium. Des morphologies en roses des sables peuvent en revanche être observées même en augmentant la composition en calcium jusqu'à un ratio Mg/Ca de 2/1. Les plus hautes valeurs de porosités et de capacités d'absorption sont obtenues à pH 10 pour l'oxalate, à pH 8 pour le stéarate et selon le ratio Mg/Ca, plutôt à pH 8 pour le carbonate. Les meilleurs résultats en capacité d'absorption à 600°C et accessibilité en CaO ont été obtenus pour le ratio 1.5/1.5 avec l'oxalate à pH 10 (40,6 $g_{CO2}/100g_{sorbent}$ and 69,7 $g_{CO2}/100g_{CaO}$) et au ratio 1/2 avec le carbonate à pH 8 (52,3 $g_{CO2}/100g_{sorbent}$ and 71,1 $g_{CO2}/100g_{CaO}$). La meilleure stabilité évaluée par des cycles d'absorption/désorption (carbonatation/calcination) est atteinte avec le composé $1/2/1_{Ox\cdot pH10}$.

Les catalyseurs suivent les mêmes tendances avec une perte conséquente des imprégnés mais des propriétés maintenues en co-précipitation surtout pour le nickel et sans dépasser 10_{wt}%. La réactivité des catalyseurs au fer est insuffisante à la température d'absorption. Le nickel à 10_{wt}% est en revanche d'autant plus actif et sélectif en H_2 que le rapport S/C est élevé jusqu'à 540 µmol/min/g dans les conditions expérimenales et un ratio $H_2/CO_2/CO$ de 72/22/6. La production d'hydrogène est stable à toute temperature, plus importante à 700°C mais plus sélective à 600°C grâce aux caractéristiques absorbante du support. Au cour des cycles de reformage/désorption, l'activité est réduite de 10 à 15% entre la production améliorée par l'absorption de CO_2 et après la saturation. Après 10 cycles, les catalyseurs démontrent une bonne stabilité permettant de soutenir une production comprise entre 70% et 95% de celle observée lors du premier cycle.

Références

[1] Milne, T.A., Evans, R.J., Abatzoglou, N.: Biomass Gasifier "Tars": Their Nature, Formation, and Conversion, Report NREL/TP-570-25357; National Renewable Energy Laboratory: Golden, CO, USA, 1998.

[2] Wei, L., Xu, S., Liu, J., Liu, C., Liu, S.: Hydrogen Production in Steam Gasification of Biomass with CaO as a CO2 Absorbent. Energy & Fuels. 22, 1997-2004 (2008).

[3] Satrio, J.A., Shanks, B.H., Wheelock, T.D.: A Combined Catalyst and Sorbent for Enhancing Hydrogen Production from Coal or Biomass. Energy & Fuels, 21, 322-326 (2007).

[4] Wang, Q., Luo, J., Zhong, Z., Borgna, A.: CO2 capture by solid adsorbents and their applications: current status and new trends. Energy Environ. Sci., 4, 42-55 (2011).

[5] Wang, J., Zhang Y., Altaf, N., O'Hare, D., Wang, Q.: Chapiter I dans Precombustion carbon dioxide capture materials, Q. Wang (ed.) RSC 2018, ISBN 978-1-78801-339-0.

[6] Theiss, F.L., Ayoko, G.A., Frost, R.L.: Synthesis of layered double hydroxides containing Mg2+, Zn2+, Ca2+ and Al3+ layer cations by co-precipitation methods – A review. Appl. Surf. Sci., 383, 200-213 (2016).

[7] Z.P. Xu, Z.P., Lu, G.Q.: Hydrothermal Synthesis of Layered Double Hydroxides (LDHs) from Mixed MgO and Al2O3: LDH Formation Mechanism. Chem. Mater., 17, 1055-1062 (2005).

[8] Rao, M.M., Reddy, B.R., Jayalakshmi, M., Jaya, V.S., Sridhar, B.: Hydrothermal synthesis of Mg-Al hydrotalcites by urea hydrolysis. Mater. Res. Bull., 40, 347-359 (2005).

[9] Debek, R., Galvez, M.E., Launay, F., Motek, M., Grzybe, T., Da Costa, P.: Low temperature dry methane reforming over Ce, Zr and CeZr promoted Ni-Mg-Al hydrotalcite-derived catalysts, Int. J. Hydrogen Energy, 41, 11616-11623 (2016).

ABSTRACT IN ITALIAN SOMMARIO

1. Contesto

La ricerca sulla produzione di energia sostenibile e la sintesi di composti chimici da biomasse sono una grande sfida per la comunità scientifica e l'industria. La valorizzazione delle biomasse permetterebbe la decarbonizzazione delle fonti energetiche e dei prodotti chimici. Come materie prime, le biomasse possono aiutare a delocalizzare la produzione di energia, garantendo una maggiore autonomia e sviluppo locale. L'ottimizzazione dei processi di trattamento delle biomasse è importante anche per la resilienza ecologica e la gassificazione è uno dei più promettenti trattamenti termochimici che si stanno affermando negli ultimi decenni come processo sostenibile da fonti energetiche rinnovabili.

La gassificazione permette la conversione delle biomasse in gas combustibile (principalmente costituito da H_2, CO, CO_2 e CH_4) [1-2] in presenza di un agente ossidante (aria, O_2 o H_2O) con alta produzione di gas a basso contenuto di carbonio e composti poliaromatici condensabili (catrami, ossia tar). Il syngas risultante (CO e H_2) può poi essere convertito in biocarburante tramite metanazione, sintesi Fischer-Tropsch, metanolo o sintesi di dimetil etere. Per migliorare la conversione delle biomasse e ridurre i costi complessivi, il progetto di ricerca ha l'obiettivo di sviluppare un processo combinato innovativo per il trattamento del syngas. La reazione di *Steam Reforming* (SR) converte le impurezze di idrocarburi (CH_4 e tar) in CO_2 e H_2 e la reazione di *Water Gas Shift* (WGS): $CO + H_2O \Leftrightarrow CO_2 + H_2$) permette di ottimizzare il contenuto di H_2 e di regolare il rapporto CO/H_2 in base al successivo utilizzo del syngas [3]. Sulla base dell'avanzamento delle reazioni simultanee, la cattura di CO_2 (ulteriormente riutilizzabile) porta ad uno spostamento dell'equilibrio di WGS verso la produzione di H_2 arricchendo la miscela di gas di questo componente (principio di Le Châtelier). Oltre ad essere un vettore energetico, l'idrogeno è il reagente utilizzato in particolare per la produzione di ammoniaca, alla base della produzione dei fertilizzanti mondiali. È anche usato per l'idrogenazione di prodotti chimici e, in particolare, per la raffinazione del petrolio, ma attualmente è prodotto principalmente da risorse fossili.

Il carattere innovativo di questo progetto sta nello sviluppo del materiale ibrido, che sia contemporaneamente un sorbente di CO_2 e un catalizzatore di WGS e SR. Questo progetto include lo sviluppo di tale materiale ibrido e lo sviluppo del processo in scala di laboratorio spendibile per lo studio di fattibilità su scala industriale. A questo scopo, i composti naturali con una struttura idrotalcitica aa doppio strato (LDH - Fig. 0.1) saranno studiati come base per il materiale ibrido. Questi composti sono idrossicarbonati di magnesio e alluminio con la formula chimica $[Mg_{(1-x)}Al_x(OH)_2]$ $[CO_{3x/2}]_ZH_2O$. In forma ossidata, dopo la calcinazione (LDO), sono ampiamente utilizzati come catalizzatori, sorbenti o precursori e presentano molti vantaggi per questo studio [4].

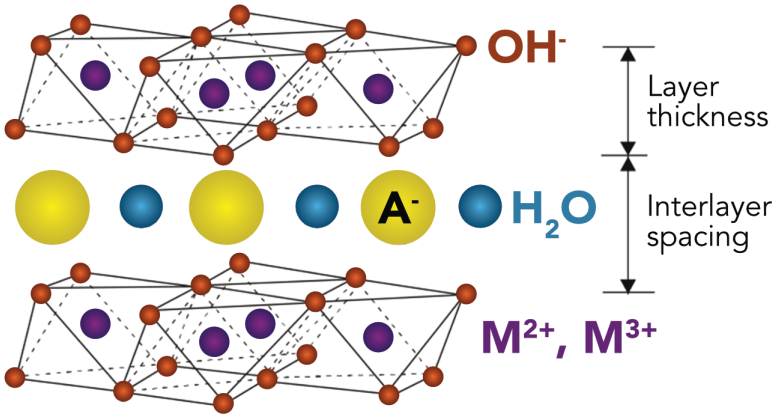

Figura 0.1: Illustrazione di una struttura idrotalcite. La neutralità di carica è rispettata tra ioni idrossido, anioni interstrato e cariche metalliche [5].

Questa struttura porosa può essere mantenuta nonostante lo scambio di anioni e cationi [5]. Un anione più grande del carbonato (ossalato o stearato) aumenta lo spazio interstrato e, quindi, l'accessibilità delle fasi assorbenti (intesa come g di CO_2 per 100 g di CaO) e per ottimizzare la capacità di assorbimento e la fase metallica cataliticamente attiva. La sostituzione parziale del Mg con il Ca permette l'assorbimento di CO_2 ad una temperatura adatta al SR catalizzato dal Ni o dal Fe. Infatti, in presenza di CO_2, l'ossido di magnesio carbonizza, ma desorbe la CO_2 sopra i 400°C, mentre l'ossido di calcio assorbe intorno ai 600°C.

2. Condizioni di sintesi

I sorbenti sono stati sintetizzati per co-precipitazione [6]. Altri metodi come la sintesi idrotermale [7] o l'idrolisi dell'urea [8] sono possibili, ma non permettono di cambiare così facilmente la composizione, l'anione e il pH. La co-precipitazione è anche un metodo facile da applicare su larga scala.

Il rapporto (Mg+Ca)/Al è fissato a 3, tipico dei valori trovati nelle idrotalciti naturali [9]. Il calcio sostituisce il magnesio e il nichel o il ferro sostituiscono l'alluminio (5, 10 o 20$_{wt}$%). Diverse tecniche di caratterizzazione come XRD, SEM, ATG e adsorbimento con N_2, analisi elementale hanno permesso di identificare la struttura cristallina, la morfologia, la porosità e la composizione. Tecniche termogravimetriche e impianti in scala da laboratorio sono stati utilizzati anche per misurare la capacità di assorbimento di CO_2 e la reattività e la stabilità durante il reforming. Per lo sviluppo dei sorbenti di CO_2, è stata studiata l'influenza del rapporto Mg/Ca = [3/0; 2/1; 1/1; 1/2; 0/3] (Tab.1). L'impatto del pH è stato anche investigato cambiandolo da 8 a 10 e l'anione è stato sostituito, usando il sale di sodio corrispondente come agente precipitante.

Mg/Ca/Al	pH	CO_3^{2-}	Ox^{2-}	St^-
3/0/1	8	v	v	v
	10	v	v	v
2/1/1	8	v	v	v
	10	v	v	v
1.5/1.5/1	8	v	-	v
	10	v	v	v
1/2/1	8	v	-	v
	10	v	v	-
0/3/1	8	-	-	-
	10	v	-	-

Metodo		Ferro			Nichel		
Mg/Ca A-	**pH**	**$_{wt}$%**	**IMP**	**OP**	**$_{wt}$%**	**IMP**	**OP**
1.5/1.5 CO_3^{2-}	8	**10**	v	v	**5**	v	v
		20	v	v	**10**	v	v
	10	**10**	-	v	**5**	-	-
		20	-	-	**10**	-	v
1.5/1.5 Ox^{2-}	10	**10**	v	v	**5**	v	v
		20	v	v	**10**	v	v
1/2 CO_3^{2-}	8	**10**	v	v	**5**	v	v
		20	v	v	**10**	v	v
	10	**10**	-	v	**5**	-	v
		20	-	v	**10**	v	v
1/2 Ox^{2-}	10	**10**	v	v	**5**	v	v
		20	v	v	**10**	v	v

Tabella 0.1: Sorbenti (a sinistra) e catalizzatori (a destra) sintetizzati secondo le condizioni (diversi pH), le composizioni e il metodo di sintesi (IMP: impregnazione, OP: *one-pot*).

I catalizzatori sono sintetizzati o per co-precipitazione (one-pot: OP) sostituendo parte dell'alluminio con ferro o nichel; o per impregnazione (IMP) di ferro o nichel sul supporto adsorbente. Le variazioni dei parametri di sintesi si riducono al rapporto 1,5/1,5 e 1/2 e agli anioni carbonato e ossalato. Il pH viene mantenuto a 8 o 10 quando si usa il carbonato e a 10 solo per l'ossalato. Le quantità di metalli aggiunti sono calcolate per rispettare la percentuale di massa di Ni^0 o Fe^0 una volta che il catalizzatore è stato calcinato e ridotto pari al 5, 10 o 20_{wt}%.

La nomenclatura degli sorbenti nella forma $Mg/Ca/Al_{A\text{-}\cdot pH}$ e dei catalizzatori nella forma ${}_{Method}M_{wt\%}Mg/Ca_{A\text{-}\cdot pH}$ indica il metodo di sintesi (IMP o OP), il metallo e la sua percentuale di massa ($M_{wt\%}$), il rapporto Mg/Ca/Al o semplicemente Mg/Ca per i catalizzatori, l'anione A utilizzato (CO_3: carbonato; Ox: ossalato; St: stearato) e il pH di sintesi.

3. Caratterizzazione dei sorbenti

La struttura idrotalcitica è presente sui campioni 3/0/1 (rapporto Mg/Ca/Al). L'introduzione di una proporzione di calcio porta alla formazione di aragonite con il carbonato e alla formazione di whewellite con l'ossalato. La calcinazione a 400°C ossida questa fase formando il carbonato di magnesio e calcio. Il periclasio (MgO) è anche debolmente visibile anche se molto meno intenso. Infine, a 650°C, si forma l'ossido di calcio (CaO). Con l'analisi elementale, i rapporti Mg/Ca e (Mg+Ca)/Al sono stati verificati su tutti i campioni rappresentativi delle diverse condizioni e sono risultati molto vicini ai valori attesi. I materiali calcinati mantengono una morfologia a forma di rosa sabbiosa (Fig. 0.2) che viene disgregata con l'aumentare del contenuto di calcio. A condizioni di pH = 8 e anione carbonato e a pH = 10 e l'ossalato, anche con un rapporto 1/2 di Mg/Ca si formano queste rose di sabbia. È su questi campioni con un rapporto Mg/Ca di 1,5/1,5 e 1/2 che la capacità di assorbimento (39 $g_{CO2}/100g_{sorbente}$) e l'accessibilità al sito di CaO (71 $g_{CO2}/100g_{CaO}$) sono risultate migliori (Tab. 0.2), anche rispetto al CaO puro (49 $g_{CO2}/100g$) a 600°C. Quindi, anche con meno calcio, una migliore accessibilità dà valori di assorbimento di CO_2 più significativi e promettenti. L'uso dell'ossalato al posto del carbonato migliora l'accessibilità al sito di CaO e la stabilità durante i cicli di adsorbimento/desorbimento. Così, la capacità

di assorbimento e l'accessibilità ai siti di CaO è principalmente influenzata dalla dimensione dell'anione, poi dalla composizione associata al parametro Mg/Ca e infine dal pH.

Mg/Ca/Al	Anione	pH	Capacità d'assorbimento	Accessibilità dei siti CaO
			gCO_2/100g **di sorbente**	gCO_2/100g **di CaO**
3/0/1 0*	Ox	10	1.0	-
2/1/1 23*	CO_3^{2-}	10	20.2	67.6
	CO_3^{2-}	8	9.2	30.9
	Ox	10	22.2	74.4
	Ox	8	9.7	32.5
	St	10	12.5	41.7
	St	8	6.5	21.7
1.5/1.5/1 34*	CO_3^{2-}	10	20.7	48.1
	CO_3^{2-}	8	11.4	26.4
	Ox	10	31.1	69.7
	St	10	15.6	36.4
	St	8	10.7	24.8
1/2/1 43*	CO_3^{2-}	10	37.2	67.5
	CO_3^{2-}	8	39.2	71.1
	Ox	10	31.2	56.6
	St	8	20.7	37.6
0/3/1 60*	CO_3^{2-}	10	32.8	42.7
CaO	Referenze		49.3	49.3
MgO			1.3	-

* Capacità terorica di assorbimento (gCO_2/100 g sorbente).

Tabella 0.2: Capacità di assorbimento di CO_2 e accessibilità dei siti di CaO per diversi campioni in funzione del rapporto Mg/Ca, anione e pH.

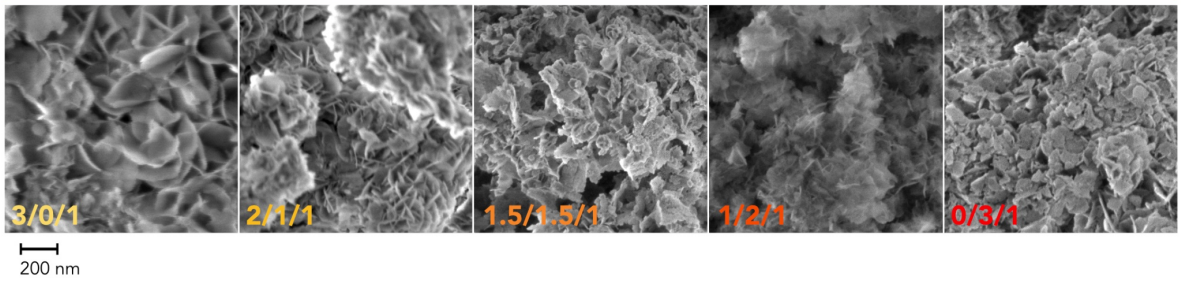

Figura 0.2: Immagini al SEM di campioni sintetizzati da carbonato a pH10 in funzione del rapporto Mg/Ca calcinati a 500°C.

4. Caratterizzazione dei catalizzatori

Le strutture osservate in XRD per i sorbenti si rinvengono anche in presenza di nichel o ferro. Alcune fasi intermedie appaiono transitoriamente durante la calcinazione e una fase metallica si aggiunge al prodotto finale calcinato a 650°C con CaO. Dall'analisi elementare, i valori dei rapporti Mg/Ca e (Mg+Ca)/Al risultano ancora accurati dopo questo trattamento. D'altra parte, le frazioni di massa dei metalli risultano inferiori alle quantità introdotte, in particolare per il contenuto di nichel. La morfologia non è disturbata dall'aggiunta di metallo nella co-precipitazione *one-pot*. Oltre alle rose di sabbia, fasi particolarmente dense si mescolano alla struttura e sono probabilmente responsabili della moderata perdita di superficie specifica. D'altra parte, i campioni impregnati perdono la caratteristica forma di rosa sabbiosa e perdono, contemporaneamente, anche molta porosità, soprattutto con l'aggiunta di ferro al 20_{wt}% e, in misura minore, di nichel al 10_{wt}%. Le capacità di assorbimento di CO_2 vengono ridotte dall'impregnazione di Fe o Ni rispetto agli corrispondenti sorbenti senza fase catalitica attiva e anche rispetto agli omologhi sintetizzati con co-precipitazione *one-pot*. In particolare, la capacità di assorbimento è mantenuta dalla co-precipitazione per i catalizzatori al nichel e l'accessibilità dei siti di CaO migliora addirittura. I valori migliori sono pertanto raggiunti dai composti Ni_{5wt}% 1/2 ossalato pH 10 (Fig. 0.3), avente 35,8 $g_{CO2}/100g_{sorbente}$ di capacità sorbente e 65,4 $g_{CO2}/100g_{CaO}$ di accessibilità l'ossido di calcio, e Ni_{5wt}% 1,5/1,5 CO_3^{2-} pH 8, con 32,9 $g_{CO2}/100g_{sorbente}$ e 76,9 $g_{CO2}/100g_{CaO}$, rispettivamente.

Nei cicli di assorbimento/desorbimento, i catalizzatori mostrano una capacità di assorbimento inferiore ai loro corrispondenti sorbenti, ma risultano più stabili: la perdita di capacità è inferiore e la capacità di assorbimento si stabilizza, soprattutto con i catalizzatori prodotti per co-precipitazione del ferro, dopo 7 cicli o meno a seconda dell'elemento catalitico.

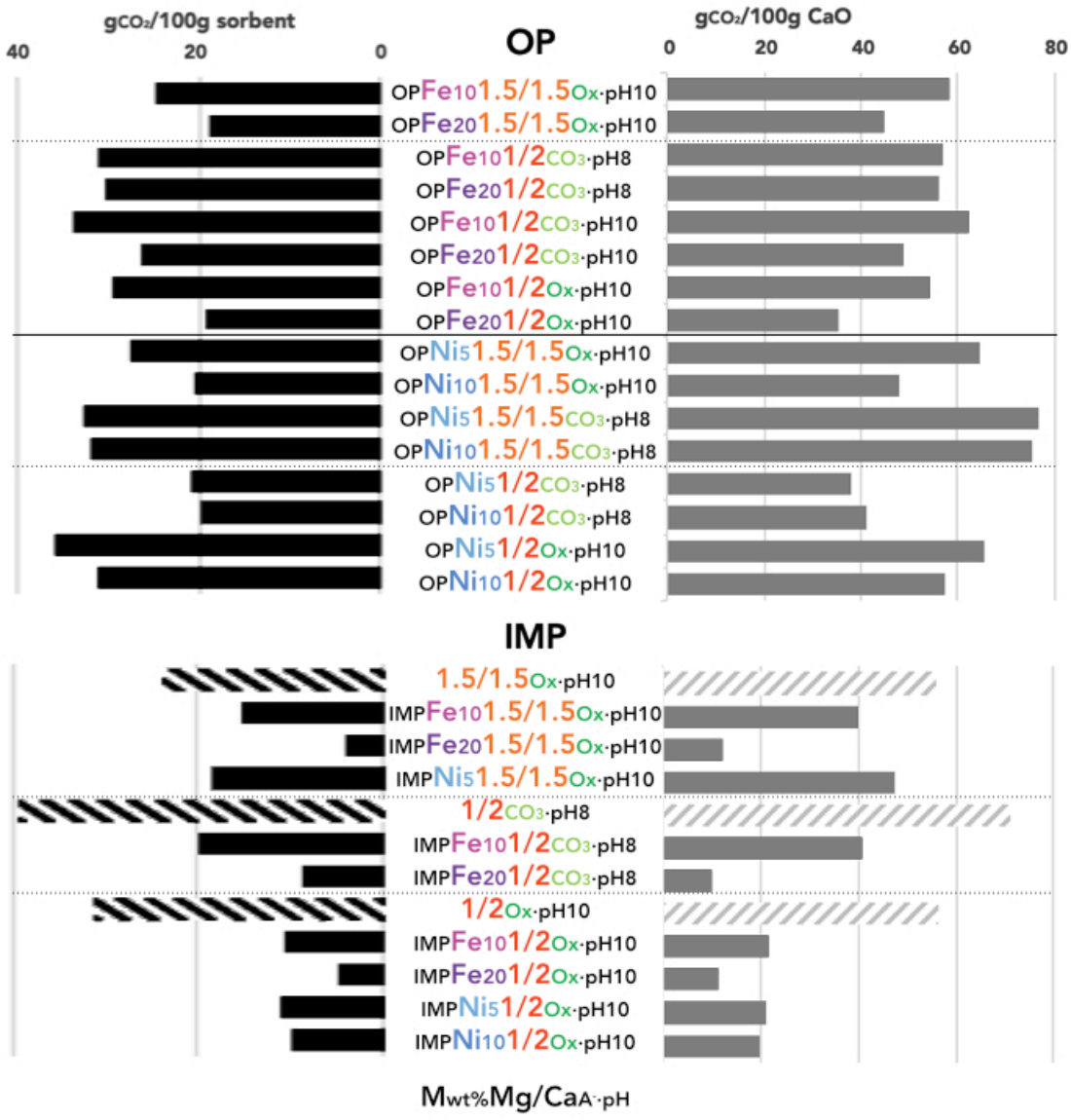

Figura 0.3: Capacità di assorbimento di CO_2 e accessibilità dei siti di CaO dei diversi catalizzatori in funzione del rapporto Mg/Ca, l'anione, il pH, il metallo e la sua percentuale in massa, e il metodo di sintesi.

5. Reattività catalitica

L'approccio sviluppato per la catalisi consiste nel simulare le impurità idrocarburiche (tar) presenti nel bio-syngas nel processo di gassificazione e nel misurare la loro conversione in idrogeno utilizzando diversi catalizzatori-sorbenti. A questo scopo, una miscela toluene/naftalene $73/27_{wt}$% viene utilizzata come miscela di riferimento a bassa concentrazione. Si valuterà anche la capacità di catturare la CO_2 prodotta in situ. La composizione e la concentrazione del tar nel flusso totale di gas nell'impianto in scala di laboratorio corrispondono a quelle tipiche di un impianto pilota, nonostante si sia scelto di limitare la composizione del tar ai due idrocarburi solitamente più abbondanti. Anche la configurazione reattoristica a letto fisso è realizzabile con successo su scale di interesse industriale.
La catalisi dello Steam Reforming è stata studiata variando la temperatura da 600°C a 750°C e il rapporto S/C (vapore/carbone) da 3,5 a 6 per i catalizzatori più promettenti seguendo due metodi sperimentali: il test di reattività e il test di stabilità in cui si alternano 10 cicli di reforming/desorbimento (rigenerazione). Lo step di pre-riduzione, condotto al disopra della temperatura di reazione, richiede che venga raggiunta la temperatura di 800°C secondo le indicazioni emerge dalla TPR-H_2: ciò consente anche per desorbire i siti del sorbente, così come di operare uno di spurgo nei test di misurazione della capacità di assorbimento.

Avendo una bassa produttività (Fig. 0.4), i catalizzatori di ferro richiedono una temperatura più alta per essere attivi, mentre i catalizzatori di nichel esibiscono la performance migliore a 700°C. La migliore produttività di H_2 si raggiunge con 429 µmol/min/g a 700°C e 365 µmol/min/g a 600°C per test catalitici in cui si è impostato un rapporto S/C = 6 e impiegato lo stesso catalizzatore sintetizzato per impregnazione $_{IMP}Ni_{10}1/2_{Ox\cdot pH10}$. Anche il catalizzatore omologo sintetizzato con un processo one-pot si distingue per accresciuta prestazione rispetto agli altri catalizzatori ottenuti con la stessa sintesi ei rapporti $H_2/CO_2/CO$ risultano ulteriormente migliorati, verso una maggiore percentuale di H_2 dalle più basse temperature (Fig. 0.4). La produttività e la selettività in H_2 è tanto maggiore quanto più l'acqua in eccesso viene alimentata, cioè all'aumentare del rapporto S/C.

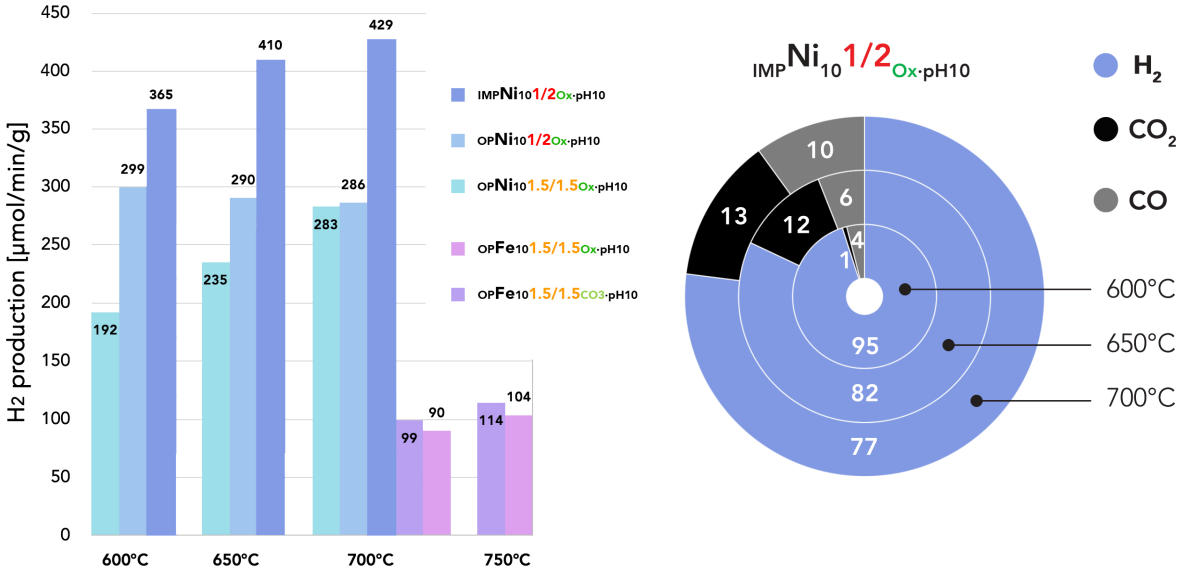

Figura 0.4: a sinistra: la produttività H_2 in funzione della temperatura per i catalizzatori di nichel e ferro selezionati con un rapporto S/C di 6; a destra: composizione del gas in uscita, espresso come rapporto $H_2/CO_2/CO$, durante il test steam reforming potenziato dall'assorbimento (SESR: sorption enhanced steam reforming) con $_{IMP}Ni_{10}1/2_{Ox\cdot pH10}$ in funzione della temperatura.

Infine, i test di stabilità mostrano una rapida caduta della produttività e si osserva un tempo più lungo per raggiungere la saturazione del sorbente tra un ciclo e il successivo. La produzione di idrogeno dopo la saturazione rimane stabile ad ogni ciclo e questo fino al 10° ciclo i reforming/desorbimento con perdite di produttività dal 5% al 30% a seconda del catalizzatore. In questi test ciclici a 600°C il rapporto S/C è stato mantenuto pari a 6 in quanto questo valore offre risultati migliori raggiungendo 540 µmol/min/g di H_2 nel primo ciclo e rimangono paria 416 µmol/min/g dopo i 10 cicli di reforming. La selettività, rappresentata dal rapporto $H_2/CO_2/CO$, varia progressivamente da 82/12/6 nel migliore dei casi per il catalizzatore $_{OP}Ni_{10}1/2_{Ox\cdot pH10}$ fino a 72/22/6 al 10° ciclo per gli altri tre catalizzatori testati in questa fase.

Le analisi post-test dei catalizzatori hanno, infine, mostrato una perdita di porosità e di capacità di assorbimento, ma nessun cambiamento di fase rilevabile con le tecniche impiegate.

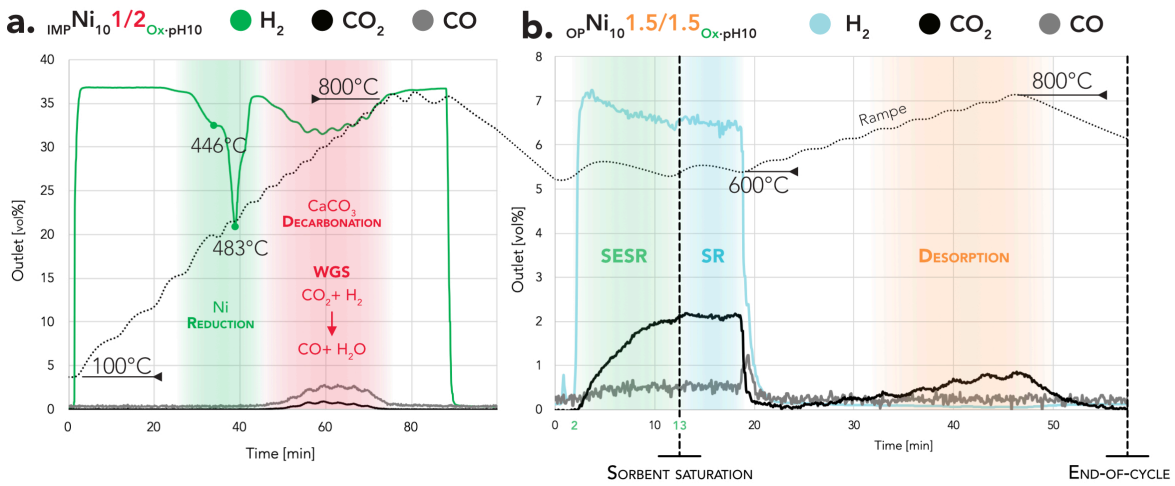

Figura 0.6: Profilo del test ciclico SESR: composizione del flusso in uscita (H_2, CO_2 e CO [vol%]) a) durante la fase di pre-riduzione con $_{IMP}Ni_{10}1/2_{Ox\cdot pH10}$; b) 8° ciclo durante il test ciclico SESR di $_{OP}Ni_{10}1.5/1.5_{Ox\cdot pH10}$.

6. Conclusione

I parametri di sintesi (anione, pH, composizione di Ca, Fe o Ni) mostrano una notevole influenza sul comportamento dei composti senza e con calcio. Una progressiva degradazione delle proprietà porosimetriche e morfologiche desiderate è globalmente promossa con l'aumento del contenuto di calcio. Le tipiche rose di sabbia, osservate al SEM, invece, si possono formare anche con una composizione di calcio crescente fino a un rapporto di 2/1. I valori più alti di porosità e capacità di assorbimento si ottengono per composti sintetizzati a pH 10 per l'ossalato, a pH 8 per lo stearato e, a seconda del rapporto Mg/Ca, a pH 8 per il carbonato. I migliori risultati nella capacità di assorbimento a 600°C e nell'accessibilità del CaO sono stati ottenuti con il rapporto Mg/Ca=1,5/1,5 con ossalato a pH 10 (40,6 $g_{CO2}/100g_{sorbente}$ e 69,7 $g_{CO2}/100g_{CaO}$) e a 1/2 con carbonato a pH 8 (52,3 $g_{CO2}/100g_{sorbente}$ e 71,1 $g_{CO2}/100g_{CaO}$). La migliore stabilità valutata dal ciclo di assorbimento/desorbimento (carbonatazione/calcinazione) si ottiene con il composto $1/2/1_{Ox\cdot pH10}$. I catalizzatori seguono gli stessi trend dei sorbenti precursori, ma con una conseguente perdita dovuta all'impregnazione, sebbenele proprietà vengano mantenute ricorrendo in co-precipitazione con nichel non superiore al 10_{wt}%. La reattività dei catalizzatori di ferro è insufficiente alla temperatura di assorbimento. Il nichel al 10_{wt}%,

invece, è ancora più attivo e selettivo in H_2 per alti rapporti S/C (*steam/carbon*) in alimentazione, ottenendo fino a 540 μmol/min/g di H_2 nelle condizioni sperimentali e un rapporto $H_2/CO_2/CO$ pari a 72/22/6. La produzione di idrogeno è stabile a tutte le temperature, più significativa a 700°C, ma più selettiva a 600°C a causa delle caratteristiche assorbenti del supporto. Durante i cicli di reforming/desorbimento, l'attività per il *Sorption Enhanced Steam Refoming* del tar si riduce del 10-15%. Dopo 10 cicli, i catalizzatori mostrano ancora una buona stabilità, conservando una produttività che varia tra il 70% e il 95% rispetto al primo ciclo.

Referenze

[1] Milne, T.A., Evans, R.J., Abatzoglou, N.: Biomass Gasifier "Tars": Their Nature, Formation, and Conversion, Report NREL/TP-570-25357; National Renewable Energy Laboratory: Golden, CO, USA, 1998.

[2] Wei, L., Xu, S., Liu, J., Liu, C., Liu, S.: Hydrogen Production in Steam Gasification of Biomass with CaO as a CO_2 Absorbent. Energy & Fuels. 22, 1997-2004 (2008).

[3] Satrio, J.A., Shanks, B.H., Wheelock, T.D.: A Combined Catalyst and Sorbent for Enhancing Hydrogen Production from Coal or Biomass. Energy & Fuels, 21, 322-326 (2007).

[4] Wang, Q., Luo, J., Zhong, Z., Borgna, A.: CO_2 capture by solid adsorbents and their applications: current status and new trends. Energy Environ. Sci., 4, 42-55 (2011).

[5] Wang, J., Zhang Y., Altaf, N., O'Hare, D., Wang, Q.: Chapiter I dans Precombustion carbon dioxide capture materials, Q. Wang (ed.) RSC 2018, ISBN 978-1-78801-339-0.

[6] Theiss, F.L., Ayoko, G.A., Frost, R.L.: Synthesis of layered double hydroxides containing Mg^{2+}, Zn^{2+}, Ca^{2+} and Al^{3+} layer cations by co-precipitation methods – A review. Appl. Surf. Sci., 383, 200-213 (2016).

[7] Z.P. Xu, Z.P., Lu, G.Q.: Hydrothermal Synthesis of Layered Double Hydroxides (LDHs) from Mixed MgO and Al_2O_3: LDH Formation Mechanism. Chem. Mater., 17, 1055-1062 (2005).

[8] Rao, M.M., Reddy, B.R., Jayalakshmi, M., Jaya, V.S., Sridhar, B.: Hydrothermal synthesis of Mg-Al hydrotalcites by urea hydrolysis. Mater. Res. Bull., 40, 347-359 (2005).

[9] Debek, R., Galvez, M.E., Launay, F., Motek, M., Grzybe, T., Da Costa, P.: Low temperature dry methane reforming over Ce, Zr and CeZr promoted Ni-Mg-Al hydrotalcite-derived catalysts, Int. J. Hydrogen Energy, 41, 11616-11623 (2016).

CHAPTER 1

BIBLIOGRAPHIC STUDIES

This chapter introduces concepts and knowledges required to understand the purpose and the scope of the draft. The thesis takes a part in a sustainable way of making chemistry by following green principles. The general environmental context and research thematic as biomass, hydrogen and CO_2 capture concerning the project are described in the subsequent paragraphs. Then specific material and reactions operated are defined under the state of the art.

1.1. Energy and environment

1.1.1. Energy production and consumption

Since 1950 and even more so nowadays, energy production has come from fossil resources: the large majority of the energy consumption comes from coal, oil, and gas as primary energy sources (Fig 1.1) which release a lot of greenhouse gas (GHG). In 1990 the first IPCC report [1] was published, which is a milestone in history and testifies the importance of global warming. This report warned the decision' makers and world citizens about the environmental consequences of GHG and preconized international and cooperative climate political actions. That year, 106,000 TWh of energy were consumed whose 78% of fossil fuel; renewable energies accounted only 6%. Other IPCC reports [1-2] (1995; 2001; 2007; 2014) became increasingly alarmists and political events followed notably in 1997 with the well-known Kyoto protocol.

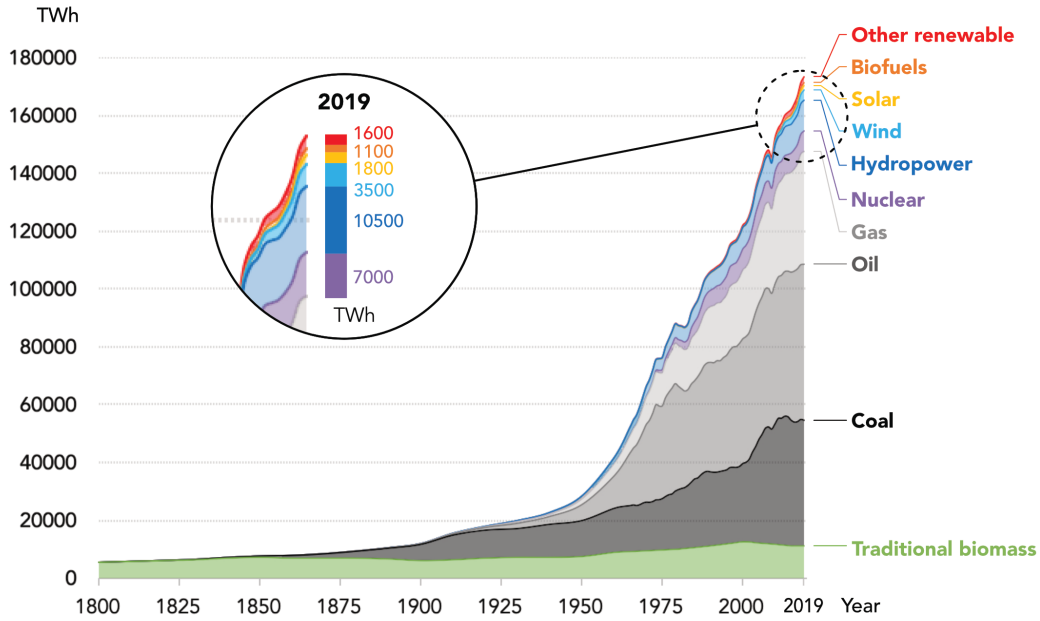

Figure 1.1: Global primary energy consumption by source [3].

Awareness of global warming consequences has spread to include rise of biodiversity extinction, oceans level, sea acidification, naturals disasters, and human resilience (agriculture, heat waves, flood-prone islands, migration, and climate inequality). Despite the recommendations of scientists, the total

energy consumption achieves 162,000 TWh in 2015 and the share of fossil sources reached 80% of energy consumption. Nuclear power (4%), traditional biomass (7%), and renewable energies such as hydropower, wind, solar, and biofuels raise the total energy mix and reach 9%. The Paris Agreement was signed in 2015 by 196 states, but the trend continues. Global primary energy consumption exceeded 173,000 TWh in 2019 [4] and has ultimately not stopped increasing since the pre-industrial era. The lastest IPCC report [5] assures that *economic and population growth continues to be the most important drivers of increases in CO_2 emission from fossil fuel combustion.*

Respect the goal of global warming below 2°C means huge systemic changes as explained in the lastest and very ambitious IEA report *Net Zero by 2050: A roadmap for the global energy system* (Fig. 1.2) [6]. Society will have to shift in production and consumption, about politics, and economic growth to a more resilient way of life. Energy, industry, transportation, and buildings are key sectors for changing the current paradigm because those are the sectors responsible for GHG emissions. Among GHG, carbon dioxide has the greatest impact on global warming, accounting for 76% of the 49 $Gt_{CO2\cdot eq}$ in 2010 (Fig. 1.3), with 65% coming from fossil fuel and industrial processes and 11% from forestry and other land uses (FOLU). The remaining 12 $Gt_{CO2\cdot eq}$ come from CH_4, N_2O, and fluorinated gases (F-gases: covered by Kyoto Protocol). The limitation of GHG is possible in many ways.

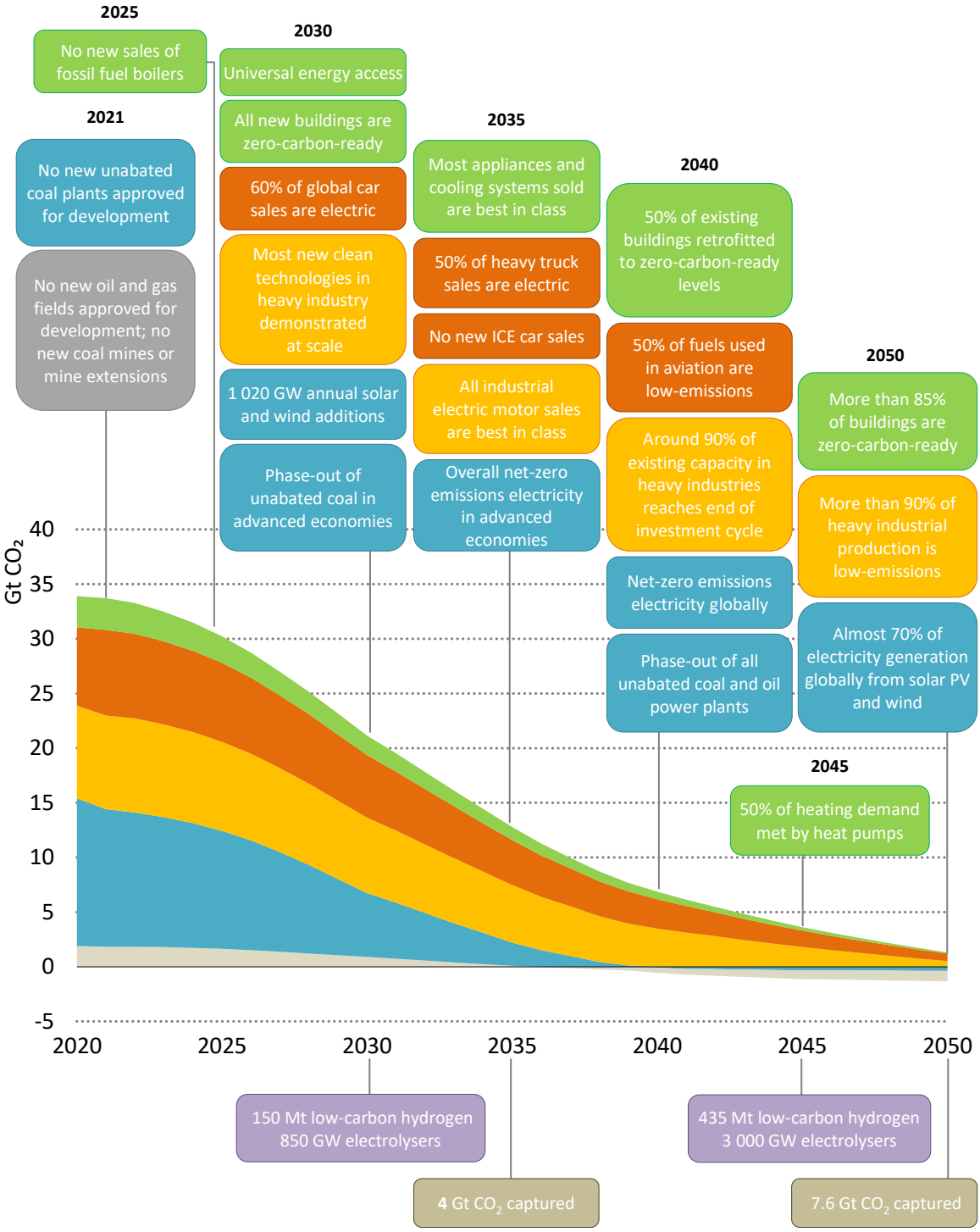

Figure 1.2: Key milestone in the pathway to net zero-emission (2021) [6].

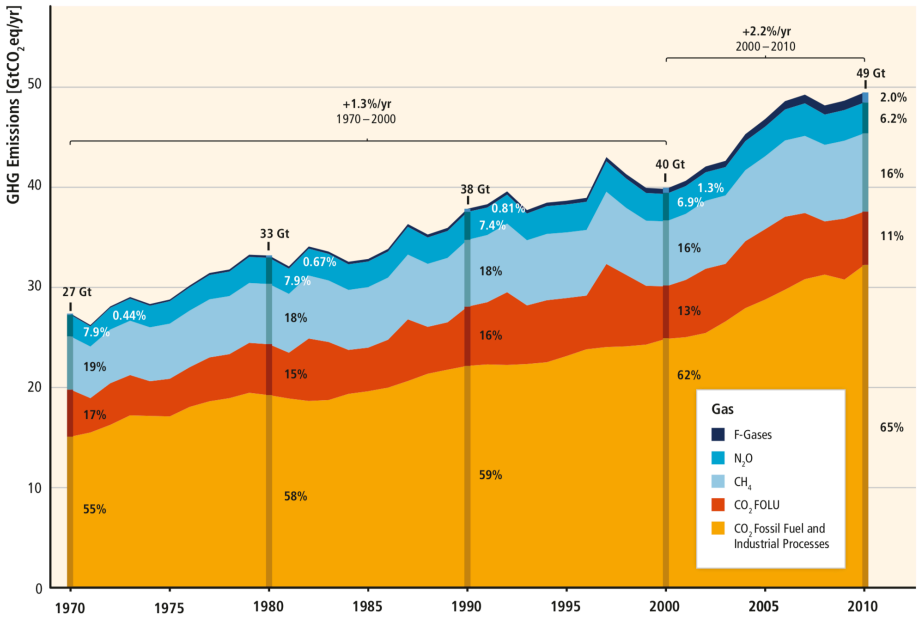

Figure 1.3: Total annual anthropogenic greenhouse gas emission by groups of gases 1970-2010.

1.1.2. Renewables and carbon-free sources

Projects and models [2-3,5-8] as explained in the pathway to net zero-emissions (Fig. 1.3), have highlighted power generation from renewable sources as carbon-free energy and nuclear power as a relatively low-carbon emission [9]. Indeed, fossil fuels consumption and extraction must decrease. In addition, major steps will need to be taken to reduce environmental impact over 30-years time horizon, for example, converting combustion engines to electric cars, retrofitting buildings to zero-carbon buildings, or replacing the main part of fossil generation with sustainable energy. The power generation from renewable energy in 2018 in Europe (EU28 – 28 member states) reached 1000 TWh including [7]: 36% wind energy, 33% of hydropower, 18% biomass and 12% of solar power. Renewable resources produce energy intermittently, depending on the weather and of course on the climatic region. Hydropower is the most suitable renewable source for regulated production. Unlike fossil fuels, wind and solar power production cannot be adapted for direct consumption. Therefore, to reduce GHG emissions and to best develop renewable energy, excess energy must be stored.

As mentioned in Figure 1.2, promising approaches spotlight the importance of hydrogen [10-13] as a vector for renewable energy and CO_2 capture to remedy the great energetic challenge of our time. Furthermore, biomass valorization is a strong asset to promote renewable and carbon-free sources. The association of diverse technologies around these themes is at the heart of the applications of this project.

1.2. Biomass and hydrogen

1.2.1. Biomass valorization

Research on sustainable energy and the production of chemical compounds from biomass is a major challenge for the scientific community and industry. The valorization of biomass feedstocks allows to decarbonize energy sources and relocatizing production for greater local autonomy. The optimization of biomass processes is also important for the ecological resilience of all countries, especially those of the global South, and in the event of a fossil resource crisis. Biomass comes from many sources on a large scale [14]: forestry, sawmill and paper industries, crops and residues, raising, agro-food industry, and locally from fisheries, aquaculture, and bio-waste (domestic waste, maintenance of public gardens, water treatment plant), etc. The valorization of green wastes can permit a more sustainable production of basic chemical compounds [15] and energy with less transport. The commission of the European Communities [16] defines biomass as follows:

> *Biomass means non-fossilised and biodegradable organic material originating from plants, animals and micro-organisms. This shall also include products, by-products, residues and waste from agriculture, forestry and related industries as well as the non-fossilised and biodegradable organic fractions of industrial and municipal wastes. Biomass also includes gases and liquids recovered from the decomposition of non-fossilised and biodegradable organic material. […] Biomass is considered as CO_2-neutral.*

Many treatments of biomass are possible by biochemical and thermochemical processes [17] depending on the applications. The composition of cellulose [18], hemicellulose, and lignin [19, 20] varies between different biomass sources, addressing on the different uses:

• Biochemical: for vegetal oils, biodiesel, bioethanol and biogas.

- Acid or enzymatic hydrolysis [18, 21] of polysaccharides (cellulose, starch) to recover glucose. The second generation of biomass from lignocellulosic can also be valorized by enzymatic way.
- Alcoholic or anaerobic fermentation (wet biomass) to produce light alcohols such as ethanol, butanol, and diesel. Sugar cane and sugar beets are the most exploited plants and corn and wheat are exploited for their grains. The third generation of biomass is microalgae and can be treated by fermentation to generate bioethanol or by mechanization to produce biogas.
- Extraction of oil crops for esterification into biodiesel. Biodiesel is composed of a mixture of fatty acid methyl esters. The first generation of biomass used comes from edible vegetable oils like rapeseed, soybean, sunflower and palm oil, animal fats, or recycled greases. Biodiesel can also be produced from trans-esterification of microalgae [22].

• Thermochemical: for methanol, dimethyl ether (DME), synthetic fuel, hydrogen.

Thermic transformation of biomass to syngas and bio-oil provides access to chemical platform compounds (Fig. 1.4) [23].

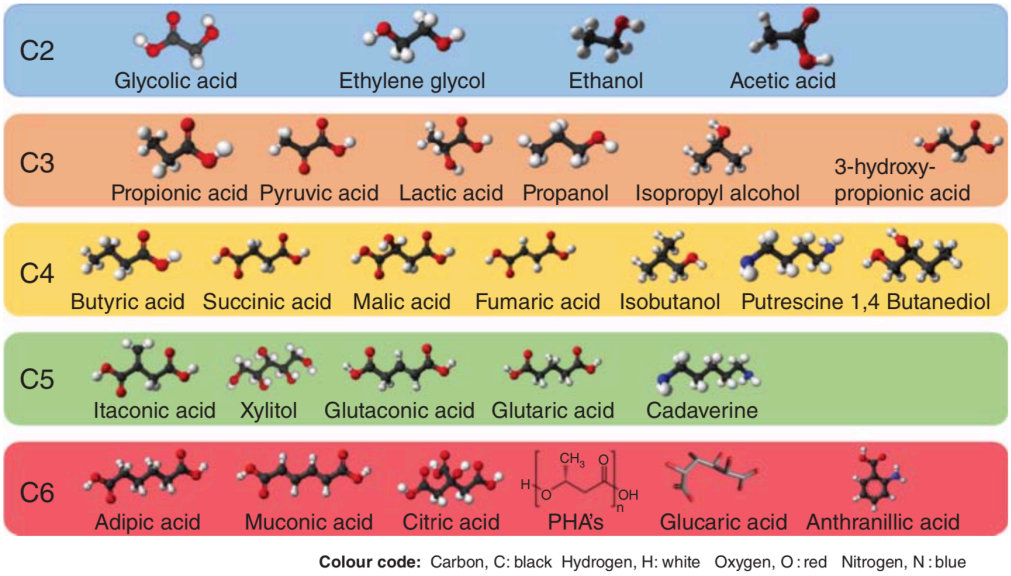

Figure 1.4: Platform chemicals production from biomass

- Methanation treatment [24-26] produces a synthetic natural gas (CH_4) from a mixture of gases (H_2, CO, CO_2),
- The combustion produces heat and electricity. This is the simplest treatment to produce energy from biomass, but it leads to CO_2 emissions.
- Pyrolysis [27-30] mainly produces bio-oils (pyrolysis oil) and biochar. The pyrolysis process may be modified by adding water to thermal depolymerization. This method is very commonly used with wood to make charcoal. The mixed gas phase (H_2, CO, CO_2, CH_4) produced is recovered for used as fuel.
- Gasification [31-40] produces H_2, CO, H_2O, and CO_2. The obtained syngas can be transformed to Fischer-Tropsch diesel [41] and methanol [42] and then to DME [43]. The thermic process starts with the drying of the biomass at 100-150°C then the fast pyrolysis between 200°C and 500°C. At this stage, the dried biomass breaks down to tar gases and biochar. The temperature continues to increase between 800°C and 1200°C with the addition of air for combustion and cracking which produces CO_2, water, and lighter tar. Between 650°C and 900°C, reduction (*Reactions 1.1, and 1.2*) is the last step and produces syngas (H_2 and carbon oxides in the gas phase), char, and ash. This process is particularly important in the

project framework. The biomass gasification process leads to the formation of carbon dioxide, water, and impurities such as methane, tar, H_2S, HCl, and NH_3. The content of these impurities varies depending on the biomass feedstock, reactor type, and gasification conditions [44]: an efficient and cost-effective process is needed to purify the produced syngas. According to temperature, reactor type, feedstock and catalyst used the content of hydrogen can be optimized [45]. Furthermore, to ensure a reduced environmental footprint, the main undesirable product (CO_2) must be separated for further use. Industrial processes generally call in a separation unit such as amine absorption (50 °C), membrane separation (<400 °C), or adsorption with activated charcoal (<300 °C), which require upstream gas cooling [46].

- $H_2O + C \rightarrow H_2 + CO$ (Reaction 1.1)
- $CO_2 + C \rightarrow 2CO$ (Reaction 1.2)

The intermittent production of electricity from renewable energies such as solar and wind power makes it necessary to store this energy excess. Thermochemical treatments of biomass consumes energy to produce a mixture of gases, especially hydrogen: this is the *Power to gas* conversion transforming electric from solar or wind energy into a chemical energy, that makes hydrogen so interesting. The storage of excess in hydrogen makes it possible to restore electricity production during deficit, which makes the production of the energy mix more flexible.

1.2.2. Hydrogen production and consumption

Hydrogen is often described as the new free-carbon combustible of the future [47-49]. In industry, hydrogen production is used for petroleum refining (52%) and the Haber-Bosch process to produce ammonia (43%) [50, 51]. This industrial process uses hydrogen at 400-500°C under 300 bar with nickel or iron catalysts. The rest of hydrogen consumption arises from a chemical product such as methanol [42], metal refining, hydrogenation, and Fischer-Tropsch process *(Reaction 1.3)* [41, 50-55].

- *(2n+1)* $H_2 + nCO \rightarrow C_nH_{2n+2} + nH_2O$ $n = [10\text{-}20]$ (Reaction 1.3)

  at 150-300°C with Co, Fe and Ru catalysts

  at 330-350°C with Fe catalysts

In details, H_2 is using in three fields [56]:

- **Fuel** for transportation and electric peaking plants,
- **Heat** for the steel, cement, paper, food, and aluminum and buildings industries,
- **Feedstock** for chemistry such as plastics, fertilizers, fuel refining and products as glass.

Hydrogen is the most abundant element in the solar system but must be synthesized on earth [57]. Indeed, some articles attest the presence of natural hydrogen on earth stay unexploited and an unknown potential yet [58-60]. Global hydrogen production was 74 Mt in 2018, but the overwhelming majority of production came from fossil fuels (Table 1.1), named grey hydrogen in contrast to green hydrogen from renewable resources. Water is the only sub-product of using hydrogen as a fuel, but grey H_2 contributes 0.8 $Gt_{CO2\cdot eq}$/yr due to its fossil origin. The H_2 economy is growing up with the increasing of industrial applications and new sectors such as transportation and electricity storage. It is considered that H_2 production expends to 200 Mt in 2030 [6]. A minor part of the H_2 production is made by water electrolysis [61]. Carbon-free hydrogen production is possible by electrolysis [62] using renewable electricity from wind and solar power, which are more and more profitable and competitive. In addition, the expansion of hydrogen from renewable and biomass treatment generating a hydrogen economy for the growth of the low-carbon energy market [55]. Industrial transition and local energy projects fall into place to decrease environmental impact of CO_2 emission by replacing fossil fuels with hydrogen for example:

• In France, the GRHYD project is studying the injection of 20% hydrogen into the city gas grid. Hydrogen has a very low density (0.09 g/L) and is stored under pressure. Comparatively, hydrogen higher and lower heating values (HHV_{H2} = 142 MJ/kg; LHV_{H2} = 120 MJ/kg) are much better than

those of natural gas (52 MJ/kg; 47 MJ/kg) (Table 1.1). This way of used hydrogen improves the energy capacity of town gas and makes use of available and operating fossil fuels installation. In addition, the French *energy transition and green growth* policy wish to increase low-carbon hydrogen production at 40% in 2030 to limit also CO_2 emission.

ping hydrogen in the steel production process. Currently, $1.6 \cdot 10^9$t/yr rising [63] of steel is produced worldwide and is responsible for about 9% of the GHG emissions from fossil fuels. Replacing natural gas with H_2 may avoid the 780 kg of coal needed in blast furnaces to produce 1 kg of steel.

Table 1.1: Higher and lower heating values of few classic fuels.

Fuel		H_2	Natural gas	Diesel Fuel	Gasoline	Charcoal	Wood (dry)
LVH	MJ/kg	120	47	43	43	28	15
HHV		142	52	46	46	30	16

Advantages of H_2:

- potentially produced from renewable sources,
- transportation cost lower than electricity,
- economically profitable,
- clean energy; zero-emission when used,
- high yields from biomass,
- high purity from electrolysis,
- storing renewable energy during a long time and during intermittent production,
- town gas adapted to contain part of H_2,
- pure when H2 come from hydrolysis.

Drawbacks of H_2:

- purification step when H_2 come from biomass thermochemical treatment mix gas,
- high reactor cost,
- gaseous state until -253°C,
- low density causes leak and storage at high pressure.

From biomass [45], hydrogen belongs to the syngas coming from pyrolysis or gasification. In the presence of water, the Sorption Enhanced Steam Reforming (SESR) and Sorption Enhanced Water Gas Shift (SE-WGS) reactions – described in the following part – allow the purification of H_2 by producing more H_2 and CO_2. The carbon dioxide must then be captured to further GHG emissions and to obtain an H_2-rich syngas.

1.3. CO_2 capture: technologies and issues

Since the eighteenth century, the emission and concentration of carbon dioxide in the atmosphere have continuously grown and risen above 400 ppm. The CO_2 emissions in 2020 reach 34 Gt and only 40 Mt have been captured by human activities, *i.e.* 0.1% [6]. From now on and in the long term, an important part of the strategy to reduce CO_2 emission includes a massive CO_2 capture [64]. To achieve several gigatons of captured CO_2, technologies and technical innovations are being studied and developed under the terms Integrated Carbon Capture and Utilization (ICCU) [65]. Captured CO_2 is firstly separated, then compressed, and finally used or transported and stored [66]. Global CO_2 capture technologies are applied in three systems using fossil energy or biomass [67].

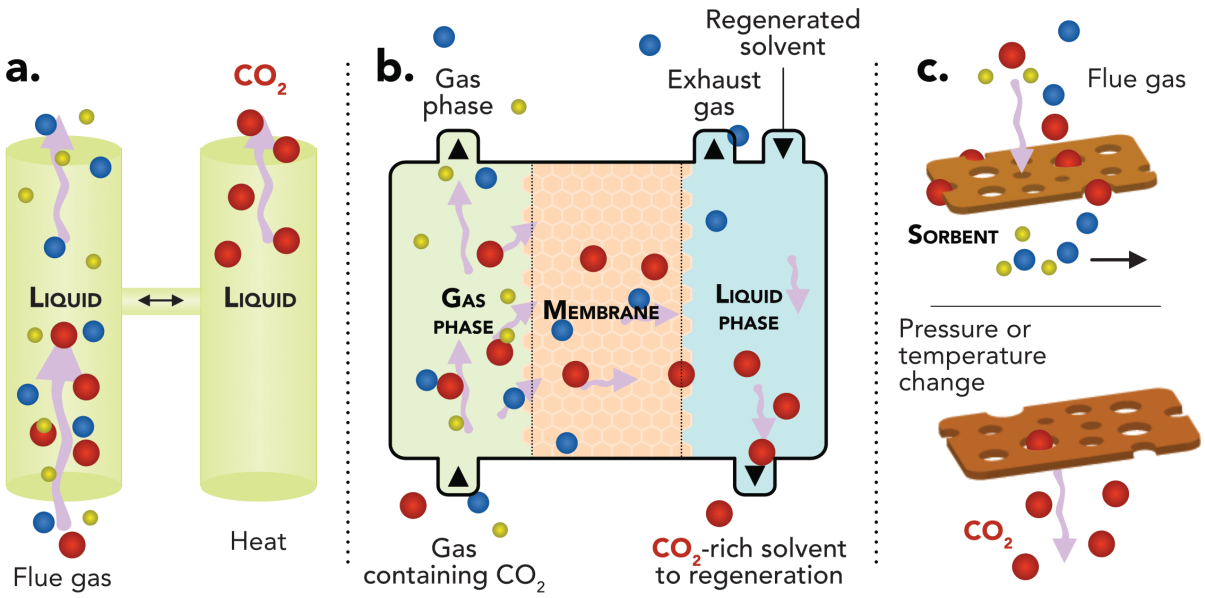

Figure 1.5: Representation of CO_2 separation methods a) by solvent, b) by membrane and c) by solid sorbent [68].

For these systems, different industrial approaches of CO_2 capture and separation are possible with adsorbed solvents (Fig. 1.5.a.), polymeric membranes (Fig. 1.5.b.), cryogenic separation of gas mixtures or solid sorbents materials (Fig. 1.5.c.) as zeolites, activated carbon and alumina:

- **Post-combustion** (Fig. 1.6) capture isolates the flue gases from combustion before they are emitted to the atmosphere. The CO_2 is then separated and adsorbed onto a chemical sorbent

[69, 70, 71]. Liquid solvents as monoethanolamine are used to capture a light fraction of CO_2 (around 3-15%) [67]. In the condition of smoke from the exhaust, for low CO_2 concentrations, aqueous amines are the appropriate adsorption sorbent/solvent. The development of ceramic and carbon-based sorbents could replace amine solvents.

- **Pre-combustion** (Fig. 1.6) from fuels to syngas production contains CO_2 [69]. By WGS reaction in the presence of water, carbon monoxide in the gas mixture is transformed to CO_2 and reducing H_2O that produces more H_2. The global process requires more energy than post-combustion method, but higher contents of H_2 and CO_2 are produced. In this way, the CO_2 concentration at the reactor outlet is currently between 15% and 60% and can be captured by a physical or chemical adsorption process. Emerging technologies also used ceramic such as membranes or carbonate hydrotalcites and silicates.

- **Oxy-fuel** (Fig. 1.6) combustion uses pure oxygen instead of air. The O_2 required is separated from the air by cryogenic distillation or by membranes [72, 73, 74]. The resulting syngas is particularly rich in CO_2 (≥80%) and H_2O and can be easily recycled by water condensation. To replace energy-intensive cryogenic distillation, O_2 separation is possible by ion transport with nascent ionic liquid [74-76], membranes, O_2/N_2 adsorbents or chemical oxygen looping [77].

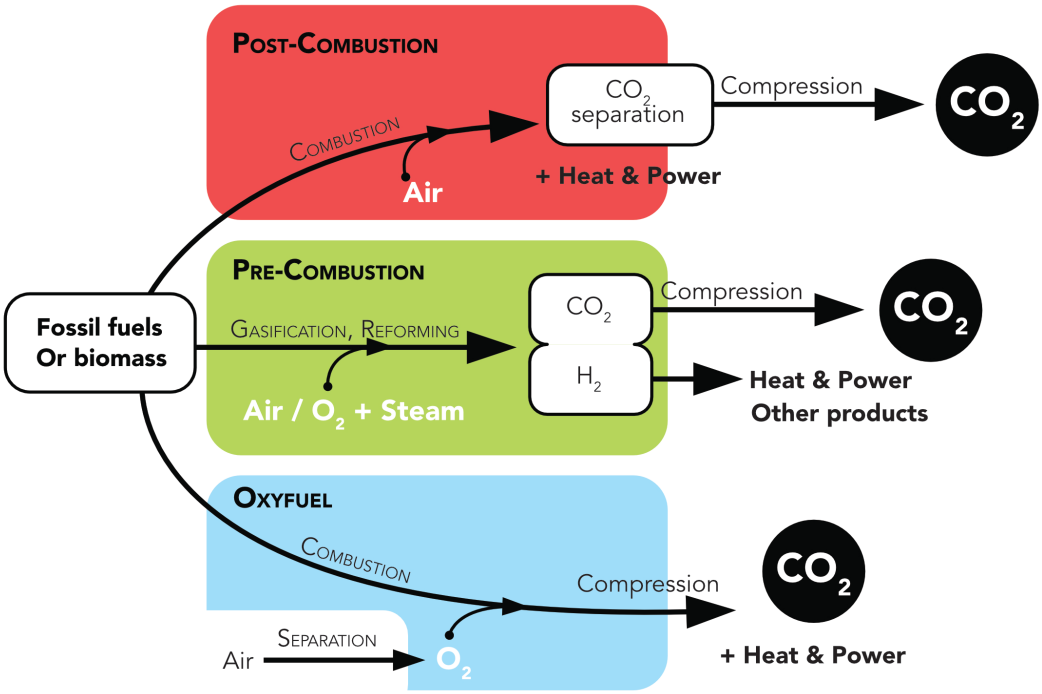

Figure 1.6: CO_2 separation according to fossil fuels or biomass treatment.

Progress about sorption capacity materials is oriented to optimization of industrial applications on economic cost [77], purity, and sorbent resistance of poising impurities increasing. In addition to CO_2 capture at industrial sites, sorbents can adsorb CO_2 at low concentrations, for example with a solid amine capable of adsorbing CO_2 at 400 ppm [78]. This value corresponding to the concentration in air is reached by physical separators such as membranes [72] or a lot of sorbents such as aqueous hydroxide, amines on support or solid alkali carbonates [79], super-basic guanidines [80] and allows direct CO_2 capture (DAC) from ambient air [71, 81-84].

Sorbents can be regenerated by adsorption/desorption cycles after CO_2 recovery by increasing temperature or decreasing pressure. Solid sorbents [66, 84] capture and desorb CO_2 at different temperatures depending on the material. CaO as a CO_2 sorbent (Reaction 1.4) is often used in the purification of high-temperature gases from coal and biomass gasification or combustion [3, 85-90] because its sorption capacity is greater than that of activated carbon [91] and mixed oxides (Mg, Zn, Cu, etc.). It is effictive over a large range of temperature (200 – 700°C) and is easily regenerated beyond 800°C [92].

$CaO + CO_2 \leftrightarrow CaCO_3$ ΔH^0_{298K} = -178.2 kJ mol^{-1} (Reaction 1.4)

The absorbed CO_2 can be valorized in chemical applications to produce nitrate fertilizers from urea, salicylic acid or polycarbonate, for example. To a lesser extent, CO_2 is used in the agri-food sector and the development of supercritical CO_2 reaction and separation [93] with a current industrial application. The tremendous amount of CO_2 emitted and potentially storable exceeds any valorization and underlies a long-term isolation of the atmosphere. The *IPCC special report: Carbon dioxide capture and storage* (2005) [67] well describes a geological technology to sequester CO_2 underground. The estimation of sequestration capacity is huge: it could be split in gas and oil empty reserves representing 675-900 $GtCO_2$, deep saline formations representing at least 1000 $GtCO_2$ and other possibilities such as coal seams, coal beds, abandoned mines and in offshore storage sites [94]. In addition, the density of CO_2 (1.87 kg/m^3 at 15°C, 1bar) increases with depth and forms a supercritical fluid below 800 m. This state of matter facilitates diffusion through the soil, small pore space thanks to a low viscosity, a diffusion coefficient close to gases, and a high density around 50-80% of the density of water.

CO_2 is sequestrated through the carbonation of magnesium and calcium oxides by reaction with natural materials [95, 96]. Among the sorbent minerals, clays, chlorites, micas, and feldspars stand in a deep surrounding geological formation.

1.4. SESR

1.4.1. Reaction and industrialization

Steam reforming (SR) is the most widely used process to produce H_2 on a wide scale and mainly methane reforming (SMR, Reaction 1.5) from natural gas [97]. The SR reaction purifies the gas mixture containing H_2, CO, CO_2, H_2O, CH_4 and other heavier hydrocarbon impurities through efficient conversion to H_2 and CO_2 capture, resulting in low concentration of residual CO and CO_2. In addition, the catalysts and sorbents are lowly subject to coking deposition [98]. In presence of water, the water gas shift reaction performed the total oxidation of CO to CO_2. With increasing temperature, the exothermic WGS reaction is less favorable for H_2 production (Reaction 1.6). In the other hand, Le Chatelier's principle improves H_2 production with excess of water. The catalysts used for SR are nickel-based materials to partially oxidize hydrocarbons at classically 700-900°C for SMR (Reaction 1.5*)*, between 14 and 20 bar.

The *in-situ* CO_2 capture (Reaction 1.4) improves biomass gasification and steam reforming (of methane for example) [99] by displacing the equilibrium of the water gas shift to hydrogen production. Both operations enrich the syngas with hydrogen and then improve its energy capacity. This process is also called Sorption Enhanced Hydrogen Production.

$CH_4 + H_2O \leftrightarrow CO + 3H_2$ ΔH^0_{298K} = 241 kJ mol^{-1} (Reaction 1.5)

$CO + H_2O \leftrightarrow CO_2 + H_2$ ΔH^0_{298K} = -41.1 kJ mol^{-1} (Reaction 1.6)

The Sorption Enhanced Steam Reforming (SESR) and Sorption Enhanced Water Gas Shift (SE-WGS) can be combined in a single reactor to intensify syngas purification. Describe by Iliuta [98], several conditions of nickel catalysts are listed to perform methane [100-106] steam reforming but also to perform ethanol [107-109], glycerol [110-111], biogas [112-113], bio-oil [114-115] and acetic acid [115-116] steam reforming between 525°C to 800°C. Nickel nanoparticles increase catalytic activity

by well-dispersed deposition on the support. The optimization of hydrocarbon conversion to hydrogen also depends on the steam/carbon ratio (S/C), which is generally between 2.5 and 5 [117]. The final concentration of H_2 in the syngas can reach 99% and usually >90% [100-116]. The reaction conditions to attain this H_2-rich syngas can be assured at 550°C until 800°C [118-119] with or without pressure. The characteristics required undertaking this process configuration led us to the development of sorbent materials, often porous materials [120] to ensure the sorption of CO_2 with high thermal stability under cyclic (sorption/desorption) operating conditions [117, 121]. The goal is then to adapt the properties of the sorption material to the temperature and pressure conditions of reforming. At high temperatures, mixed oxides and especially those containing CaO [122-124] are often studied and used for CO_2 sorption capacity.

1.4.2. Sorbent/catalyst bifunctional materials

The development of bifunctional materials allows to adapt active sites properties: catalytic and chemisorption. The term *in-situ* CO_2 capture referring to mass transfer earning improve by closeness of both active sites [125]. Nickel can be associated with different sorbent supports such as natural-based materials: mayenite [126, 127], limestone [53], dolomite [128-129], hydrotalcite/CaO phases [130-131] for SMR. Ni-based catalysts/sorbents [100] containing CaO sites can be synthetized to obtain hybrid materials with interesting structures due to their porous properties, dispersion of CaO and Ni sites. Beyond or together with the nickel catalyst, metals such as Cu [132-133], Co [109, 134-135], Pd [136], Fe [137] often supported by mayenite [138] are used for methane [100], methanol [132], ethanol [139] and tar [135] reforming also in the SESR.

Bifunctional materials based on Ni and CaO form catalysts in combination with a support such as Al_2O_3 [140-143] or hydrotalcite often described in the literature [144-153]. Hydrotalcite is a magnesium-aluminum hydroxycarbonate, a layered double hydroxide (LDH).

1.4.3. State of the art and LDH applications – Composition modification

The hydrotalcite structure has well-known CO_2 sorption properties [154, 155], and the mixed oxides obtained by calcination them at moderate temperature lead to optimal CO_2 sorption capacity and regeneration capability [154, 156]. The LDH (Figure 1.7) formula is globally $[M^{2+}_{(1-x)}M^{3+}_{x}(OH)_2][A]^{n-}_{x/n}\cdot zH_2O$ where M^{2+} is a divalent cation, M^{3+} is a trivalent cation, *n*- is the anion charge, and z is the hydration.

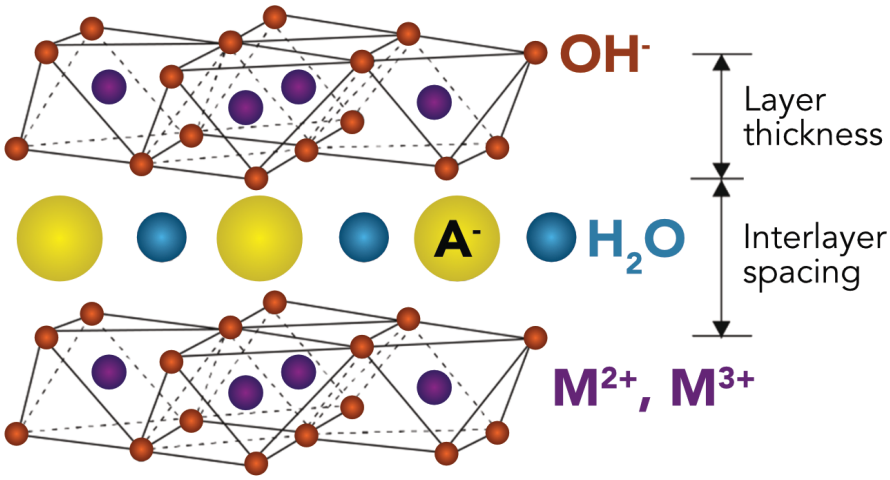

Figure 1.7: Illustration of LDH structure. The neutral charge is respected between hydroxide, interlayer anions and metal charges.

The most advantage of this structure is the possibility to exchange alkaline earths (Ca^{2+} instead of Mg^{2+}) to increase the sorption temperature and improve the sorption capacity [157]. The exchange of a part of the Mg^{2+} by Ca^{2+} will permit to adapt the CO_2 sorption/desorption temperature to the effective boundary conditions of catalytic reforming. Indeed, at atmospheric pressure, magnesium oxide-based hydrotalcite absorbs until 400°C whereas calcium oxide-based hydrotalcite absorbs between 400°C and 600°C and desorbs beyond according to Ca/Al ratio of the hydrotalcite [158]. On the other hand, CaO sorbents, subject to a loss of CO_2 sorption capacity during regeneration cycles, have been effectively stabilized by Mg and/or Al incorporation as an inert support [159]. These materials lead to the dispersion of CaO particles during the synthesis procedure, limiting the sintering phenomenon due

to multiple carbonation/calcination cycles. Then, the CO_2 sorption capacity can be maintained at a level of theoretical values for more than 20 cycles by the addition of MgO [160] and for 10 cycles by the addition of Al in an optimal Ca/Al molar ratio of 7/1 [161]. The maximum sorption capacity of CaO is theoretically 0.78 $g_{CO2}/g_{sorbent}$.

A width interlayer space in which the nature of the anions (CO_3^{2-}, SO_4^{-2}, or NO_3^-) can be altered to affect the kinetics and sorption capacity of carbon dioxide [162]. The "sand rose" spheroidal morphology observed with CO_3^{2-} anions explained the large BET surface area and the better CO_2 sorption capacity [163]. The exchange of stearate (and longer molecules) has been extensively studied as a long-carbon-chain organic anion and resulted in a better CO_2 capture performance due to more surface basicity sites (O^{2-}) after calcination [164].

The CO_2 sorption is favored by the presence of steam that also assists the desorption step [165, 166]. According to Reddy et al. [167], the sorption capacity of an LDH material between 100 and 400°C is lower under dry conditions than under wet conditions (water saturation of 12%) and presents easier desorption.

LDH structures also present the possibility of exchanging Mg^{2+} and Al^{3+} ions with Ni^{2+} and Fe^{3+}, respectively, to add a catalytic effect to these sorbents for WGS and reforming reactions. This goal will be further investigated. In the case of iron as an active metal, the conversion of carbon formed on the catalyst surface can be improved [168].

Different methods of synthesizing hydrotalcite are available and each of them may bring benefit. Urea hydrolysis [169], hydrothermal [170, 171], sol-gel process [172], or co-precipitation [173] are the more common methods. Among these possibilities, the method chosen must allow the substitution of magnesium by calcium, of carbonate by a bigger anion, and aluminum by a transition metal like nickel or iron. In the urea hydrolysis method, urea decomposes to a carbonate anion that cannot be replaced by a bigger anion. In the hydrothermal method, diffusion of metal ions is expected to be difficult without available and efficive stirring equipment for the addition of calcium oxide. The sol-gel process is interesting to change carboxyl groups in hydrogel matrices and pH at the same time, but needs many reagents. Finally, the co-precipitation method is not only the more used and easiest to

scale up, but it also allows cations and pH modification independent of the anion used and its solubility.

1.4.4. H_2S poisoning

Catalytic poisoning by H_2S is not studied in this thesis but stay an interesting and important problem for heterogeneous catalysts, which are deactivated by hydrogen sulfide.

Among the gases produced by biomass gasification, hydrogen sulfide is present in different proportions ranging from a few hundred ppm to a few percent according to various biomass sources [167, 174]. H_2S is a corrosive gas that deteriorates natural gas infrastructure and metal piping. This gas is also very toxic to living beings at a threshold limit value (TLV) for workers of time-weighted average (TWA) at 5 ppm i.e. 7 mg/m^3; of short-term exposure limit (STEL) at 10 ppm i.e. 14 mg/m^3 and a lethal one at CP_{50} = 444 ppm (median lethal concentration) [175, 176]. In heterogeneous catalysis, H_2S is a poison that deactivates metal active sites, hence the importance of syngas purification. The historic industrial process for the separation of H_2S is the amine gas treatment or the Girbotol process developed since the 1930's [177]. By the same company, other gases, such as CO_2, HCl, SO_2, NO_2, and HCN are removed. Different amines are used to optimize gas separation, such as fromalkylamine solution of diethanolamine (DEA), diglycolamine (DGA), diisopropylamine (DIPA), methyldiethanolamine (MDEA) and monoethanolamine (MEA) associated to RNH_2, all of them carry out an acid-base reaction for H_2S treatment (Reaction 1.7). Ion formation separates H_2S from the syngas without reversibility and the post-treatment produces concentrated H_2S via a boiling step.

$$RNH_2 + H_2S = RNH_3^+ + HS^- \qquad \text{(Reaction 1.7)}$$

The wet process of sulfuric acid removal is realized in desulfurizing industrial facilities (scrubbers) to produce commercial sulfuric acid [178, 179]. Successive reactions transform H_2S to SO_2 by combustion with O_2, oxidation of SO_2 to SO_3 and hydration to H_2SO_4. The acid is then condensed.

Other options for H_2S removal are possible using a fixed bed of adsorbent for example:

- Natural-based zeolites [180-182]: Zn/zeolite doped efficient at 200-300°C, zeolite 13X or with impregnated activated carbon also for CO_2 capture;
- Activated carbons [183-184]: prepared from sweet potato leaves at room temperature and regenerable at 220°C. The choice of biomass source is explained by the presence of iron oxide in this vegetable capable of removing 0.60 g_{H2S}/g_{Fe2O3}.
- Metal oxides, mixed oxides and nanocomposites [185-187] such as Mn_2O_3, ZnO_2 Fe_2O_3, V_2O_5, CuO, CoO to selectively oxidize H_2S. The H_2S removing process using molybdenum oxide operates at 65-90°C under pressure (10-19 bar) and is efficive at a low concentration of 38-73 ppm. The oxide can be supported on a mesoporous material such as alumina and able to adsorb PH_3 in addition to H_2S.

Adsorption sites effictive to capturing CO_2 are also able to capture H_2S [188-190]. In particular, sorption on LDH is partially irreversible, competitive with CO_2, and stronger than CO_2 sorption, but also slower [156]. Van Dijk *et al.* [169] suggest that LDH sorption capacity decreases during CO_2 sorption/desorption cycles in the presence of H_2S, but becomes quite stable after few cycles. The chemical issues of H_2S sorbent are to understand the saturation time of the absorption sites which could counteract the deactivation problem of the metal sites.

1.5. Objectives of the thesis

The concept of this thesis tends to be part of the overall sustainable research project. Each step of the development of the study takes into account the concepts of green chemistry until the application.
This thesis presents the development of hydrotalcite-derived mixed oxides as CO_2 sorbents. First the Chapter 2 describes the synthesis method, the types of analysis used to characterize sorbents and catalysts, the setup and conditions used to measure sorption capacity and SESR catalytic activity.

To produce LDH and then LDO, different parameters are studied and explained in the Chapter 3: the method of sorbent synthesis (urea hydrolysis, hydrothermal, co-precipitation) at various excess of anion equivalent and the calcination temperature. Several fundamental parameters were studied in this work for one the synthesis method selected. If the (Mg+Ca)/Al molar ratio is still equal to 3/1 as commonly reported in the literature [174], variables Mg/Ca ratios were evaluated to improve CO_2 sorption properties and stability. Sodium carbonate typically used as the interlayer space anion was changed by bigger anions. The literature reports studies on interlayer charge-compensating anions (Cl^-, NO_3^-, CO_3^{2-}, HCO_3^-, SO_4^{2-}…) [162, 163, 175] to increase the porosity of the materials. Better sorption sites accessibility of LDHs intercalated with long carbon chain carboxylic acids (from stearate to palmitic acid) is expected [164, 176] through the creation of more surface basicity sites (O^{2-}) but no obvious difference in CO_2 capture capacity was observed for carbon chain lower than 10. Moreover, Yong et al. [162] previously reported the positive effect of the higher valence of CO_3^{2-} compared to OH^- on CO_2 sorption capacity [162]. Thereby, this work focuses on another sodium anion (oxalate) with the same valence of sodium carbonate (2), a different shape and valence from stearate (1), and not yet reported in the literature. The very bigger size of the stearate could largely increase the interlayer spacing and bring particular porosity properties if the structure does not collapse. Finally, two different pH values were evaluated affecting structural and morphological properties. The composition, structure, morphology, porosity, stability and sorption capacity are analyzed and the data are compared according to synthesis parameters.

The Chapter 4 presents the characterization of catalyst as a sorbent in the Chapter 3 with the same different techniques. The comparison focuses on the different methods of synthesis by one-pot or impregnation of Ni or Fe at different molar percenttages (Ni 5_{wt}%, Ni 10_{wt}%, Fe 10_{wt}% and Fe 20_{wt}%) and the evolution between the characteristics of the catalysts and their corresponding sorbents. The iron catalysts were synthesized and compare to the nickel ones, even the iron has a lower activity [137] at low temperature. In addition to all the analysis realized on the sorbent samples, an H_2-TPR was performed. The catalysts thus compared to each other and with their corresponding sorbent permits to evaluate the impact, influence and behaviors of the metal content on porosity, morphology, sorption capacity and stability.

The reactivity and stability is presenting in Chapter 5. The SESR activity according to the Ni and Fe catalysts selected at this stage is measured from 600°C to 750°C at each 50°C at various steam/carbon ratio (2.3, 3.5, 4.6, 6). The evaluation of the selectivity and productivity of H_2, CO_2 and CO is done in short and cyclic tests corresponding to a succession of reforming/desorption steps to study the stability of the performance. The conversion of tar and H_2 yield complete the interpretation to determine trends, characteristics and the final best synthesis conditions with reaction parameters to optimize SESR activity. The analysis of the post SESR tests brings also the causes of catalytic desactivation, structure and porosity transformation.

Finally, a general conclusion allows to take over the principal results, the synthesis and experimental trends and to expose the optimized conditions accompanied by a reflection, perspectives and criticism on the realized project.

References

[1] First IPCC Assessment report (1990).

[2] Second to Fifth IPCC Assessment report (1995, 2001, 2007, 2014).

[3] Smil, V.: Energy Transitions: Global and National Perspectives (2017).

[4] BP Statistical Review of World Energy analyses data on world energy markets from prior year. (2020).

[5] Climate change 2014, Mitigation of climate change – Working groupe III contribution of the Fifth Assessment report of the Intergovernmental Panel on Climate Change (2014).

[6] IEA report – Net Zero by 2050: a roadmap for the global energy system (2021).

[7] 19th EurObserv'ER report summary: the state of renewable energies in Europe (2019).

[8] Stratégie Française pour l'énergie et le climat – Programmation pluriannuelle de l'énergie, Ministère de la transition écologique et solidaire (2019).

[9] ADEME – Guide des facteurs d'émission et sources bibliographiques utilisées v.6.1, Chapitre 2: facteurs associés à la consommation direct d'énergie (2010).

[10] Hydrogen in Europe – SINTEF Final report of pre-study (2019).

[11] Durville, J.L., Gazeau, J.C., Nataf, J.M., Cuengniet, J., Legait, B.: Filière hydrogène-énergie – Ministère de l'écologie, du développement durable et de l'énergie & Ministère de l'économie, de l'industrie et du numérique (2015).

[12] Avis de l'ADEME, Le vecteur hydrogène dans la transition énergétique (2018).

[13] Wang, A., Van der Leun, K., Peters, D., Buseman, M.: European hydrogen backbone – How a dedicated hydrogen infrastructure can be created (2020).

[14] Long, H., Li, X., Wang, H., Jia, J.: Biomass resources and their bioenergy potential estimation: A review, Renewable and Sustainable Energy Reviews, 26, 344-352 (2013).

[15] De Jong, Stichnothe, H., Bell, G., Jorgensen, H.: Bio-based chemicals – Update 2020, IEA Bioenergy report (2020).

[16] Commission decision establishing guidelines for the monitoring and reporting of greenhouse gas emissions pursuant to directive 2003/87/EC of the European Parliament and of the Council, Official Journal of the European Union (2004/156/EC).

[17] Girad, P., Fallot, A.: Review of existing and emerging technologies for the production of biofuels in developing countries, Energy for Sustainable Development, 10, 92-108 (2006).

[18] Singh, S.K.: Biological treatment of plant biomass and factors affecting bioactivity, Journal of Cleaner Production, 279, 12356 (2021).

[19] Gillet, S., Aguedo, M., Petitjean, L., Morais, A.R.C., da Costa Lopes, A.M., Lukasik, R.M., Anastas, P.T.: Lignin Transformations for high value applications: towards targeted modifications using green chemistry, Green Chemistry, 19, 4200-4233 (2017).

[20] Ragauskas, A.J., Beckham, G.T., Biddy, M.J., Chandra, R., Chen, F., Davis, F.M., Davison, B.H., Dixon, R.A., Gilna, P., Keller, M., Langan, P., Naskar, A.K., Saddler, J.N., Tschaplinski, T.J., Tuskan, G.A., Wyman, C.E.: Lignin Valorization – Improving lignin processing in the biorefinery, Science, 344, 709-719 (2014).

[21] Baig, M.: Extraction de composants de biomasse lignocellulosique oléagineuse en milieu eau et CO_2 supercritique et fonctionnalisation enzymatique, PhD thesis Montpellier II University (2012).

[22] Peng, B., Yao, Y., Zhao, C., Lercher, J.A.: Towards quantitative conversion of microalgae oil to diesel-range alkanes with bifunctional catalysts, Angew. Chem. Int. Ed., 51, 2072-2075 (2012).

[23] Juneja, A., Singh, V.: Green Energy to Sustainablility – Stratégies for Global Industries, Chapter 8: Sustainable Platform Chemicals from Biomass, First Ed., 2020.

[24] Yadav, M., Paritosh, K., Pareek, N., Vivekanand, V.: Coupled treatment of lignocellulosic agricultural residues for augmented biomethanation, Journal of Cleaner Production, 213, 75-88 (2019).

[25] Albero, J., Dominguez, E., Corma, A., Garcia, H.: Continuous flow photoassisted CO_2 methanation, Sustainable Energy Fuels, 1, 1303-1307 (2017).

[26] Schubert, M., Wilhelm, M., Bragulla, S., Sun, C., Neumann, S., Gesing, T.M., Pfeifer, P., Rezwan, K., Bäumer, M.: The Influence of the pyrolysis temperature on the material properties of cobalt and nickel containing precursor derived ceramics and their catalytic used for CO_2 methanation and Fischer-Tropsch synthesis, Catalysis Letters, 147, 472-482 (2017).

[27] Mohan, D., Pittman, C.U., Steele, P.H.: Pyrolysis of Wood/Biomass for Bio-oil: A critical review, Energy & Fuel, 20, 848-889 (2006).

[28] Vamvuka, D.: Bio-oil, solid and gaseous biofuels from biomass pyrolysis processes – An overview, Int. J. Energy Res., 35, 835-862 (2011).

[29] Jahirul, M.I., Rasul, M.G., Chowdhury, A.A., Ashwath, N.: Biofuels production through biomass pyrolysis – A technological review, Energies, 5, 4952-5001(2012).

[30] Tripathi, M., Sahu, J.N., Ganesan, P.: Effect of process parameters on production of biochar from biomass waste through pyrolysis: A review, Renewable & Sustainable Energy Reviews, 55, 467-481 (2016).

[31] De Andrés, J.M, Narros, A., Rodriguez, M.E.: Air-steam gasification of sewage sludge in a bubbling bed reactor: Effect of alumina as a primary catalyst, Fuel Process. Technol., 92, 433-440 (2011).

[32] Gerber, S., Behrendt, F., Oevermann, M.: An Eulerian modeling approach of wood gasification in a bubbling fluidized bed reactor using char as bed material, Fuel, 89, 2903-2917 (2010).

[33] Mahishi, M.R., Goswami, D.Y.: An experimental study of hydrogen production by gasification of biomass in the presence of a CO_2 sorbent, Int. J. Hydrogen Energy, 32, 2803-2808 (2007).

[34] Mohd Salleh, M.A., Kisiki, N.H., Yusuf, H.M., Ghani, W.A.: Gasification of biochar from empty fruit bunch in a fluidized bed reactor, Energies, 3, 1344-1352 (2010).

[35] Singh, D., Yadav, S., Rajesh, V.M., Mohanty, P.: Groundnut shell gasification performance in a fluidized bed gasifier with bubbling air as gasification medium, Environ. Technol., 40, 3140-3152 (2018).

[36] Mastellone, M.L., Arena, U.: Olivine as a tar removal catalyst during fluidized bad gasification of plastic waste, AIChE J., 54, 1656-1667 (2008).

[37] Noda, R., Ito, T., Tanaka, N., Horio, M.: Steam gasification of cellulose ad wood in a fluidized bed of porous clay particles, J. Chem. Eng. Jpn., 42, 490-501 (2009).

[38] Kumar, A., Jones, D.D., Hanna, M.A.: Thermochemical biomass gasification: a review of the current status of the technology, Energies, 2, 556-581 (2009).

[39] Loha, C., Chattopadhyay, H., Chatterjee, P.K.: Thermodynamic analysis of hydrogen rich synthetic gas generation from fluidized bed gasification of rice husk, Energy, 36, 4063-4071 (2011).

[40] Corella, J., Toledo, J.M., Molina, G.: A review on duel fluidized-bed biomass gasifiers, Ind. Eng. Chem. Res., 46, 6831-6839 (2007).

[41] Van Thuijl, E., Roos, C.J., Beurskens, L.K.M.: An overview of biofuel technologies, markets and policies in Europe (2003).

[42] L'Hospital, V., Angelo, L., Zimmermann, Y., Parkhomenko, K., Roger, A.C.: Influence of the Zn/Zr ratio in the support of a copper-based catalyst fot the synthesis of methanol from CO_2, Catalysis Today, 369, 95-104 (2021).

[43] Xu, M., Lunsford, J.H., Goodman, D.W., Bhattacharyya, A.: Synthesis of dimethyl ether (DME) from methanol over solid-acid catalysts, Applied Catalysts A: General, 149, 289-301 (1997).

[44] Milne, T.A., Evans, R.J., Abatzoglou, N.: Biomass Gasifier "Tars": Their Nature, Formation, and Conversion, Report NREL/TP-570-25357; National Renewable Energy Laboratory: Golden, CO, USA, 1998.

[45] Ni, M., Leung, D.Y.C., Leung, M.K.H, Sumathy, K.: An overview of hydrogen production from biomass, Fuel Process. Tech., 87, 461-472 (2006).

[46] Courson, C., Gallucci, K.: CaO-based High-temperature CO_2 Sorbents. In: Wang, Q. (ed.) Pre-combustion Carbon Dioxide Capture Materials, pp. 144-237. Royal Society of Chemistry (2018).

[47] Zakkour, P., Cook, G.: CCS Roadmap for industry: High-purity CO_2 sources – Sectoral Assessment Final report (2010).

[48] Wallace, J.S., Ward, C.A.: Hydrogen as a fuel, Int. J. Hydrogen Energy, 8, 255-268 (1983).

[49] Veziroglu, T.N., Barbir, F.: Hydrogen – The wonder fuel, Int. J. Hydrogen Energy, 17, 391-404 (1992).

[50] Balonek, C.M., Lillebo, A.H., Rane, S., Rytter, E., Schmidt, L.D., Holmen, A.: Effect of alkali metal impurities on Co-Re caralysts for Fischer-Tropsch synthesis from biomass-derived syngas, Catal. Lett., 138, 8-13 (2010).

[51] IEA report for the G20: The Future of Hydrogen – Seizing today's opportunities (2019).

[52] Unruh, D., Pabst, K., Schaub, G.: Fischer-Tropsch synfuels from biomass: Maximizing carbon efficiency and hydrocarbon yield, Energy Fuels, 24, 2634-2641 (2010).

[53] Broda, M., Manovic, V., Imtiaz, Q., Kierzkowska M.A., Anthony, E.D., Mueller, C.R.: High-purity hydrogen via the sorption enhanced steam methane reforming reaction over a synthetic CaO-based sorbent and a Ni-catlayst, Environ. Sci. Technol., 47, 6007-6014 (2013).

[54] Zhang, F., Zhao, P., Niu, M., Maddy, J.: The servey of key technologies in hydrogen energy storage, Int. J. Hydrogen Energy, 41, 14535-14552 (2016).

[55] Harrison, D.P.: Sorption-enhanced hydrogen production – A review, Int. Eng. Chem. Res., 47, 6486-6501 (2008).

[56] BloombergNEF report: Hydrogen Economy Outlouk – Key message (2020).

[57] Da Silva Veras, T., Mozer, T.S.: Hydrogen – Trends, Production and Characterization of the main process worldwide, Int. J. Hydrogen Energy, 42, 2018-2033 (2017).

[58] Arrouvel, C., Prinzhofer, A.: Genesis of natural hydrogen: New insights from thermodynamic simulations, Int. J. Hydrogen Energy, 46, 18780-18794 (2021).

[59] Donzé, F.V., Truche, L., Namin, P.S., Lefeuvre, N., Bazarkina, E.F.: Migration of natural hydrogen from deep-seated sources in the São Francisco Basin, Brazil, Geosciences, 10, 346-362 (2020).

[60] Moretti, I., Prinzhofer, A., Françolin, J., Pacheco, C., Rosanne, M., Rupin, F., Mertens, J.: Long-term monitoring of natural hydrogen superficial emissions in a brazilian cratonic environment. Sporadic large pulses

versus daily periodic emissions, Int. J. Hydrogen Energy, 46, 3615-3628 (2021). Brazil, Geosciences, 10, 346-362 (2020).

[61] Holladay, J.D., Hu, J., King, D.L., Wang, Y.: An overview of hydrogen production technologies, Catal. Today, 139, 244-260 (2009).

[62] Stambouli, A.B., Traversa, E.: Solid oxide fuel cells (SOFCs): A review of an environmentally clean and efficient source of energy, Renew. Sustain. Energy Rev., 6, 433-455 (2002).

[63] Global Steel Report, U.S. Department of Commerce - International Trade Administration (2019).

[64] Ding, Y., Alpay, E.: High temperature recovery of CO_2 from flue gases using hydrotalcite adsorbent, Inst. Chem. Eng., 79, 45-52 (2001).

[65] Sabri, M.A., Jitan, S.A., Bahamon, D., Vega, L.F., Palmisano, G.: Current and future perspectives on catalytic-based integrated carbon capture and utilization, Sci. Total Env., 790, 128081 (2021).

[66] Wang, J., Huang, L., Yang, R., Zhang, Z., Wu, J., Gao, Y., Wang, Q., O'Hare, D., Zhong, Z.: Recent advances in solid sorbents for CO_2 capture and new development trends, Energy, Environ. Sci., 7, 3478 (2014).

[67] Metz, B., Davidson, O., de Coninck, H., Loos, M., Meyer, L.: IPCC special report on Carbon Dioxide Capture and Storage (2005)

[68] CO2CRC Ltd ressources

[69] Blomen, E., Hendriks, C., Neele, F.: Capture technologies: Improvements and Promising Developments, Energy Procedia, 1, 1505-1512 (2009).

[70] Samanta, A., Zhao, A., Shimizu, G.K.H., Sarkar, P., Gupta, R.: Post-combustion CO_2 capture using solid sorbents: A review, Ind. Eng. Chem. Res., 51, 1438-1463 (2012).

[71] Wang, T., Wang, X., Hou, C., Liu, J.: Quaternary functionalized mesoporous adsorbents for ultra-high kinetics of CO_2 capture from air, Sci. Rep., 10, 21429 (2020).

[72] Brunetti, A., Scura, F., Barbieri, G., Drioli, E.: Membrane technologies for CO_2 separation, J. Membr. Sci., 359, 115-125 (2010).

[73] Fujikawa, S., Selyanchyn, R., Kunitake, T.: A new strategy for membrane-based direct air capture, Polym. J., 53, 111-119 (2021).

[74] Klemm, A., Lee, Y.Y., Mao, H., Gurkan, B.: Facilitated transport membranes with ionic liquids for CO_2 separations, Front. Chem., 8, 637-645 (2020).

[75] Karadas, F., Atilhan, M., Aparicio, S.: Review on the use of ionic liquids (ILs) as alternative fluids for CO_2 capture and natural gas sweetening, Energy Fuels, 24, 5817-5828 (2010).

[76] Hospital-Benito, D., Lemus, J., Moya, C., Santiago, R., Palomar, J.: Process analysis overview of ionic liquids on CO_2 chemical capture, Chem. Eng. J., 390, 124509 (2020).

[77] Szima, S., Cormos, C.C.: CO_2 utilization technologies: A techno-economic analysis for synthetic natural gas production, Energies, 14, 1258-1276 (2021).

[78] Bos, M.J., Pieterson, S., Brilman, D.W.F.: Production of high purity CO_2 from air using solid amine sorbents, Chem. Eng. Sci. X, 2, 100020 (2019).

[79] Wang, Q., Tay, H.H., Chen, W., Liu, Y., Chang, J., Zhong, Z.Y., Luo, J.Z., Borgna, A.: Preparation and CO_2 capture capacity of alkali metal carbonates promoted hydrotlacite, J. Nanoeng. Nanomanuf., 1, 298-303 (2011).

[80] Zhou, H., Chen, W., Liu, J.H., Zhang, W.Z., Lu, X.B.: Highly effective capture and subsequent catalytic transformation of low-concentration CO_2 by superbasic guanidines, Green Chem., 22, 7832-7838 (2020).

[81] Sanz-Pérez, E., Murdock, C.R., Didas, S.A., Jones, C.W.: Direct Capture of CO_2 from ambient air, Chem. Rev., 116, 11840-11876 (2016).

[82] Zhu, X., Ge, T., Yang, F., Wang, R.: Design of steam-assisted temperature vacuum-swing adsorption processes for efficient CO_2 capture from ambient air, Renew. Sustain. Energy Rev., 137, 110651 (2021).

[83] Leung, D.Y.C., Caramanna, G., Maroto-Valer, M.M.: An overview of current status of carbon dioxide capture and storage technologies, Renew. Sustain. Energy Rev., 39, 426-443 (2014).

[84] Riboldi, L., Bolland, O.: Overview on Pressure Swing Adsorption (PSA) as CO_2 capture technology: state-of-the-art, limits and potentials, Energy Procedia, 114, 2390-2400 (2017).

[85] Wei, L., Xu, S., Liu, J., Liu, C., Liu, S.: Hydrogen Production in Steam Gasification of Biomass with CaO as a CO_2 Absorbent. Energy & Fuels. 22, 1997-2004 (2008).

[86] Acharya, B., Dutta, A., Basu, P.: An investigation into steam gasification of biomass for hydrogen enriched gas production in presence of CaO. Int. J. Hydrogen Energy, 35, 1582-1589 (2010).

[87] Luo, C., Zheng, Y., Ding, N., Wu, Q.L., Zheng, C.G.: SGCS-made ultrafine CaO/Al_2O_3 sorbent for cyclic CO_2 capture. Chin. Chem. Lett., 22, 615-618 (2011).

[88] An, H., Song, T., Shen, L., Qin, C., Yin, J., Feng, B.: Coal gasification with in situ CO_2 capture by the synthetic CaO sorbent in a 1 kWth dual fluidised-bed reactor. Int. J. Hydrogen Energy, 37, 14195-14202 (2012).

[89] Wang, Q., Rong, N., Fan, H., Meng, Y., Fang, M., Cheng, L., Cen, K.: Enhanced hydrogen-rich gas production from steam gasification of coal in a pressurized fluidized bed with CaO as a CO_2 sorbent. Int. J. Hydrogen Energy, 39, 5781-5792 (2014).

[90] Zamboni, I., Debal, M., Matt, M., Girods, P., Kiennemann A., Rogaume, Y., Courson, C.: Catalytic gasification of biomass (Miscanthus) enhanced by CO_2 sorption. Environ. Sci. Pollut. Res., 23, 22253-22266 (2016).

[91] Heuchel, M., Davies, G.M., Buss, E., Seaton, N.A.: Adsorption of Carbone Dioxide and Methane and their mixtures on an activated carbon: simulation and experiment. Langmuir, 15, 8695-8705 (1999).

[92] Gupta, H., Fan, L.S.: Carbonation-Calcination Cycle Using High Reactivity Calcium Oxide for Carbon Dioxide Separation from Flue Gas. Ind. Eng. Chem. Res., 41, 4035-4042 (2002).

[93] Bourne, R.A., Stevens, J.G., Ke, J., Poliakoff, M.: Maximising opportunities in supercritical chemistry: the continuous conversion of levulinic acid γ-valerolactone in CO_2, Chem. Comm., 4632-4634 (2007).

[94] Cook, P.J., Carleton, C.M.: Continental Shelf Limits: The Scientific and Legal Interface, Oxford University Press, 360 (2000).

[95] Gunter, W.D., Parkins, E.H., McCann, T.J.: Aquifer disposal of CO_2-rich gases: reaction design for added capacity, Energy Conversion and Management., 34, 941-948 (1993).

[96] Gunter, W.D., Wiwchar, B., Perkins, E.H.: Aquifer disposal of CO_2-rich gases: Extension of the time scale of experiment for CO_2-sequestering by geochemical modelling, Mineralogy and Petrology, 59, 121-140 (1997).

[97] Kothari, R., Buddhi, D., Sawhney, R.L.: Comparison of environmental and economic aspects of various hydrogen production methods, Renew. Sust. Energy Rev., 12, 553-563 (2008).

[98] Iliuta, M.C.: CO2 Sorbents for Sorption-Enhanced Steam Reforming, Adv. Chem. Eng, 51, ISSN: 0065-2377.

[99] Go, K.S., Son, S.R., Kim, S.D., Kang, K.S., Park, C.S.: Hydrogen production from two-step steam reforming in a fluidized bed reactor, Int. J. Hydrogen Energy, 34, 1301-1309 (2009).

[100] Pecharaumporn P., Wongsakulphasatch S., Glinrun T., Maneedaeng A., Hassan Z., Assabumrungrat S.: Synthetic CaO-based sorbent for high-temperature CO_2 capture in sorption-enhanced hydrogen production, Int. J. Hydrogen Energy, 44, 20663-20677 (2019).

[101] Kim, S.M., Abdala, P.M., Hosseini, D., Armutlulu, A., Margossian, T., Cope, C.: Bi-functional $Ru/Ca_3Al_2O_6$-CaO catalyst-CO_2 sorbent for the production of high purity hydrogen via sorption-enhanced steam methane reforming, Catal. Sci. Technol., 9, 5745-5756 (2019).

[102] Zhao, C., Zhou, Z., Cheng, Z., Fang, X.: Sol-gel-derived, $CaZrO_3$ stabilized Ni/CaO-$CaZrO_3$ bifunctional catalyst for sorption-enhanced steam methane reforming, Appl. Catal. B, 196, 16-26 (2016).

[103] Di Giuliano, A., Giancaterino, F., Courson, C., Foscolo, P., Gallucci, K.: Development of a Ni-CaO-mayenite combined sorbent-catalyst material for multicycle sorption enhanced steam methane reforming, Fuel,

234, 687-699 (2018).

[104] Dewoolkar, K.D., Vaidya, P.D.: Improved hydrogen production by sorption-enhanced steam methane reforming over hydrotalcite-and calcium-based hybrid materials, Energy Fuels 29, 3870 -3878 (2015) .

[105] Hafizi, A., Rahimpour, M., Heravi, M.: Experimental investigation of improved calcium-based CO_2 sorbent and Co_3O_4/SiO_2 oxygen carrier for clean production of hydrogen in sorption-enhanced chemical looping reforming, Int. J. Hydrogen Energy 44, 17863-172877 (2019).

[106] Chen, C., Yu C., Chen, W., Kuo, H.: Effect of in-situ carbon dioxide sorption on methane reforming by nickel-calcium composite catalyst for hydrogen production, Earth Environ. Sci., 463, 012102 (2020).

[107] Nimmas, T., Jamrunroj, P., Wongsakulphasatch, S., Kiatkittipong, W., Laosiripojana, N., Gong, J.: Influence of CaO precursor on CO_2 capture performance and sorption- enhanced steam ethanol reforming, Int. J. Hydrogen Energy, 44, 20649-20662 (2019).

[108] Rahmanzadeh, L., Taghizadeh, M.: Sorption-enhanced ethanol steam reforming on Ce-Ni/MCM-41 with simultaneous CO_2 adsorption over Na-and Zr-promoted CaO based sorbent, Int. J. Hydrogen Energy, 44, 21238-21250 (2019).

[109] Ghungrud, S.A., Vaidya, P.D.: Improved hydrogen production from sorption-enhanced steam reforming of ethanol (SESRE) using multifunctional materials of cobalt catalyst and Mg-, Ce-, and Zr-modified CaO sorbents, Ind. Eng. Chem. Res., 59, 693-703 (2019).

[110] Dang, C., Yu, H., Wang, H., Peng, F., Yang, Y.: A bi-functional Co- CaO-$Ca_{12}Al_{14}O_{33}$ catalyst for sorption-enhanced steam reforming of glycerol to high-purity hydrogen, Chem. Eng. J., 286, 329-338 (2016).

[111] Jiang, B., Li, L., Bian, Z., Li, Z., Sun, Y., Sun, Z.: Chemical looping glycerol reforming for hydrogen production by Ni@ZrO_2 nanocomposite oxygen carriers, Int. J. Hydrogen Energy, 43, 13200-13211 (2018).

[112] Capa, A., Garcìa, R., Chen, D., Rubiera, F., Pevida, C., Gil, M.: On the effect of biogas composition on the H_2 production by sorption enhanced steam reforming (SESR), Renew. Energy, 160, 575-583 (2020).

[113] Phromprasit, J., Powell, J., Wongsakulphasatch, S., Kiatkittipong, W., Bumroongsakulsawat, P., Assabumrungrat, S.: H_2 production from sorption enhanced steam reforming of biogas using multifunctional catalysts of Ni over Zr-, Ce- and La-modified CaO sorbents, Chem. Eng. J., 313, 1415-1425 (2017).

[114] Xie, H., Yu, Q., Zuo, Z., Han, Z., Yao, X., Qin, Q.: Hydrogen production via sorption-enhanced catalytic steam reforming of bio-oil, Int. J. Hydrogen Energy, 41, 2345-2353 (2016).

[115] Li, D., Xue, H., Hu, R.: Effect of Ce/Ca ratio in Ni/CeO_2-ZrO_2-CaO catalysts on high-purity hydrogen production by sorption-enhanced steam reforming of acetic acid and bio-oil, Ind. Eng. Chem. Res., 59, 1446-1456 (2019).

[116] Zhao, X., Xue, Y., Yan, C., Guo, C., Huang, S.: Sorbent assisted catalyst of Ni-CaO-La_2O_3 for sorption enhanced steam reforming of bio-oil with acetic acid as the model compound, Chem. Eng. Process, 119, 106-112 (2017).

[117] Zhang, Z., Qin, C., Ou, Z., Xia, H., Ran, J., Wu, C.: Experimental and thermodynamic study on sorption-enhanced steam reforming of toluene for H_2 production using the mixture of Ni/perovskite-CaO, Fuel, 305, 121447 (2021).

[118] Wang, Y., Memon, M.Z., Seelro, M.A., Fu, W., Gao, Y., Dong, Y., Ji, G.: A review of CO2 sorbents for promoting hydrogen production in the sorption-enhanced steam reforming process, Int. J. Hydrogen Energy, 46, 23358-23379 (2021).

[120] Basile, F., Benito, P., Fornasari, G., Vaccari, A.: Hydrotalcite-type precursors of active catalysts for hydrogen production, Applied Clay Science, 48, 250-259 (2010).

[121] Li, Z.S., Cai, N.S., Huang, Y.Y., Han, H.J.: Synthesis, experimental studies, and analysis of a new calcium-based carbon dioxide absorbent, Energy & Fuels, 19, 1447-1452 (2005).

[122] Sun, Z., Toan, S., Chen, S., Xiang, W., Fan, M., Zhu, M., Ma, S.: Biomass pyrolysis-gasification over Zr promoted CaO-HZSM-5 catalysts for hydrogen and bio-oil co-production with CO_2 capture, Int. J. Hydrogen Energy, 43, 16031-16044 (2017).

[123] Li, D., Wang, L., Koike, M., Nakagawa, Y., Tomishige, K.: Steam reforming of tar from pyrolysis of biomass over Ni/Mg/Al catalysts prepared from hydrotalcite-like precursors, Applied Catalysts B: Environmental, 102, 528-538 (2011).

[124] Basile, F., Fornasiri, G., Rosetti, V., Trifiro, F., Vaccari, A.: Effect of the Mg/Al ratio of the hydrotalcite-type precursor on the dispersion and activity of Rh and Ru catalysts for the partial oxidation of methane, Catalysis Today, 91-92, 293-297 (2004).

[125] Wang, X., He, Y., Xu, T., Xiao, B., Liu, S., Hu, Z.: CO_2 sorption-enhanced steam reforming of phenol using Ni-M/CaO-$Ca_{12}Al_{14}O_{33}$ ($M_{1/4}$ Cu, Co, and Ce) as catalytic sorbents, Chem. Eng. J., 393, 124769 (2020).

[126] Xie, Huaqing, Zhang, W., Zhao, X., Chen, H., Yu, Q., Qin, Q.: Sorption-enhanced reforming of tar: influence of the preparation method of CO2 absorbent, Kor. J. Chem. Eng., 35, 2191-2197 (2018).

[127] Micheli, F., Sciarra, M., Courson, C., Gallucci, K.: Catalytic steam methane reforming enhanced by CO_2 capture on CaO based bi-functional compounds, J. Energy Chem., 26, 1014-1025 (2017).

[128] Di Giuliano, A., Gallucci, K., Kazi, S., Giancaterino, F., Di Carlo, A., Courson, C.: Development of Ni- and CaO-based mono- and bi-functional catalyst and sorbent materials for sorption enhanced steam methane reforming: performance over 200 cycles and attrition tests, Fuel Process Technol., 195, 106160 (2019).

[129] Pacciani, R., Müller, C.R., Davidson, J.F., Dennis, J.S., Hayhurst, A.N.: Synthetic Ca-based solid sorbents suitable for capturing CO_2 in a fluidized bed, Can. J. Chem. Eng., 86, 356-366 (2008).

[130] Basile, F., Fornasiri, G., Rosetti, V., Trifiro, F., Vaccari, A.: Effect of the Mg/Al ratio of the hydrotalcite-type precursor on the dispersion and activity of Rh and Ru catalysts for the partial oxidation of methane, Catalysis Today, 91-92, 293-297 (2004).

[131] Fornasari, G., Gazzano, M., Matteuzzi, D., Trifiro, F., Vaccari, A.: Structure and reactivity of high-surface-area Ni/Mg/Al mixed oxides, Applied Clay Science, 10, 69-82 (1995).

[132] Li, H., Tian, H., Chen, S., Sun, Z., Liu, T., Liu, R.: Sorption enhanced steam reforming of methanol for high-purity hydrogen production over Cu-MgO/Al_2O_3 bifunctional catalysts, Appl. Catal. B, 276, 119052 (2020).

[133] Nimmas, T., Wongsakulphasatch, S., Cheng, C.K., Assabumrungrat, S.: Bi-metallic CuO-NiO based multifunctional material for hydrogen production from sorption-enhanced chemical looping autothermal reforming of ethanol, Chem. Eng. J., 398, 125543 (2020).

[134] Dang, C., Li, Y., Yusuf, S.M., Cao, Y., Wang, H., Yu, H.: Calcium cobaltate: a phase-change catalyst for stable hydrogen production from bio-glycerol, Energy Environ. Sci., 11, 660-668 (2018).

[135] Memon, M.K., Zhao, X., Sikarwar, V.S., Vuppaladadiyam, A.K., Milne, S.J., Brown, A.P., Li, J., Zhao, M.: Alkali matal CO_2 sorbents and the resulting metal carbonates: potential for process intensification of sorbent-enhanced steam reforming, Environ. Sci. Technol, 51, 12-27 (2017).

[136] Gil, M.V., Fermoso, J., Pevida, C., Chen, D., Rubiera, F. Production of fuel-cell grade H_2 by sorption enhanced steam reforming of acetic acid as a model compound of biomass-derived bio-oil, Appl. Catal. B, 184, 64-76 (2016).

[137] Zamboni, I., Zimmermann, Y., Kiennemann, A., Courson, C.: Improvement of steam reforming of toluene by CO2 capture using Fe/CaO-$Ca_{12}Al_{14}O_{33}$ bi-functional materials, Int. J. Hydrogen Energy, 40, 5297-5304 (2015).

[138] Kim, J.N., Ko, C.H., Yi, K.B.: sorption enhanced hydrogen production using one-body CaO- $Ca_{12}Al_{14}O_{33}$-Ni composite as catalytic absorbent, Int. J. Hydrogen Energy, 38, 6072-6078 (2013).

[139] Sang, S., Zhao, Z.J., Tian, H., Sun, Z., Li, H., Assabumrungrat, S.: Promotional role of MgO on sorption-enhanced steam reforming of ethanol over Ni/CaO catalysts, AlChE J., 66, 16877 (2020).

[141] Radfarnia, H.R., Iliuta, M.C.: Development of Al-stabilized CaO-nickel hybrid sorbent-catalyst for sorption-enhanced steam methane reforming, Chem. Eng. Sci., 109, 212-219 (2014).

[142] Wu, G., Zhang, C., Li, S., Huang, Z., Yan, S., Wang, S., Ma, X., Gong, J.: Sorption enhanced steam reforming of ethanol on Ni-CaO-Al_2O_3 multifunctional catalysts derived from hydrotalcite-like compounds, Energy Environ. Sci., 5, 8942-8949 (2012).

[143] Kong, M., Albrecht, K.O., Shanks, B.H., Wheelock, T.D.: Development of a combined catalyst and sorbent for the water gas shift reaction, Ind. Eng. Chem. Res., 53, 9570-9577 (2014).

[144] Wang, Q., Tay, H.H., Ng, D.J.W., Chen, L., Liu, Y., Chang, J., Zhong, Z., Luo, J., Borgna, A.: The effect of trivalent cations on the performance of Mg-M-CO_3 layered double hydroxides for high-temperature CO2 capture. Chem. Sus. Chem., 3, 965-973 (2010).

[145] Debek, R., Galvez, M.E., Launay, F., Motak, M., Grzybek, T., Da Costa, P.: Low temperature dry methane reforming over Ce, Zr and CeZr promoted Ni-Mg-Al hydrotalcite-derived catalysts, Int. J. Hydrogen Energy, 41, 11616-11623 (2016).

[146] Dewoolkar, K.D., Vaidya, P.D.: Tailored Ce- and Zr-doped Ni/hydrotalcite materials for superior sorption-enhanced steam methane reforming, Int. J. Hydrogen Energy, 42, 21762-21774 (2017).

[147] Li, D., Wang, L., Koike, M., Nakagawa, Y., Tomishige, K.: Steam reforming of tar from pyrolysis of biomass over Ni/Mg/Al catalysts prepared from hydrotalcite-like precursors, Applied Catalysts B: Environmental, 102, 528-538 (2011).

[141] Zhu, X., Wang, Q., Shi, Y., Cai, N.: Layered double oxide/activated carbon-based composite absorbent for elevated temperature H_2/CO_2 separation, Int. J. Hydrogen Energy, 40, 9244-9453 (2015).

[148] Yang, J.I., Kim, J.N.: Hydrotalcite for adsorption of CO_2 at high temperature, Korean J. Chem. Eng., 23, 77-80 (2006).

[149] Bhatta, L.K.G., Subramanyam, S., Chengala, M.D., Bhatta, U.M., Venkatesh, K.: Enhancement in CO_2 adsorption on hydrotalcite-based material by novel carbon support combined with K_2CO_3 impregnation, Ind. Eng. Chem. Res., 54, 10876-10884 (2015).

[150] Walspurger, S., Cobden, P.D., Safonova, O.V., Wu, Y., Anthony, E.J.: High CO_2 storage capacity in alkali-promoted hydrotalcite-based material: in situ detection of reversible formation of magnesium carbonate, Chem. Eur. J., 16, 12694-12700 (2010).

[151] Zhu, X., Chen, C., Suo, H., Wang, Q., Shi, Y., O'Hare, D., Cai, N.: Synthesis of elevated temperature CO_2 adsorbents from aqueous miscible organic-layered double hydroxides, Energy, 167, 960-969 (2019).

[152] Peng, J., Iruretagoyena, D., Chadwick, D.: Hydrotalcite/SBA15 composites for pre-combustion CO_2 capture: CO2 adsorption characteristics, J. CO2 Util., 24, 73-80 (2018).

[153] Li, S., Shi, Y., Yang, Y., Zheng, Y., Cai, N.: high-temperature CO_2 adsorbent from interlayer potassium-promoted stearate-pillared hydrotalcite precursors, Energy Fuels, 27, 5352-5358 (2013).

[154] Wang, Q., Luo, J., Zhong, Z., Borgna, A.: CO_2 capture by solid adsorbents and their applications: current status and new trends. Energy Environ. Sci., 4, 42-55 (2011).

[155] Yang, J.I., Kim, J.N.: Hydrotalcite for absorption of CO_2 at high temperature. Korean J. Chem. Eng., 23, 77-80 (2006).

[156] Reddy, M.K.R, Xu, Z.P., Lu, G.Q., Diniz da Costa, J.C.: Layered Double Hydroxides for CO_2 capture: structure evolution and regeneration. Ind. Eng. Chem. Res., 45, 7504-7509 (2006).

[157] Wang, X.P., Yu, J.J., Cheng, J., Hao, Z.P., Xu, Z.P.: High-temperature adsorption of carbon dioxide on mixed oxides derived from hydrotalcite-like compounds. Environ. Sci. Technol., 42, 614-618 (2008).

[158] Lwin, Y., Abdullah, F.: High temperature adsorption of carbon dioxide on Cu-Al hydrotalcite-derived mixed oxides: kinetics and equilibria by thermogravimetry. J. Therm. Anal. Calorim., 97, 885-889 (2009).

[159] Yancheshmeh, M.S., Radfarnia, H.R., Iliuta, M.C.: High temperature CO2 sorbents and their application for hydrogenproduction by sorption enhanced steam reforming process. Chem. Eng, J., 283, 420-444 (2016).

[160] Liu, W.Q., Feng, B., Wu, Y.Q., Wang, G.X., Barry, J., da Costa, J.C.D.: Synthesis of sintering-resistant sorbents for CO2 capture. Environ. Sci. Technol. 44, 3093–3097 (2010).

[161] Yu, C.T., Chen, W.C.: Hydrothermal preparation of calcium-aluminum carbonate sorbent for high-temperature CO2 capture in fixed-bed reactor. Fuel, 122, 179–185 (2014).

[162] Yong, Z., Mata, V., Rodrigues, A.E.: Adsorption of Carbon Dioxide onto Hydrotalcite-like compounds (HTIcs) at high temperatures. Ind. Eng. Chem. Res., 40, 204-209 (2001).

[163] Wang, Q., Wu, Z.H., Tay, H.H., Chen, L.W., Liu, Y., Chang, J., Zhong, Z.Y., Luo, J.Z., Borgna, A.: High temperature adsorption of CO2 on Mg-Al hydrotalcite: effect of the charge compensating anions and the synthesis pH. Catal. Today, 164, 198-203 (2011).

[164] Wang, Q., Tay, H.H., Zhong, Z., Luo, J., Borgna, A.: Synthesis of high-temperature CO_2 adsorption from organo-layered double hydroxides with markedly improved CO_2 capture capacity. Energy Environ. Sci., 5, 7526-7530 (2012).

[165] Reijers, H.T.J., Valster-Schiermeier, S.E., Cobden, P.D., van den Brink, R.W.: Hydrotalcite as CO_2 Sorbent for Sorption-Enhanced Steam Reforming of Methane. Ind. Eng. Chem. Res., 45, 2522-2530 (2006).

[166] Hufton, J.R., Mayorga, S., Sircar, S.: Sorption-enhanced reaction process for hydrogen production. AIChE J., 45, 248-256 (1999).

[167] Reddy, M.K.R., Xu, Z.P., Lu, G.Q., Diniz da Costa, J.C.: Influence of water on high-temperature CO_2 capture using Layered Double Hydroxide derivatives. Ind. Eng. Chem. Res., 47, 2630-2635 (2008).

[168] Simell, P.A., Leppalahti, J.K., Bredenberg, J.B.S.: Catalytic purification of tarry fuel gas with carbonate rocks and ferrous materials. Fuel, 71, 211-218 (1992).

[169] van Dijk, H.A.J., Walspurger, S., Cobden, P.D., van den Brink, R.W., de Vos, F.G.: Testing of hydrotalcite-based sorbents for CO_2 and H_2S capture for use in sorption enhanced water gas shift. Int. J. Greenhouse Gas Control, 5, 505-511 (2011).

[170] Rao, M.M., Reddy, B.R., Jayalakshmi, M., Jaya, V.S., Sridhar, B.: Hydrothermal synthesis of Mg-Al hydrotalcites by urea hydrolysis. Mater. Res. Bull., 40, 347-359 (2005).

[171] Z.P. Xu, Z.P., Lu, G.Q.: Hydrothermal Synthesis of Layered Double Hydroxides (LDHs) from Mixed MgO and Al_2O_3: LDH Formation Mechanism. Chem. Mater., 17, 1055-1062 (2005).

[172] Lee, W.F., Chen, Y.C.: Effects of intercalated hydrotalcite on drug release behavior for poly(acrylic acid-co-N-isopropyl acrylamide)/intercalated hydrotalcite hydrogels. Eur. Polym. J., 42, 1634-1642 (2006).

[173] Theiss, F.L., Ayoko, G.A., Frost, R.L.: Synthesis of layered double hydroxides containing Mg^{2+}, Zn^{2+}, Ca^{2+} and Al^{3+} layer cations by co-precipitation methods – A review. Appl. Surf. Sci., 383, 200-213 (2016).

[174] Mashapa, T.N., Rademan, J.D., Jense van Vuuren, J.: Catalytic performance and deactivation of precipitated iron catalyst for selectrive pxidation of hydrogen sulfide to elemental sulfur in the waste gas steams from coal gasification, Ind. Eng. Chem. Res., 46, 6338-6344 (2007).

[175] Daniel, C., Guadalupe, G., Nayeli, M.: Occupational risk assessment for hydrogen sulfide concentration from a geothermal power plant, Proceedings Thirty-sixth Workshop on Geothermal Reservoir Engineering Stanford University (2012).

[176] Suflure d'hydrogène - Fiche toxicologique n°32, INRS Database.

[177] Handbook of Natural Gas Transmission and Processing, Chapter 7: Acid Gas Treating, 261-294 (2006).

[178] Husnil, Y.A., Andika, R., Lee, M.: Optimal plant-wide control of the wet sulfuric acid process in an integrated gasification combined cycle power plant, J. Process Control, 74, 147-159 (2019).

[179] Choi, B., Lim, S., Andika, R., Jeon, J., Lee, M.: Detailed process simulation of syngas treatment with wet sulfuric acid process in a 300 MWe IGCC power plant, Energy Procedia, 61, 2211-2214 (2014).

[180] Manullang, F., Ahmad, A., Andrio, D.: The effects of Zn/natural zeolite ratio and adsorbent calcination on H_2S adsorption in biogas on the processing of Palm Oil Mill Effluent (POME), J. Phys.: Conf. Ser., 1351 (2019) 012105.

[181] Ahn, Y., Pandi, K., Lee, M., Choi, J.: Removing hydrogen sulfide from a feed stream using suitable adsorbent materials, J. Cleaner Production, 272, 122849 (2020).

[182] Anuwattana, R., Phungngamphan, P., Chawakitchareon, P.: The efficiency of carbon dioxide and hydrogen sulphide adsorption using impregnated granular activated carbon and zeolite, J. Phys. Sci., 29, 29-36 (2018).

[183] Juma, G., Machunda, R., Pogrebnaya, T.: Performance of sweet potato's leaf-derived activated carbon for hydrogen sulphide removal from biogas, Journal of Energy, 2020, 10 pages (2020).

[184] Yang, C., de Falco, G., Florent, M., Fan, H., Bandosz, T.J.: Support feature govern the properties of the active phase and the performance of bifunctional $ZnFe_2O_4$-based H_2S adsorbents, Carbon, 169, 327-337 (2020).

[185] Wei, S., Ning, P., Wang, C., Sun, X., Li, K., Song, X., Wang, F., Ma, Y., Wang, Y.: Research into the simultaneous removal process of H_2S and PH_3 by Cu-Fe-Ce composite metal oxide adsorbent, Res. Chem. Intermed., 46, 4017-4032 (2020).

[186] Kim, S., Gupta, N.K., Bae, J., Kim, K.S.: Fabrication of coral-like Mn_2O_3/Fe_2O_3 nanocomposite for room temperature removal of hydrogen sulfide, J. Environ. Chem. Eng., 9, 105216 (2021).

[187] Hassankiadeh, M.N., Hallajisani, A.: Application of Molybdenum oxide nanoparticles in H2S removal from natural gas under different operational and geometrical conditions, J. Petroleum Sci. Eng., 190, 107131 (2020).

[188] Albertazzi, S., Basile, F., Brandin, J., Einvall, J., Fornasari, G., Hulteberg, C., Sanati, M., Trifirò, F., Vaccari, A.: Effect of fly ash and H_S2 on a Ni-based catalyst for the upgrading of a biomass-generated gas, Biomass and Bioenergy, 32, 345-353 (2008).

[189] Sitthikhankaew, R., Predapitakkun, S., Kiattikomol, R., Pumhiran, S., Assabumrungrat, S., Laosiripojana, N.: Comparative study of hydrogen sulfide adsorption by using alkaline impregnated activated carbons for hot fuel gas purification, Energy Procedia, 9, 15-24 (2011).

[190] Chen, T., Wu, H.C., Li, Y., Lin, Y.S.: Poisoning effect of H2S on CO2 permeation of samarium-doped-ceria/carbonate dual-phase membrane, Ind. Eng. Chem. Res., 56, 14662-14669 (2017).

CHAPTER 2

EXPERIMENTAL AND METHODS

In the chapter the synthesis methods of sorbent and catalysts are presenting than all techniques used to characterize each product. The last sections explain the sorption capacity and reactivity specific set up and calculation to interpret measurements.

2.1. Synthesis methods

This section describes the different synthesis methods and different conditions to produce sorbents and then catalysts. The conditions studied were chosen based on the state of the art of hydrotalcites (LHDs) and with the purpose of optimizing the CO_2 sorption capacity.

The global LDH formula applied to this research project is represented by $[Mg_{3-y}Ca_yAl(OH)_8]^{+}\cdot[A]^{n-}{}_{1/n}.zH_2O$ where A is the sodium anion, *n*- is the anion charge and z is the hydration. For the following synthesis conditions, the *y* parameter picks different values namely [0, 1, 1.5, 2, and 3].

2.1.1. LDH-LDO synthesis methods

The influence of the LDH synthesis method is evaluated for high-temperature CO_2 sorbents synthesized by hydrothermal (HYD), urea hydrolysis (UREA), and co-precipitation (COP) methods. The study restricts to three synthesis methods as explained in paragraph *§1.3.3*. All the studied sorbents respect the (Mg+Ca)/Al molar ratio equal to 3/1 like the natural mineral composition. For this first comparison, the parameters studied are the method of synthesis at the same ratio Mg/Ca = 3/0 and the use of carbonate to have the same anion for all method of synthesis as that resulting from the decomposition of urea ($CO(NH_2)_2$). The synthesis methods dictate their temperature, time, and pressure conditions because of the use of an autoclave for the hydrothermal and urea hydrolysis methods. So, the goal of the study is not to understand the determining parameter to produce the best LDH but just to keep and continue with the easiest and the most promising synthesis method. The selection criteria are the formation of hydrotalcite structure, *sand roses* morphology, and high porosity. Common products from the same supplier are used for all synthesis:

• Sigma Aldrich: magnesium nitrate hexahydrate $Mg(NO_3)_2\cdot6H_2O$ (CAS: 13446-18-9 – ≥99.0%), calcium nitrate tetrahydrate $Ca(NO_3)_2\cdot4H_2O$ (CAS: 13477-34-4 – ≥99.0%), aluminum nitrate nonahydrate $Al(NO_3)_3\cdot9H_2O$ (CAS: 7784-27-2 – ≥98.5%), iron(III) nitrate nonahydrate

$Fe(NO_3)_3 \cdot 9H_2O$ (CAS: 7782-61-8 – ≥99.9%), sodium citrate tribasic dehydrate $Na_3C_6H_5O_7 \cdot 2H_2O$ (CAS: 6132-02-3 – ≥99.0%) and sodium oxalate $Na_2C_2O_4$ (CAS: 62-76-0 – ≥99.5%).

• Alfa Aesar: sodium carbonate Na_2CO_3 (CAS: 479-19-8 – ≥98%), sodium stearate $C_{18}H_{35}NaO_2$ (CAS: 822-16-2 – ≥98.0%).

The three different synthesis methods are presented in the following paragraphs. To respect the stoichiometry *i.e.* the charge equilibrium as defined in the formula $[Mg_3Al(OH)_8]^+.[A]^{n-}_{1/n}$, a minimum amount of 1/n anion is required. For each synthesis investigated, the quantity of carbonate in the solution is introduced in excess and corresponds to 4 times the charge equilibrium. The structure of hydrotalcite with carbonate as interlayer anion is $[Mg_3Al(OH)_8]^+.[CO_3]^{2-}_{1/2}.zH_2O$ and the excess of carbonate in the solution will be erased by filtration and water washing.

• Hydrothermal synthesis (HYD): first, magnesium nitrate and aluminum nitrate are calcined separately at 500°C to obtain the corresponding oxides (MgO, 1.50 g and Al_2O_3, 0.63 g). The products are stirred together in an aqueous sodium carbonate solution (Na_2CO_3, 1.31 g) in an autoclave (100 mL). The volume of the autoclave is chosen so that it is only 2/3 is full. The autoclave is heated to 110°C (10°C/min) for 7 days. The product is filtrated, washed with deionized water (50 mL – 2 times), dried overnight at 90°C, and calcined at 500°C (10°C/min) for 1 h.

• Urea hydrolysis (UREA): an aqueous solution of magnesium nitrate (6.04 g) and aluminum nitrate (2.95 g) is prepared inside an autoclave. Urea ($CO(NH_2)_2$, 0.94 g) is added. The same filling volume as for the hydrothermal method is respected. The mixture is mechanically stirred before closing the autoclave (100 mL) and then heated to 180°C (3°C/min) for 2 h. Urea decomposes in ammonia and CO_3^{2-} in solution. The product is filtrated, washed with deionized water (50 mL – 2 times), and dried overnight at 90°C. The solid is calcined at 500°C (10°C/min) for 1 h.

• Co-precipitation (COP): magnesium (3.00 g) and aluminum (2.20 g) nitrates are solubilized in 50 mL of deionized water and added dropwise to an aqueous solution of sodium carbonate (1.24 g). The

mixture is vigorously stirred during the addition. The pH is measured during the co-precipitation by a pHmeter (type HI2202-02 from Hanna Instruments) and adjusted by a dropwise addition of sodium hydroxide (3 mol/L). After 1 h of maturation, the produced LDH is filtered, washed with deionized water (50 mL – 2 times) at room temperature, and dried overnight at 100°C.

Various synthesis parameters for the co-precipitation method are investigated: (1) anion quantity to optimize hydrotalcite precipitation speed and quality, (2) the size of the anion to improve the interlayer spacing and then the CO_2 sorption capacity, and (3) substitution of Mg for Ca in LDH to enhance the CO_2 sorption temperature and make it compatible with the temperature range of steam reforming.

The optimization of the anion quantity is studied by 3 different concentrations of the sodium carbonate solution corresponding to the charge equilibrium (1), to the previously studied excess (4 times the charge equilibrium), and to a large excess (12 times the charge equilibrium). The samples arising from these syntheses are named COP_1, COP_4, and COP_{12}, respectively.

Then, the anion size comparison to Na_2CO_3 is performed with three other sodium salts: oxalate ($Na_2C_2O_4$), citrate ($Na_3C_6H_5O_7$), and stearate ($NaC_{18}H_{35}O_2$). The hydrotalcite formula without calcium corresponds to $[Mg_3Al(OH)_8].[C_2O_4^{-2}]_{1/2}.zH_2O$ for oxalate, $[Mg_3Al(OH)_8].[C_6H_5O_7^{-3}]_{1/3}.zH_2O$ for citrate and to $[Mg_3Al(OH)_8].[C_{18}H_{35}O_2^{-}].zH_2O$ for stearate anion.

Finally, calcium nitrate ($Ca(NO_3)_2{\cdot}6H_2O$) is added instead of a part of the magnesium nitrate to study the different values of the Mg/Ca ratio (between 3/0 and 0/3). The solubility of stearate being better by decreasing the pH, each sorbent formulation is synthesized at pH 8 and pH 10. It was reported that at pH 10, Al^{+3} and Mg^{2+} are simultaneously precipitated as $Al(OH)_3$ and $Mg(OH)_2$ nanoparticles, and immediately converted to Mg_3Al_2-CO_3 LDH. At higher pH, Mg^{2+} precipitates first as $Mg(OH)_2$ nanoparticles. The solubility of thevprecursor was assured by a lower pH value (8).

The valence of stearate being lower than that of other anions and the molecular weight of sodium stearate being the highest of anions studied, its weight requirement for LDH synthesis is largely higher than that for sodium di-anion. For example: for an Mg/Ca molar ratio of 2/1, the weights used are as follows: $Mg(NO_3)_2{\cdot}6H_2O$ (3.00 g), $Ca(NO_3)_2{\cdot}4H_2O$ (1.38 g), $Al(NO_3)_3{\cdot}9H_2O$ (2.20 g), and sodium carbonate (1.24 g), sodium oxalate (1.57 g), sodium citrate (3.44 g) or sodium stearate (3.59 g).

The formula of calcium-containing LDH is globally $[Mg_{3-y}Ca_yAl(OH)_8]^+\cdot[A^{n-}]_{1/n}.zH_2O$. For all three methods, the Layer Double Oxides (LDOs) are obtained after calcination at 500°C or 700°C for 1 h after a ramp of 10°C/min and crushed to powder with grains smaller than 250 µm. After calcination, the LDO formula becomes $(MgO)_{3-y}(CaO)_y(Al_2O_3)_{1/2}$ with y = [0, 1, 1.5, 2, 3]. In the name of each sample studied Mg/Ca/Al, the molar ratio of these three elements (Mg, Ca, and Al) is followed by the sodium anion name and then the pH used as indicated in Table 2.1.

Table 2.1: Nomenclature of synthesized sorbents

Mg/Ca/Al	pH	CO_3^{2-} carbonate	Ox^{2-} oxalate	St^- stearate	Cit^{3-} citrate
3/0/1	8	$3/0/1_{CO3.pH8}$	$3/0/1_{Ox.pH8}$	$3/0/1_{St.pH8}$	-
	10	(COP_4) $3/0/1_{CO3.pH10}$	$3/0/1_{Ox.pH10}$	$3/0/1_{St.pH10}$	$3/0/1_{Cit.pH10}$
2/1/1	8	$2/1/1_{CO3.pH8}$	$2/1/1_{Ox.pH8}$	$2/1/1_{St.pH8}$	$2/1/1_{Cit.pH8}$
	10	$2/1/1_{CO3.pH10}$	$2/1/1_{Ox.pH10}$	$2/1/1_{St.pH10}$	$2/1/1_{Cit.pH10}$
1.5/1.5/1	8	$1.5/1.5/1_{CO3.pH8}$	-	$1.5/1.5/1_{St.pH8}$	-
	10	$1.5/1.5/1_{CO3.pH10}$	$1.5/1.5/1_{Ox.pH10}$	$1.5/1.5/1_{St.pH10}$	-
1/2/1	8	$1/2/1_{CO3.pH8}$	-	$1/2/1_{St.pH8}$	-
	10	$1/2/1_{CO3.pH10}$	$1/2/1_{Ox.pH10}$	-	-
0/3/1	8	-	-	-	-
	10	$0/3/1_{CO3.pH10}$	-	-	-

2.1.2. Catalysts synthesis

Iron and nickel catalysts are synthesized by two different methods: wet impregnation and one-pot co-precipitation synthesis. The quantity of matterial of iron or nickel nitrate ($Fe(NO_3)_3$ or $Ni(NO_3)_2$) is calculated to obtain 10_{wt}% or 20_{wt}% of iron and 5_{wt}% or 10_{wt}% of nickel in the calcined compounds.

The wet impregnation method uses the sorbent as a support for the addition if the metal phase. Iron or nickel nitrate is solubilized in 50 mL of deionized water in a round-bottom flask. The LDO sorbent (already calcined) is added to the solution and the suspension is stirred vigorously for 1 h in a rotary evaporator before beginning evaporation of the water. The collected product is calcined for 1 h at 500°C with a ramp at 10°C/min.

One-pot co-precipitation takes again the co-precipitation method used to synthesize the sorbents but replacing part of aluminum nitrate with iron or nickel nitrate. So, magnesium, calcium, aluminum, and iron or nickel nitrates are solubilized together and the basic solution is added dropwise at 60°C to control the pH. After 1 h of maturation, the LDH produced is filtered, washed with deionized water (50 mL – 2 times) at room temperature, and dried overnight at 100°C. The metal-doped LDO are recovered after calcination at 500°C for 1 h after a ramp of 10°C/min and crushed to obtain a powder with grains smaller than 250 µm.

Even if the iron or nickel content is the same in both synthesis methods, some differences should be noted particularly because the addition of iron or nickel changes the Mg/Ca/Al ratio according to the synthesis method. Indeed, by impregnation, the molar ratio (Mg+Ca)/Al stays equal to 3/1. On the other hand, in the one-pot method iron or nickel replaces aluminum, and the ratio (Mg+Ca)/(Al+M) = 3/1 (M = Fe or Ni) is still constant. So, the Al content decreases and the ratio (Mg+Ca)/Al increases with the increase of the M_{wt}%. In both cases, the catalysts will be compared wth the same Mg/Ca ratio. The next tables inventory all synthesized catalysts according to the synthesis parameters for iron (Table 2.2) and nickel (Table 2.3) catalysts.

Table 2.2: Nomenclature of synthesized iron catalysts

				Method	
Mg/Ca	A^-	pH	Fe_{wt}%	Wet impregnation	One-pot co-precipitation
1.5/1.5	CO_3^{2-}	8	**10**	$_{IMP}Fe_{10}1.5/1.5_{CO3.pH8}$	$_{OP}Fe_{10}1.5/1.5_{CO3.pH8}$
			20	$_{IMP}Fe_{20}1.5/1.5_{CO3.pH8}$	$_{OP}Fe_{20}1.5/1.5_{CO3.pH8}$
		10	**10**	-	$_{OP}Fe_{10}1.5/1.5_{CO3.pH10}$
			20	-	-
	Ox^{2-}	10	**10**	$_{IMP}Fe_{10}1.5/1.5_{Ox.pH10}$	$_{OP}Fe_{10}1.5/1.5_{Ox.pH10}$
			20	$_{IMP}Fe_{20}1.5/1.5_{Ox.pH10}$	$_{OP}Fe_{20}1.5/1.5_{Ox.pH10}$
1/2	CO_3^{2-}	8	**10**	$_{IMP}Fe_{10}1/2_{CO3.pH8}$	$_{OP}Fe_{10}1/2_{CO3.pH8}$
			20	$_{IMP}Fe_{20}1/2_{CO3.pH8}$	$_{OP}Fe_{20}1/25_{CO3.pH8}$
		10	**10**	-	$_{OP}Fe_{10}1/2_{CO3.pH10}$
			20	-	$_{OP}Fe_{20}1/2_{CO3.pH10}$
	Ox^{2-}	10	**10**	$_{IMP}Fe_{10}1/2_{Ox.pH10}$	$_{OP}Fe_{10}1.5/1.5_{Ox.pH10}$
			20	$_{IMP}Fe_{20}1/2_{Ox.pH10}$	$_{OP}Fe_{20}1/2_{Ox.pH10}$

Table 2.3: Nomenclature of synthesized nickel catalysts

				Method	
Mg/Ca	A^-	pH	**Ni_{wt}%**	Wet impregnation	One-pot co-precipitation
1.5/1.5	CO_3^{2-}	8	**5**	$_{IMP}Ni_5 1.5/1.5_{CO3.pH8}$	$_{OP}Ni_5 1.5/1.5_{CO3.pH8}$
			10	$_{IMP}Ni_{10} 1.5/1.5_{CO3.pH8}$	$_{OP}Ni_{10} 1.5/1.5_{CO3.pH8}$
		10	**5**	-	-
			10	-	$_{OP}Ni_{10} 1.5/1.5_{CO3.pH10}$
	Ox^{2-}	10	**5**	$_{IMP}Ni_5 1.5/1.5_{Ox.pH10}$	$_{OP}Ni_5 1.5/1.5_{Ox.pH10}$
			10	$_{IMP}Ni_{10} 1.5/1.5_{Ox.pH10}$	$_{OP}Ni_{10} 1.5/1.5_{Ox.pH10}$
1/2	CO_3^{2-}	8	**5**	$_{IMP}Ni_5 1/2_{CO3.pH8}$	$_{OP}Ni_5 1/2_{CO3.pH8}$
			10	$_{IMP}Ni_{10} 1/2_{CO3.pH8}$	$_{OP}Ni_{10} 1/25_{CO3.pH8}$
		10	**5**	-	$_{OP}Ni_5 1/2_{CO3.pH10}$
			10	$_{IMP}Ni_{10} 1/2_{CO3.pH10}$	$_{OP}Ni_{10} 1/2_{CO3.pH10}$
	Ox^{2-}	10	**5**	$_{IMP}Ni_5 1/2_{Ox.pH10}$	$_{OP}Ni_5 1.5/1.5_{Ox.pH10}$
			10	$_{IMP}Ni_{10} 1/2_{Ox.pH10}$	$_{OP}Ni_{10} 1/2_{Ox.pH10}$

2.2. Characterization techniques

Firstly, a characterization is performed on the LDHs by Thermal Gravimetric Analysis (TGA) in order to evaluate their decomposition profile during a subsequent calcination according to the various parameters and compositions synthesized.

The LDOs samples are characterized by:

- ICP-AES to measure their elementary analysis, and deduce their molar ratios Mg/Ca and (Mg+Ca)/Al and Fe_{wt}% or Ni_{wt}%;
- X-Ray Diffraction (XRD) to identify the crystalline phases present;
- N_2 adsorption to determine the textural propertie;
- Scanning Electron Microscopy (SEM) for morphology;

- Sorption tests to evaluate their CO_2 sorption capacity;
- Thermal Gravimetric Analysis (TGA) to study their stability during carbonation/calcination (absorption/desorption) cycles;
- Temperature-Programmed Reduction (TPR) for reducibility, reactivity tests to evaluate Fe or Ni activity and stability during reforming/desorption cycles.

All analyses are made on samples crushed to obtain a powder with grains smaller than 250 µm with the exception of the SESR catalytic activity test mentioned below.

2.2.1. Elementary analysis

The solid sorbent or catalyst (100 mg) is dissolved in a strong acid of HNO_3 concentrated solution. The mineralized product in solution is diluted and then nebulized in Inductively Coupled Plasma, Atomic Emission Spectroscopy (ICP-AES) for analysis. Elements detected are Mg, Ca, Al for each sample and in addition Fe or Ni for catalysts by a Varian 720-ES apparatus. The error determination is informed by the apparatus according to elements and the sensitivity of the detector for these elements.

2.2.2. Thermal Gravimetric Analysis (TGA)

A Linseis L81 is used for TGA. The sample (from 1 mg to 4 mg) with particle diameter smaller than 250 µm is calcined under 25 mL/min during a heating ramp of 10°C/min up to 700°C.

2.2.3. X-Ray Diffraction (XRD)

XRD spectra are recorded by a X-ray diffractometer Brucker AXS D8 Advanced using CuKα radiation to detect crystalline phases. Phase identification is performed by comparison with JCPDS (Joint Committee on Powder Diffraction Standards) files. Spectra are recorded in a 2θ range from 10° to 90°, with a scanning step equal to 0.0158° and a sampling time of 1 sec per step. The ray selected

for CaO phase is at 2θ = 37.5°, for MgO phase at 2θ = 43.0°, for Ni phase at 2θ = 44.5° and for Fe phase at 2θ = 44.5°.

XRD thermo-analysis are recorded by X-ray powder diffractometer D8 Discover in Bragg Brentano geometry equipped with a Cu tube (λ = 1.540 Å), monochromator, and Lynxeye XE-T linear detector. The temperature chamber used is an Anton Paar HTK 1200N model supporting a range of 25-1200°C. The samples are deposited in an alumina crucible under a slow flow of air. Spectra are recorded in a 2θ range from 10° to 70° every 25°C from room temperature to 700°C.

2.2.4. N_2 physisorption

A Micromeritics ASAP 2420 analyzer is used to record N_2 adsorption and desorption isotherms over 52 relative pressure points at -196°C for each sample (40 mg), previously degassed at 250°C under vacuum for at least 7 h. Properties such as specific surface area and pore volume are calculated from the desorption isotherm and BET (Brunauer-Emmet-Teller) and BJH (Barrett-Joyner-Halenda) methods, respectively [1].

2.2.5. Scanning Electron Microscopy (SEM)

Few grains of each sample are stacked on a cylindrical Dural sample carrier using double-sided adhesive tape. Pictures are acquired by a Zeiss GeminiSEM 500 equipped with an In-lens SE detector, an electron high tension usually at EHT = 2kV, a sample-objective distance of WD = 4-5 mm, and different field width values between 2 µm and 200 nm.

2.2.6. Temperature programmed reduction (TPR-H_2)

The metallic phase is the active phase for catalyzed reforming reactions. The TPR-H_2 allows figuring out the reducibility and pre-reduction temperature needed for catalyst activation. A Micromeretics

AutoChem II 2920 was used for TPR-H_2 analysis. During the temperature ramp of 10°C/min until 900°C, an H_2 in Ar ($10\%_{vol}$) gas mixture at 50 mL/min flows through the quartz reactor (inner diameter Ø = 15 mm) and the sample (50 mg) maintained by two small layers of quartz wool.

2.3. CO_2 Sorption properties

The specific setup for CO_2 sorption capacity measurement is described with temperature, flows, and detector materials. The equations used to calculate the sorption capacity values from the raw data are also precise. Then the cyclic method to study sorption stability by TGA and the corresponding equations are spelled out.

2.3.1. CO_2 sorption capacity

100 mg of a sorbent is charged into a U-shaped quartz reactor with an inner diameter of 0.6 cm. Thanks to a 4-ways valve, the reactor can be supplied by a $15_{vol}\%$ of CO_2 gas mixture (7.5 NmL/min of CO_2 in 42.5 NmL/min of He) for the sorption step or by a pure He flow (50 NmL/min) for the purge and desorption steps (Fig. 2.1). $15_{vol}\%$ for the CO_2 composition is chosen, which corresponds to the typical CO_2 concentration of the gasification gas mixture concentration: from coal or biomass, CO_2 can be between 1% and 30%, often 20-25% [2-3].

The flow at the reactor outlet is sent to a CO_2 IR detector (Emerson X2GP IR). An additional He flow (200 NmL/min) permits to dilute the analyzed flow before the analyzer. The analyzer possesses three CO_2 infrared detectors with sensibility limits of 3000 ppm, 10000 ppm, and 200000 ppm, respectively.

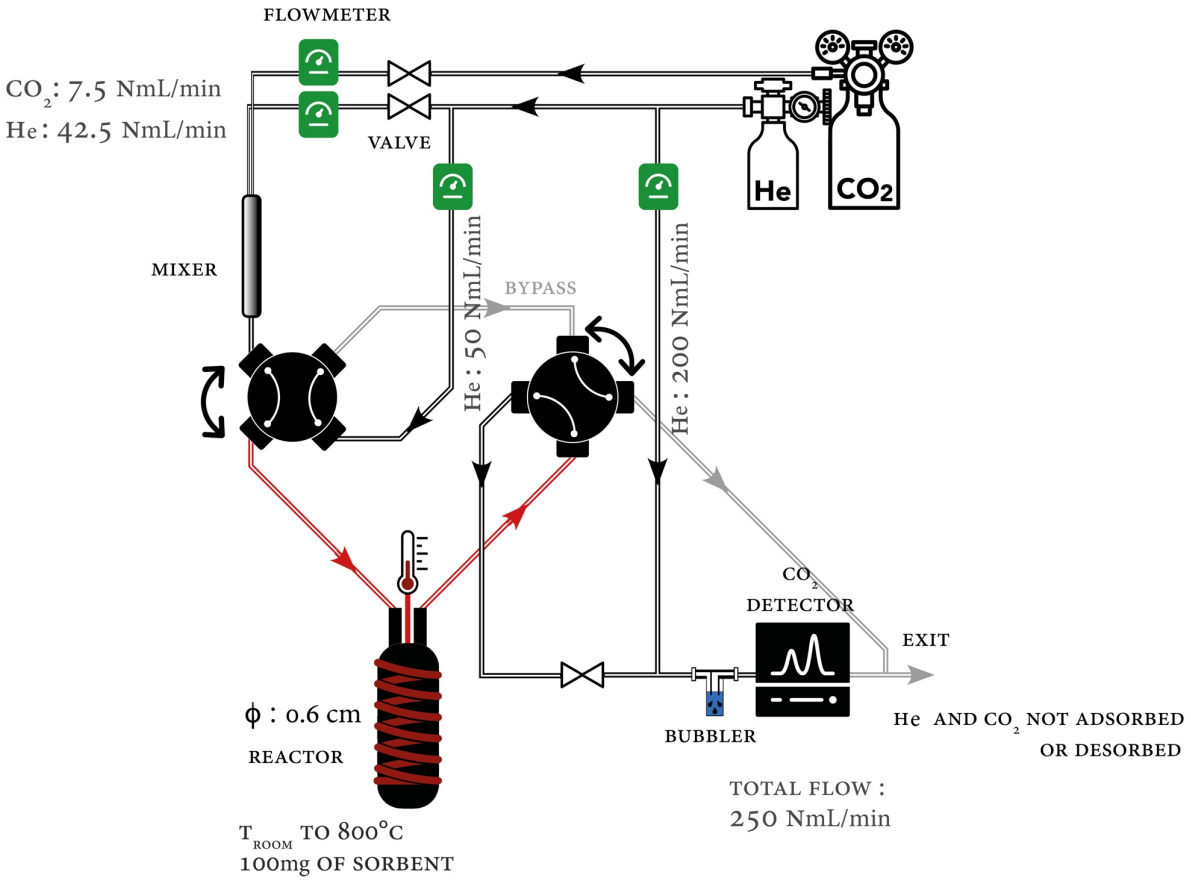

Figure 2.1: Setup for sorption capacity measurement

The sorption capacity test consists of 3 steps (Fig. 2.2):

• The Purge Step under He from room temperature (10°C/min) to 800°C. The CO_2 desorbed during this step corresponds to the decomposition of $CaCO_3$ remaining after calcination at 500°C or formed during the storage of the samples. Reaching 800°C under inert gas allows to purge the line and to come back to the baseline gas detection (end of CO_2 desorption). Then, the temperature decreases to 600°C.

• The Carbonation Step starts when the CO_2 inlet is purged, continues during a temperature increase (rate 5°C/min) until 800°C, and finishes when no more CO_2 is detected. Then, the reactor oven is turned off and the He flow is maintained through the rector until the room temperature is reached.

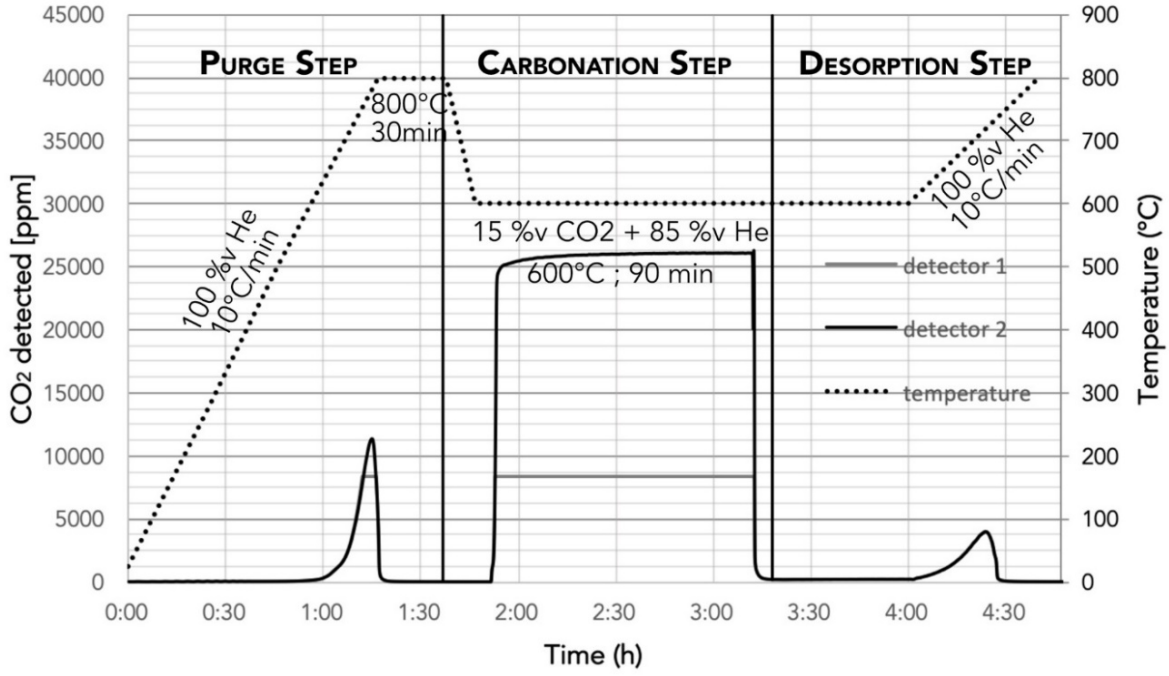

Figure 2.2: Raw curve of CO_2 sorption capacity for $0/3/1_{CO3\cdot pH10}$ sample taken as an example

From these raw curves, the sorption capacity of sorbent was calculated by $X_{sorbent}$, the weight of CO_2 capture by LDO or X_{CaO} the weight of CO_2 capture relates to CaO content into sorbent (Eq.1).

$$X_{sorbent} = \frac{A_{EXP\cdot sorbent}}{A_{TH\cdot sorbent}} \quad \text{Equation 1.a} \qquad ; \qquad X_{CaO} = \frac{A_{EXP\cdot CaO}}{A_{TH\cdot CaO}} \quad \text{Equation 1.b}$$

With • $A_{EXP\cdot sorbent}$: experimental sorption capacity ($g_{CO2}/100g_{sorbent}$) (Eq.2.a)

$$A_{EXP\cdot sorbent} = \frac{M_{CO_2}.\sum \Delta n_{CO_2,desorb}}{(m_i - \sum \Delta n_{CO_2,purge}.M_{CO_2}).100} \quad \text{Equation 2.a}$$

• $A_{TH\cdot sorbent}$: theoretical sorption capacity ($g_{CO2}/100g_{sorbent}$) (Eq.3.a)

$$A_{TH\cdot sorbent} = M_{LDO}/M_{CO_2} \quad \text{Equation 3.a}$$

With • $A_{EXP\cdot CaO}$: experimental sorption capacity ($g_{CO2}/100g_{CaO}$) (Eq.2.b)

$$A_{EXP\cdot CaO} = \frac{M_{CO_2}.\sum \Delta n_{CO_2,desorb}}{(m_i - \sum \Delta n_{CO_2,purge}.M_{CO_2}).100}.CaO_{wt\%} \quad \text{Equation 2.a}$$

• $A_{TH\cdot CaO}$: theoretical sorption capacity ($g_{CO2}/100g_{CaO}$) (Eq.3.b)

$$A_{TH\cdot CaO} = \frac{CaO_{wt\%}}{M_{CaO}}.M_{CO_2} \quad \text{Equation 3.a}$$

With $\Sigma\Delta n_{CO_2,purge}$: CO_2 total quantity (mol) detected during the purge (1st step)

$\Sigma\Delta n_{CO_2,\,desorb}$: CO_2 total quantity (mol) detected during the desorption (3rd step)

M_i: molar weight (g/mol)

m_i: initial sample mass (g)

$M_{wt\%}$: mass fraction of MgO and CaO in the sample (%)

2.3.2. Sorption stability (TGA cycles)

The same Linseis L81 thermobalance previously described for TGA is used for TGA-multicycles carbonation/calcination tests. Between 1 and 2 mg of a powder sample is charged onto the cradle. For sorbents and catalysts tested in TGA-multicycles beyond 9 carbonation/calcination cycles, a Linseis PT1000 is used.

The cycles begin with a Purge step to decompose $CaCO_3$ or $Ca(OH)_2$ formed during storage under room atmosphere. It is composed of a treatment under N_2 (25 mL/min) during a temperature ramp up to 800°C at 10°C/min then a plateau at this temperature for 20 min. Then, an alternation of Carbonation Step and Desorption Step is repeated from 7 to 10 times for each sample.

The Carbonation Step takes place at 600°C under CO_2 flow (25 mL/min containing 20% CO_2 in He) for 90 min to saturate the sorbent (conversion of oxides into carbonates).

The Desorption Step is performed under N_2 (25 mL/min) during a temperature ramp to 800°C at 5°C/min and an isotherm for 20 min.

Three main differences between this multicycles test and the sorption test should be noted:

• The weight is about five hundred times less in TGA-multicycles tests than in sorption tests;

• The gas flow passes through the sorbent bed during sorption tests contrary to TGA-multicycle tests in which gas flow breaths above sample. So, the sorption will be more limited in the second case;

• The sorption step duration is the same for all sorption tests but for TGA-multicycle tests it is not enough to reach sorbent saturation.

The values of the sorbent capacity (A_i) are calculated according to the highest weights (so after at least 40 min of sorption for the test made in Strasbourg and 120 min for samples made in L'Aquila– Fig.

2.3) and lowest for each cycle (Eq. 4) and the gradually decreasing or loss of sorption capacity (S_i) after each cycle represents the stability (Eq.5).

$$A=\frac{(\%m_{max}-\%m_{min})}{m_i}\cdot 100\cdot\frac{M_{CO2}}{M_{LDO}} \quad \text{Equation 4}$$

$$S_i=A_1-A_i \quad \text{Equation 5}$$

With %m: weight measured according to initial weight

m_i: initial sample mass (g)

M: molar weight (g/mol)

A: mass of CO_2 sorbed (g)

S_i: sorption capacity loss at the *i* cycle according to the first cycle sorption value

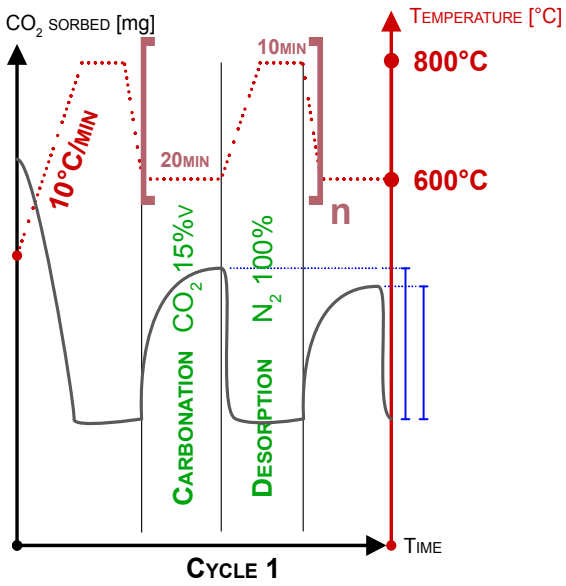

Figure 2.3: Pattern for cyclic sorption/desorption TGA

2.4. Catalytic activity in Sorption Enhanced Steam Reforming

The reaction takes place in a tubular stainless steel reactor (AISI 316 L) inside a cylindrical oven. The internal diameter is equal to 1 cm and the length is 55 cm. The fixed bed reactor corresponds to 5-6 g of the catalyst with a particle size between 350 µm and 800 µm (Fig. 2.4). Two small layers of quartz wool maintain the bed. The remaining volume is completed with zirconia balls (diameter Ø = 2-2.5 mm).

Pre-reduction: the catalyst is reduced during the temperature increasing until 800°C (10°C/min) with a gas mixture H_2 in N_2 ($50\%_{vol}$) at 350 NmL/min of each gas. This temperature corresponds to the purge temperature in the sorption capacity analyzes and ensures the reduction of the nickel or iron oxide phases determined by TPR. After an isotherm at 800°C for 20 min, the temperature decreases to the reforming temperature under 1 NL/min of nitrogen and remains stable for 10 min before the next hydrogen purge step.

The reactor is fed by three Bronkhorst mass flowmeters/controllers for N_2, H_2, and CH_4 and two syringes for H_2O (50 mL) and tar solution ($27_{wt}\%$ naphthalene, $73_{wt}\%$ toluene – 8 mL) fixed to automatic pistons (electric motor KDS Legato 110). The composition of the tars is constant and corresponds to a reference mixture that can simulate the more complex mixtures of tars not converted by gasification. The catalytic activity required for the reforming of cyclic hydrocarbons is close to naphthalene and systematically easier than toluene which is the smallest of them. The reagents used to produce the tar mixture are toluene (≥ 98%) and naphthalene (99%) from Sigma-Aldrich. The tar solution has a density of 0.91 g/m^3. An evaporation chamber heated to 220°C connects all input before the inlet of the reactor. The connection between the evaporation chamber and the reactor is also heated at 220°C. A cooling liquid (ethylene glycol) at 0°C in a refrigerant managed by a Julabo cryostat condenses the steam and tar inside a flask. The dry outlet gas passes through a Bronkhorst mass flow controller to measure, monitor the total outlet mass flow rate and consider the gas flow correction. Then, the flow goes to an ABB Advance Optima gas analyzer. A Caldos (thermal conductivity detector: TCD) module allows analyzing the molar fraction of hydrogen and an Uras (non-dispersive

infrared: NDIR) module detecting the CO, CO_2 and CH_4 every 5 sec. Gas flows rates, water piston, and oven heating are programmable on the computer where the data is collected via the DIGIPOWER customed software.

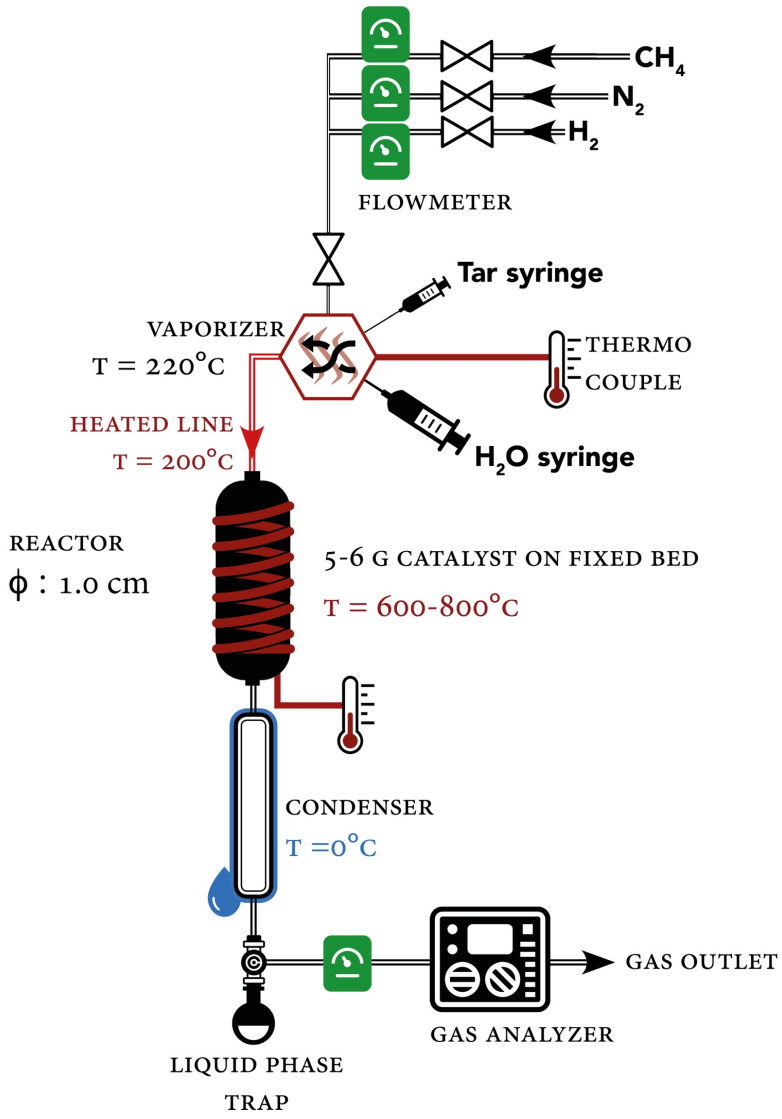

Figure 2.4: Setup for catalytic SESR reaction measurement

2.4.1. Catalytic activity in Sorption Enhanced Steam Reforming

These tests are performed to compare iron and nickel catalysts and to study the production of hydrogen according to temperature and the steam/carbon (S/C) molar ratio.

In addition to a nitrogen flow of 1 NL/min, and firstly at 500°C, the tar and water syringes are started simultaneously to feed 20 µL/min for the tar solution and 91 µL/min, 121 µL/min or 151 µL/min for

water. Tar and 'N_2 flow rates are chosen to obtain a tar content close to 1% and the N_2 flow rate is chosen to avoid the problems of over-pressure at the passage of the catalytic bed which occurred during the white tests. Then, the S/C molar ratio changes from 3.5 to 4.6 and then to 6 respectively, after 20 min of reactivity testing. Afterward, the syringes stop simultaneously, and the temperature increases until 600°C (10°C/min) under N_2 before the new start of reforming at S/C = 3.5, 4.6 then 6. The same step allows the reactivity test at 700°C.

The hydrogen productivity is calculated (Eq. 6) from its molar fraction after 20 min of reaction. The values are stable after this time and correspond to the productivity for a CO_2 saturated sorbent. The H_2/CO_2 (Eq. 7) and H_2/CO (Eq. 8) ratios are also calculated.

$$P_X = \frac{X_{vol\%} \cdot D_{out}}{100 \cdot g_{cat}} \cdot V_0 \qquad \textit{Equation 6}$$

$$H_2/_{CO_2} = \frac{P_{H_2}}{P_{CO_2}} \qquad \textit{Equation 7}$$

$$H_2/_{CO} = \frac{P_{H_2}}{P_{CO}} \qquad \textit{Equation 8}$$

With P_X: productivity of x (mol/min/g_{cat})

$X_{vol\%}$: molar fraction of x (%)

D_{out}: outlet flow (NL/min)

V_0: molar volume (22.414 L/mol)

g_{cat}: catalyst weight (g)

The tar flow is constant for all SESR tests and induces 730 µmol/min/g_{cat} of products.

Selectivity is interpreted by the $H_2/CO_2/CO$ ratio correspond to the production of each detected gas from outlet flow. The conversion of tar, toluene and naphthalene undistinguished, is calculated from the sum of H_2, CO_2 and CO produced relative to the theoretical H_2 and CO produced by complete SR reaction. At last, the hydrogen yield is evaluated based on the H_2 selectivity multiplied by tar conversion.

2.4.2. Catalyst and sorbent stability in Sorption Enhanced Steam Reforming

These tests are performed to evaluate whether the catalyst undergoes deactivation and loss of sorption capacity during the reforming-carbonation/desorption cycles.

At 600°C, the water and tar syringes are started and stopped at the same time as for the reactivity tests. The water flow is maintained at 151 µL/min and the tar solution at 20 µL/min to have the highest S/C ratio (S/C = 6). After 15 min of reforming, the temperature increases until 800°C (10°C/min) under N_2 to decarbonize the bi-functional material. Then the temperature decreases at 600°C and the reactor is ready for a new reforming-carbonation/desorption cycle.

The hydrogen productivity is calculated for each cycle between the highest point of the hydrogen content (pre-breakthrough) and after stabilization of hydrogen content (post-breakthrough). According to the cycle and the catalyst used, the breakthrough point time changes and coincides with the CO_2 saturation point (Fig. 2.5). The hydrogen production can be compared at pre- and post-breakthrough points and pre-H_2/CO_2 and H_2/CO ratios are compared to post-breakthrough values.

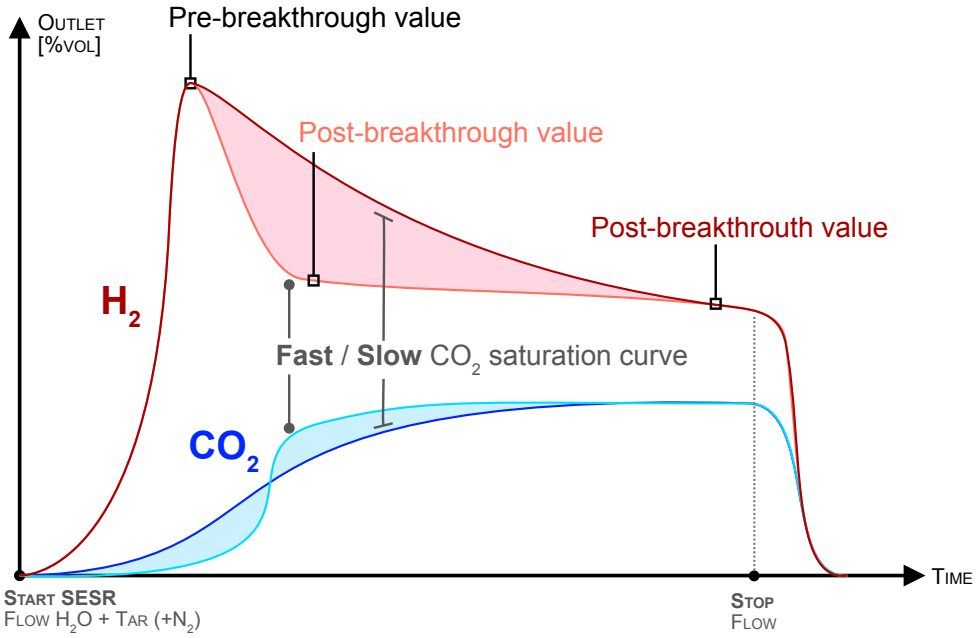

Figure 2.5: Pattern and method for catalytic SESR reactivity test measurement

2.5. Post-SESR tests characterization

The catalysts used in the SESR tests (activity and stability studies) are analyzed to compare the pore degradation, crystalline evolution of the structure, and CO_2 sorption capacity with the same measurement instruments and methods in N_2 adsorption, XRD, and CO_2 sorption capacity set up.

References

[1] Thommes, M., Kaneko, K., Neimark, A.V., Olivier, J.P., Rodriguez-Reinoso, F., Rouquerol, J., Sing, K.S.W.: Physisorption of gases, with special reference to the evaluation of surface area and pore size distribution (IUPAC Technical Report), Pure Appl. Chem., 87, 1051-1069 (2015).

[2] Yao, Y., Hildebrandt, D., Glasser, D., Liu, X.: Fischer-Tropsch synthesis using $H_2/CO/CO_2$ syngas mixtures over a cobalt catalyst, Ind. Eng. Chem. Res., 49, 11061-11066 (2010).

[3] Badoga, S., Sohani, K., Zheng, Y., Dalai, A.K.: Mesoporous alumina and alumina-titania supported KCuFe catalyst for Fischer-Tropsch synthesis: Effects of CO_2 and CH_4 present in syngas, Fuel Processing Technology, 168, 140-151 (2017).

CHAPTER 3

SORBENT CHARACTERIZATION

This chapter contains the description of analysis results for LDH and LDO sorbents produced according to conditions and parameters described in *Chapter 2.1.1*. XRD, N_2 physisorption and SEM analysis are interpreted first to understand properties of sorbents synthetized with different methods and anion quantity. Next, elementary analysis, TGA and thermo-XRD analysis are added to LDHs analysis to complete characterization and apprehend behaviors during calcination. Then LDOs are also analyzed by XRD, N_2 physisorption and SEM. Last but not least, CO_2 sorption capacity and sorption stability tests are performed.

3.1 LDHs characterization

3.1.1 Synthesis method and sodium carbonate quantity

First, samples synthetized with different methods were compared by XRD. Before calcination the main phase corresponds to hydrotalcite structure (JCPDS n° 00-022-0700) (Fig. 3.1a) and the hydrothermal synthesis method produced a second phase of brucite (H_2MgO_2 - JCPDS n° 01-071-5972). COP_4 conditions form pure hydrotalcite contrary to COP_{12} with very less crystalline and defined hydrotalcite peaks. COP_1 appears as an intermediate crystallinity between COP_4 and COP_{12}. X-ray diffractograms of sample synthesized by urea hydrolysis show a mixture of magnesite ($MgCO_3$)[1], bohmite (AlO_2H)[2] and carbon residu phases [3].

After calcination at 500°C (Fig. 3.1b), the periclase structure (MgO) is the main phase for all products whatever the synthesis method but a second spinel phase (Al_2MgO_4 JCPDS n° 00-021-1152) [4] is also present in the urea hydrolysis and in lower proportion in the co-precipitation method with COP_{12}. So, the quantity of sodium carbonate seems more appropriate for co-precipitation synthesis starting from COP_4.

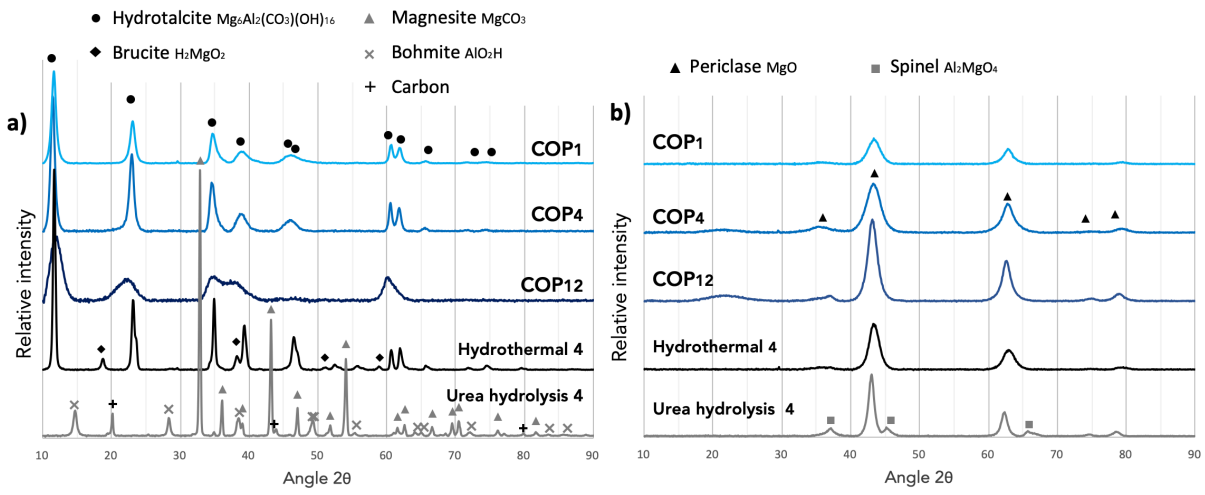

Figure 3.1: X-ray diffractograms of a) LDH prepared according to synthesis method and sodium carbonate quantity, b) corresponding LDO samples calcined at 500°C.

The BET surface area (SSA) of the LDO compounds varied from 158 m^2/g with the hydrothermal synthesis to 217 m^2/g with the urea hydrolysis synthesis (Fig. 3.2 left). The hydrothermal product also has the lowest BJH pore volume (Pv = 0.39 cm^3/g) close to the urea hydrolysis product at 0.44 cm^3/g versus 0.82 cm^3/g for co-precipitation. The adsorption/desorption isotherms (Fig. 3.3) inform about the porosity and the curve type IVa [5] indicates that macroporosity is obtained by hydrothermal method, mesoporosity by urea hydrolysis and both with co-precipitation synthesis. Macroporosity is defined beyond 50 nm against mesoporosity between 2 and 50 nm. Otherwise, the mesoporosity in the co-precipitation sample is lost with the decrease in the amount of sodium carbonate and follows the trend of pore volume decreasing (Fig. 3.2 right).

The highest amount of N_2 adsorbed is obtained with co-precipitation LDO compared to other synthesis methods. The quantity adsorbed at saturated pressure (Fig. 3.3a) reaches 510 cm^3/g_{STP}. This is a higher value than those obtained with the hydrothermal and the urea hydrolysis methods. For the other sodium carbonates, the largest quantity adsorbed reaches 550 cm^3/g_{STP} with COP_{12} against 355 cm^3/g_{STP} for COP_1.

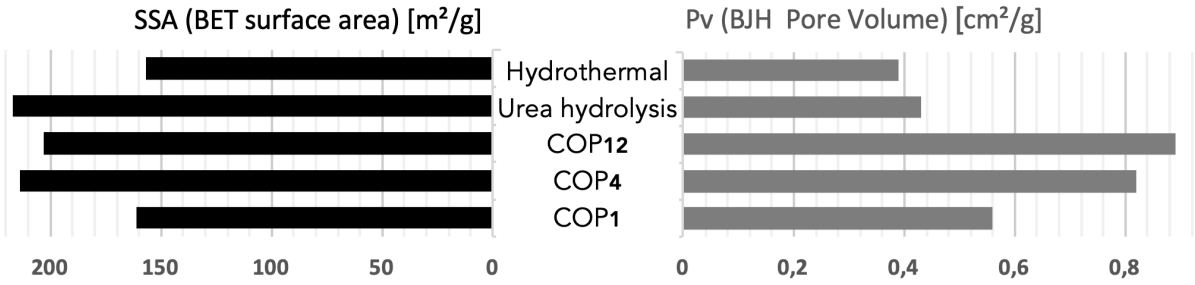

Figure 3.2: BET surface area (SSA) and BJH pore volume (Pv) for LDO samples calcined at 500°C according to synthesis method and sodium carbonate quantity.

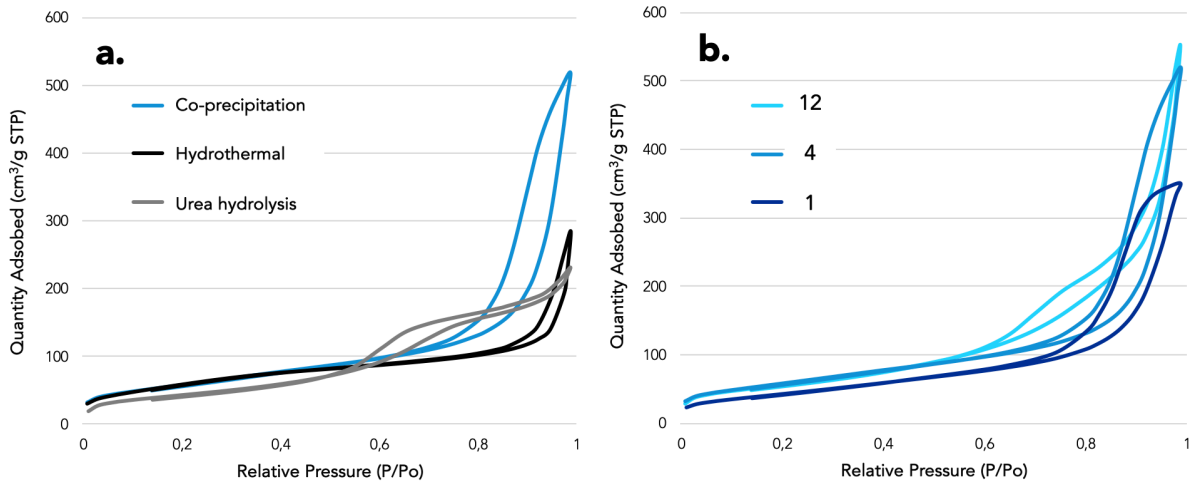

Figure 3.3: BET adsorption/desorption isotherms of LDO samples calcined at 500°C according to a) synthesis method and b) sodium carbonate quantity (stoichiometry: 12, 4 and 1).

The porosity of co-precipitation products is sensitive to the sodium carbonate quantity mostly for the charge equilibrium (COP_1) which presents the lowest SSA and Pv values. This sodium carbonate quantity was firstly chosen to respect the stoichiometric charge of the hydrotalcite structure $[Mg_{3-y}Ca_yAl(OH)_8]^+.[A]^{n-}_{1/n}.zH_2O$ with $A^{n-} = CO_3^{-2}$, so 1/n = 1/2 but the excess of anion in solution produces better porosity properties. The first excess of sodium carbonate (COP_4) is enough to improve SSA and Pv. The further excess (COP_{12}) slightly impacts the porosity properties for additional consumption of sodium carbonate.

In addition to N_2 physisorption, SEM pictures (Fig. 3.4a) show very different morphologies between COP and UREA samples: layers in the form of *sand roses* and flat, agglomerated stems, respectively. COP_1 and COP_4 samples also present differences: very well-defined *sand roses* for COP_4, denser morphology for COP_1 and COP_{12}, reducing their porosity. The overview (Fig. 3.4b) does not allows anything that homogeneity is better in COP_4 and confirms the other analysis in favor of this sample for the continuation of the study.

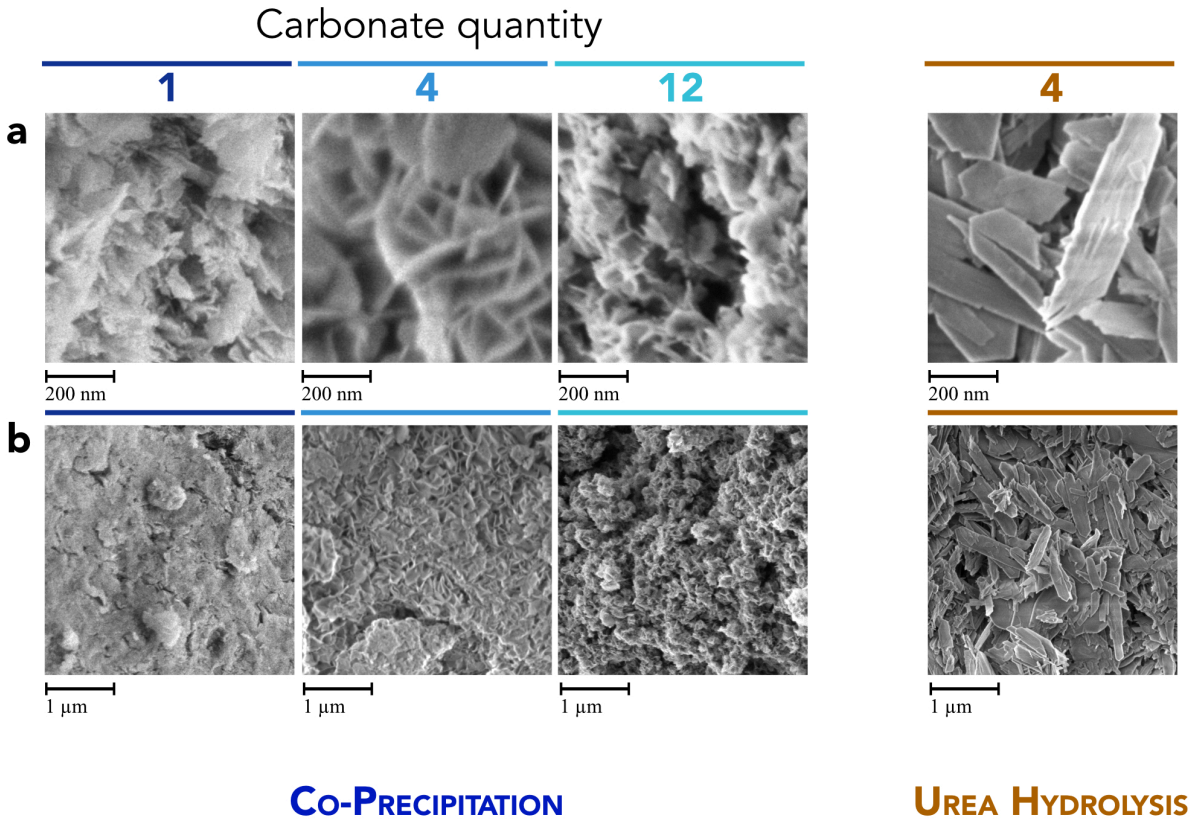

Figure 3.4: SEM pictures of samples a) on a 200 nm scale, b) on a 1 µm scale calcined at 500°C according to synthesis method and sodium carbonate quantity for co-precipitation.

This short comparison comforts the idea of studying the optimization of the synthesis condition with the co-precipitation method. In addition to the flexibility to change the conditions and reagents described in *Chap. 2*, the COP_4 is a suitable starting sample. So, all the further syntheses will use the co-precipitation method. The anion excess at 4 times charge equilibrium is maintained for carbonate, oxalate (di-anion as carbonate) and citrate (tri-anion). One equivalent of stearate (St^-) is chosen, which is enough to abide by the stoichiometry because the very low solubility in water does not experimentally allow to ensure the synthesis.

3.1.2 Co-precipitation method

The further optimization of the sorbents synthesis is continued by changing the anion size and/or charge, pH and Mg/Ca ratio. The trends and behaviors of the LDH products and calcination step are construed in this section with elementary analysis, TGA curves, and XRD thermo-analysis.

3.1.2.1 Elementary analysis

The Mg/Ca molar ratio is a capital parameter for the study. So, it is important to know the real values of Mg/Ca and (Mg+Ca)/Al which are accessible by elementary analysis. The nomenclature of each sample is noted based on the weight added for co-precipitation of the reactants. According to the magnesium and calcium nitrates, the real Mg/Ca molar ratio (Fig. 3.5a) is very close to the desired ratio. The values are systematically a little bit higher than the theoretical values. The $2/1/1_{CO3\cdot pH10}$ is the farthest away with Mg/Ca = 2.12 ± 0.06. Samples synthesized with carbonate seem rather off but their composition is still within the measurement uncertainty. So, the choice of the anion has no impact on the real Mg/Ca molar ratio.

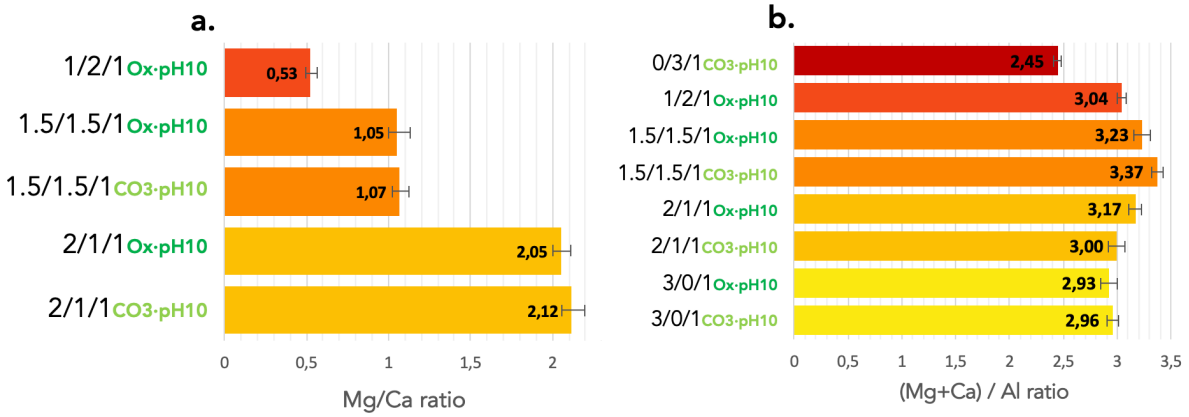

Figure 3.5: a) Mg/Ca and b) (Mg+Ca)/Al ratios of LDO samples calculated from elementary analysis values according to anion and composition.

Moreover, the theoretical (Mg+Ca)/Al molar ratio is constant and equal to 3 but it varies clearly (Fig. 3.5b) for $0/3/1_{CO3\cdot pH10}$ (2.45 ± 0.03) and for $1.5/1.5/1_{CO3\cdot pH10}$ (3.37 ± 0.05). Whatever the anion, the 3/0/1, 2/1/1 and 1/2/1 samples have a molar ratio (Mg+Ca)/Al close to or equal to 3 taking into account the measurement uncertainly.

3.1.2.2 TGA precursors oxidation

3.1.2.2.1 Anion effect

Thermogravimetric analysis of $Mg/Ca/Al_{pH10}$ samples prepared from various sodium anions shows the typical two-stage weight loss for 3/0/1 samples (Fig. 3.6). After a first step (between 50–250°C) attributed to the removal of water (physisorbed and inter-layer), a second step (between 220-700°C) is due to the removal of the octahedral layer hydroxyls and inter-layer anion groups [6].

After water removal, their weight losses after 250°C occur in one or two steps more or less distinguishable and become stable above 500°C. Due to the molecular weight of the interlayer stearate, the remaining weight at the end of calcination is lower for stearate (22%) than for carbonate (62%) and oxalate (60%) anions.

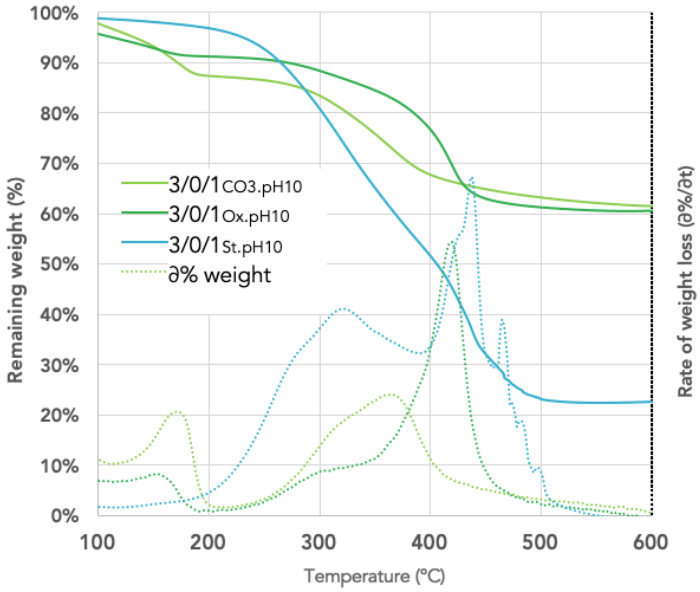

Figure 3.6: TGA oxidation of 3/0/1pH10 samples with various anions.

3.1.2.2.2 pH effect

The TGA profiles are similar for the carbonate samples (Fig. 3.7a) with both pH values ($3/0/1_{CO3\cdot pH8}$ and $3/0/1_{CO3\cdot pH10}$). The decomposition of the LDH structure begins around 200°C and finishes around 500°C. The same behavior is observed for oxalate (Fig. 3.7b) and stearate (Fig. 3.7c) samples for which the decomposition always ends at a temperature below 500°C.

It is important to note that for oxalate sample at pH 8 ($3/0/1_{Ox.pH8}$) and stearate sample at pH 10 ($3/0/1_{St.pH10}$), the rate of weight loss passes through several distinct maximum values corresponding to the dihydroxylation of the layer hydroxyl groups and the decomposition of interlayer anion. For both carbonate samples, these two steps are less visible (just a shoulder on the left side of the peak) and we obtain very similar curves revealing no effect of pH.

It is worth noting that for the oxalate samples ($3/0/1_{Ox}$) and stearate samples ($3/0/1_{St}$), the rate of weight loss presents various distinct maximum values for the two different pH studied, while very similar curves are obtained for the two carbonate samples. In fact, the study of the thermal decomposition of LDH precursors under air revealed thermogravimetric losses in two or three steps [7]. The first stage at low temperature is assigned to surface adsorbed or interlayer water molecules and the two other stages (between 200 and 500°C) to the dihydroxylation of the layer hydroxyl groups and the decomposition of interlayer carbonate.

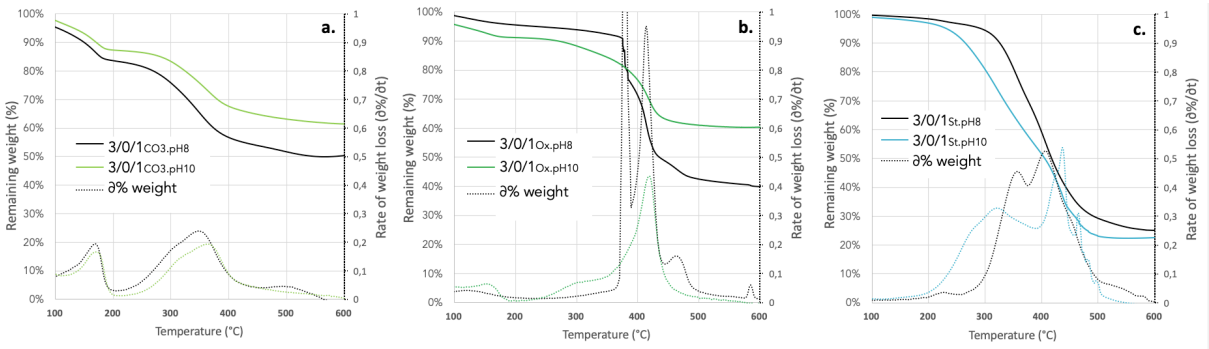

Figure 3.7: TGA oxidation of 3/0/1 LDH versus pH for a) carbonate, b) oxalate, and c) stearate interlayer anion.

3.1.2.2.3 Mg/Ca ratio effect

TGA oxidation of the carbonate samples indicates (Fig. 3.8) that for the sample with Mg/Ca = 0/3, the only mass loss after water removal starts at high temperature (around 560°C) with a maximum of about 645°C associated with $CaCO_3$ decomposition. Contrariwise, for the sample with Mg/Ca = 3/0, the mass loss starts just after water removal with a maximum of about 365°C associated with the decomposition of $MgCO_3$. For intermediate samples (other Mg/Ca values), after water removal, the TGA profiles present a two-stage mass loss combining the decomposition of $MgCO_3$ and $CaCO_3$ as observed previously [8].

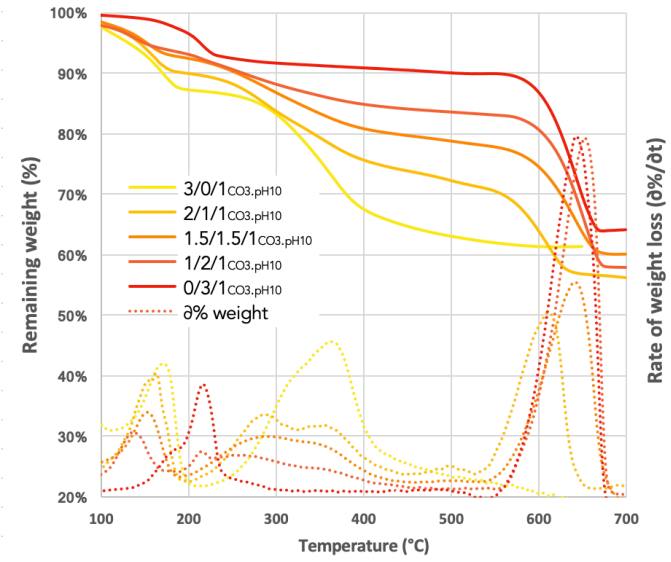

Figure 3.8: TGA oxidation of Mg/Ca/$Al_{CO3\cdot pH10}$ samples with various Mg/Ca ratios.

Then, TGA thermograms of various Mg/Ca/$Al_{CO3.pH10}$ samples indicate that, if the 3/0/$1_{CO3.pH10}$ sample is decarbonized after calcination at 500°C, the substitution of Mg for Ca needs a higher calcination temperature of at least 700°C for the total decomposition of $CaCO_3$. After calcination at 700°C, a weight loss of about 40% is observed for each sample (Fig. 3.8). oxalate samples goes through the decomposition of the oxalate and then the carbonate and finishes around 700°C with a remaining weight between 50% and 60% (Fig. 3.9a) while the calcination of the stearate samples is complete at 500°C with a remaining weight around 25% (Fig. 3.9b).

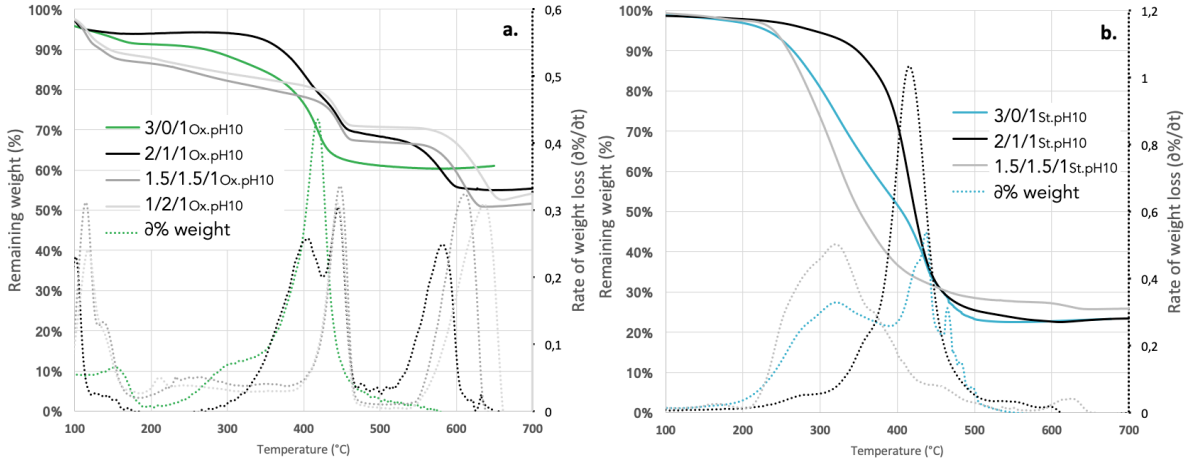

Figure 3.9: TGA oxidation of a) Mg/Ca/$Al_{Ox\cdot pH10}$ and b) Mg/Ca/$Al_{St\cdot pH10}$ samples with various Mg/Ca ratios.

As conclusion of the characterization of LDHs, the calcination temperature of 500°C is enough to obtain LDOs from LDHs prepared without Ca at pH 8 or 10 and with carbonate or oxalate anion ($3/0/1_{\cdot pH10}$ and $3/0/1_{\cdot pH8}$ samples) and for those prepared with a stearate interlayer anion with various compositions. Contrariwise, other compositions e.g. with Ca and carbonate and oxalate interlayer anions need a higher temperature of calcination (700°C) to produce calcium oxide available for CO_2 sorption.

3.1.2.2.4 Thermo-analysis

Before calcination, the phases obtained depend on the anion used. For example, Fig. 3.10 reports the X-ray thermo-diffractograms of LDH to LDO for $1/2/1_{CO3\cdot pH10}$, $1/2/1_{Ox\cdot pH10}$, and $1.5/1.5/1_{Ox\cdot pH10}$ samples, according to temperature. Indeed, for a Mg/Ca ratio = 1/2, co-precipitation with sodium carbonate produces a calcium carbonate phase named aragonite (JCPDS n° 05-0453) (Fig. 3.10a) in contrast to sodium oxalate which forms mainly a calcium oxalate phase named whewellite (JCPDS n° 20-321) (Fig. 3.10b) and an aragonite phase in lower proportion. The formation of this calcium carbonate phase in this oxalate sample is probably due to a small amount of carbon dioxide dissolved in the solution during the solubilization of sodium oxalate and competitive carbonation. This peculiarity is not observed on the $1.5/1.5/1_{Ox\cdot pH10}$ (Fig. 3.10c).

The first LDH structure transformation is well visible at 400°C for both phases and leads to the formation of the magnesium calcium carbonate phase ($Mg_{0.03}Ca_{0.97}CO_3$ JCPDS n° 01-089-1304) whatever the anion and composition. In fact, this structure is already present in small quantities at 100°C and only detectable by its main ray at $2\theta = 29°$. The second step consists in the oxidation of carbonate, it starts at 600°C and is complete at 700°C to form lime (CaO JCPDS n° 01-070-4968).

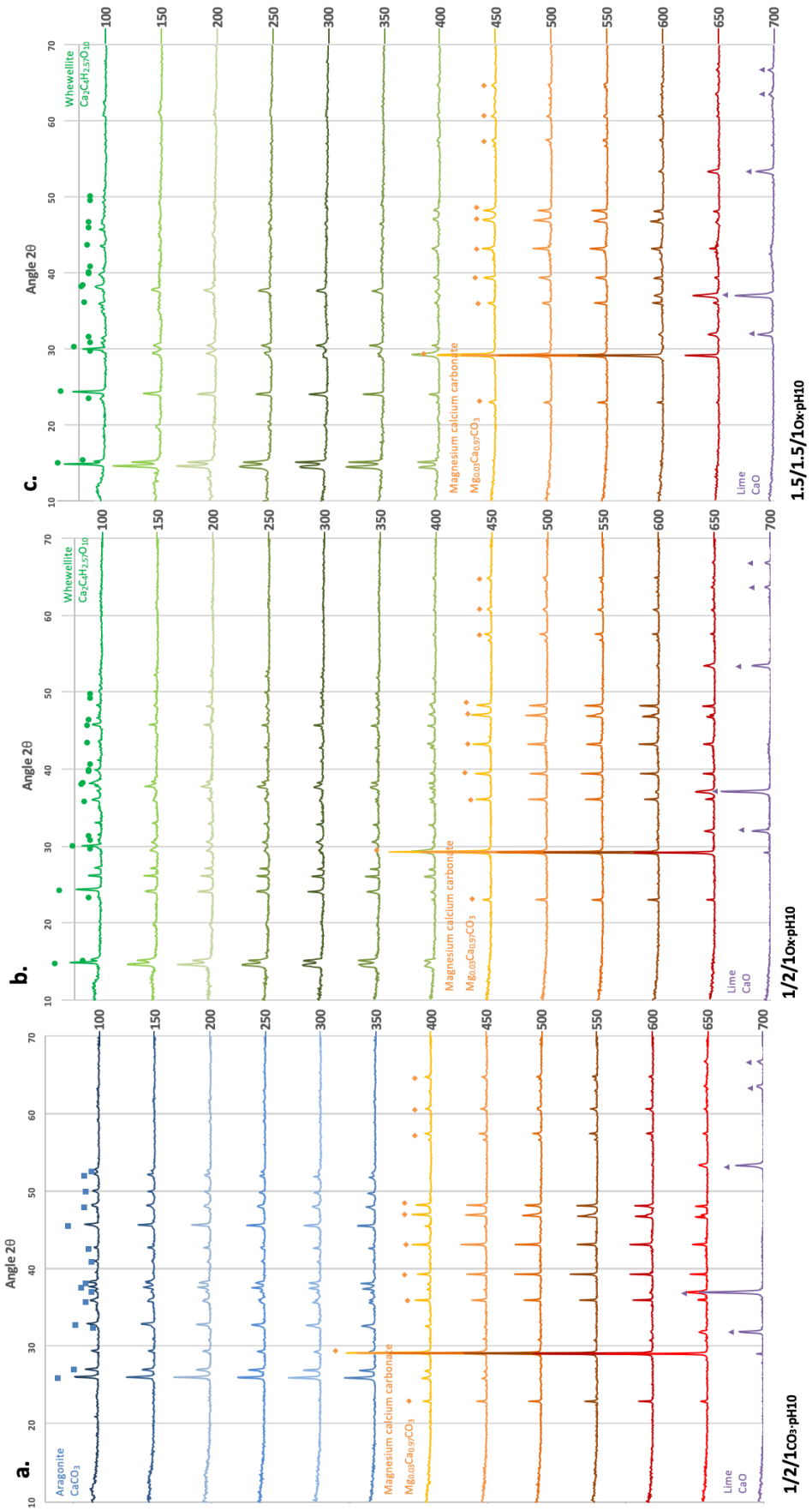

Figure 3.10: X-ray thermo-diffractograms of LDH to LDO samples from a) $1/2/1_{CO3 \cdot pH10}$, b) $1/2/1_{Ox \cdot pH10}$, c) $1.5/1.5/1_{Ox \cdot pH10}$, according to temperature.

3.2 LDOs characterization

After calcination, the LDO sorbents are characterized according to anion size, pH and Mg/Ca ratio. In this section, N_2 physisorption, XRD analysis and SEM pictures are reported to evaluate the sorbent properties. This part ends with the CO_2 sorption capacity test and CO_2 sorption stability results.

3.2.1 XRD

3.2.1.1 Anion effect

For all 3/0/1 compounds calcined at 500°C, the organic part of the material decomposes (dehydroxylation and decarbonation), leading to the formation of the LDH structure, and then mixed oxide (LDO) with a 3D network [7]. As predicted to the TGA results, for all the 3/0/1 compounds calcined at 500°C, the only phase produced is that of amorphous mixed oxides ($MgAlO_x$), with the features of periclase (JCDPS n° 00-045-0946) [8] regardless of the interlayer anion used for the LDH synthesis and its size or valence (Fig. 3.11).

3.2.1.2 pH effect

XRD identifies the formation of MgO periclase as the main phase regardless of the pH used. However, for $3/0/1_{Ox.pH8}$ sample, the spinel phase ($MgAl_2O_4$) is also identified [9]; the same as that observed in the UREA LDO sample. So, pH has little no or no effects on the formation of LDO from the carbonate interlayer anion or other anions (Fig. 3.11) for the 3/0/1 composition.

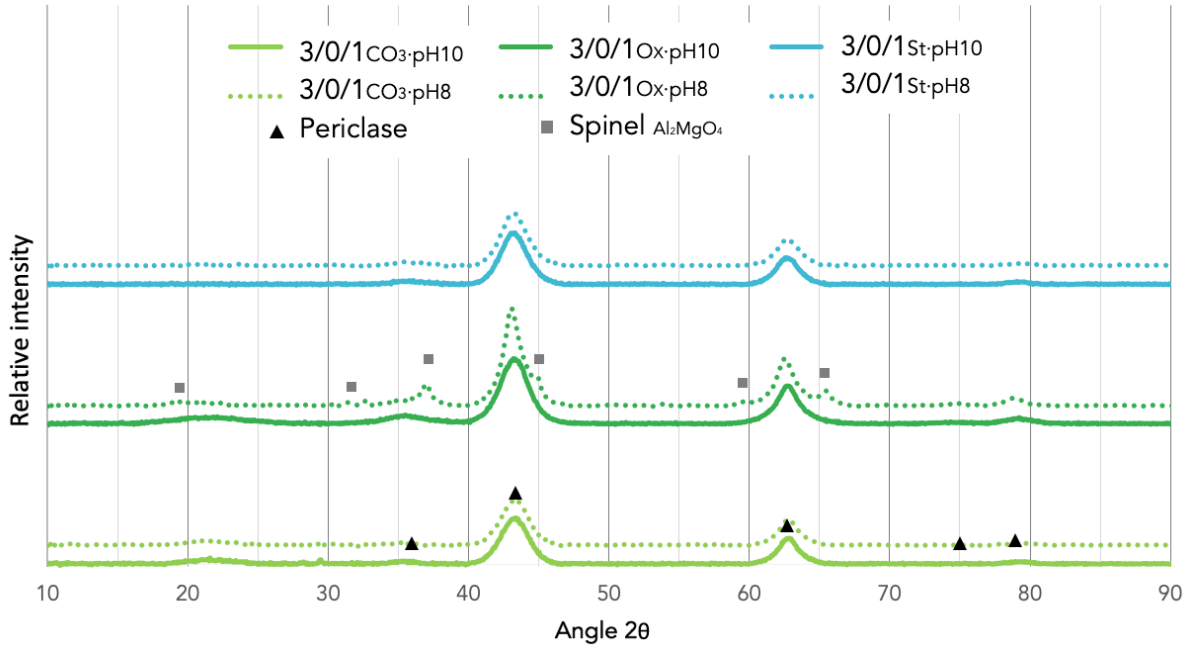

Figure 3.11: X-ray diffractograms of LDO samples calcined at 500°C prepared from LDH 3/0/1 ratio and pH 10, according to interlayer anion and to pH value.

3.2.1.3 Mg/Ca ratio effect

For the sample containing calcium carbonate (Fig. 3.12a) and oxalate (Fig. 3.12b), XRD analysis allows attesting of the formation of a phase mixture after calcination at 500°C. In fact, a MgO periclase and a magnesium calcium carbonate are observed in all sorbents containing calcium even from interlayer anions of oxalate and stearate (not shown). In all these samples, the magnesium calcium carbonate phase is visible and is much more crystallized than the periclase phase. The main periclase intense ray (2θ = 42.9°) is hidden by the magnesium calcium carbonate ray at 2θ = 43.3° and disappears for the largest Ca contents.

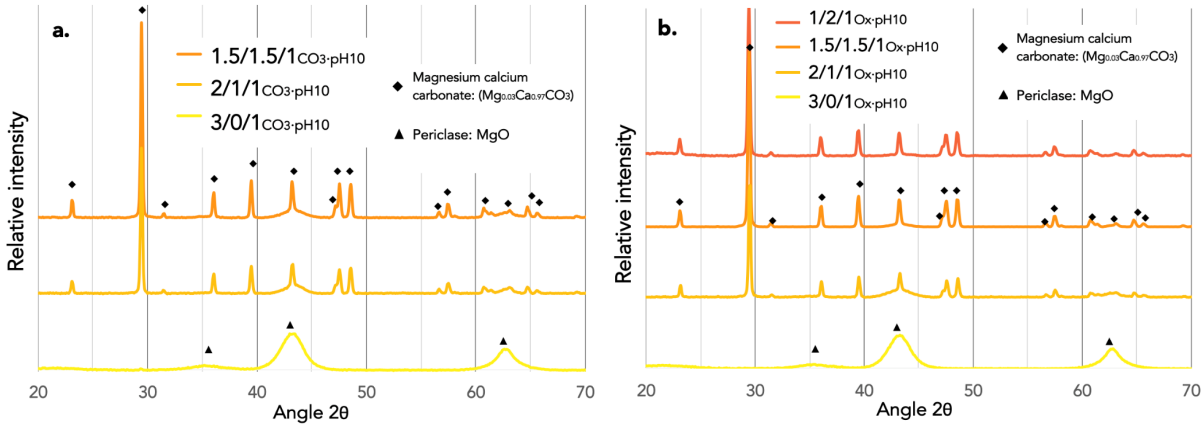

Figure 3.12: X-ray diffractograms of LDO samples prepared from LDH a) carbonate and b) oxalate interlayer anion and pH 10, calcined at 500°C, according to various Mg/Ca ratios.

The evolution of the Mg/Ca ratio does not affect the phase distribution in the sample prepared from various anions: the XRD diffractograms are similar for materials using the carbonate anion for the 2/1/1 and 1.5/1.5/1 Mg/Ca/Al compositions (Fig. 3.12a) and using the oxalate anion for the 2/1/1, 1.5/1.5/1, and 1/2/1 Mg/Ca/Al compositions (Fig. 3.12b). XRD of materials using stearate anion for the same compositions indicates the same phase distribution (not shown).

3.2.1.4 Calcination temperature effect

First, the calcination temperature between 500°C and 700°C does not affect the formation of calcium-free LDOs (3/0/1 ratio) from various interlayer anions. XRD analysis shows the higher intensity of MgO periclase (as the only phase) with higher calcination temperature (not shown), indicating better crystallinity of this phase as previously reported [9].

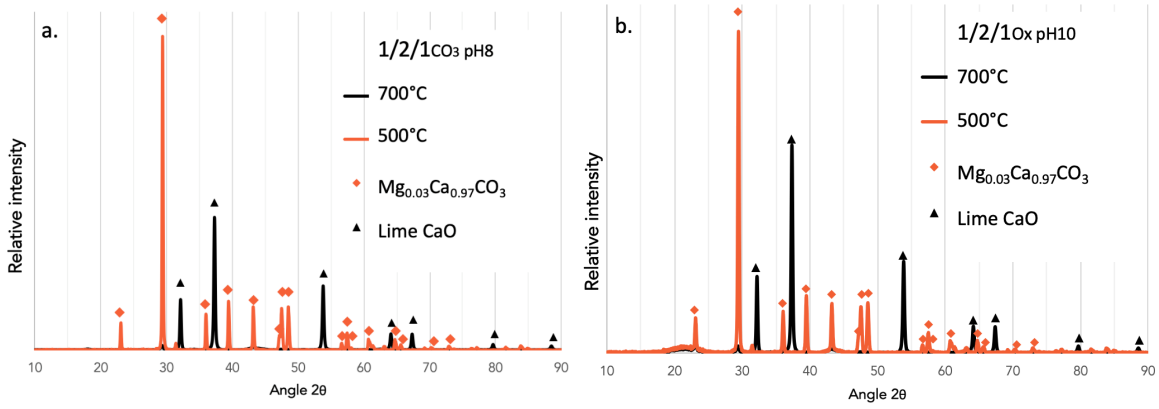

Figure 3.13: X-ray diffractograms of LDO samples prepared from a) $1/2/1_{CO3\cdot pH8}$, and b) $1/2/1_{Ox\cdot pH10}$ LDHs according to the calcination temperature.

However, calcination temperature has a noticeable effect on the formation of LDOs containing calcium from carbonate or oxalate interlayer anions for all other Mg/Ca/Al ratios as presented, for example, for $1/2/1_{CO3.pH8}$ (Fig. 3.13a) and $1/2/1_{Ox.pH10}$ (Fig. 3.13b). In fact, the modification in the sorbents of the structure is due to the decomposition of a magnesium calcium carbonate, containing a large part of calcium in favor of CaO formation and is expected by the TGA results of LDHs (Section 3.1.2.2). For LDOs containing calcium from stearate interlayer anion and for all other Mg/Ca/Al studied ratios, increasing the calcination temperature from 500°C to 700°C does not affect the structure (XRD not shown), because of the complete decomposition of the stearate in the oxide at a temperature below 500°C as presented by TGA (Fig. 3.9b).

3.2.2 N_2 physisorption

The LDOs samples present type IVa isotherms [5] associated with mesoporous adsorbents (Fig. 3.14). CO_2 capture capacity depends on the number of CaO sites and their accessibility. So, to optimize the calcium sorption efficiency, the porosity properties (specific surface area and pore size) of the sorbents must be improved [10].

3.2.2.1 Anion & pH effect

In the adsorption/desorption curves (Fig. 3.14), a difference appears for the stearate samples which present the flat line characteristic of mesoporous materials, whereas for the carbonate and oxalate samples, the adsorption curves do not end with a plateau and have a nearly vertical segment revealing the presence of some meso-porosity. This reduces the calculations significance of average pore size [10].

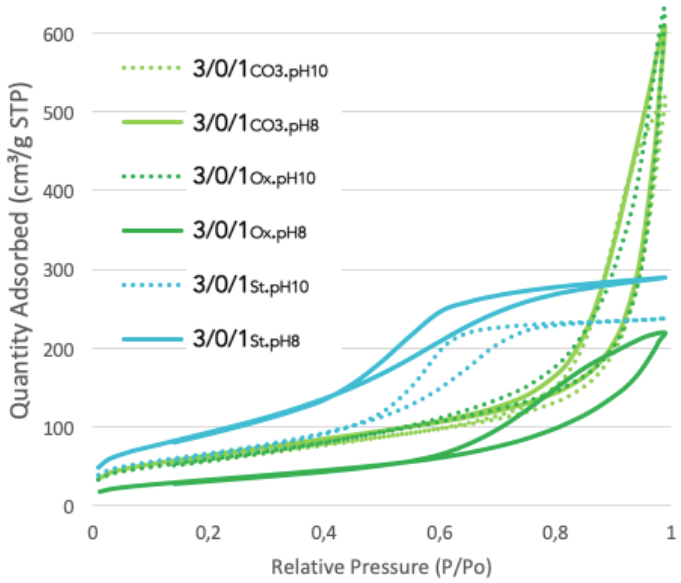

Figure 3.14: BET adsorption/desorption isotherms of LDO samples calcined at 500°C from 3/0/1 LDHs prepared at pH 8 or 10 and with various anions.

Similar results (Fig. 3.15 left) of BET surface area (SSA) were observed for the samples prepared at pH 10 (214-242 m^2/g) but at pH 8, the stearate sample presented the highest SSA value (350 m^2/g) while the SSA of the oxalate sample was deteriorated (117 m^2/g). However, for carbonate and oxalate samples, the Pv (0.8-1.0 cm^3/g) is twice that of stearate samples (0.4-0.5 cm^3/g) regardless of the synthesis pH (Fig. 3.15 right). Looking at the results in Figure 3.16, the size of the anion improves the quantity of N_2 adsorbed as shown by the values for oxalate higher than for carbonates. But the trend is slight and particularly limited and unfavorable with larger anions because of the solubility of the latter.

Thus, the correlation between anion size and SSA is not so evident. The cause could also be to a lesser extent the difference in charge, different from -2 with citrate and stearate, and disturb the formation of small pores.

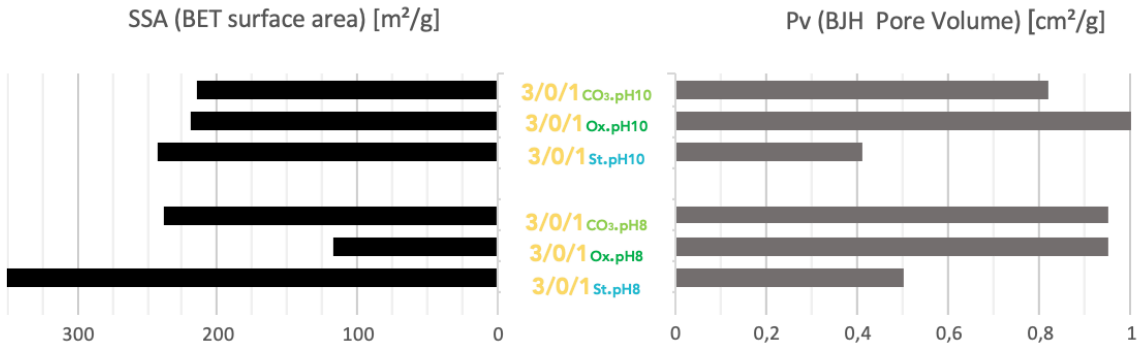

Figure 3.15: BET surface area (SSA) and BJH pore volume (Pv) for LDO samples calcined at 500°C from 3/0/1 LDH prepared at pH 8 or 10 and with various anions.

The greatest SSA is obtained at pH 8 with sodium stearate (350 $m^2.g^{-1}$) but with a middle PV value compared to the highest Pv at pH 10 with sodium oxalate (1.00 $cm^3.g^{-1}$). As a function of interlayer anions, meso-porosity is associated with the highest SSA value for samples from stearate and macro-porosity correlates with the greatest Pv values for carbonate and oxalate samples. So, whatever the pH used, the best anions appear to be carbonate and oxalate for the CO_2 sorption application. For stearate, the most appropriate pH (pH=8) is kept for the following studies. The size of the anion is then determining in the quality of precipitation independently of the pH by allowing the formation of LDH structure probably due to the favorable reaction speed.

3.2.2.2 Mg/Ca ratio & pH effect

All carbonate samples (Fig.16a) seem to present some meso-porosity because of their near vertical segment. While the oxalate samples with and without calcium (Fig. 3.16b), and stearate samples (Fig. 3.16c) with calcium have the same behavior, a very different adsorption curve is observed for the 3/0/1

St pH 8 sample with a flat line characteristic of mesoporous materials. The citrate samples are apart with very lower meso-porosity than others (Fig. 3.16d) while they are low calcium content.

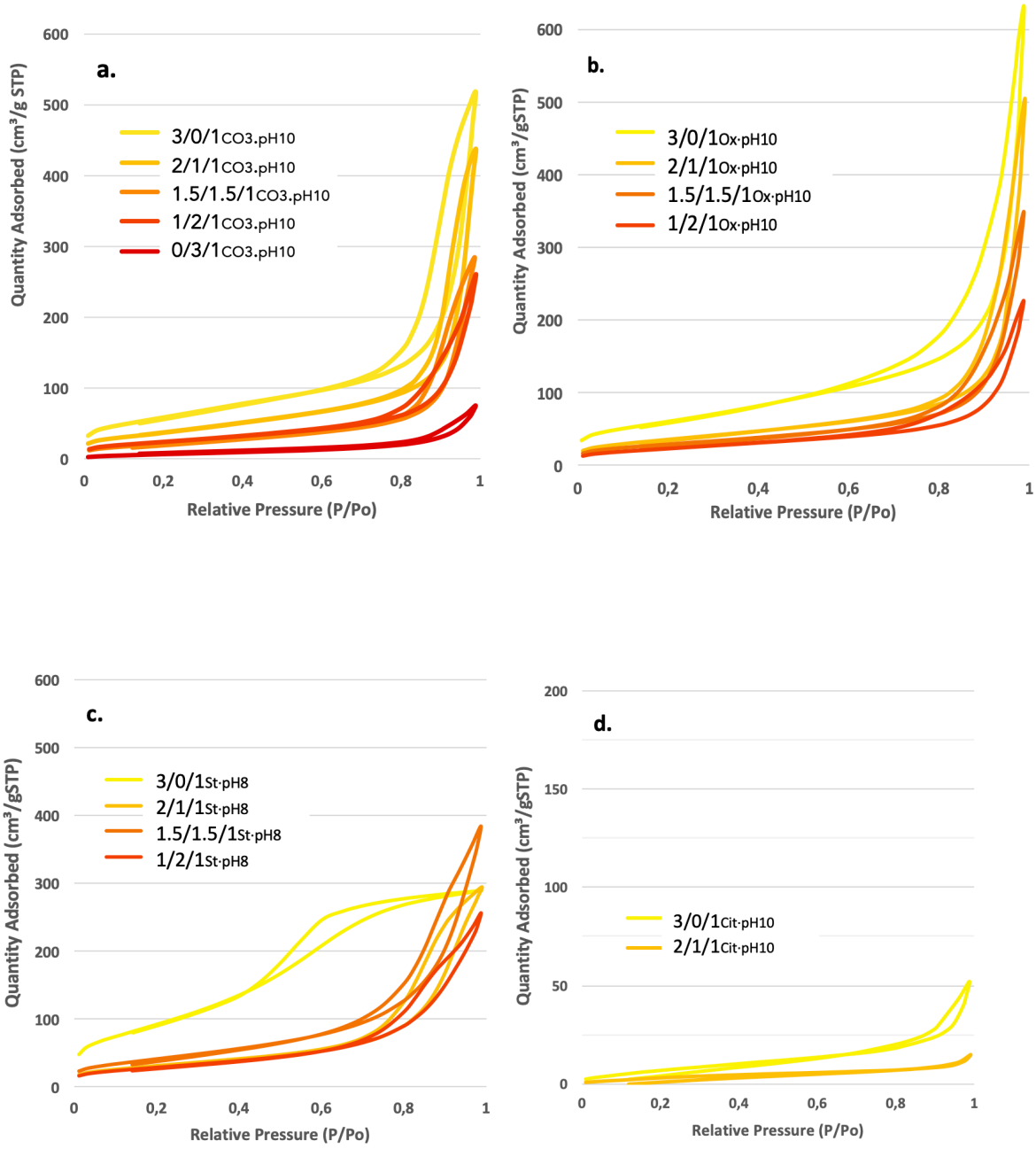

Figure 3.16: BET adsorption/desorption isotherms of LDO samples calcined at 500°C a) from carbonate LDH, b) from oxalate LDH, c) from stearate LDH, d) from citrate LDH with various Mg/Ca ratios

When Mg/Ca ratio decreases, the SSA and Pv of the carbonate samples fall progressively (from 214-242 m^2/g to 30 m^2/g and from 0.8-1.0 to less than 0.2 cm^3/g, respectively) whatever the pH value (Fig.3.17). While oxalate samples give comparable SSA results to carbonate LDO whatever Ca content (Fig.3.17), their Pv is greater especially for pH 10 (0.2-0.8 cm^3/g compared to 0.4-1.0 cm^3/g for various Mg/Ca ratios). The decrease of pH appears unfavorable for oxalate compounds. Citrate sorbents SSA only reach 29 m^2/g, which corresponds to the value obtained with the worst CO_3 sample without magnesium ($0/3/1_{CO3.pH10}$). This anion is clearly the least promising. Citrate does not react as well as the other anions with metallic nitrate and does not allow operating proper co-precipitation synthesis.

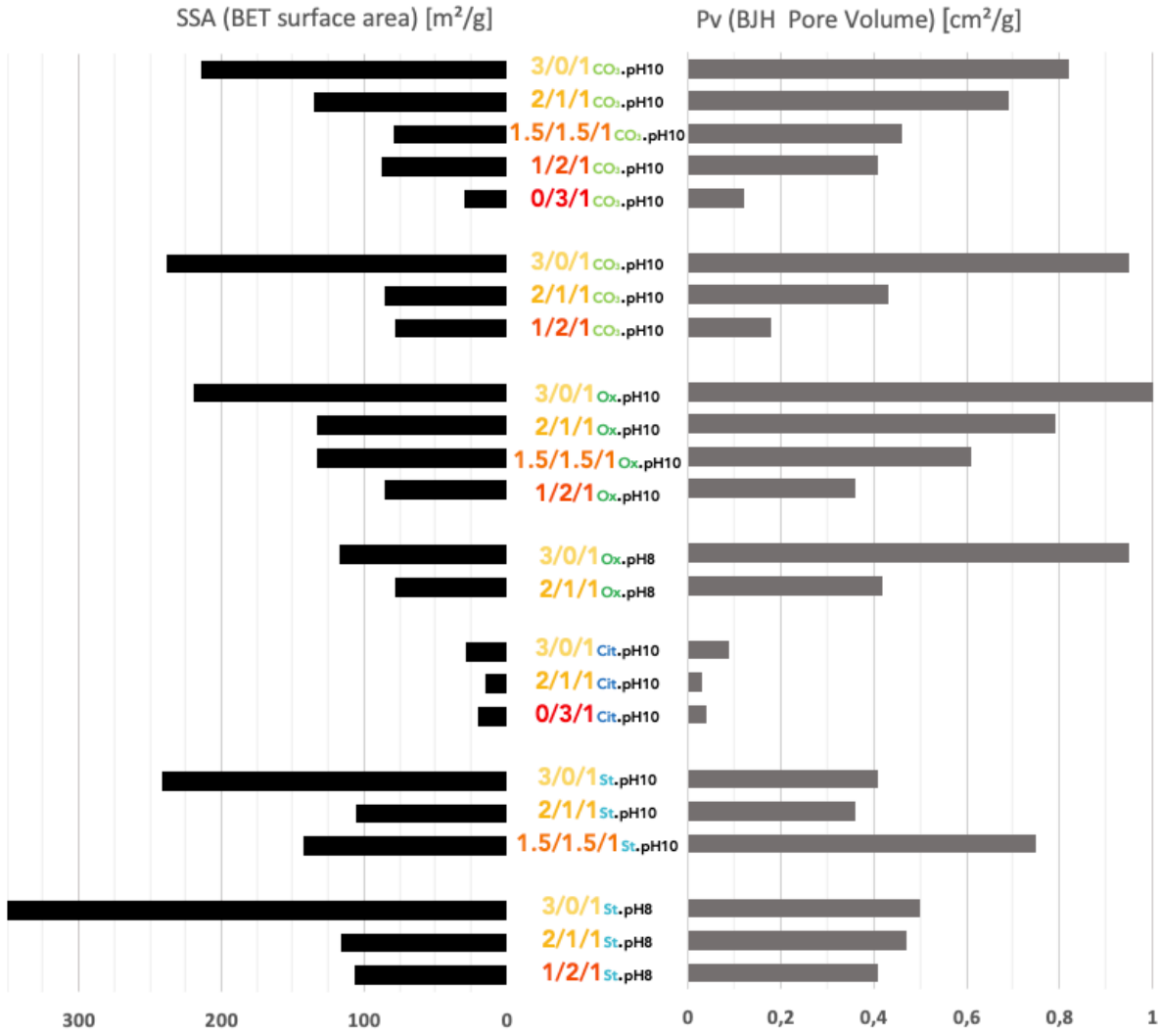

Figure 3.17: BET surface area (SSA) and BJH pore volume (Pv) for LDO samples calcined at 500°C from 3/0/1 LDH prepared at pH 8 or 10 and with various anions.

The stearate samples containing Ca are not interesting from the point of view of their SSA, which match to the values observed with the other anions and the same compositions (106-143 m^2/g). The same behavior is observed for Pv values that reach similar or lower levels the corresponding Ca-containing carbonate and oxalate sorbents (Fig.17). For example, $2/1/1_{St.pH8}$ presents a very similar value to all the interlayer anions (between 0.4-0.5 cm^3/g). So, N_2 adsorption analysis results attested to the increase in SSA by the BET method with the size of the anion (from carbonate to stearate) as previously reported [6] but only for the samples without Ca. Stearate is an overweight anion and could then collapse the layered structure during calcination, but in the presence of Ca, this phenomenon does not appear when samples are calcined at 500°C. In fact, the presence of a magnesium calcium carbonate phase ($Mg_{0.03}Ca_{0.97}CO_3$) observed by XRD for all Ca-containing samples keeps the strength of the structure until 550°C. However, this phase disappears before 700°C in favor of the oxide phases (CaO and MgO). Thus, the effect of calcination temperature up to 700°C has to be studied to evaluate the samples after the decarbonation phase. Because of forthcoming calcium addition, the anionic and pH parameters can be fixed at carbonate or oxalate and at pH 10, respectively.

3.2.2.3 Calcination temperature effect

Increasing the temperature from 500°C to 700°C generally decreases the SSA for carbonate and oxalate samples for all Mg/Ca ratios (Fig.18).

Pv follows the same downwars trend for oxalate samples, with increasing in temperature. However, an opposite behavior is observed for carbonate samples for which Pv increases with calcination temperature only for greater contents of Ca.

This difference in behavior between carbonate and oxalate samples can be explained as follow: calcium carbonate decomposes to calcium oxide between 500°C and 700°C, leading in a higher pore volume left by removal of calcium carbonate, with a higher volume of calcium carbonate than calcium

oxide. In the oxalate samples, a spinel phase (observed by XRD) after calcination at 500°C could sinter during calcination starting from 500°C and 700°C and more easily lead to sorbent collapse [11].

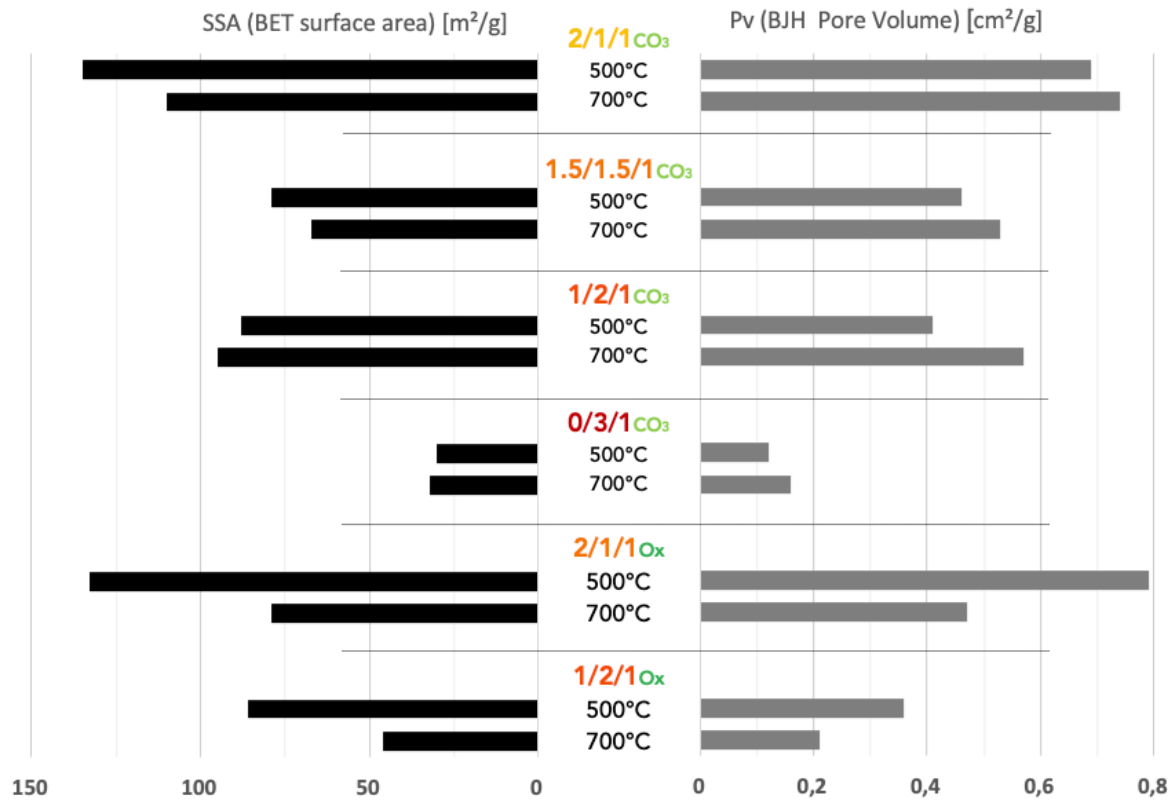

Figure 3.18: BET surface area (SSA) and BJH pore volume (Pv) for LDO samples from Mg/Ca/$Al_{CO3.pH10}$ and Mg/Ca/$Al_{Ox.pH10}$ with various compositions calcined at 500 or 700°C.

3.2.3 SEM

The results obtained by SEM can be correlated with the porosity trends obtained by N_2 adsorption associated with BET and BJH methods, respectively, for all studied parameters (anion, pH, and Mg/Ca ratio).

Indeed, for the carbonate samples , the morphology of the layers appeared in the typical form [10] of *sand roses*, equally apparent for the lower pH (Fig. 3.19 a and b). However, for pH 8, *sand roses*

morphology was most evident in the absence of Ca (Fig. 3.19b) and occasionally as Mg/Ca decreased. For pH 10, while the morphology was maintained by decreasing the Mg/Ca, the thickness of the floral pattern was reduced (Fig. 3.19c).

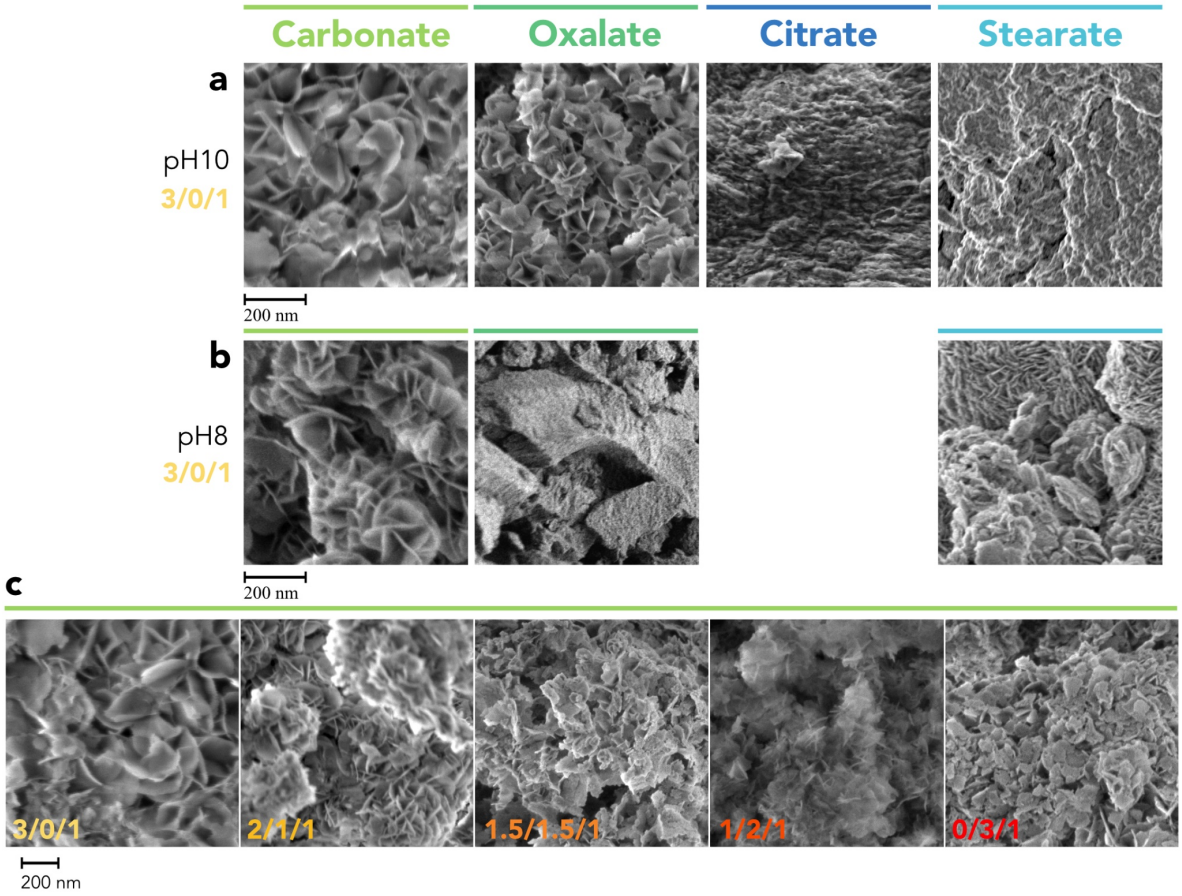

Figure 3.19: SEM pictures of a) Mg/Ca/Al$_{\cdot pH10}$ samples versus interlayer anions, b) Mg/Ca/Al$_{\cdot pH8}$ samples versus interlayer anions, and c) Mg/Ca/Al$_{CO3\cdot pH10}$ samples versus Mg/Ca ratio calcined at 500°C.

For the oxalate samples, morphology in the form of *sand roses* appeared at pH 10 in all sorbents with various Mg/Ca ratios (Fig. 3.19a). Here again, the finest *sand roses* were observed for the lowest Mg/Ca ratio. Contrariwise, the floral pattern disappeared at pH 8 and SEM analysis showed a *stone*-like morphology with no apparent layer or porosity (Fig. 3.19b) [12].

Without surprise, the citrate sample morphology looks very dense and almost no apparent porosity was observed (Fig. 3.19 a and b).

Finally, for stearate samples, *sand roses* are present only in the absence of Ca at pH 8 (Fig. 3.19b) and in dense form. At pH 10, the stearate sorbents looked bulkier.

Then in all cases, the apparent porosities and the presence of *sand roses* observed by SEM were fully correlated to the highest SSA and Pv values obtained by N_2 adsorption (Fig. 3.17) as previously reported [12] but the finesse of the *sand roses* was linked to the lowest SSA and Pv values (Fig. 3.17).

3.2.4 Sorption properties

3.2.4.1 Sorption capacity

The sorption capacity (in gCO_2/100 g sorbent) was evaluated for several samples (Table 3.1). Considering that no CO_2 sorption is possible on MgO sites at 600°C, the theoretical value of this property (indicated below each Mg/Ca/Al composition) changes according to the Ca content, increasing when Mg/Ca decreases. This hypothesis was validated by the very low values obtained with $3/0/1_{Ox\cdot pH10}$ and MgO (1.4 and 1.3 gCO_2/100 g sorbent, respectively).

A global increase in CO_2 sorption capacity with calcium content rise was observed for each anion at the same pH despite the decrease in porosity previously observed by N_2 physisorption analysis. However, the upper limit of sorption capacity should be given by the highest Ca content ($0/3/1_{CO3\cdot pH10}$) but its sorption capacity (32.8 $g_{CO2}/100g_{sorbent}$) is lower than that of $1/2/1CO_{3\cdot pH10}$ (37.2 $g_{CO2}/100g_{sorbent}$). This behavior can be explained by the absence of Ca dispersant (Mg) and the lower accessibility of CaO by CO_2. On the other side, $0/3/1CO_{3\cdot pH10}$ also exhibited a lower sorption capacity than pure CaO (49.3 $g_{CO2}/100g_{sorbent}$) which cannot be justified in the same way but by the involvement of Ca in another phase as calcium aluminate or the low accessibility due to low surface area of this sample associated with its sintering during calcination (Fig. 3.16).

Then, the CaO sites accessibility (given by the sorption capacity in $g_{CO2}/100g_{CaO}$ in the sample) permits comparison of sorbents of various compositions (Table 3.1). These values can be compared to the both theoretical sorption capacity of CaO (78 $g_{CO2}/100g_{CaO}$) and the experimental capacity of pure

CaO (49.3 $g_{CO2}/100g_{CaO}$). The improvement of this property when CaO is dispersed in LDO of composition 2/1/1 Mg/Ca/Al with carbonate and pH 10 (67.6 $g_{CO2}/100g_{CaO}$) is highlighted. The maximum value of 74.4 $g_{CO2}/100g_{CaO}$ very close to the theoretical value can be reached by LDOs from an oxalate precursor.

For most of the Mg/Ca/Al ratio, the effect of decreasing pH is a strong loss of sorption capacity proven with carbonate for 2/1/1, 1.5/1.5/1, and 1/2/1, with oxalate for 2/1/1, and with stearate for 2/1/1 and 1.5/1.5/1. An exception was revealed for $1/2/1_{CO3\cdot pH8}$, which reached the highest sorption capacity (39.2 $g_{CO2}/100g_{sorbent}$). However, comparison of CaO site accessibility revealed the highest value for $2/1/1_{Ox\cdot pH10}$ and more generally, for samples prepared at pH 10.

Table 3.1: Sorption capacity and CaO sites accessibility of different samples according to Mg/Ca ratio, anion and pH.

Mg/Ca/Al	*Anion*	*pH*	*Sorption capacity*	*CaO sites accessibility*
			gCO_2/100 g **sorbent**	gCO_2/100 g **CaO**
*3/0/1 0**	Ox	10	1.0	-
*2/1/1 23**	CO_3^{2-}	10	20.2	67.6
	CO_3^{2-}	8	9.2	30.9
	Ox	10	22.2	74.4
	Ox	8	9.7	32.5
	Cit	10	14.5	48.5
	Cit	8	7.8	26.1
	St	10	12.5	41.7
	St	8	6.5	21.7
*1.5/1.5/1 34**	CO_3^{2-}	10	20.7	48.1
	CO_3^{2-}	8	11.4	26.4
	Ox	10	31.1	69.7
	St	10	15.6	36.4
	St	8	10.7	24.8
*1/2/1 43**	CO_3^{2-}	10	37.2	67.5
	CO_3^{2-}	8	39.2	71.1
	Ox	10	31.2	56.6
	St	8	20.7	37.6
*0/3/1 60**	CO_3^{2-}	10	32.8	42.7
CaO			49.3	49.3
MgO	References		1.3	-

** Theoretical sorption capacity (gCO_2/100 g sorbent).*

An optimal Mg/Ca/Al ratio of 1/2/1 could be found for the carbonate at pH 8 which possessed both a high sorption capacity (39.2 $g_{CO2}/100g_{sorbent}$) and CaO sites accessibility (71.1 $g_{CO2}/100g_{CaO}$) to make the most of its CO_2 sorption capacity. Besides, the CaO sites accessibility of $1.5/1.5/1_{CO3\cdot pH10}$ was (48 $g_{CO2}/100g_{CaO}$) very close to pure CaO (49 $g_{CO2}/100g_{CaO}$), while the corresponding oxalate sorbent ($1.5/1.5/1_{Ox\cdot pH10}$) led to 69.7 $g_{CO2}/100g_{CaO}$ one of the most appreciable values. The use of oxalate also resulted in the highest accessibility of CaO sites (74.4 $g_{CO2}/100g_{CaO}$) for 2/1/1 Mg/Ca/Al composition and pH10.

Despite the porosity and morphology observed in the citrate sorbents, the CO_2 sorption capacity is better than the corresponding stearate sorbent. Indeed, $2/1/1_{Cit.pH10}$ reaches 14.5 $g_{CO2}/100g_{sorbent}$ which is 48.5 $g_{CO2}/100g_{CaO}$. The sorption capacity of $2/1/1_{Cit.pH8}$ is lower than that of $2/1/1_{Cit.pH10}$ so the pH effect follows the same trend as for oxalate sorbents.

Finally, stearate samples always had the lowest CO_2 sorption capacities and CaO sites accessibilities whatever the composition, or pH.

To conclude, the accessibility of CaO sites and the CO_2 sorption capacity are directly linked to the interlayer anion, pH, and calcium content, but not so clearly related to the porosity properties measured by N_2 adsorption.

3.2.4.2 Stability of sorption capacity

As mentioned previously (*§ II.2.5*), the sorption capacity values differ from those obtained by the sorption test (*§ III. 3.1*) because of the different conditions used: weight of samples, type of solid/gas contact, and carbonation state of the samples.

The four samples with both the highest CO_2 sorption capacity and the highest accessibility of CaO sites (Table 3.1) were studied by TGA to evaluate the stability of their sorption capacity depending on interlayer anion, pH, and calcium content. That concerned $1/2/1_{Ox\cdot pH10,}$ $1/2/1_{CO3\cdot pH10}$, $1/2/1_{CO3\cdot pH8}$, and $1.5/1.5/1_{Ox\cdot pH10}$ (Fig. 3.20).

Absorption/desorption cycles on calcium oxide sorbents are well known to reduce CO_2 sorption capacity because of the formation of calcium carbonate (bulkier than CaO) and its possible sintering [13]. Kuo et al. adds that an aggregation of CaO is induced by the adsorption/desorption cycles all the more at high temperature (930°C) and thus decreases the SSA and thus the capacity of absorption by decline of the accessibility of the CaO sites. The synthesis and composition of the materials remain quite different, however, the results of the adsorption/desorption cycles - quite similar to the tests performed on our samples - on limestone-based sorbents are marked by the same flucuations of mass loss and gain. After 7 cycles in their condition, the loss of adsorption capacity amounts to about 27% (with a sample whose Mg/Ca/Al ratio is 1/7/1); this is less than carbonate-based sorbents and more than oxalate-based ones.

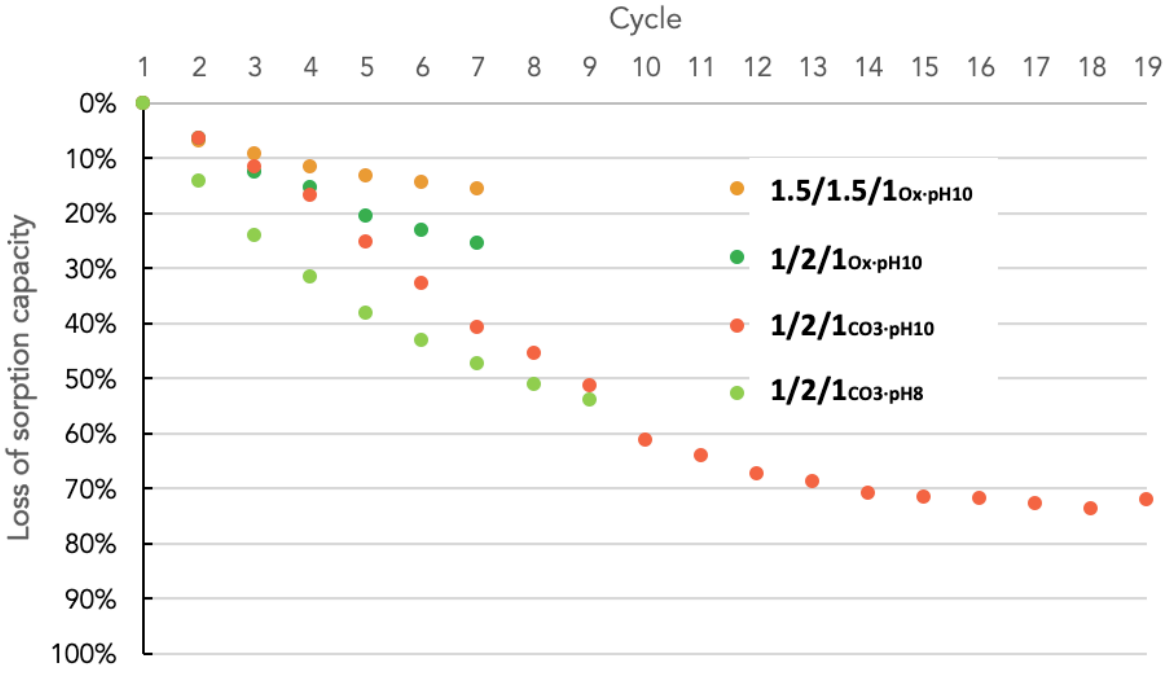

Figure 3.20: Sorption capacity versus absorption/desorption cycles number for various sorbents at 500°C (the number of cycles depends on the availability of the device with a minimum of 7 cycles).

The carbonate-based sorbents presented much worse stability than the oxalate-based sorbents. Their sorption capacity decreased very rapidly for the first few cycles, still rapidly until the 10th cycle to reach a 70% loss and stabilize for the next 10 cycles (Fig. 3.20).

A slight influence of pH on the stability of the sorption capacity was observed for carbonate samples with a Mg/Ca ratio of 1/2. Indeed, $1/2/1_{CO3\cdot pH10}$ slowly lost this capacity for the first cycles and then reached the value obtained for $1/2/1_{CO3\cdot pH8}$ after 10 cycles.

The oxalate samples presented lower loss of sorption capacity (25% and 16% for $1/2/1_{Ox\cdot pH10}$ and $1.5/1.5/1_{Ox\cdot pH10}$, respectively) than carbonate samples after 7 cycles depending on their composition: the higher the Ca content, the higher the loss of sorption capacity (Fig. 3.20) because of the sintering of calcium carbonate. However, for $1.5/1.5/1_{Ox\cdot pH10}$, this loss started to stabilize by the 6th cycle.

Then, the most influential parameter on the sorption capacity appeares to be the interlayer anion (oxalate versus carbonate) following by the composition (Ca content), and finally the pH for carbonate-derived sorbents.

3.3 Conclusion

LDHs decomposition was evaluated by TGA analysis under air to understand the formation of the corresponding LDOs as a function of the interlayer anion, the synthesis pH and the Ca content but also the calcination temperature. It appeared that the decomposition behavior depends on the anion choice (carbonate, oxalate, citrate, or stearate) but occurs for all of them between 200°C and 500°C if the samples are free of calcium.

As far as LDOs properties are concerned, the same parameters (interlayer anion, pH, Ca content, and calcination temperature) were evaluated thanks to XRD, N_2 adsorption, and SEM. It appeared different behaviors for Ca-containing samples and Ca-free samples.

For the Ca-free LDOs, XRD revealed that the periclase (MgO) phase is always the main phase whatever the interlayer anion and pH values except for the oxalate sample and pH 8 for which a spinel phase ($MgAl_2O_4$) was also observed. N_2 adsorption indicated different types of porosity depending on the interlayer anion: macro-porosity for stearate samples and meso-porosity for carbonate and oxalate samples, associated with the highest SSA values and the highest Pv values, respectively. This

difference in behavior is also observed by SEM with the presence of *sand roses* for all anions produced that pH 8 for the stearate anion and pH 10 for that of oxalate. The use of a larger anion slightly increases the SSA but is very probably limited by the solubility of the latter in water or the risk of collapse of the morphology. An optimum is found with oxalate, larger than carboante which does not pose a solubility problem but is much more sensitive to low pH.

For LDOs with various Ca contents, XRD indicated the formation of a $Mg_{1-y}Ca_yCO_3$ phase with the MgO phase after calcination at 500°C which decomposed into the CaO phase after calcination at 700°C, for all anions studied. Meso-porosity was observed for all samples and associated with a decrease in SSA and Pv values with increasing Ca content, with the best values associated with oxalate samples and pH 10. The presence of *sand roses* morphology observed by SEM confirmed the tendencies obtained by N_2 adsorption.

For the CO_2 sorption capacity results, it seemed important to us to evaluate both sorption capacity ($g_{CO2}/100g_{sorbent}$) and the accessibility of CaO sites ($g_{CO2}/100g_{CaO}$). Thus, the best results were obtained for $1.5/1.5/1_{Ox\cdot pH10}$ (40.6 $g_{CO2}/100g_{sorbent}$ and 69.7 $g_{CO2}/100g_{CaO}$), $1/2/1_{Ox\cdot pH10}$ (41.6 $g_{CO2}/100g_{sorbent}$ and 56.6 $g_{CO2}/100g_{CaO}$), $1/2/1_{CO3\cdot pH10}$ (49.6 $g_{CO2}/100g_{sorbent}$ and 67.5 $g_{CO2}/100g_{CaO}$), and finally for $1/2/1_{CO3\cdot pH8}$ (52.3 $g_{CO2}/100g_{sorbent}$ and 71.1 $g_{CO2}/100g_{CaO}$). The stability of these samples was then evaluated by cyclic absorption/desorption (carbonation/calcination) tests and gave the advantage to the oxalate samples and, not surprisingly, to the highest Mg/Ca ratio.

Despite the samples were not evaluated for a high number of cycles, the stability of the absorption/desorption cycles is a promising signal to combine them with a metal phase (Ni or Fe) to produce bi-functional catalyst and sorbent materials for Sorption Enhanced Steam Reforming processes (SESR).

References

[1] Graf, D.L.: Crystallographic tables for the rhombohedral carbonates, American Mineralogist, 46, 1283-1316 (1961).

[2] Wyckoff, R.W.F.: Crystal Structures, Second Edition, Intersciences publishers, New York, New York, 1, 290-295, 1963.

[3] Lajaeghere, K., Van Speybroeck, V., Van Oost, G., Cottenier, S.: Error estimates for solid-state density-functional theory predictions: an overview by means of the ground-state elemental crystals, Critical Reviews in Solid State and Materials Sciences, 39, 1-24, 2014.

[4] Andreozzi, G.B., Princivalle, F.: Kinetics of cation ordering in synthetic $MgAl_2O_4$ spinel, American Mineralogist, 87, 838-844 (2002).

[5] Thommes, M., Kaneko, K., Neimark, A.V., Olivier, J.P., Rodriguez-Reinoso, F., Rouquerol, J., Sing, K.S.W.: Physisorption of gases, with special reference to the evaluation of surface area and pore size distribution. Pure Appl. Chem., 87, 1051-1069 (2015).

[6] Wang, Q., Tay, H.H., Zhong, Z., Luo, J., Borgna, A.: Synthesis of high-temperture CO2 adsorption from organo-layered double hydroxides with markedly improved CO2 capture capacity, Energy Environ. Sci., 5, 7526-7530 (2012).

[7] Wang, X.P., Yu, J.J., Cheng, J., Hao, Z.P., Xu, Z.P.: High-Temperature Adsorption of Carbon Dioxide on Mixed Oxides Derived from Hydrotalcite-Like Compounds. Environ. Sci. Technol., 42, 614-618 (2008).

[8] Wang, J., Zhang, Y., Altaf, N., O'Hare, D., Wang, Q.: Layered Double Hydroxides-derived intermediate-temperature CO_2 absorbents, in Wang, Q. (ed.) Pre-combustion Carbon Dioxide Materials, pp. 1-60, Royal Society of Chemistry (2018).

[9] Wang, Q., Tay, H.H., Ng, D.J.W., Chen, L., Liu, Y., Chang, J., Zhong, Z., Luo, J., Borgna, A.: The effect of trivalent cations on the performance of Mg-M-CO_3 layered double hydroxides for high-temperature CO_2 capture, Chem. Sus. Chem., 3, 965-973 (2010).

[10] Wang, Q., Wu, Z.H., Tay, H.H., Chen, L.W., Liu, Y., Chang, J., Zhong, Z.Y., Luo, J.Z., Borgna, A.: High temperature adsorption of CO_2 p, Mg-Al hydrotalcite: effect of the charge compensating anions and the synthesis pH, Catal. Today, 164, 198-203 (2011).

[11] Jing, Y., Liu, Q., Mao, X., Su, S., Li, X., Liu, X., Xie, T., Li, J.: Influence of presintering temperature on magnesium aluminate spinel transparent ceramics fabricated by solid-state reactive sintering, Int. J. App. Ceramic Tech., 19, 367-374 (2022).

[12] Yong, Z., Mata, V., Rodrigues, A.E.: Adsorption of carbon dioxide onto hydrotalcite-like compounds (HTIcs) at high temperatures, Ind. Eng. Chem. Res., 40, 204-209 (2001).

[13] Courson, C., Gallucci, K.: CaO-based high-temperature CO_2 sorbents, in Wang, Q. (ed.) Pre-combustion Carbon Dioxide Materials, pp. 144-237, Royal Society of Chemistry (2018).

CHAPTER 4

CATALYSTS CHARACTERIZATION

This chapter presents the results of the catalysts characterization. According to the synthesis method, the anion (carbonate or oxalate), the Mg/Ca ratio (1.5/1.5 or 1/2), the metal used (Fe or Ni), and the metal content (5_{wt}%, 10_{wt}% or 20_{wt}%), the properties of the catalysts are compared to each other and to the corresponding sorbents. The catalysts are studied before calcination (LDH) for one-pot synthesis by TGA and XRD, and after calcination (LDO) for one-pot and impregnation synthesis by XRD, N_2 physisorption analysis, SEM, and CO_2 sorption capacity. The reducibility of iron and nickel species in the catalysts was studied by TPR-H_2 for a selection of samples after all these characterizations and will be presented in the following chapter 5.

4.1 One-Pot M-LDH catalysts characterization

Focusing on M-LDH, this part describes XRD analysis of the precursors before calcination and studies the transformation steps during calcination by TGA and thermo-XRD until 700°C. This comparison was limited to samples produced by one-pot synthesis because impregnated samples are directly calcined.

4.1.1 Structure

4.1.1.1 Iron catalysts

The same phases are observed in the sorbents and iron catalysts (Fig. 4.1). Hydrotalcite (JCPDS n° 00-022-0700) is present only for a Mg/Ca ratio=1/2 at pH10 with both anions. The major crystalline phase corresponds to aragonite (JCPDS n° 05-0453) with the carbonate anion and whewellite (JCPDS n° 20-321) with the oxalate anion. The magnesium calcium carbonate (JCPDS n° 01-089-1304) structure is also present to a weaker part using carbonate anion at pH 8 and to a lesser extent at pH 10. No further phase containing metal appears indicating its good integration and great dispersion in the hydrotalcite structure. The unidentified peak at 19-20° in the samples using oxalate corresponds to a minor phase of vaterite structure ($Al_6Ca_4O_{13}$) [3] which is formed only in samples using oxalate independent of the metal present.

To develop the comparison, additional XRD analyses are presented with iron (10_{wt}% and $20_{wt}^{\%}$) catalysts according to the anion, pH, and Mg/Ca (Fig. 4.2). Once again, the structures of the catalyst are the same as those of the corresponding sorbents. First, for CO_3·pH8 (*a*), the aragonite crystallinity decreases when iron content rises; the minor hydrotalcite phase presents the same trend and the magnesium calcium carbonate phase is present in a small proportion. For CO_3·pH10 (*b*), the latter phase is also observable but the trend is less marked while hydrotalcite and aragonite phases stay with comparable intensities. The crystallinity of the $1/2_{Ox\cdot pH10}$ catalysts (*d*) changes with increasing iron content. Despite the use of the oxalate anion, the aragonite phase is present in sorbent as a minor phase

as described in the previous chapter (3) and stays in the corresponding catalysts. There is no hydrotalcite phase detected for these samples. Finally, for the $1.5/1.5_{Ox\cdot pH10}$ samples (*c*), no change appears between the sorbent and the corresponding catalysts.

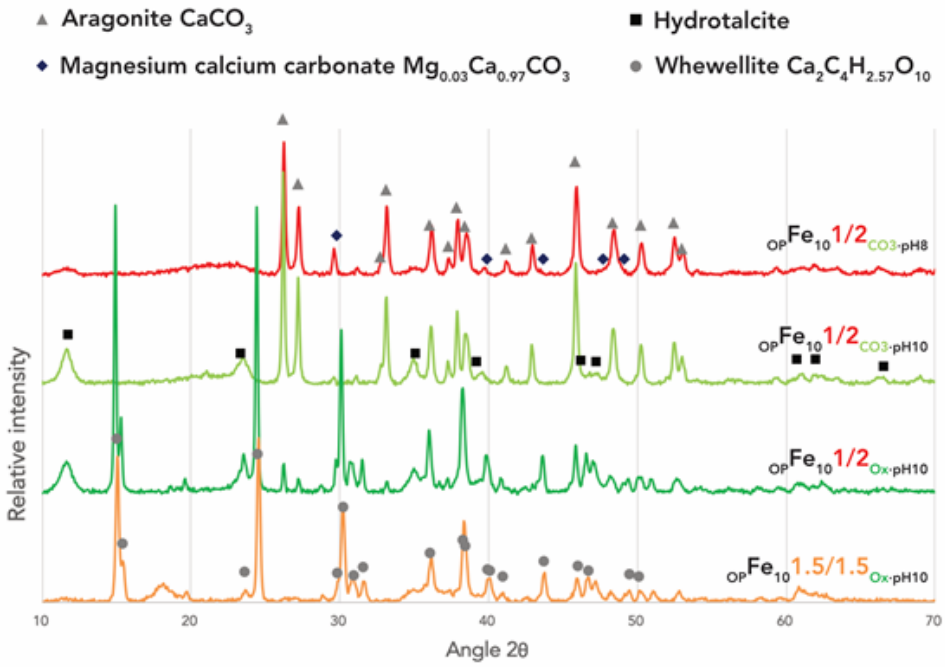

Figure 4.1: X-ray diffractograms of $_{OP}Fe_{10}$ catalysts precursor prepared according to Mg/Ca ratio, anion size, and pH.

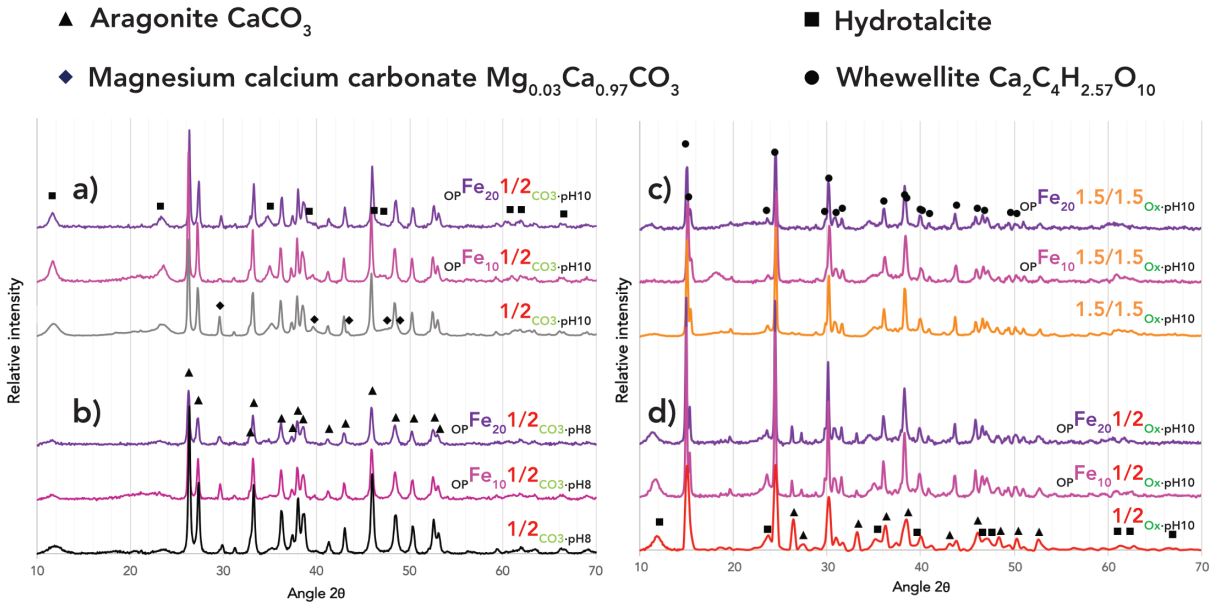

Figure 4.2: X-ray diffractograms of $_{OP}Fe$ catalysts precursor prepared according to Mg/Ca ratio, anion size, and pH compared to the corresponding sorbents.

4.1.1.2 Nickel catalysts

The one-pot nickel catalysts present the same phases as the iron catalysts and their corresponding LDH sorbents (Fig. 4.3). Samples synthesized from carbonate seem less appropriate to produce hydrotalcite while the only phase observed is aragonite (*a*). The intensity of the spectra is close to that of the $1/2_{CO3\cdot pH10}$ sorbent, higher than that of its catalysts, which meens the crystallinity decrease a little bit with the addition of nickel. The hydrotalcite structure is observed for both ratios 1/2 (*b*) and 1.5/1.5 (*c*) using the oxalate anion which leads to the whewellite structure, the main phase. In contrast, the magnesium calcium carbonate structure does not appear at pH 8 even in a lesser proportion. The aragonite crystallinity slowly decreases with nickel content rising. A highlight is bringing by the $_{OP}Ni_5 1.5/1.5_{Ox\cdot pH10}$ catalyst forms superior hydrotalcite and whewellite crystallinities. At least, the aragonite noticed in a minor part in $1/2_{Ox\cdot pH10}$ does not form on the equivalent nickel catalysts.

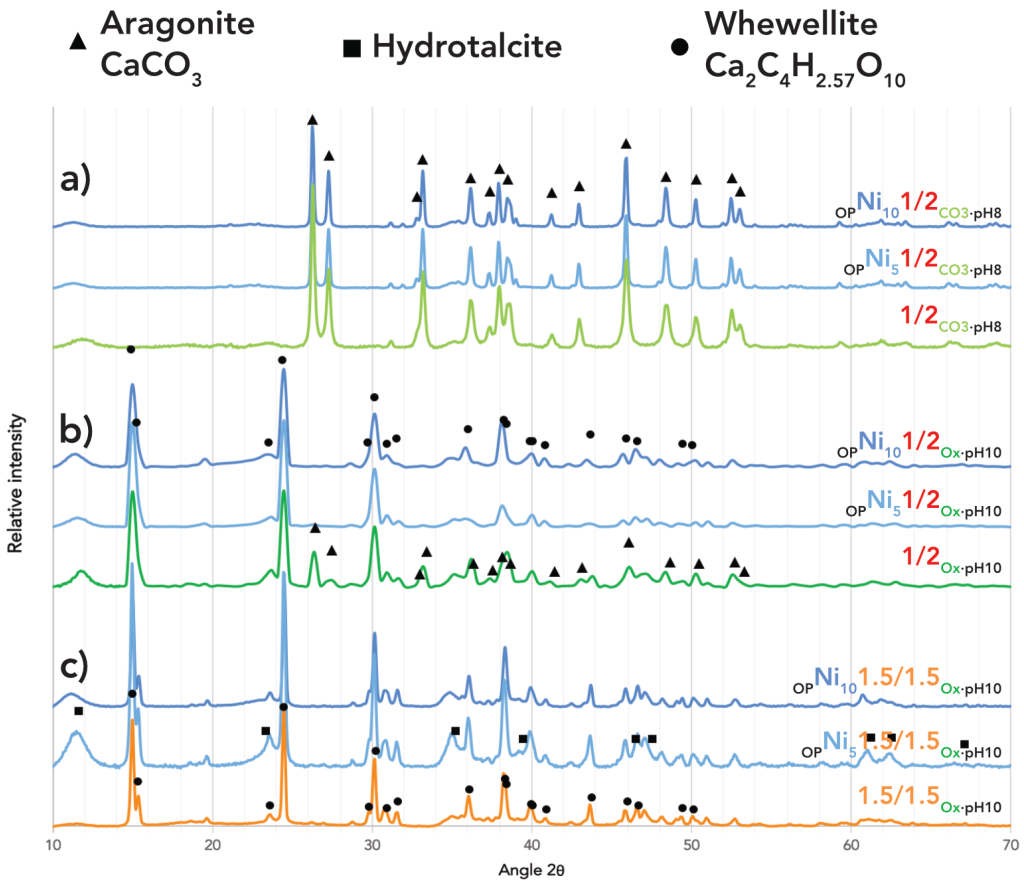

Figure 4.3: X-ray diffractograms of $_{OP}Ni$ catalysts precursor prepared according to Mg/Ca ratio and anion size compared to the corresponding sorbents.

4.1.2 Thermo-analysis

4.1.2.1 Decomposition steps by TGA

Decomposition of the OP catalysts attested to the great similarity to their corresponding sorbents (Fig. 4.4 and 4.5). The addition of nickel or iron does not modify the weight loss and temperature of the decomposition steps. The first step (until 200°C) is attributed to the water removal. The second step (until 500°C) corresponds to the layer hydroxyls and interlayer anion groups of the hydrotalcite phase and the $MgCO_3$ oxidation. Finally, the oxidation of calcium carbonate to CaO is observed between 550°C and 700°C [1].

The curves of the remaining weight percent of catalyst are very similar for the same Mg/Ca ratio and the same anion whatever the metal studied and its content. Thus, the $1.5/1.5_{Ox\cdot pH10}$ catalyst (Fig. 4.5) decomposes in the same way as the related nickel and iron catalysts with various weight percentages of metal. The results recorded for the iron catalysts with $1/2_{CO3\cdot pH10}$, $1/2_{Ox\cdot pH10}$, and $1/2_{CO3\cdot pH8}$ (Fig. 4.6) are unchanged based on their corresponding sorbents.

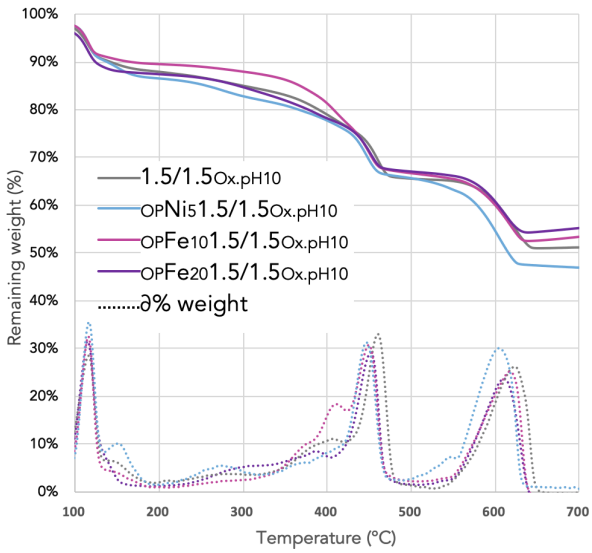

Figure 4.4: TGA oxidation of $_{OP}1.5/1.5_{Ox\cdot pH10}$ catalysts compared to their corresponding sorbent.

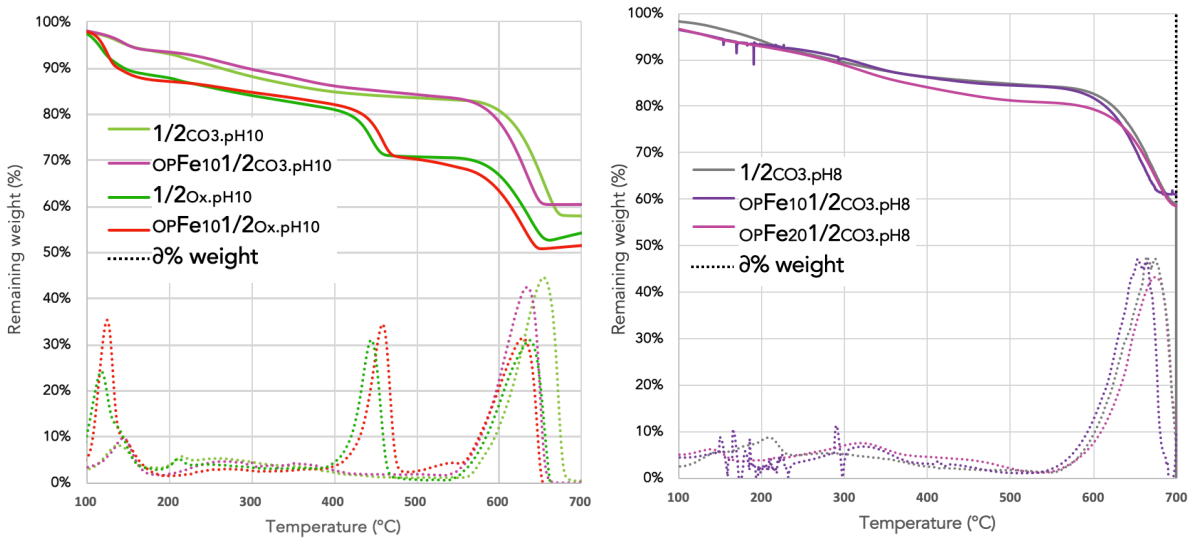

Figure 4.5: TGA oxidation of $_{OP}Fe_{10}1/2_{CO3\cdot pH10}$, $_{OP}Fe_{10}1/2_{Ox\cdot pH10}$ catalysts (left) and $_{OP}Fe_{10\&20}1/2_{CO3\cdot pH8}$ (right) compared to their corresponding sorbents.

4.1.2.2 Calcination follow-up by XRD

As mentioned previously, the whewellite structure is visible for both oxalate precursor catalysts (Fig. 4.6) at room temperature. Magnesium calcium carbonate is also formed in a minor part as early as the initial temperature. The evolution of structure follows the corresponding sorbents calcination. The first decomposition appears at 250°C, the magnesium calcium carbonate is forming before 300°C, and starts to oxidize at 600°C. The main structure thus constituted is lime CaO (JCPDS n° 01-070-4968) and MgO present but less defined. The rays corresponding to metal oxides are not observable and would appear at 44.5° and 52.2° [2].

In addition to the known structures of the corresponding sorbents, an unidentified transitory structure emerges (main ray at 27.7°) in both catalysts between 250°C and 325°C. This structure present in the iron (Fig. 4.6.a) and nickel (Fig. 4.6.b) catalysts never appears in the spectra of the corresponding sorbents. So, this phase would be due to the addition of metal but is not referenced in the usual database. This structure can also only be formed at high temperature but it is no more referenced in high-temperature databases. The calcination reduces the weight of the sample (see TGA analyses) that

could perhaps downsize its powder level on the rack during the measurement and lead to an angle shift but this was not visible.

Therefore, the catalysts precursors were calcined at 300°C in the oven and then analyzed by the routine XRD method at room temperature (Fig. 4.7). XRD of $_{OP}Fe_{10}1.5/1.5_{Ox\cdot pH10}$ and $_{OP}Ni_{10}1/2_{Ox\cdot pH10}$ recorded at room temperature after calcination at 300°C presents magnesium calcium carbonate structure and to a lesser extent the remaining whewellite not decomposed. The unknown structure is absent. At 300°C, a probable interaction operates between iron/nickel and calcium or magnesium carbonate during the oxidation transition.

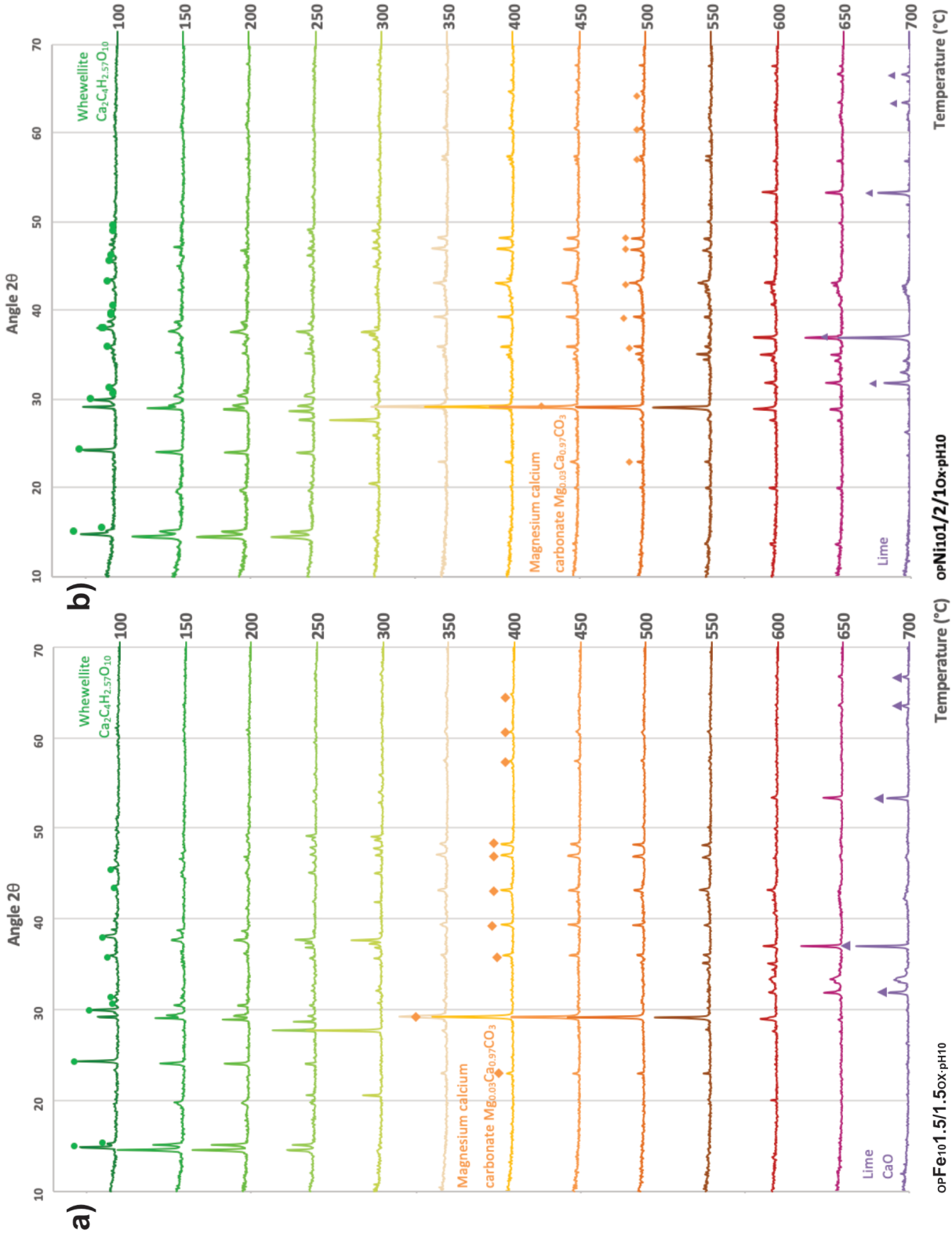

Figure 4.6: X-Ray thermo-diffractograms of a) $_{OP}Fe_{10}1.5/1.5_{Ox\cdot pH10}$, and b) $_{OP}Ni_{10}1/2_{Ox\cdot pH10}$ precursors according to temperature.

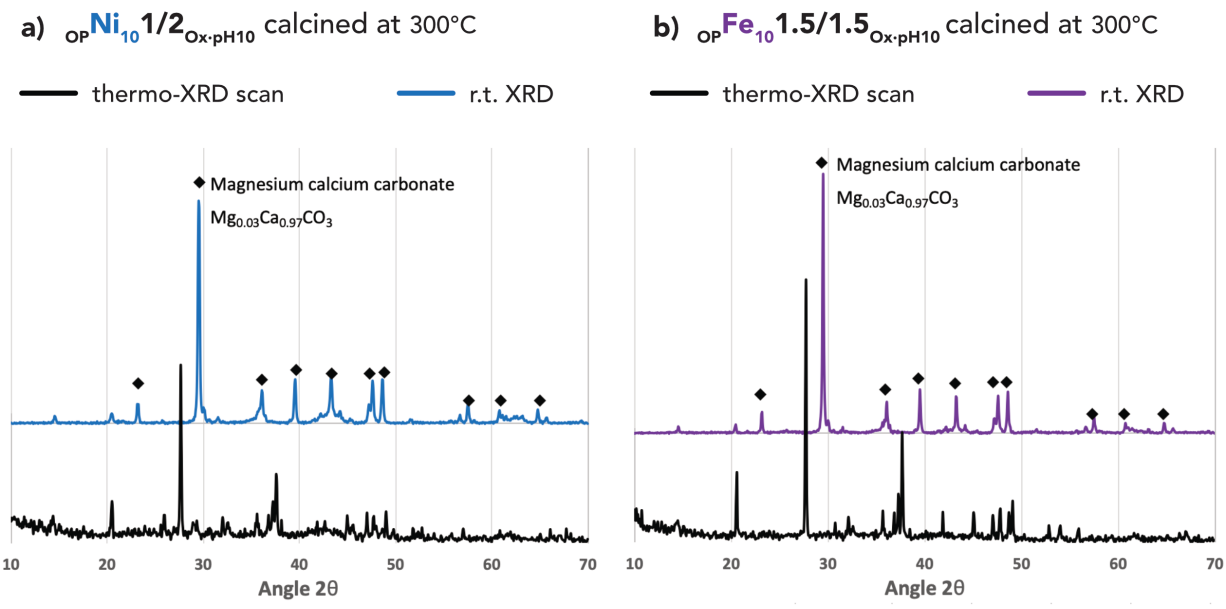

Figure 4.7: X-ray diffractograms of a) $_{OP}Ni_{10}1/2_{Ox\cdot pH10}$, and b) $_{OP}Fe_{10}1.5/1.5_{Ox\cdot pH10}$ catalysts calcined at 300°C recorded at room temperature (r.t.) and compare to X-ray thermo-diffractogram at 300°C of the corresponding precursors.

In addition, $_{IMP}Ni_{10}1/2_{Ox\cdot pH10}$ (Fig. 4.8) is calcined during XRD analysis from 500°C to 700°C because the IMP catalysts are already calcined at 500°C. The observed phases are magnesium calcium carbonate from 500°C to 650°C and lime structure at 700°C. A minor transition structure is also observed between 550°C and 650°C could correspond to vaterite ($Al_6Ca_4O_{13}$) [3] and natrite ($Al_4Na_{14}O_{13}$) [4] which is formed at 700°C due to the excess of NaOH not enough washed during the synthesis. The sodium content has not been measured, but its presence can interfere in the CO_2 sorption capacity by improving it as explained by López-Ortiz et al. [5] and other studies [6-7] involving alkali metal promotion. A conductimetric measurement of the filtrate during the work up of the syntesis could then be systematically added to the procedure to ensure the efficient washing of the precipitate. Finally the presence of sodium could be exploited and quantitatively controlled for a further study of the influence of this alkaline metal in the sorption capacity.

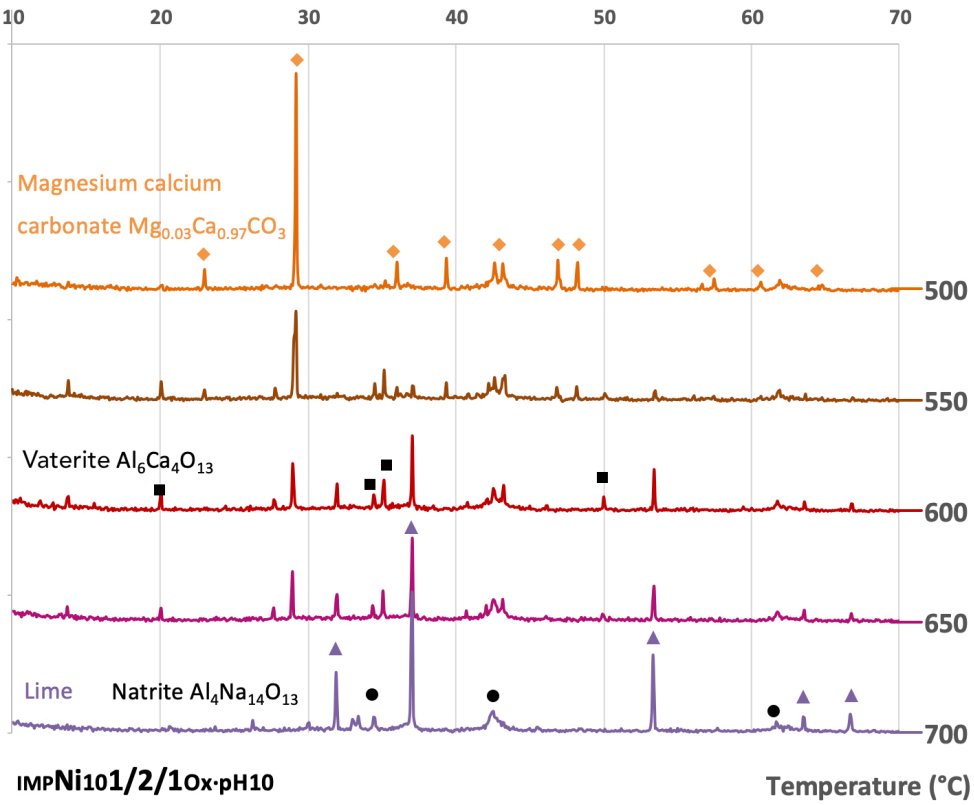

Figure 4.8: X-ray thermo-diffractograms of $_{IMP}Ni_{10}1/2_{Ox\cdot pH10}$ precursor according to temperature.

4.2 M-LDO catalysts characterization

This part concerns M-LDO catalysts prepared by one-pot and impregnation synthesis methods. Comparisons with the corresponding sorbents are also included to understand the impact of metal addition and content on porosity properties by N_2 adsorption, structure by XRD, morphology by SEM, sorption capacity, and CaO sites accessibility.

4.2.1 Elementary analysis

As an elementary analysis of the sorbent, the Mg/Ca ratio is important to confirm the role of CaO in the sorption capacity of the catalysts. For any samples, Mg/Ca values are close to the theoretical Mg/Ca value (Fig. 4.9.a): between 1.00 and 1.04 ± 0.03 for Mg/Ca = 1.5/1.5 and between 0.49 and

0.53 ± 0.02 for Mg/Ca = 1/2. Then the anion, metal content and the synthesis method have no significant influence on the magnesium and calcium precipitation.

Otherwise, (Mg+Ca)/Al related to the M^{2+}/M^{3+} ratio becomes (Mg+Ca)/(Al+M) for catalysts synthesized by one-pot (OP) with M = Fe or Ni. In both cases, the weights engaged for the syntheses are calculated to have (Mg+Ca)/(Al+M) = 3. This value is chosen to compare the one-pot (OP) and impregnated (IMP) compounds with metal to the corresponding LDO sorbents with (Mg+Ca)/Al = 3. However, if the iron precursor is iron(III) nitrate and the iron content respects the M^{2+}/M^{3+} ratio of 3, implying the neutrality of iron catalysts, nickel(II) nitrate is chosen as Ni precursor, unbalancing this characteristic for Ni catalysts.

For the samples synthesized by the OP method, the (Mg+Ca)/(Al+M) ratios are very similar to the expected (Mg+Ca)/(Al+M) ratio of 3 with values varying from 2.93 to 3.14 ± 0.03 (Fig. 4.9.b), which means a variation systematically lower than 4%. So in the one hand, the co-precipitation method is patently adapted to magnesium substitution by calcium and aluminum by metal, but on the other hand the molar percentages of metallic Fe and worse with Ni are particulary lower than the quantity engaged. Most part of thhe Fe and Ni are not integrated. The expected values are 10_{wt}% or 20_{wt}% of iron and 5_{wt}% or 10_{wt}% of nickel, respectively. Each sample has a lower metal content, except for ${}_{IMP}Fe_{20}1/2_{Ox\cdot pH10}$ which contains 21.7_{wt}% of iron. Thus, there is a weight loss due to the non-precipitated amount. At last, for the samples synthesized by the IMP method (${}_{IMP}Fe_{20}1/2_{Ox\cdot pH10}$ and ${}_{IMP}Ni_{10}1.5/1.5_{Ox\cdot pH10}$), Fig. 4.9.b indicates an important deviation of the (Mg+Ca)/Al ratio that is equal to 3.65 instead of 3. This difference comes from the sorbent synthesis and leads to lower (Mg+Ca)/(Al+M) values (1.41 and 2.05 for iron and nickel impregnated catalysts, respectively).

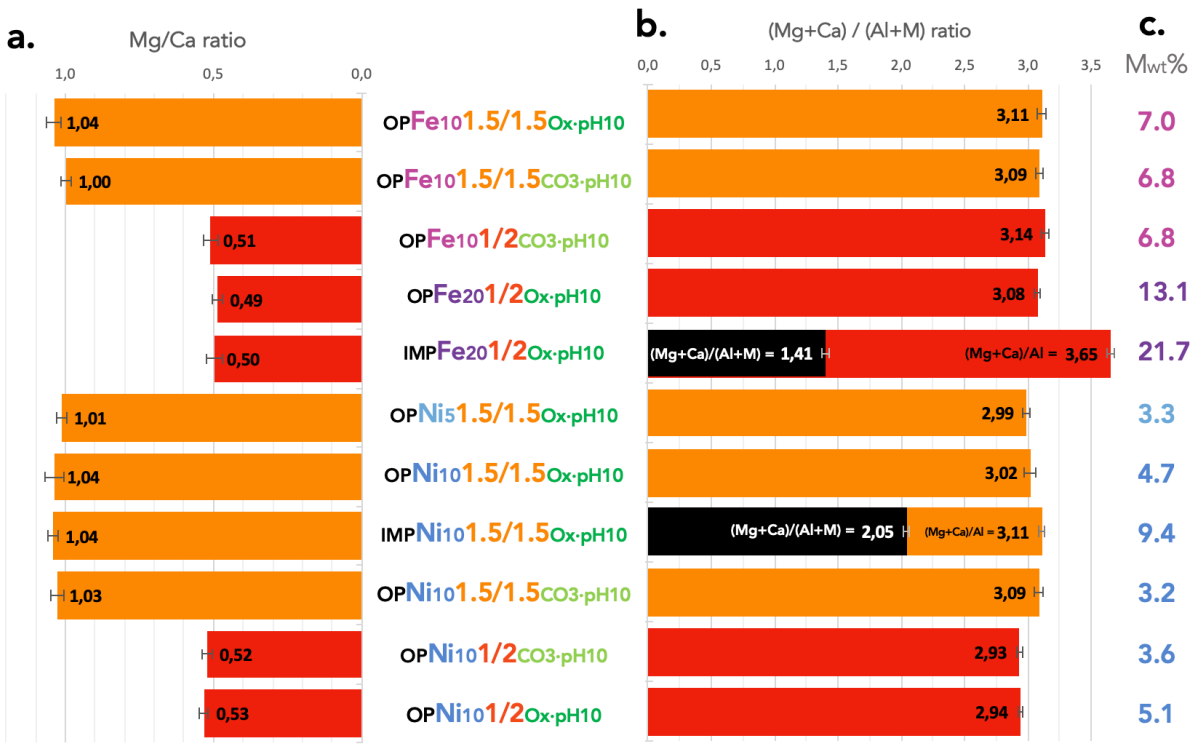

Figure 4.9: a) Mg/Ca, b) (Mg/Ca)/Al ratios and c) metal weight percent of LDO samples calculated from elementary analysis values according to ion and metal content.

For the iron samples, the lower metal content indicates a difference in the precipitation rate of the various nitrates. However, the difference between the experimental and expected values at 10_{wt}% and 20_{wt}% is the same (32% less for ${}_{OP}Fe_{10}1/2_{CO3\cdot pH10}$ and 35% less for ${}_{OP}Fe_{10}1/2_{Ox\cdot pH10}$) and the anion and Mg/Ca ratio have no effect on the iron weight percent of the catalysts. Iron catalysts have globally a weight percent higher than the corresponding nickel catalysts. Furthermore, the Ni content of ${}_{IMP}Ni_{10}1.5/1.5_{Ox\cdot pH10}$ is close to 10_{wt}%, indicating the worst co-precipitation than impregnation of the nickel precursor. The difference between the experimental and expected values is particularly significant in the nickel catalysts, even more so at low weight percent (66% less for ${}_{OP}Ni_5 1.5/1.5_{Ox\cdot pH10}$ and 53% less for ${}_{OP}Ni_{10}1.5/1.5_{Ox\cdot pH10}$), and with the oxalate anion (64% less for ${}_{OP}Ni_5 1/2_{Ox\cdot pH10}$ and 49% less for ${}_{OP}Ni_{10}1/2_{CO3\cdot pH10}$). The increase in the M^{2+}/M^{3+} ratio by the nickel addition and the unbalance of charge could also explain the loss of nickel during the synthesis.

The catalysts selected for elementary analysis correspond to a few representative samples. Many catalysts were not analyzed by this method; therefore, the actual weight percentage of metal is probably overrated for these samples. However, the catalysts nomenclature ($_{wt\%}$ in subscript) remains generally unchanged for the following study.

4.2.2 Structure

After calcination at 500°C, magnesium calcium carbonate is the only phase that appears evenly for the $1/2_{Ox\cdot pH10}$ (Fig. 4.10.a), $1.5/1.5_{Ox\cdot pH10}$ (Fig. 4.10.b) and $1/2_{CO3\cdot pH8}$ (Fig. 4.11) catalysts containing iron or nickel such as for their corresponding sorbents. The formation of this structure is observed indifferently with nickel and iron, and increasing their content in the one-pot synthesis method has no significant effect on their crystallinity. For Mg/Ca=1/2 (Fig. 4.10.a), the $_{IMP}Ni_{10}1/2_{Ox\cdot pH10}$ sample seems less crystallized because the rays are less defined and allow to distingue the periclase MgO phase much less crystallized than the magnesium calcium carbonate phase with main ray at 43° as a ray enlargement (JCDPS n° 00-045-0946). For Mg/Ca=1.5/1.5 (Fig. 4.10.b), induced by a higher Mg content, this MgO phase is more evident especially for the OP and IMP nickel catalysts. The impregnation method meets the limits with $_{IMP}Fe_{20}1.5/1.5_{Ox\cdot pH10}$ with a huge loss of crystallinity which allows however to identify the main rays of magnesium calcium carbonate and MgO phases. So, the addition of iron and nickel instead of aluminum does not modify the major structures composed of MgO and CaO; still noted a few losses of crystallinity at 20_{wt}% for the OP method.

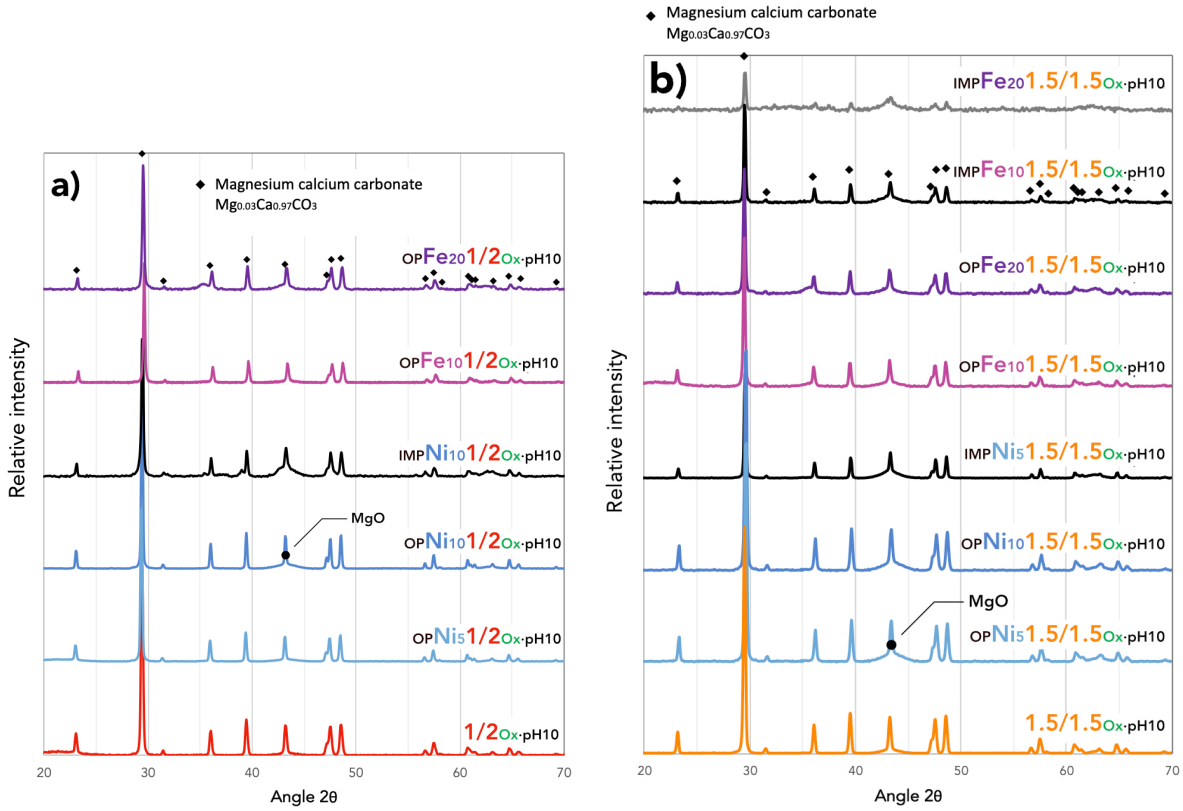

Figure 4.10: X-ray diffractograms of Ni and Fe catalysts prepared using Ox·pH10 according to Mg/Ca ratio (a) 1/2 and b) 1.5/1.5) and synthesis method compared to their corresponding sorbents.

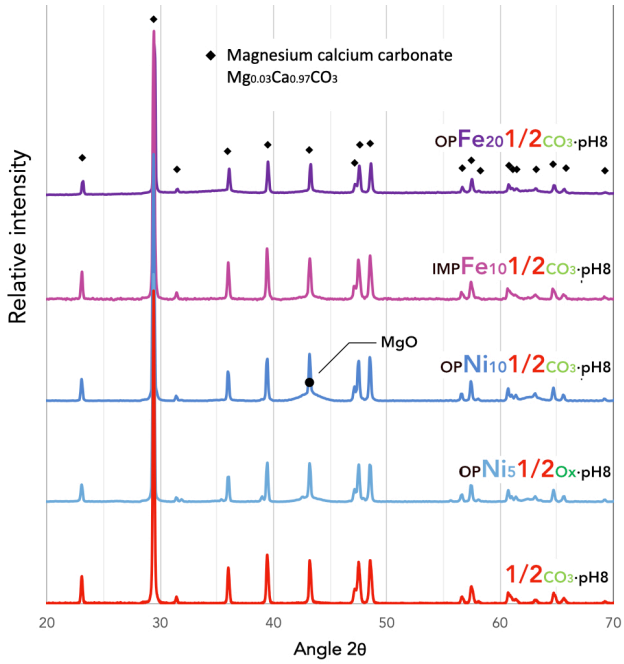

Figure 4.11: X-ray diffractograms of nickel and iron catalysts prepared using $1/2_{CO3\cdot pH8}$ and compared to their corresponding sorbent.

4.2.3 Porosity

The results of N_2 physisorption are presenting below from Fig. 4.12 representing the SSA values of OP and IMP catalysts according to the synthesis conditions to Fig. 4.13, Fig. 4.14 and Fig. 4.15 for the BET curves for each synthesis parameter (metal content, pH value, Mg/Ca ratio, anion choice, and synthesis method).

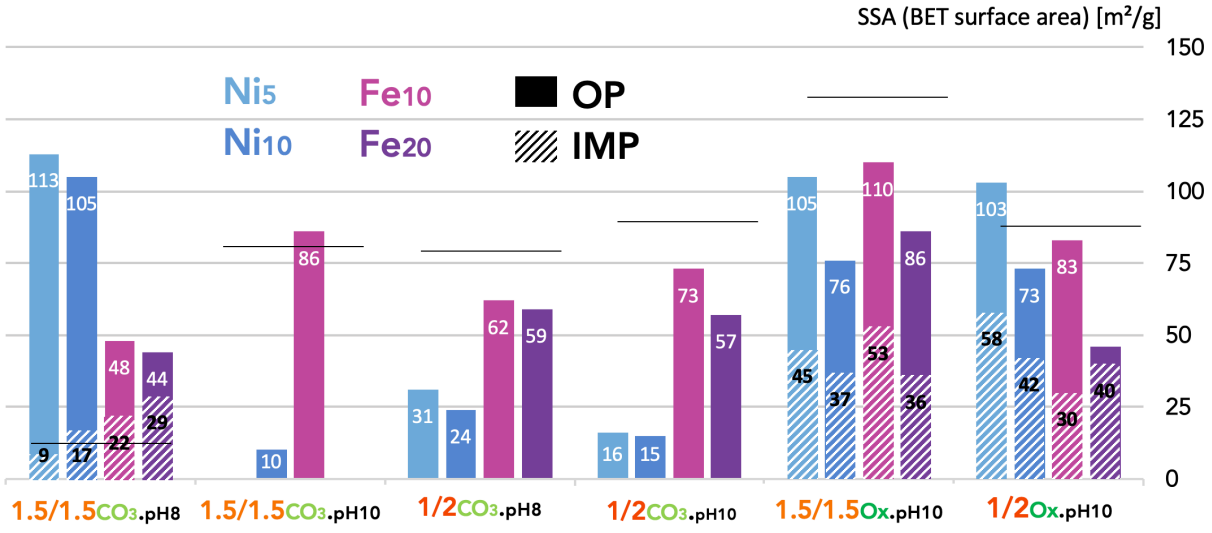

Figure 4.12: BET surface area (SSA) of catalysts prepared at Mg/Ca ratio of 1.5/1.5 and 1/2, calcination at 500°C, pH 8 or 10, and with various anions and metal weight percents and synthesis methods. Black lines indicate the SSA values of the corresponding sorbents.

It appears that all the synthesis parameters (metal content, pH value, Mg/Ca ratio, choice of anion, and synthesis method) have an impact on the amount of N_2 adsorbed and/or type of porosity. The influence of each parameter will be investigated separately.

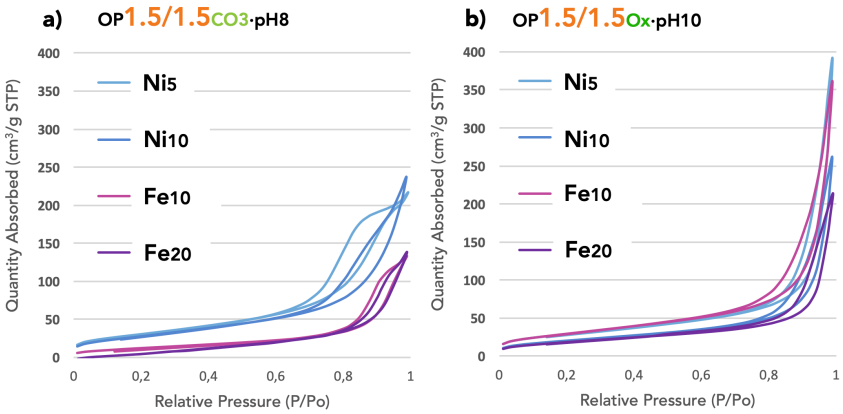

Figure 4.13: BET curves for a) $_{OP}1.5/1.5_{CO3\cdot pH8}$ and b) $_{OP}1.5/1.5_{Ox\cdot pH10}$ catalysts calcined at 500°C prepared according to metal weight percent.

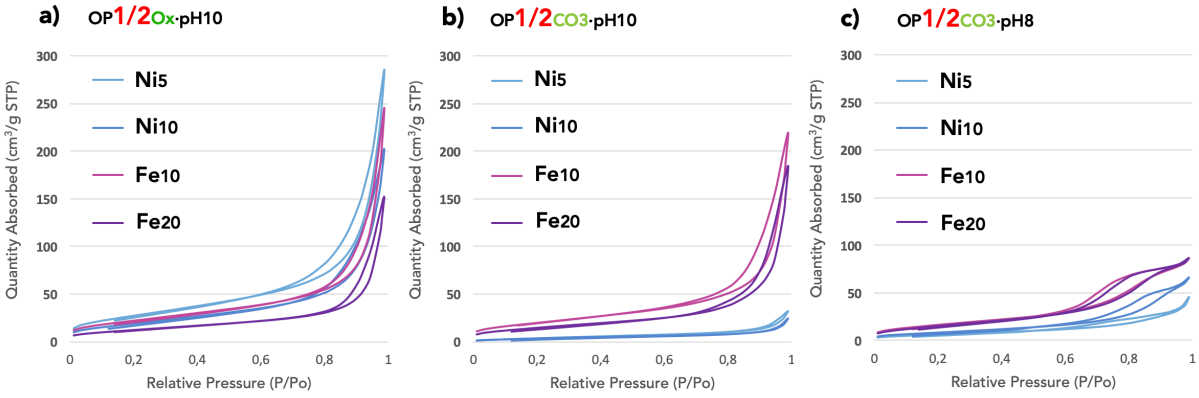

Figure 4.14: BET curves for a) $_{OP}1/2_{Ox\cdot pH10}$, b) $_{OP}1/2_{CO3\cdot pH10}$, and c) $_{OP}1/2_{CO3\cdot pH8}$ catalysts calcined at 500°C prepared according to metal weight percent.

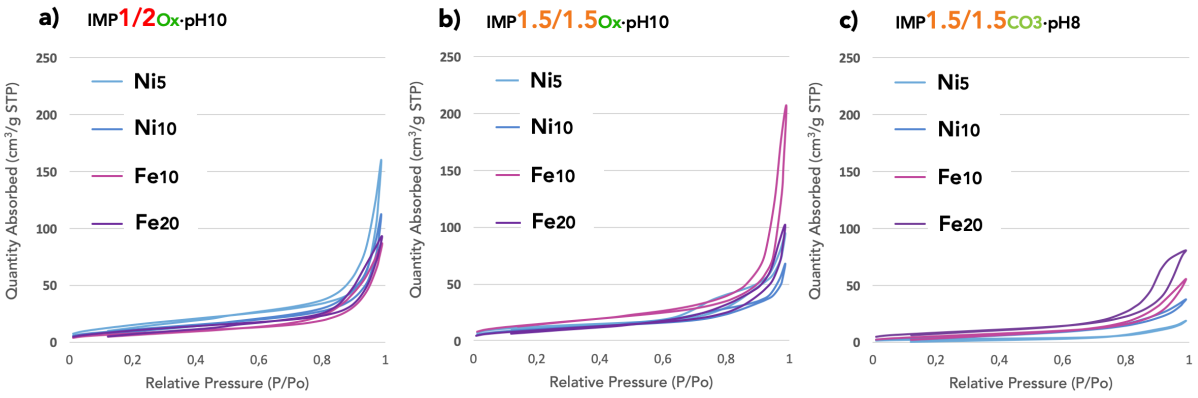

Figure 4.15: BET curves for a) $_{IMP}1/2_{Ox\cdot pH10}$, b) $_{IMP}1.5/1.5_{Ox\cdot pH10}$, and c) $_{OP}1.5/1.5_{CO3\cdot pH8}$ catalysts calcined at 500°C prepared according to metal weight percent.

4.2.3.1 Synthesis method effect

Whatever the metal addition method (OP or IMP), the catalysts porosity is modified (Fig. 4.12). Mostly, the catalysts have a lower surface area than their corresponding sorbents for various metal additions (element and content), pH values, Mg/Ca ratios, and anions. Some exceptions are observed for the catalysts corresponding to: (1) the $1.5/1.5_{CO3\cdot pH8}$ sorbent, which presents a lower SSA before metal addition than the expected one in the trend of the other sorbents; and (2) for two catalysts ($_{OP}Fe_{10}1.5/1.5_{CO3\cdot pH10}$ and $_{OP}Ni_5 1/2_{Ox\cdot pH10}$) possessing higher SSA values than their corresponding sorbents (86 m^2/g against 79 m^2/g and 103 m^2/g and 86 m^2/g, respectively).

OP synthesis allows obtaining higher SSA values than the corresponding IMP equivalent (Fig. 4.12). However, the very low SSA value of the $1.5/1.5_{CO3\cdot pH8}$ sorbent (12 m^2/g) that implies an uncertain pores accessibility by the metal salt solution in IMP synthesis method can explain the weaker SSA values of the corresponding IMP catalysts (9 to 29 m^2/g) against the corresponding OP catalysts (44 to 113 m^2/g).

The most common type of isotherms curves (IVa) is the same as their corresponding sorbents (Chapter 3 - Fig. 3, Fig. 14) associated to mesoporosity [8]. However, the H2(b) type of isotherm curves is observed for only two IMP catalysts ($_{IMP}Fe1.5/1.5_{CO3\cdot pH10}$ and $_{IMP}Ni1.5/1.5_{CO3\cdot pH10}$) and corresponds to mesoporosity with some pores obstruction [8].

4.2.3.2 Metal nature and content effects

For a constant weight percent (10_{wt}% theoretical), Ni has an negative impact on the surface area in a more pronounced way than Fe. Moreover, the gap between Ni_{10} and Fe_{10} is even more important because the theoretical weight percentage is more overestimated for nickel than for iron catalysts. Once again, the $1.5/1.5_{CO3\cdot pH8}$ constitutes an exception to this rule. Thus, $_{OP}Ni_5 1.5/1.5_{CO3\cdot pH8}$ reaches 113 m^2/g that corresponds to the best surface area of Ni catalysts, followed by $_{OP}Fe_{10}1.5/1.5_{Ox\cdot pH10}$ at 110 m^2/g, the best Fe catalyst.

In both synthesis methods, iron catalysts generally attest to higher SSA than Ni_5 and Ni_{10} catalysts. Precisely, 80% of the $1/2_{CO3}$ SSA persists in the corresponding iron OP catalysts at pH 8 and 10

(Fig. 4.12) with 62 m^2/g for $_{OP}Fe_{10}1/2_{CO3\cdot pH8}$ versus 78 m^2/g for $1/2_{CO3\cdot pH8}$ and 73 m^2/g for $_{OP}Fe_{10}1/2_{CO3\cdot pH10}$ versus 88 m^2/g for $1/2_{CO3\cdot pH10}$. As far as the nickel OP catalysts are concerned, the catalysts SSA values only represent 40% of those of the corresponding sorbents.

The comparison of the various Ni_5 and Ni_{10} samples, on the one hand, and the various Fe_{10} and Fe_{20} samples, on the other hand, indicates a general loss of porosity with increasing metal content (Fig. 4.12). However, this trend is completely turned for the IMP nickel and iron catalysts from the $1.5/1.5_{CO3\cdot pH8}$ sorbent and fot the IMP iron catalyst from the $1/2_{Ox.pH10}$ sorbent.

Nickel and iron catalysts (Fig. 4.13, Fig. 4.14, Fig. 4.15) generally present the same type of isotherms (IVa) such as their corresponding sorbents (Chapter 3 - Fig. 3, Fig. 14) associated to mesoporosity [8]. In some cases, the modification of the BET curves towards H2(b) type isotherms indicates the obstruction of some pores. This behavior is to be noted for $_{OP}1.5/1.5_{CO3\cdot pH8}$ (Fig. 4.13.a), $_{OP}1/2_{CO3\cdot pH8}$ (Fig. 4.14.c), and $_{IMP}1.5/1.5_{CO3\cdot pH8}$ (Fig. 4.15.c) and then exclusively for the catalysts prepared at pH 8.

4.2.3.3 pH effect

Despite the particular behavior of the $1.5/1.5_{CO3}$ sorbents and the corresponding catalysts, the pH variation effect is similar for the catalysts with carbonate anion and various Mg/Ca ratios (Fig. 4.12). The pH 8 leading to higher SSA values for Ni catalysts seems more appropriated than pH 10. The reverse trend is to be noted for Fe catalysts.

However, the main difference induced by the decrease of pH on the OP $1/2_{CO3}$ samples consists in the isotherm shape and then in the porosity type (Fig. 4.14.b and c). In fact, these sample BET curves illustrate again an evolution of the H2(b) isotherm type associated to the obstruction of some pores in the mesoporous materials. This porosity type is only due to pH lowering and is not affected by studied Mg/Ca ratio nor by the anion.

4.2.3.4 Mg/Ca ratio effect

Comparison of the sorbents comparison determined a overall decrease in SSA with a decrease in the Mg/Ca ratio (Chapter 3, Fig. 3.16). Optimized conditions result in a higher SSA value for the $1.5/1.5_{Ox\cdot pH10}$ sorbent (133 m^2/g) than for the $1.5/1.5_{CO3\cdot pH10}$ sorbent (79 m^2/g) and the $1/2_{Ox\cdot pH10}$ sorbent (86 m^2/g).

The SSA value of iron catalysts is overall higher for the 1.5/1.5 compositions than for the 1/2 compositions too, except for pH 8 and the reverse trend is observed for nickel catalysts. For carbonate catalysts at different Mg/Ca ratios, the trend is less clear than for oxalate catalysts and depends on the metal. The most interesting outcomes are for Ox·pH10 conditions. In fact, for the 1.5/1.5 $_{Ox\cdot pH10}$ and 1/2 $_{Ox\cdot pH10}$ catalysts, close SSA can be noticed for the Ni_5 and Ni_{10} catalysts: the SSA of $_{OP}Ni_5 1/2_{Ox\cdot pH10}$ and $_{OP}Ni_5 1.5/1.5_{Ox\cdot pH10}$ are similar (103 and 105 m^2/g, respectively); the SSA of $_{OP}Ni_{10} 1.5/1.5_{Ox\cdot pH10}$ is maintaining for $_{OP}Ni_{10} 1/2_{Ox\cdot pH10}$ (73 and 76 m^2/g, respectively). Other notable point for this anion (Ox) is reflected in the IMP catalysts, which reach higher SSA values for the 1/2 than 1.5/1.5 composition for $_{IMP}Ni_5$ (58 m^2/g against 47 m^2/g), $_{IMP}Ni_{10}$ (42 m^2/g against 35 m^2/g) and $_{IMP}Fe_{20}$ (40 m^2/g against 36 m^2/g).

The only change in the isotherm type can be observed between samples Ni containing $1.5/1.5_{CO3\cdot pH8}$ and $1/2_{CO3\cdot pH8}$: for both Mg/Ca ratio, samples containing 5_{wt}% of nickel have an isotherm type IVa and seems to evolve to a type III at 10_{wt}% which mean a change in pore size from mesoporous to macroposous [8].

4.2.3.5 Anion effect

Finally, the comparison of $1.5/1.5_{CO3\cdot pH10}$ and $1.5/1.5_{Ox\cdot pH10}$ on the one hand, and $1/2_{CO3\cdot pH10}$ and $1/2_{Ox\cdot pH10}$, on the other hand, indicates the large interest of the oxalate anion compared to carbonate anion as well as for nickel-based than for iron-based catalysts (Fig. 4.12). The isotherm type are very similar for the OP synthesis method at pH 10 for each anion whatever the metal added (Fig. 4.14.a and b). Furthermore, the constancy of the results with this anion allows for understanding and anticipation of the porosity properties in the OP and IMP synthesis methods.

As a conclusion of the porosity study, the various parameters effect are:

- Synthesis method: OP > IMP
- Metal nature: Fe > Ni except for $_{OP}1.5/1.5_{\ CO3\ pH10}$ and $_{OP}1/2_{CO3}$
- Metal content: $Ni_5 > Ni_{10}$ and $Fe_{10} > Fe_{20}$ except for $_{IMP}1.5/1.5_{CO3\ pH8}$ and $_{IMP}Fe1/2_{Ox\ pH10}$
- pH: 10 > 8 except for $_{OP}Ni1.5/1.5_{CO3\ pH8}$
- Mg/Ca ratio: 1.5/1.5 > 1/2 except for $_{OP}Fe_{CO3\ pH8}$
- Anion choice: Ox > CO_3 except for $_{OP}Fe_{20}1/2_{pH10}$

However, the best SSA values obtained for the impregnated samples for a 1/2 Mg/Ca ratio also constitutes a promising way for the following sorption capacity study.

4.2.4 Morphology

Catalysts are analyzed by SEM to identify their morphology behaviors properties according to synthesis method the addition of iron or nickel, pH, Mg/Ca ratio, and anion size.

4.2.4.1 Synthesis method effect

The morphology of the impregnated (IMP) samples stays porous and quite similar to that of the OP samples despite the lower values obtained by N_2 physisorption. However, IMP catalysts generally present worst homogeneity than OP catalysts (Fig. 4.16).

For the oxalate catalysts (Fig. 4.16), the global *sand roses* architecture shown in all the samples appears to be thicker and a secondary, flat and bulker morphology than for the OP samples is observable for the IMP samples.

4.2.4.2 Metal nature and content effects

For the various catalysts respecting $1.5/1.5_{Ox\cdot pH10}$, a *sand roses* morphology is observed as for the corresponding sorbent (Chapter 3 - Fig. 3.19). Apart the *sand roses* morphology, a flat morphology appears and is more visible at 10_{wt}% for both metals (Fig. 4.16). This morphology, less present in $Ni_5 1.5/1.5_{Ox\cdot pH10}$ (a.) containing less metal, is not accentuated in ${}_{OP}Fe_{20}1.5/1.5_{Ox\cdot pH10}$ (d.) with higher metal content. Therefore, the $Ni_5 1.5/1.5_{Ox\cdot pH10}$ (a.) catalyst resembles the corresponding $1.5/1.5_{Ox\cdot pH10}$ sorbent. There is also similarities between ${}_{OP}Ni_{10}1.5/1.5_{Ox\cdot pH10}$ (b.) and ${}_{OP}Fe_{10}1.5/1.5_{Ox\cdot pH10}$ (c.) that indicate an influence of the metal content but not of the nature of the metal on the morphology. Nevertheless, the substitution of aluminum by iron or nickel in the OP method has very little influence on the morphology; at low weight percent, in particular, the second flat melted morphology is not visible. Less impregnated samples were analyzed by SEM and compared to higher metal content samples because the previous SSA conclusions (Fig. 4.12) indicated lower porosity. However, the common morphology observed on ${}_{IMP}Ni_{10}1.5/1.5_{Ox\cdot pH10}$ (f.) is also shown on ${}_{IMP}Ni_5 1.5/1.5_{Ox\cdot pH10}$ (e.).

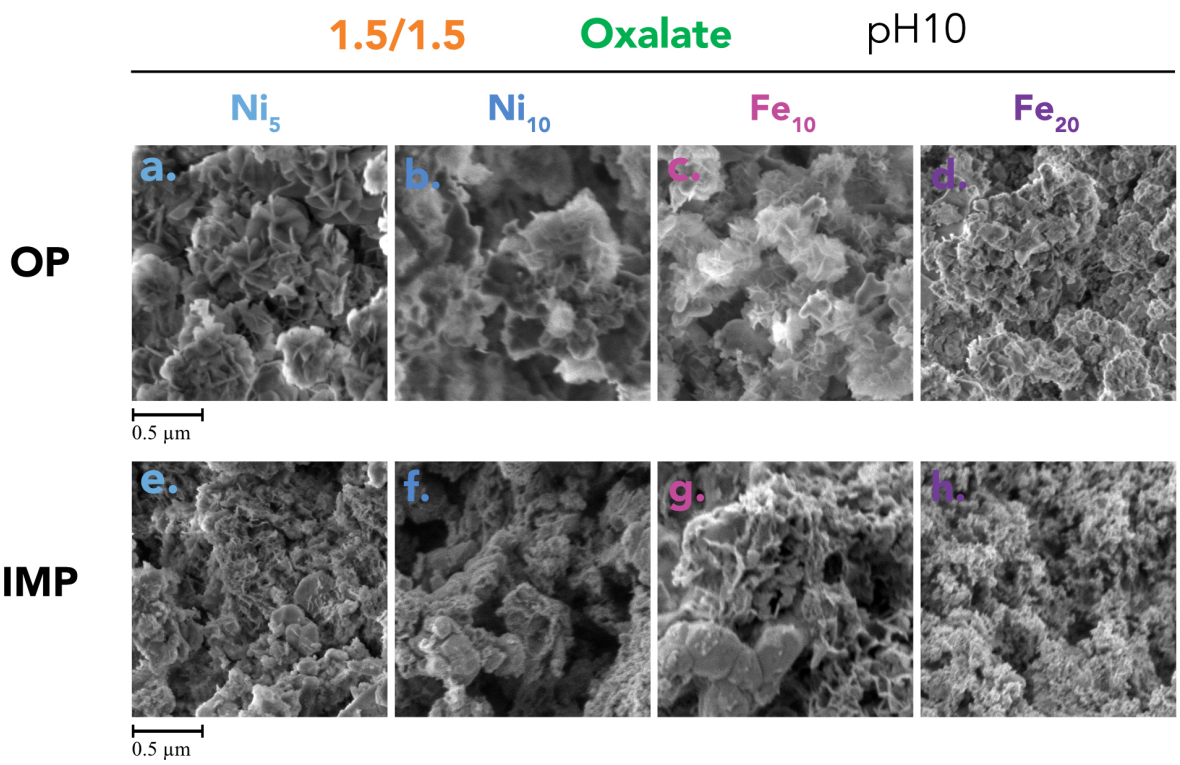

Figure 4.16: SEM pictures of M-LDO $1.5/1.5_{Ox\cdot pH10}$ catalysts calcined at 500°C according to synthesis method, and metal nature and content.

4.2.4.3 Synthesis method effect

The morphology of the impregnated samples stays porous and quite similar to that of the OP despite the lower values obtained in N_2 physisorption (Fig. 4.16). The global architecture also resembles thicker *sand roses* thatr constitute a second, flat, bulker and voluminous morphology than the OP equivalent sample.

By the impregnation synthesis method using carbonate at pH8 (Fig. 4.17.e. & f.), flat and thick clustered lamellar shape completely changes morphology. The synthesis results are not homogeneous and much less advisable than the corresponding oxalate sample at pH10.

Less impregnated samples were analyzed by SEM and compared due to the previous SSA conclusions (Fig. 4.12) and a not uncommon morphology like $_{IMP}Ni_{10}1.5/1.5_{Ox\cdot pH10}$ representing in Fig. 4.16.f.

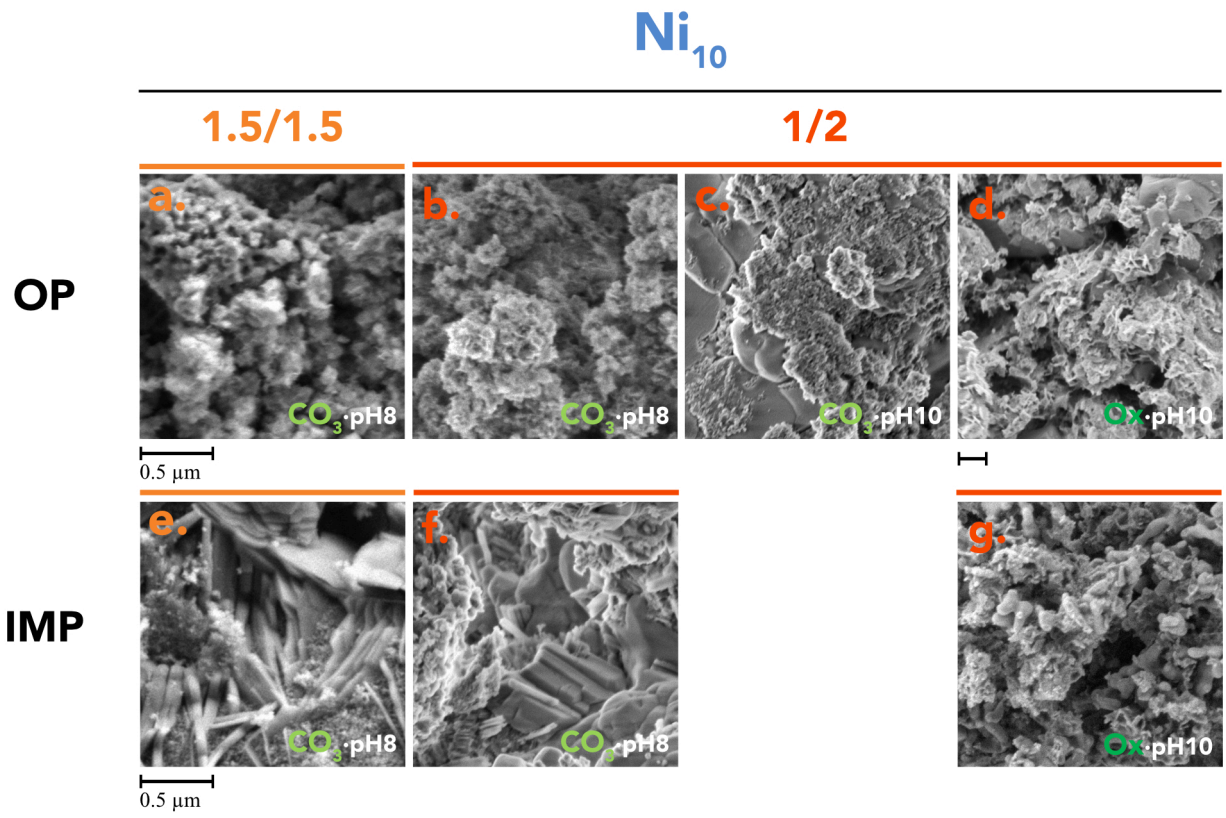

Figure 4.17: SEM pictures of Ni_{10}-LDO based catalysts calcined at 500°C according to synthesis method, Mg/Ca ratio, pH, and anion.

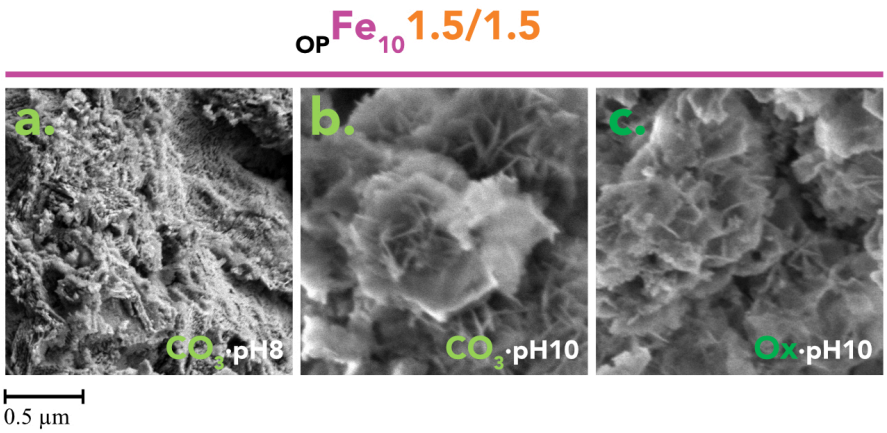

Figure 4.18: SEM pictures of $_{OP}Fe_{10}1.5/1.5$ catalysts calcined at 500°C according to pH and anion.

4.2.4.4 pH effect

The morphology of the $_{OP}Fe_{10}1.5/1.5_{CO3\cdot pH8}$ (Fig. 4.18.a) is different from that of the $_{OP}Fe_{10}1.5/1.5_{CO3\cdot pH10}$ catalyst (Fig. 4.18.b) and shows a surface with fluffy layers. However, this airy morphology does not assure a sufficient SSA value (48 m^2/g) as previously reported (Fig. 4.12). At pH 10, the *sand roses* morphology is obvious whatever the anion used for the $_{OP}Fe_{10}1.5/1.5$ catalysts (Fig. 4.18). For catalysts derived from the carbonate anion at least, the ratio Mg/Ca = 1/2 seems favorable to a lower dense morphology at pH 8 (Fig. 4.17.b). Indeed, $_{OP}Ni_{10}1/2_{CO3\cdot pH10}$ (c.) seems to be bulkier than $_{OP}Ni_{10}1/2_{CO3\cdot pH8}$ (b.) that is confirmed by a lower SSA value (15 m^2/g against 24 m^2/g).

4.2.4.5 Mg/Ca ratio effect

Extensive study on the nickel ($Ni_{10wt\%}$) catalysts synthesized at various Mg/Ca ratios by impregnated method displays an evolution of the morphology (Fig. 4.17.e, f. & g.): the higher the Mg/Ca ratio, the finest the *sand roses*. SEM pictures of Ni_{10} catalysts using oxalate anion at pH 10 (Fig. 4.16.f. and Fig. 4.17.g.) allows to observe *sand roses* and the bulkier phase in a higher proportion for Mg/Ca = 1/2 than for Mg/Ca = 1.5/1.5, for both OP and IMP methods.

Contrariwise, varying the Mg/Ca ratio in the catalysts synthesized by the OP method at pH 8 did not alter the porous morphology. Note that the N_2 adsorption values indicated a dicrease in SSA with the same type of isotherm curve (IVa) i.e. mesoporosity for both Mg/Ca ratio.

4.2.4.6 Anion size

By impregnation synthesis method using carbonate at pH 8 (Fig. 4.17.f.), the flat and thick clustered lamellar shape changes completely in morphology. This latter is not homogeneous and much less advisable than the corresponding oxalate sample at pH 10 (Fig. 4.17.g.).

At pH 10, the oxalate samples present thinner *sand roses* than the carbonate samples for $_{OP}Ni_{10}1/2$ (Fig. 4.17.d) and $_{OP}Fe_{10}1.5/1.5$ (Fig. 4.18.c). Then oxalate still seems the best anion tby maintaining morphology and moderate porous degradation for the OP synthesis method, for which the decrease in textural properties is relatively simple to predict.

As a conclusion of the morphology study, the various parameters effect are:

- Synthesis method: OP > IMP
- Metal nature: no distinctive impact
- Metal content: $Ni_5 > Ni_{10}$; $Ni_{10} < Fe_{10}$ and $Fe_{10} > Fe_{20}$
- pH for carboante: 8 > 10 for Mg/Ca = 1/2; 10 > 8 for Mg/Ca = 1.5/1.5
- Mg/Ca ratio: 1.5/1.5 > 1/2
- Anion choice: Ox > CO3

The comparison between this summary and the proposity conclusion (§4.2.3.) indicates a really corelation of the behaviors evolution with common trends and brings the synergy of the optimized conditions to produce the desired porous and morphology properties.

4.3 Sorption properties

4.3.1 Sorption capacity and CaO sites accessibility

Keeping the same test conditions as for the sorbent sorption study, the sorption capacity of the catalysts is represented in terms of $g_{CO2}/100g_{sorbent}$ and $g_{CO2}/100g_{CaO}$ representing the CaO sites accessibility (Fig. 4.19). Besides metal and weight percent comparisons, the sorption capacity of the corresponding sorbent is added to data for the selected samples. In contrast to what was presented in chapter 3, the theoretical sorption capacity values of the sorbent samples are avoided here because they change when nickel or iron is added and for each weight percentage as well: the sorption capacity is calculated in grams per mole and after the metal impregnation, the molar mass is unknown and this would have required the basic analysis of each sample.

The evolution of CO_2 adsorption during the carbonation step (Fig. 4.19) is always quite similar to the representatif curve in Chapter 2 (§2.3.1 - Fig. 2.2) and has no impact on the sorption capacity measurement. This evolution is well described by J.M. Valverde [9] for CaO-based materials.

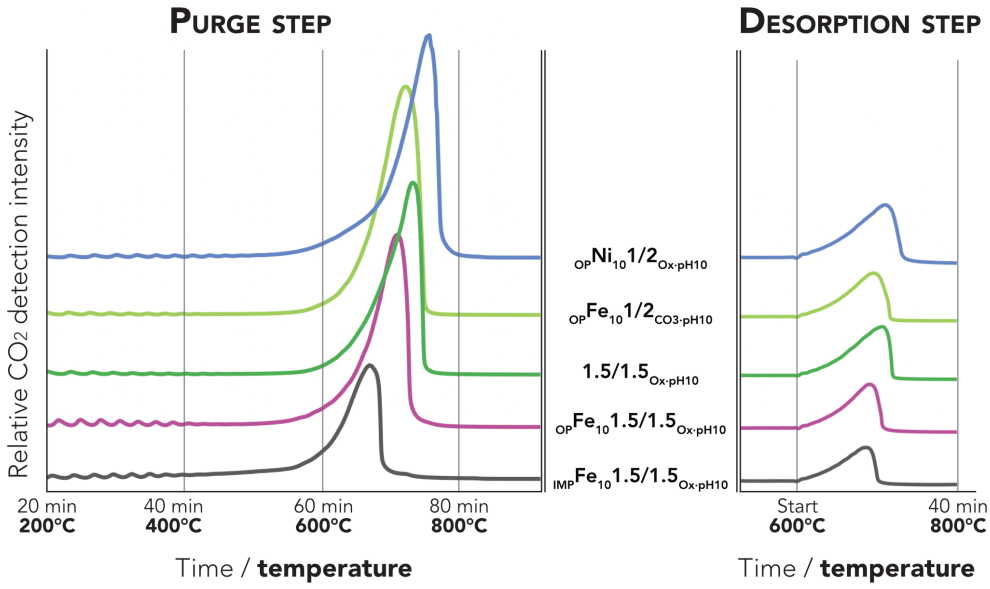

Figure 4.19: Raw live CO_2 signal during the purge and the desorption step of the sorption capacity tests of different catalysts.

4.3.1.1 Synthesis method effect

The sorption capacities of the impregnated catalysts are always lower than their equivalent values in OP catalyst and sorbent (Fig. 4.20). For the $_{IMP}1/2_{Ox\cdot pH10}$ catalysts, the sorption capacities are particularly low while the conditions notably allowed in the OP method to perform a better property than the sorbent equivalent. Indeed, two thirds are loss in the IMP compared to the OP equivalent catalysts. The best sorption capacity of IMP catalysts is reaching by $_{IMP}Fe_{10}1/2_{CO3\cdot pH8}$ at 20.1 $g_{CO2}/100g_{sorbent}$ followed by $_{IMP}Ni_5 1.5/1.5_{Ox\cdot pH10}$ at 18.3 $g_{CO2}/100g_{sorbent}$.

$_{IMP}Fe_{10}1/2_{CO3\cdot pH8}$ and $_{IMP}Ni_5 1.5/1.5_{Ox\cdot pH10}$ also have the highest accessibility of CaO sites with 40.6 $g_{CO2}/100g_{CaO}$ and 47.4 $g_{CO2}/100g_{CaO}$ respectively (Fig. 4.21). As observed in the comparison of sorbent accessibilities, the 1.5/1.5 samples provide better accessibility than the 1/2 equivalents. This same pattern is observed for the catalysts in the OP but also in the IMP method.

Lastly at equal weight percent, the sorption capacity and CaO sites accessibility of $_{IMP}Fe_{10}1/2_{Ox\cdot pH10}$ compared to $_{IMP}Ni_{10}1.5/1.5_{Ox\cdot pH10}$ are surely too close to conclude which metal is more suitable for impregnation.

4.3.1.2 Metal nature and content effects

First of all, the OP catalyst sorption capacities (Fig. 4.20) are in general lower than their sorbent equivalent (Chapter 3 - Table 3.1) except for $_{OP}Ni_{5\&10}1.5/1.5_{CO3\cdot pH8}$. As explained in the commentary on the BET result (§4.2.3.1), the synthesis of $1.5/1.5_{CO3\cdot pH8}$ had probably failed due to the too low pH at 8 to maintain proper precipitation and thus experimental reproductibility. Each iron catalyst has a better sorption capacity at 10_{wt}% than at 20_{wt}%; this is also true between Ni_5 and Ni_{10}. However, the three comparable Fe_{10} versus Ni_{10} cases do not bring out a clear trend. So, increasing the metal content reduces the sorption capacity.

The best sorption capacity reaches 35.8 $g_{CO2}/100g_{sorbent}$ for $_{OP}Ni_5 1/2_{Ox\cdot pH10}$ for the nickel catalyst which is better than the $1/2_{Ox\cdot pH10}$ sorbent and 34.1 $g_{CO2}/100g_{sorbent}$ for $_{OP}Fe_{10}1/2_{CO3\cdot pH10}$ for the iron catalyst. $1/2_{Ox\cdot pH10}$ corresponds to the conditions to best save the sorption capacity regarding sorbent equivalent.

By impregantion, observing $_{IMP}Fe_{10}1.5/1.5_{Ox\cdot pH10}$ and $_{IMP}Fe_{10}1/2_{CO3\cdot pH8}$, 10_{wt}% of iron is enough to waste half the sorption capacity versus sorbent equivalent. The loss is even substantial more at higher weight percent. Thus at 1.5/1.5, the impregnation of only $5_{wt\%}$ of nickel limits this loss but remains 59% of the sorption capacity compared to $1.5/1.5_{Ox\cdot pH10}$ and 67% against $_{OP}Ni_5 1.5/1.5_{Ox\cdot pH10}$. The impact of increasing metal content on sorption capacity is even worse with the impregnated method than one-pot synthesis. However, the trend of high weight percentage persists, but only a few differencs between Ni_5 (11.0 $g_{CO2}/100g_{sorbent}$) and Ni_{10} (9.7 $g_{CO2}/100g_{sorbent}$).

4.3.1.3 pH effect

Samples at pH8 have the property of being less subject to the decreasing of sorption capacity when the weight percent of metal increases (Fig. 4.20). Indeed, the difference between $_{OP}Ni_5 1.5/1.5_{CO3\cdot pH8}$ and $_{OP}Ni_{10}1.5/1.5_{CO3\cdot pH8}$ is minimal, less than 1 $g_{CO2}/100g_{sorbent}$; between $_{OP}Ni_5 1/2_{CO3\cdot pH8}$ versus $_{OP}Ni_{10}1/2_{CO3\cdot pH8}$ and $_{OP}Fe_{10}1.5/1.5_{CO3\cdot pH8}$ and $_{OP}Fe_{20}1.5/1.5_{CO3\cdot pH8}$ also. So, low pH positively trends to stabilize the sorption capacity at higher metal weight percent.

4.3.1.4 Mg/Ca ratio effects

With the addition of metal, the trend observed for the sorbent depends on Mg/Ca and the different anions. On the one hand, the sorption capacities of $_{OP}Fe1.5/1.5_{Ox\cdot pH10}$ are a bit lower than $_{OP}Fe1/2_{Ox\cdot pH10}$ for both weight percent. A significant gain is observed for $_{OP}Fe1/2_{CO3}$ particularly at pH10. On the other hand, for nickel catalysts, carbonate at pH8 appears to be a better condition for Mg/Ca = 1.5/1.5, and oxalate at pH10 seems better conditions at Mg/Ca = 1/2.

Borgna et al. [6] presents a review of CO_2 sorption capacity as a function of sorbents types and consider the capacity of Ca-based at high temperature (600- 700°C) to be maximum sorbents at 53 $g_{CO2}/100g_{sorbent}$ in the literature. The pure CaO described in Chapter 3 (§3.2.4.1 - Table 3.1) get closer to this high value. However, the sorption capacity of the catalysts (Fig. 4.20) move away from this value but remains competitif with the accessibility of the CaO sites. The CaO content in the sorbent is 42_{wt}% for OP catalysts respecting the ratio Mg/Ca = 1.5/1.5 and 54_{wt}% for catalysts with the reatio Mg/Ca = 1/2. In this regard, comparison can be made from mayenite and derivate sorbents of Pacciani et al. [12] or Broda et al. [11-12] with a close composition (MgO, CaO, $Ca_{12}Al_{14}O_{33}$) in

various proportions. The materials studied provide access to a good sorption capacity at 50 $g_{CO2}/100g_{sorbent}$ for sorbents with the highest Ca_{wt}% (85_{wt}%) but decreases with the content of Ca_{wt}% until 35 $g_{CO2}/100g_{sorbent}$ and lower at 50_{wt}% of CaO; so, the values are very similar to those observed Fig. 4.20. The values of accessibility of CaO sites (Fig. 4.21) indicated the same trends as sorption capacity. The best CaO accessibility is obtained with $_{OP}Ni_5 1.5/1.5_{CO3\cdot pH8}$ at 76.9 $g_{CO2}/100g_{CaO}$ following by the same with Ni_{10}. The SSA values $_{OP}M1.5/1.5_{CO3\cdot pH8}$ are also very different from the sorbent equivalent so the gap is logical in the accessibility of CaO. After this exception, the best iron catalyst remains the $_{OP}Fe_{10}1/2_{CO3\cdot pH10}$ reaching 62.5 $g_{CO2}/100g_{CaO}$. It should be noted what only $_{OP}Ni_{5\&10}1/2_{Ox\cdot pH10}$ exceeds the CaO accessibility of it sorbent equivalent, *i.e.* 56.6 $g_{CO2}/100g_{CaO}$.

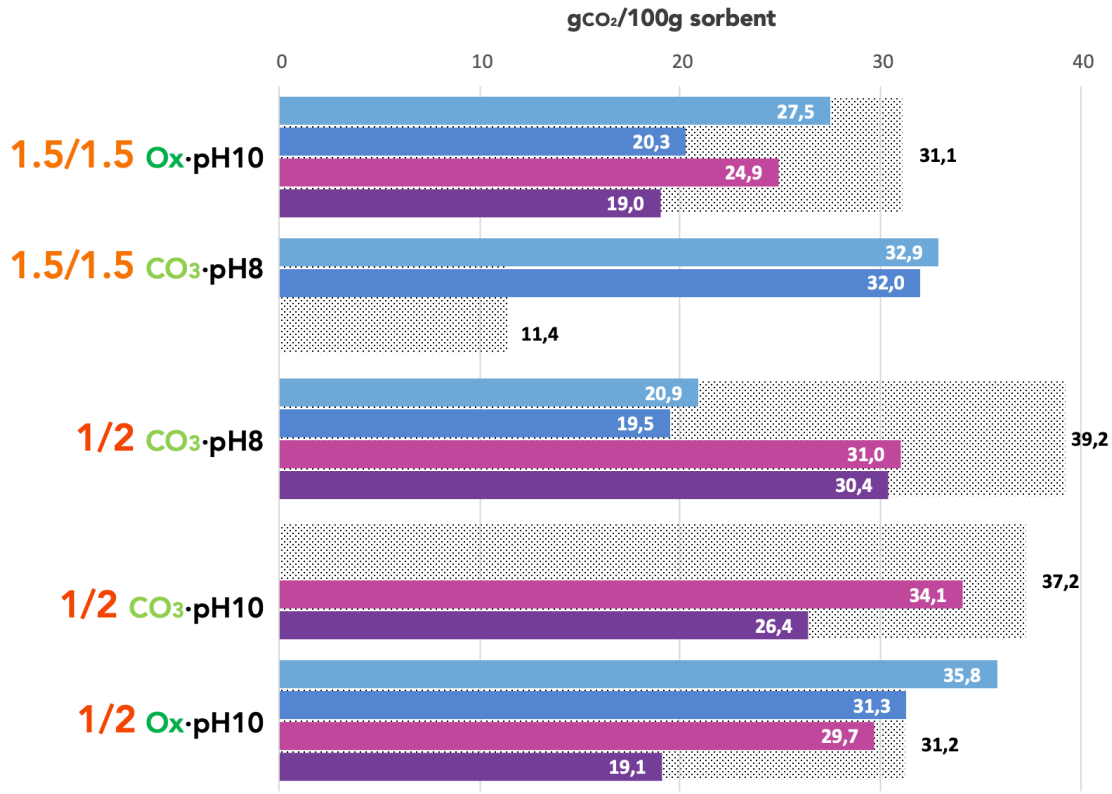

Figure 4.20: Sorption capacity of different one-pot synthesis M-LDO samples according to Mg/Ca ratio, anion, and pH. Grey dotted lines indicate the sorbent capacity of the corresponding sorbents.

The comparison can be completed on the basis of references of sorption capacity meseared at 650°C which is more tested in the literature. Luo et al. [13] demonstrate rate of CaO carbonation during CO_2 sorption between 60 $g_{CO2}/100g_{CaO}$ and 72 $g_{CO2}/100g_{CaO}$ with CaO/Al_2O_3 materials. So, the tested sorbents are in the same range of values and best catalysts keep it up too like $_{OP}Ni_5 1/2_{Ox\cdot pH10}$ and $_{OP}Fe_{10} 1/2_{CO3\cdot pH10}$.

With the highest content of Ca_{wt}% between 75_{wt}% and 98_{wt}%, CaO sites accessibility in Ca-Al mixte oxides [14-16] reaches at 650°C from 50 to 75 $g_{CO2}/100g_{CaO}$ and allows to spotlighting the performance of $_{OP}Ni_{5\&10} 1.5/1.5_{CO3\cdot pH8}$ samples.

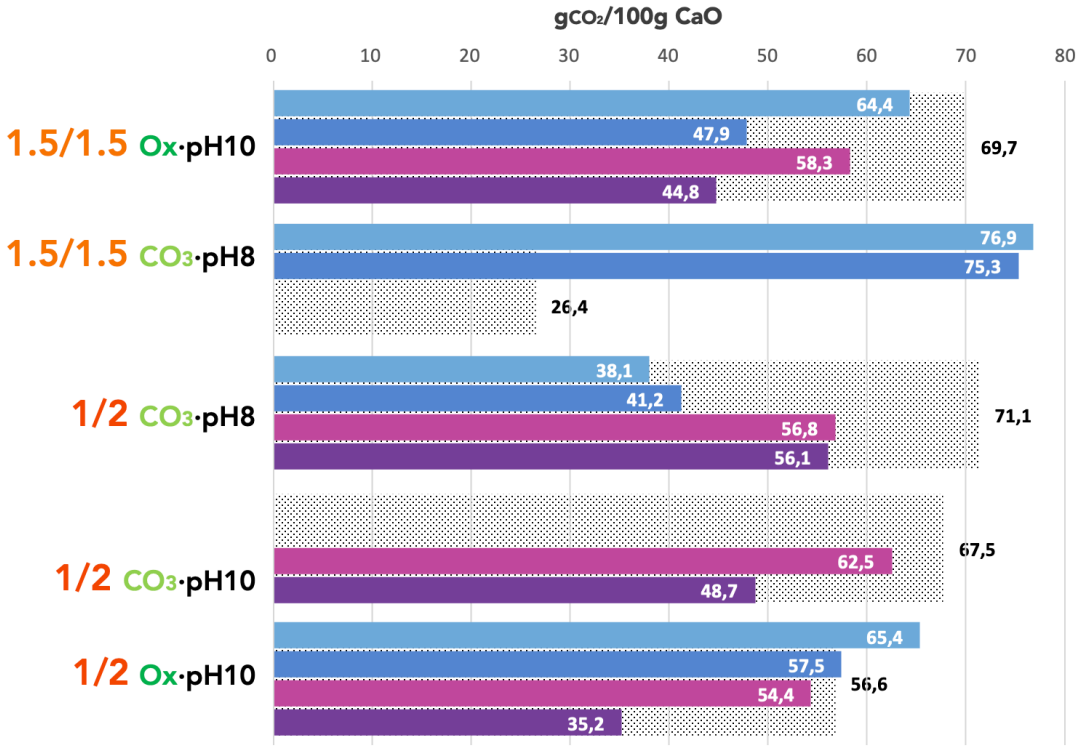

Figure 4.21: Sorption accessibility of different one-pot synthesis M-LDO samples according to Mg/Ca ratio, anion, and pH. Grey dotted lines indicate the sorption accessibilities of the corresponding sorbents.

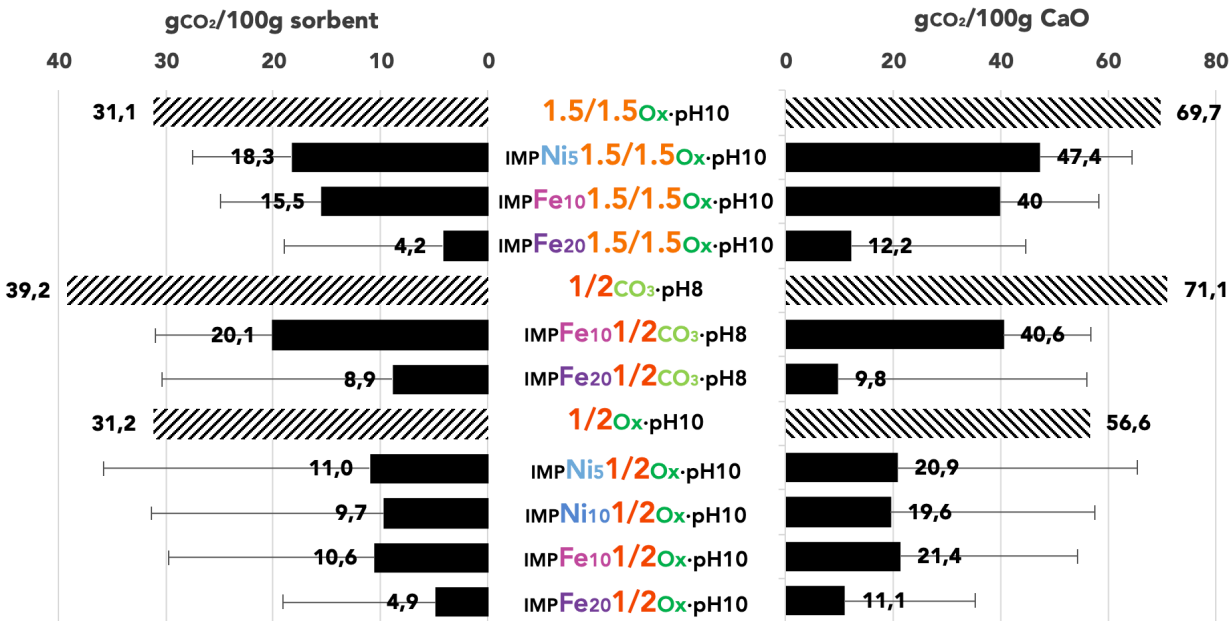

Figure 4.22: Sorption capacity and CaO sites accessibility of different IMP M-LDO samples according to Mg/Ca ratio, anion and pH. Striped lines indicate the values for the corresponding sorbents. Grey segments indicate the difference between IMP samples values and OP corresponding values.

4.3.2 Sorption stability

The study of the sortion stability is particulary important for the next step of the project where the catalysts are subject to cyclic resforming/desorption tests.

In addition, the sorption capacity of some catalysts is measured by cyclic-TGA (Fig. 4.23 & 24). For the Ni catalysts (Fig. 4.23), the $_{OP}Ni_{10}1.5/1.5_{Ox\cdot pH10}$ sample is the only studied catalyst that has a higher sorption capacity than its nickel-free counterpart $1.5/1.5_{Ox\cdot pH10}$. This sample stays the best catalyst after 10 cycles reaching 21 $g_{CO2}/100g_{sorbent}$ corresponding to a minimal loss of sorption capacity (13%). The losses after 10 cycles are quite similar for the other nickel catalysts: from 16 $g_{CO2}/100g_{sorbent}$ to 14 $g_{CO2}/100g_{sorbent}$ (i.e. -14%) for $_{OP}Ni_{10}1/2_{Ox\cdot pH10}$ and from 11 $g_{CO2}/100g_{sorbent}$ to 8 $g_{CO2}/100g_{sorbent}$ (i.e. -31%) for $_{OP}Ni_{10}1.5/1.5_{CO3\cdot pH8}$, which presents the lowest sorption capacity from the beginning of the analysis. According to the corresponding sorbent ($1/2_{Ox\cdot pH10}$), $_{OP}Ni_{10}1/2_{Ox\cdot pH10}$ is more stable even through the sorption capacity is maintained over the 10 cycles studied. So, the addition of nickel generally decreases the sorption capacity but keeps or

improves the stability of sorbent. The conditions to optimize the sorption stability for nickel catalysts are $1.5/1.5_{Ox\cdot pH10}$.

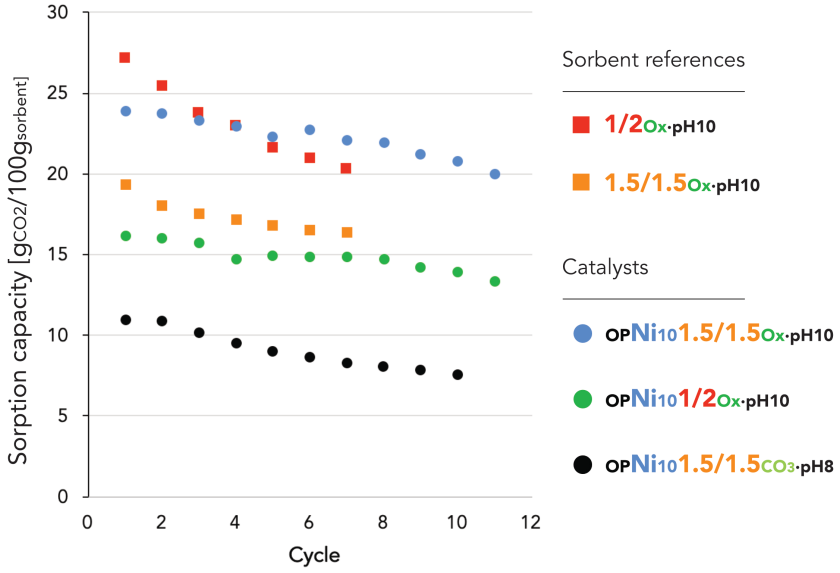

Figure 4.23: Sorption capacity versus sorption/desorption cycles number for various nickel catalysts calcined at 500°C and the corresponding sorbents.

The iron catalysts follow the same trend with lower sorption capacity and better stability than their corresponding sorbents (Fig. 4.24). In fact, in the first few cycles, $_{OP}Fe_{10}1.5/1.5_{CO3\cdot pH10}$ reaches 19 $g_{CO2}/100g_{sorbent}$ and the sorption capacity of all other iron catalysts starts at 13 $g_{CO2}/100g_{sorbent}$. $_{OP}Fe_{10}1/2_{Ox\cdot pH10}$ is fully stable up to 20 cycles without loss of sorption capacity. In contrast, at the 10th cycle, $_{OP}Fe_{10}1.5/1.5_{CO3\cdot pH10}$, $_{OP}Fe_{10}1/2_{CO3\cdot pH10}$ and $_{OP}Fe_{20}1/2_{Ox\cdot pH10}$ loss 20%, 30% and 31% of their initial sorption capacity, respectively; between the 10th and 15th cycle, the decrease is much less significant and reaches an asymptote.

At 20_{wt}%, if the sorption capacity tends to decrease faster the sorption capacity than the 10_{wt}% sample during the first cycles it seems to settled down after 5 cycles. This rate of decrease remains well below the values of the corresponding sorbents, which decrease not only faster but also longer, such as $1/2_{CO3\cdot pH10}$ which is stable only after 14 cycles. Moreover, due to the stability provided by the iron content, the sorption capacity of $_{OP}Fe_{10}1/2_{CO3\cdot pH10}$ equals that of $1/2_{CO3\cdot pH10}$ and then becomes better after the 12th cycle. The previous publications cited [11-13] and Li et al. [17] brings values of sorption

stability especially stable accroding to cycle as iron catalysts in Fig. 4.24. The apparent stability due to the addition of iron comes either from the iron interacting with the other oxides of the structure and could limit the sintering; or from a stabilization due to the modification of the M^{2+}/M^{+3} ratio. This second hypothesis would indicate that the nature of the metal is not in question but rather its degree of oxidation. Indeed, samples containing nickel, with a M_{2+}/M_{+3} ratio higher than their ferrous equivalent, are not more stable than their metal-free sorbent. A complementary analysis by Mössbauer spectroscopy could bring more information on this influence of iron on the stability of the absorption capacity.

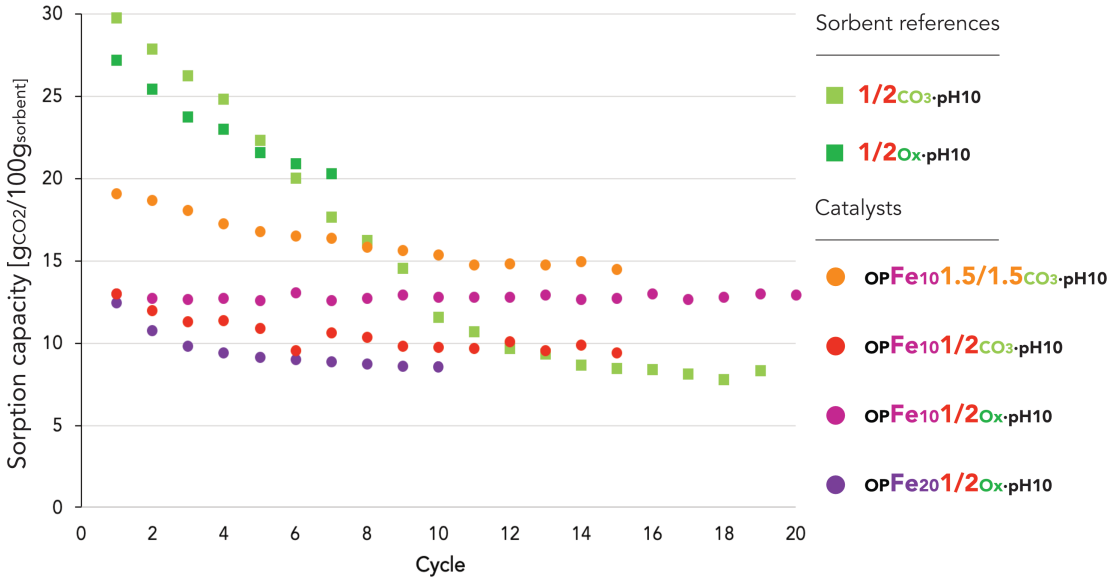

Figure 4.24: Sorption capacity versus sorption/desorption cycles number for various iron catalysts and the corresponding sorbents.

4.4 Conclusion

First, in elementary analysis, the Mg/Ca ratio – the main key parameter for the sorption capacity – is maintained despite different metal contents, synthesis methods and as accurate as sorbent equivalents. However, the amount of metal is overestimated for both metals and the impregnation method moderates this gap according to the theoretical values.

The precursors were evaluated by XRD analysis and the decomposition by TGA under air and XRD as well. A strong correspondence between sorbents and catalyst appears for each anion with the same weight loss step in TGA and same phases in XRD. The reported trebds according to synthesis conditions are preserved from sorbents to catalysts.

As a whole, the porosity property of the catalysts shows mesoporosity with less SSA and Pv compared to the sorbent equivalent for the OP method and in the worse case for the impregnation method. Besides, the $1.5/1.5_{Ox\cdot pH10}$ (best iron catalyst for ${}_{OP}Fe_{10}$) is among the high-performance conditions with $1.5/1.5_{CO3\cdot pH8}$ for nickel only (best nickel catalyst for ${}_{OP}Ni_5$). In addition, the surface area can be enhanced through the metal content with the stringent conditions ${}_{OP}Fe_{10}1.5/1.5_{CO3\cdot pH10}$ and ${}_{OP}Ni_5 1/2_{Ox\cdot pH10}$ reaching 86 m^2/g and 103 m^2/g respectively. In contrast, the impregnated catalysts ensure 30-58 m^2/g with Ox·pH10 conditions.

The porosity values can be correlated with SEM analysis which revealed a partial morphology of remaining *sand roses* for the OP catalysts at low metal weight percent. At higher content, nickel and iron participate in the increasing formation of a second bulky morphology mixed with *sand roses*. The trend at 1.5/1.5 versus 1/2 ratio is preserved for both anions. The impregnation method causes the collapse of porous morphology and fomr a massive bulky shape at Mg/Ca = 1/2. But this synthesis method nevertheless seems more appropriate at $1.5/1.5_{Ox\cdot pH10}$ with a retained porous morphology for both metals at each weight percent.

Afterward, the CO_2 sorption results describe a loss of capacity and CaO sites accessibility according to sorbent equivalent and with increasing metal amount. At OP 10_{wt}%, same anion, same pH and same Mg/Ca, the sorption properties of iron catalysts are quite equal to or often better than those of nickel equivalents. At large, different conditions achieve 30 $g_{CO2}/100g_{sorbent}$ and 50 $g_{CO2}/100g_{CaO}$ for both metals and each OP condition. The deterioration of sorbents by impregnation was also apparent with lower values than sorbent and OP catalyst equivalents. The trend observed for OP catalysts is exacerbated in the IMP synthesis. Hence, $_{IMP}Ni_5 1.5/1.5_{Ox\cdot pH10}$ (18.3 $g_{CO2}/100g_{sorbent}$; 47.4 $g_{CO2}/100g_{CaO}$ and $_{IMP}Fe_{10} 1/2_{CO3\cdot pH8}$ (20 $g_{CO2}/100g_{sorbent}$; 40.6 $g_{CO2}/100g_{CaO}$) stand out for the rest with the highest IMP results.

At last, the performance of the catalyst-sorbents measured by cyclic absorption/desorption test demonstrates a real improvement of sorption stability, which surpasses the initial sorption capacity. Even after few cycles, the enhancement are still notably with $_{OP}Ni_{10} 1.5/1.5_{Ox\cdot pH10}$ for nickel catalyst and with $_{OP}Fe_{10} 1.5/1.5_{CO3\cdot pH10}$ for iron one.

In general, the results of the catalyst analysis bring to highlight the effictiveness of the co-precipitation method in tailoring the addition of nickel and iron nitrate in the synthesis. The properties and structural characteristics are maintained or at the worst diminished but systematically greater than impregnated sample equivalents.

This second method should be effictive in improving the catalytic activity. Thus, the SESR test will be approached with selected catalysts, which appear more promising. Therefore, $_{OP}Ni_{10} 1/2_{Ox\cdot pH10}$ and $_{OP}Ni_{10} 1.5/1.5_{Ox\cdot pH10}$ are chosen for the nickel part as well as $_{OP}Fe_{10} 1.5/1.5_{CO3\cdot pH10}$ for the iron catalyst. To complete the comparison, $_{IMP}Ni_{10} 1/2_{Ox\cdot pH10}$, $_{OP}Ni_{10} 1/2_{CO3\cdot pH10}$ and $_{OP}Fe_{10} 1.5/1.5_{Ox\cdot pH10}$ will be tested for a representative selection of synthesis conditions.

References

[1] Wang, Q., Tay, H.H., Ng, D.J.W., Chen, L., Liu, Y., Chang, J., Zhong, Z., Luo, J., Borgna, A.: The effect of trivalent cations on the performance of Mg-M-CO_3 layered double hydroxides for high-temperature CO_2 capture, Chem. Sus. Chem., 3, 965-973 (2010).

[2] Leineweber, A., Jacobs, H., Hull, S.: Ordering of nitogen in nickel nitride Ni_3N determined by neutron diffraction, Inorg. Chem., 40, 5818-5822 (2001).

[3] Kahlenberg, V., Fischer, R., Shaw, C.: High-pressure $Ca_4Al_6O_{13}$: an example of a calcium aluminate with three different types of coordination polyhedral for aluminum, American Mineralogist, 85, 1492-1496 (2000).

[4] Griesfeller, F., Köhler, J., Hoppe, R.: Das erste Oligo-Oxo-Aluminat: $Na_{14}[Al_4O_{13}]$, ZAAC, 507, 155-162 (1983).

[5] López-Ortiz, A., Perez Rivera, N. G., Reyes Rojas, A., Lardizabal Gutierrez, D.: Novel Carbon Dioxide Solid Acceptors Using Sodium Containing Oxides, Separation Science and Technology, 39, 3559-3572 (2005).

[6] Wang, Q., Luo, J., Zhong, Z., Borgna, A.: CO_2 capture by solid adsorbents and their applications: current status and new trends, Energy Environ. Sci., 4, 42-55 (2011).

[7] Walspurger, S., Cobden, P.D., Safonova, O.V., Wu, Y., Anthony, E.J.: High CO2 Storage Capacity in Alkali-Promoted Hydrotalcite-Based Material: In Situ Detection of Reversible Formation of Magnesium Carbonate, Chem. Eur. J., 16, 12694-12700 (2010).

[8] Thommes, M., Kaneko, K., Neimark, A.V., Olivier, J.P., Rodriguez-Reinoso, F., Rouquerol, J., Sing, K.S.W.: Physisorption of gases, with special reference to the evaluation of surface area and pore size distribution. Pure Appl. Chem., 87, 1051-1069 (2015).

[9] Valverde, J.M.: Ca-based synthetic materials with enhanced CO_2 capture efficiency, J. Mater. Chem. A, 1, 447 (2013).

[10] Pacciani, R., Müller, C.R., Davidson, J.F., Dennis, J.S., Hayhurst, A.N.: Synthetic Ca-based solid sorbents suitable for capturing CO_2 in a fluidized bed, Can. J. Chem. Eng., 86, 356-366 (2008).

[11] Broda, M., Müller, C.R.: Synthesis of highly efficient, Ca-based, Al_2O_3-stabilized, carbon gel-templated CO_2 sorbents, Adv. Mater., 24, 3059-3064 (2012).

[12] Broda, M., Kierzkowska, A.M., Müller, C.R.: Influence of the calcination and carbonation conditions on the CO_2 uptake of synthetic Ca-based CO_2 sorbents, Environ. Sci. Technol, 46, 10849-10856 (2012).

[13] Luo, C., Zheng, Y., Ding, N., Wu, Q.L., Zheng, C.G.: SGCS-made ultrafine CaO/Al_2O_3 sorbent for cyclic CO_2 capture, Chinese Chem. Lett., 22, 615-618 (2011).

[14] Florin, N., Fennell, P.: Synthetic CaO-based sorbent for CO_2 capture, Energy Procedia 4, 830-838 (2011).

[15] Shan, S., Ma, A., Hu, Y., Jia, Q., Wang, Y.: Development of sintering-resistant CaO-based sorbent derived from eggshells and bauxite tailings for cyclic CO_2 capture, Environ. Pollu., 208, 546-552 (2016).

[16] Xu, P., Xie, M., Cheng, Z., Zhou, Z.: CO2 capture performance of CaO-based sorbents prepared by a sol-gel method, Ind. Eng. Chem. Res, 52, 12161-12169 (2013).

[17] Li, Z.S., Cai, N.S., Huang, Y.Y., Han, H.J.: Synthesis, experimental studies, and analysis of a new calcium-based carbon dioxide absorbent, Energy & Fuels, 19, 1447-1452 (2005).

CHAPTER 5

CATALYTIC ACTIVITY

This chapter presents first the reducibility of few catalysts measured by TPR-H_2. Then, the SESR reactivity studies are shared in two different tests: on the one hand, the temperature, the S/C ratio and the catalysts composition are explored; on the other hand, via SESR/desorption cycles, the stability of of the catalysts performance was evaluated. Finally, the catalyst characterization ends with the analysis of post-SESR test, N_2 adsorption and sorption capacity.

5.1. Reducibility

Before the reactivity tests, reduction of the metal sites on the catalysts is performed by TPR-H_2 to evaluate the reducibility and reduction temperature according to the synthesis conditions and parameters. The reduction temperatures found indicate the need or not to schedule a pre-reduction for subsequent SESR tests. The conclusion of *Chapter 4* explains the selection of iron catalysis using oxalate anion in the synthesis which is compared in Fig. 5.1 associated with reducibility in Table 5.1. The difference in the integration of the total H_2 consumption in TPR-H_2 depends on the reducibility but also on the real amount of iron. Indeed, the preceding elementary analysis (*§ 4.1*) showed that the OP method involves less iron than the IMP one and less than the theoretical method at 10_{wt}% and 20_{wt}%. The consideration of the reducibility value is therefore to be put into perspective for the OP samples which are underestimated there.

Table 5.1: Reductibility of iron catalysts.

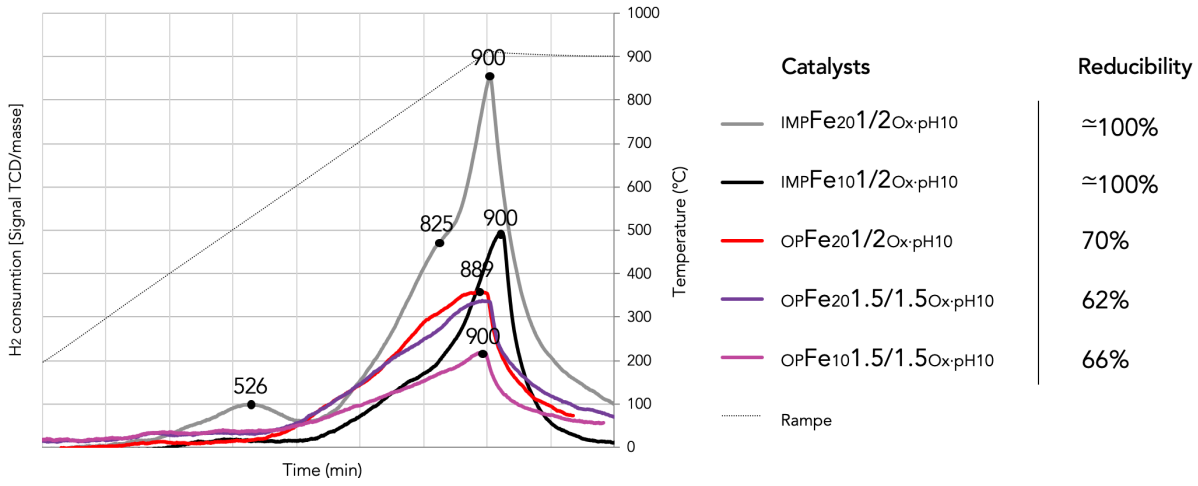

Figure 5.1: TPR-H_2 profiles of iron catalysts. Numbers on curves correspond to the temperature (°C) in the black points.

The iron catalysts start their reduction beyond 600°C with the highest H_2 consumption observed at 900°C, *i.e.* the end of temperature range. The OP catalysts seem to reach this experimental limit at the top of the H_2 consumption, so the curves differ from the IMP profiles. $_{IMP}Fe_{20}1/2_{Ox\cdot pH10}$ stands out with the first H_2 consumption at 526°C and the second one at 825°C in addition to the last at 900°C which corresponds to the reduction temperature of iron oxide on stabilized structure [1].

The reducibility of the IMP catalysts reaches 100% against 62% to 70% for the OP thanks to the accessibility of partially unattainable metal sites in the bulk of the sorbent material. The impregnation method allowing to deposit the metal on the surface of the porous support is more interesting for the reactivity. The TPR-H_2 of the nickel catalysts (Fig. 5.2 – Table 5.2) exhibit a lower reduction temperature than the homologous iron catalysts with a maximum H_2 consumption at 795-847°C. The reducution range is narrow and ends at 900°C during the isotherm to form a Gaussian distribution. $_{IMP}Ni_{10}1/2_{Ox\cdot pH10}$ varies with reduction from 612°C and a second high H_2 consumption at 900°C and reaches 78% reducibility, the best value of $_{OP}Ni_{10}$ catalysts behind $_{IMP}Ni_{10}1.5/1.5_{Ox\cdot pH10}$. The variation of the reduction temperature can be explained by the interaction between the NiO phase and the support [2-3]. Fornasari et al. [2] states about the reduction temperature of pure NiO occurs at 240-270°C but increases accroding to the support interaction notably with MgO structure until 520-750°C and further [3] for the maximum H_2 consumption point even with slower TPR temperature ramp. From the same reference, the free NiO starts to consume hydrogen from 380°C. The Ni species has negligible interaction with the support when the reduction temperature is so low. So, the values observed indicate a well interaction between NiO and the composition of the sorbent $MgO/CaO/Al_2O_3$. The $_{IMP}Ni_{10}1.5/1.5_{Ox\cdot pH10}$ sample with an earlyer reduction temperature demonstrates a lower interaction because of the impregnation method.

Table 5.2: Reductibility of nickel catalysts.

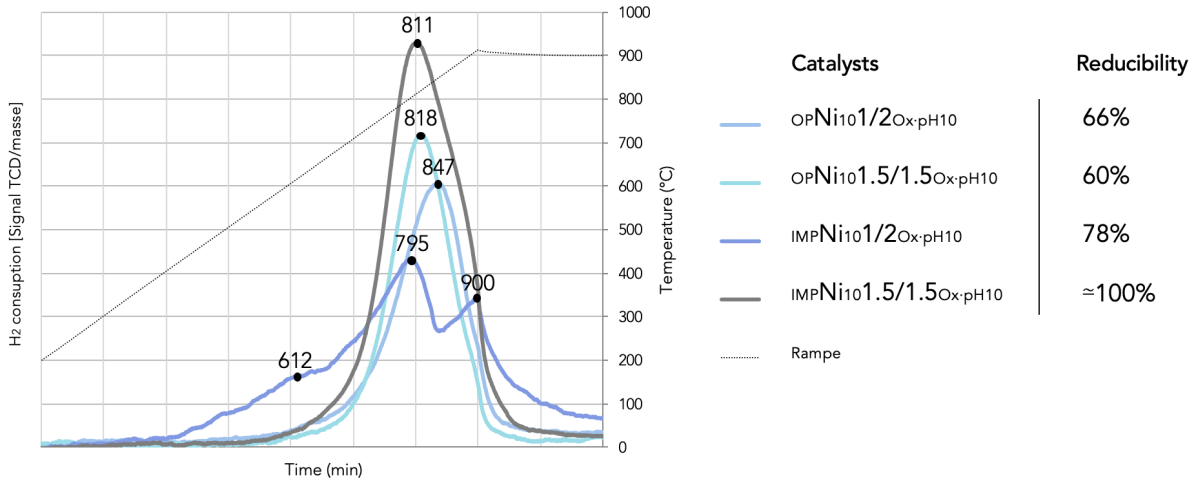

Figure 5.2: TPR-H_2 profiles of nickel catalysts. Numbers on curves correspond to the temperature (°C) in the black points.

The reducibility of the iron and nickel catalysts is quite similar, the IMP is still better than the OP equivalent, and a small benefit at 1/2 versus 1.5/1.5 is notified. In both cases, a pre-reduction is required before the SESR reactivity operated at 600-700°C. In fact, the ramp of temperature until 800°C and an isotherm under H_2/N_2 50:50 is decided, this corresponds to a sufficient temperature for the reduction and a longer time than the TPR analysis to optimize the reduction and avoid sintering or the risk of spinel formation at higher temperatures.. This step avails to purge the sorbent part ($CaCO_3$ decarbonized).

5.2. Catalytic SESR reactivity

The catalytic activity is evaluated in two ways. The first tests aim to study the effect of S/C and the temperature on the production of H_2, CO_2, and CO. The second tests aim to evaluate the effect of SESR/desorption cycles on the stability of H_2 production and CO_2 capture.

5.2.1. Short tests

Five catalysts are used to perform short test i.e. at four different temperatures: 600°C, 650°C, 700°C, and 750°C and different S/C ratio. Fig. 5.3. represents an exemple of the raw curve optained for one step of the short test. The gas production value chosen corresponds to the post-breakthrough point at 30 min where the outlet gas is stable and it is also the important point where the H_2 selectivity and production is maximum.

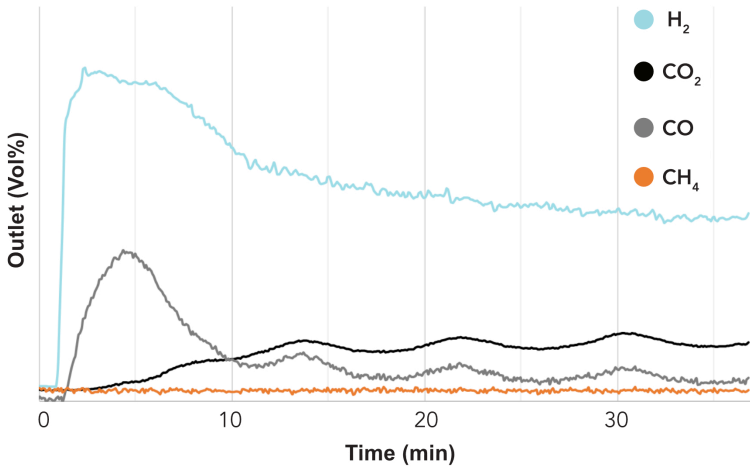

Figure 5.3: H_2, CO_2, CO and CH_4 outlet flow [$_{vol}$%] raw profiles of short SESR tests at 650°C for $_{OP}Ni_{10}1.5/1.5_{Ox\cdot pH10}$ and S/C at 6.

1.1.1.1. Metal effect

The S/C is fixed at 6, yet. The reactivity of the Ni_{10} catalysts is better than that of the iron catalysts (Fig. 5.4.a). The comparison can be made at 700°C between $_{OP}Ni_{10}1.5/1.5_{Ox\cdot pH10,}$ which is the less efficient nickel catalyst, and $_{OP}Fe_{10}1.5/1.5_{Ox\cdot pH10}$: the H_2 productivity is 283 µmol/min/g_{cat} and 90 µmol/min/g_{cat} respectively, i.e. the nickel catalyst is three-time more effecient than the iron one. In terms of gases production (Fig. 5.5) (still 700°C), $_{OP}Ni_{10}1.5/1.5_{Ox\cdot pH10}$ generates a ratio $H_2/CO_2/CO$ at 70/21/9 compared to 68/32/0 of $_{OP}Fe_{10}1.5/1.5_{Ox\cdot pH10}$. So, that is a result more favorable to nickel too.

1.1.1.2. Anion effect

Only all two iron catalysts differ in anion and the difference is minimal (Fig.5.4.a). The trend is the same at 700°C and 750°C. At 700°C, $_{OP}Fe_{10}1.5/1.5_{CO3\cdot pH10}$ produces (99 µmol/min/g_{cat}) slightly more H_2 than $_{OP}Fe_{10}1.5/1.5_{Ox\cdot pH10}$ (90 µmol/min/g_{cat}). No difference in the $H_2/CO_2/CO$ ratio is noticed with perfectly similar values for both iron catalysts at 68/32/0 at 700°C and 65/33/2 at 750°C (Fig. 5.5). At this temperature, the carbonate seems better, but the anionic effect is negligible, and probably the Mg/Ca ratio impacts more the productivity at lower temperature corresponding to favorable conditions for CO_2 capture and WGS enhancement.

1.1.1.3. Temperature effect

The H_2 productivity increases with temperature, at 700°C versus 750°C for iron catalysts and from 600°C to 700°C for nickel catalysts also with the exception of $_{OP}Ni_{10}1.5/1.5_{Ox\cdot pH10}$ (Fig. 5.4.a). The H_2 production of the latter slowly decreases from 299 µmol/min/g_{cat} at 600°C to 286 µmol/min/g_{cat} at 700°C and reaches a value close to that of $_{OP}Ni_{10}1/2_{Ox\cdot pH10}$ (283 µmol/min/g_{cat}). This trend may reflect a deactivation of the nickel sites due to the fouling of catalysts by carbon deposition [5-6] – it is recalled that the test start at 600°C, 650°C then 700°C. So, inherent to the chosen conditions, H_2 production at high temperature can be underestimated for other catalysts too due to deactivation. An easiest explanation could be that the Ni sites are more sensitive to steam at the Mg/Ca ratio of 1.5/1.5. The post-test analysis (§5 .3) attempts to explain this behavior. The comparison with iso-conversion not being possible, the Fig. 5.4.b allows another vision of the phenomena by calculating the productivity per converted carbon: the decrease in productivity due to

the increase in temperature is then also visible for $_{IMP}Ni_{10}1/2_{Ox\cdot pH10}$ and remains stable for $_{OP}Ni_{10}1.5/1.5_{Ox\cdot pH10}$. Thus at 600°C, the lack of conversion compared to higher temperatures is compensated by a better hydrogen selectivity to produce more hydrogen per converted carbon and relates it to the results of Fig. 5.5 which the increase in temperature inhibits the WGS reaction, with a decrease in CO2 production.

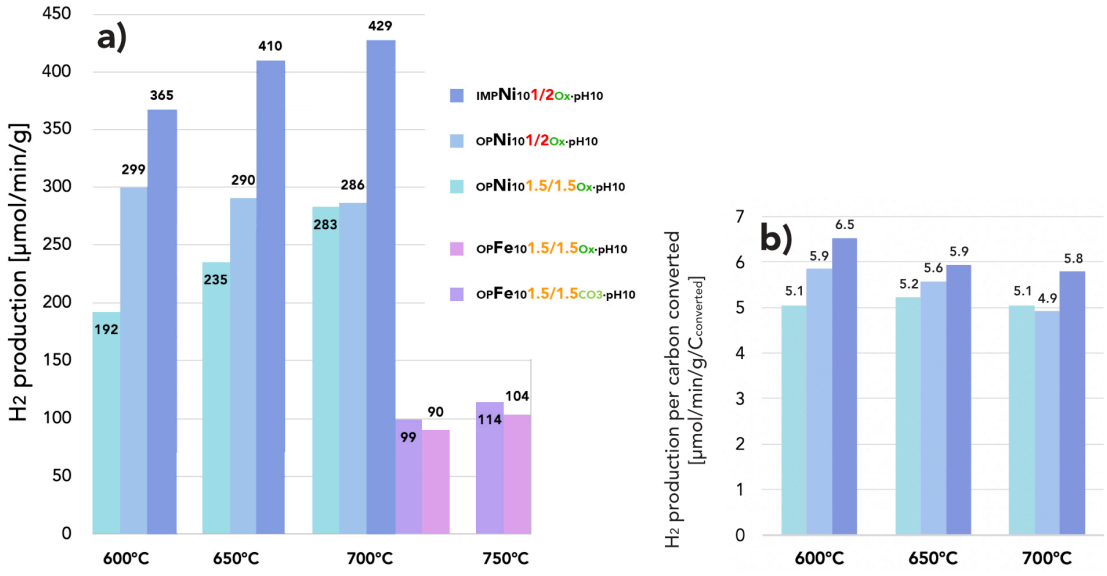

Figure 5.4: a) Productivity of H_2 according to temperature for selected nickel and iron catalysts at S/C ratio at 6, b) Productivity expressed per carbon converted.

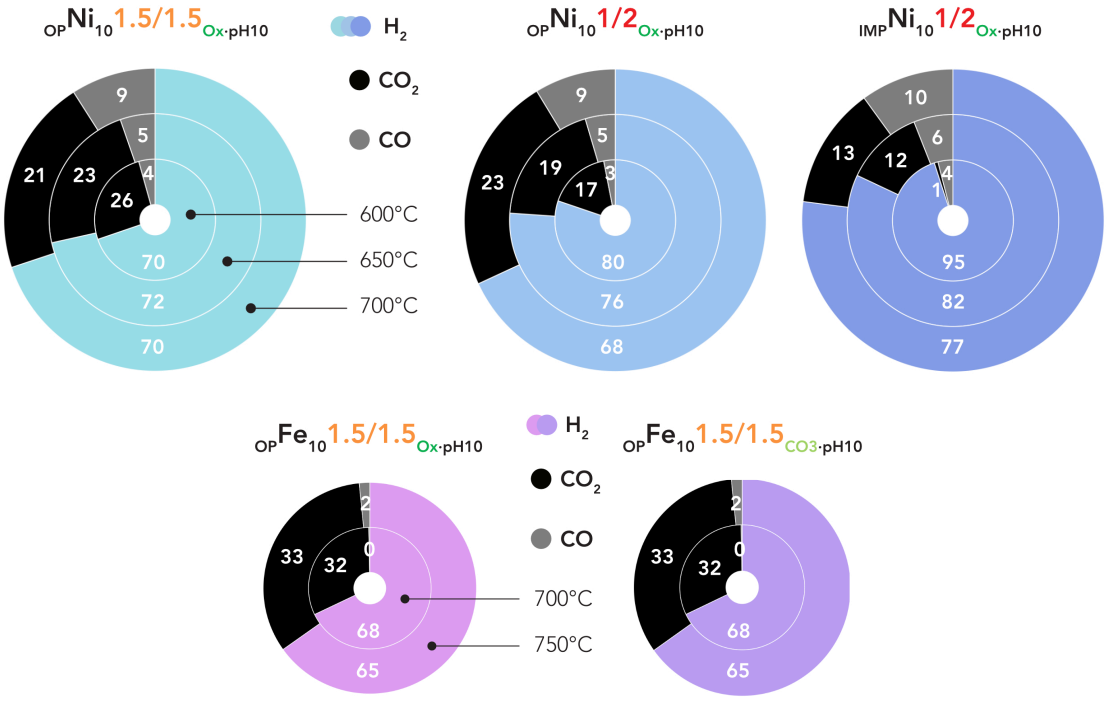

Figure 5.5: $H_2/CO_2/CO$ ratio of outlet gas for nickel and iron catalysts according to temperature.

Table 5.3: Productivity of H_2, CO2 and CO, tar conversion and H_2 yield according to temperature for selected nickel catalysts at S/C ratio at 6.

Catalysts	$_{OP}Ni_{10}1.5/1.5_{Ox\cdot pH10}$			$_{OP}Ni_{10}1/2_{Ox\cdot pH10}$			$_{IMP}Ni_{10}1/2_{Ox\cdot pH10}$		
production µmol/min/g_{cat}	H_2	CO_2	CO	H_2	CO_2	CO	H_2	CO_2	CO
600°C	192	71	12	235	76	18	283	85	37
650°C	299	62	11	290	74	18	286	97	37
700°C	365	38	2	410	60	30	429	71	38
%	H_2 Yield	Conversion		H_2 Yield	Conversion		H_2 Yield	Conversion	
600°C	27	38		32	45		39	56	
650°C	41	51		39	52		39	58	
700°C	50	56		57	69		59	74	

The productivity gap is more important for the two catalysts of ratio Mg/Ca 1/2 between two temperature steps which shows sorption enhancing. In addition to the selectivity and H_2 production, Table 5.3 presents the H_2 conversion and yield for comparison with the literature. Tan et al. [7] used a fixed-bed Ni-dolomite catalyst and a more complex tar mixture (phenol, toluene, naphthalene, pyrene) at 700°C with an H_2 yield of 55-60%. Then the selectivity corresponding to $H_2/CO_2/CO$ at 60/38/2. So, this H_2 yield is reached with all three nickel catalysts and even exceeded at the same temperature. Despite the dicrease in selectivity at higher temperature, the H_2 and CO content are better, certainly due to the major difference in the S/C ratio at only 1 and in the publication; that are discussed in the next paragraph. Zhang et al. [3] showed 81% conversion of carbon (toluene) at 700°C with Ni-CaO-perovskite material and S/C ratio at 4 and 48% dicrease at 600°C. The K_2CO_3 promoted in the catalysts improved the conversion efficiency but the selectivity $H_2/CO_2/CO$ at 72/21/7 at 650°C for exemple appears quiet similar to that of the $_{OP}Ni_{10}1.5/1.5_{Ox\cdot pH10}$ and a bit lower than other selected catalysts at this temperature.

From 650°C, the sorption capacity efficiency weakens [8] so the temperature range for optimizing SESR by CO_2 capture is always from 600°C to 700°C maximum at the expense also of the WGS reaction. In contraste, the conversion increases at higher temperature due to the atalytic activity of the metal and CaO [9-10]. Negligible below 650°C with a fast resitence time, the aromatic compound are mainly dehydrogenated and produce H_2. Some cracking also can occur and produces CO_2 through present of CaO at high temperature [11] but no phenolic compounds are present in the feeding. The carbonatation of CaO is no longer the goal even the CO_2 separation and the selectivity dicreases.

1.1.1.4. Effect of Steam/Carbon ratio

The S/C was fixed at 6 and was changed during the short test of nickel catalysts to 4.6 and 3.5 (Fig. 5.6). At S/C = 6.0 for $_{OP}Ni_{10}1.5/1.5_{Ox\cdot pH10}$, increasing the temperature produces more H_2 from 157 µmol/min/g at 600°C to 233 µmol/min/g at 700°C. The reverse trend is observed for $_{OP}Ni_{10}1/2_{Ox\cdot pH10}$ producing H_2 from 275 µmol/min/g at 600°C to 259 µmol/min/g at 700°C. This feature was already observed at S/C = 6 and demonstrates well the impact of the Mg/Ca ratio at both S/C ratio. With a higher calcium content, a decrease in temperature not only promotes the WGS reaction in the desired direction, but also allows for more efficient CO2 absorption. Both effects together compensate for, and even exceed, the loss of hydrogen productivity due to reforming. The decrease in H_2 production when S/C decrease is effective for each Ni-catalyst and marks the gap from the result of Tan et al. [6]. Between 6.0 and 4.6, $_{OP}Ni_{10}1.5/1.5_{Ox\cdot pH10}$ loses 18% of productivity at 700°C and also at 600°C; $_{OP}Ni_{10}1/2_{Ox\cdot pH10}$ exhibits lower losses with an average of 8% at each temperature level and an additional 6% loss by further decreasing the S/C ratio from 6.0 to 4.6, both at 650°C and 700°C.

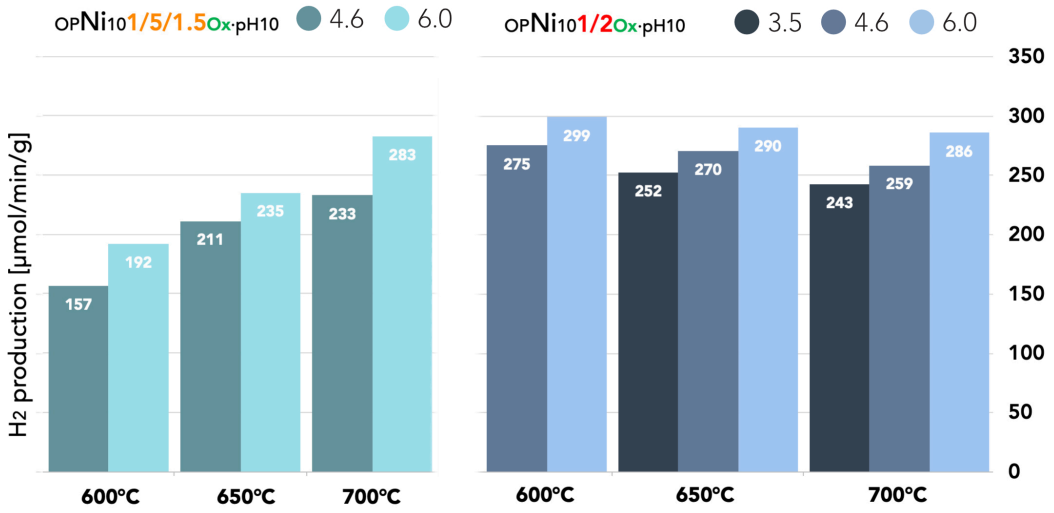

Figure 5.6: Productivity of H_2 for $_{OP}Ni_{10}1.5/1.5_{Ox\cdot pH10}$ and $_{OP}Ni_{10}1/2_{Ox\cdot pH10}$ according to S/C ratio [3.5; 4.6; 6.0] and temperature.

Fig. 5.7 and Fig. 5.8 allow observing the variation in $H_2/CO_2/CO$ ratio for the nickel catalysts. Thus the $H_2/CO_2/CO$ data at S/C = 6.0 in Fig. 5.4 are completed and compared: for both catalysts, the results show a humble increase of CO_2 and CO at the detriment of H_2 with a decrease of S/C ratio. So, the excess of water is important to increase the productivity as well as the H_2 selectivity. At each temperature, the loss of H_2 selectivity is not significantly different to deduce an impact trend of S/C ratio:

- 70_{H2}% at S/C 6.0 to 67_{H2}% at 4.6 at 600°C against 70_{H2}% at S/C 6.0 to 66_{H2}% at 4.6 at 700°C for $_{OP}Ni_{10}1.5/1.5_{Ox\cdot pH10}$. Despites the increasing H_2 production at 700°C, the selectivities are surprinsigly constant and certainly originate in the one hand from WGS at low temperature and in the other hand from the better Ni sites efficiency whose selectivity at high temperature. So, the contribution offset each other.
- 80_{H2}% at S/C 6.0 to 68_{H2}% at 4.6 at 600°C against 68_{H2}% at S/C 6.0 to 66_{H2}% at 4.6 at 700°C for $_{OP}Ni_{10}1/2_{Ox\cdot pH10}$. For this catalyst at the highest temperatures, the additional reduction of S/C at 3.5 demonstrates an admittedly supplementary loss of H_2 selectivity in favor of CO nearly reaching CO_2 selectivity.

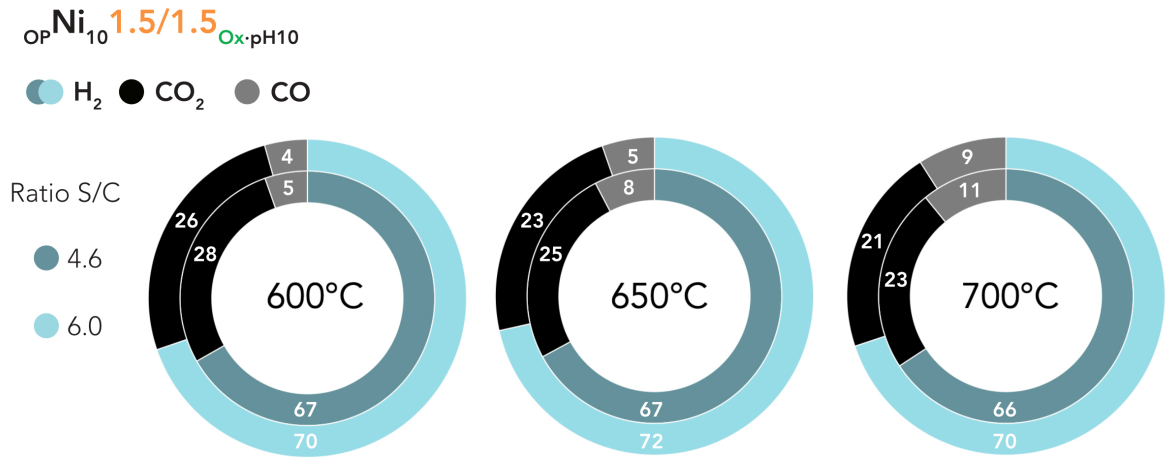

Figure 5.7: $H_2/CO_2/CO$ ratio of outlet gas for $_{OP}Ni_{10}1.5/1.5_{Ox\cdot pH10}$ according to S/C ratio and temperature.

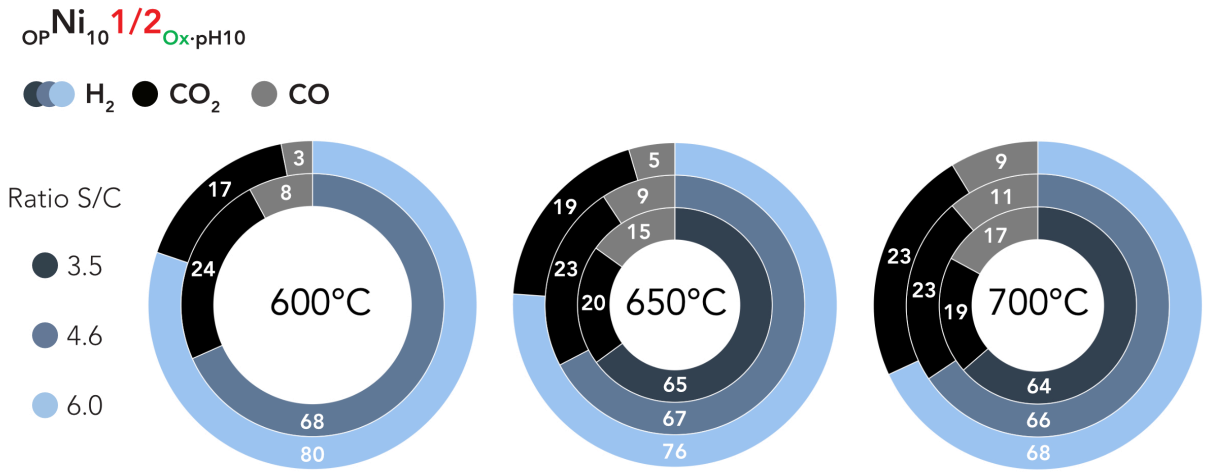

Figure 5.8: $H_2/CO_2/CO$ ratio of outlet gas for $_{OP}Ni_{10}1/2_{Ox\cdot pH10}$ according to S/C ratio and temperature.

A complementary comparison can be made with the results of Wang et al. [11] who developed nickel catalysts on a CaO-$Ca_{12}Al_{14}O_{33}$ absorbent support. At 650°C and a S/C ratio of 3, *i.e.* conditions close to the tests presented here, they give hydrogen concentrations also close to 65_{H2}% and 70 $_{H2}$% against 65 $_{H2}$% for $_{OP}Ni_{10}1/2_{Ox\cdot pH10}$ at the closer condition (S/C : 3.5). In this article, the CO and CO_2 concentration are also particulary close to us study with a ratio $H_2/CO_2/CO$ at 65/20/15 at 600°C and

70/16/14 at 650°C; it gives credibility to the results obtained by proposing an alternative to the studies already undertaken by the scientific community..

5.2.2. SESR/desorption cyclic test

The data of the cyclic test are preceded by the interesting steps of pre-reduction (green area Fig. 5.9.a) and decarbonation (red area) and the associated reactions of calcination and reverse water gas shift. The interpretation of the curves (Fig. 5.9.b) is linked to the values used to calculate the H_2 productivity during *(1)* pre-breakthrough (green area - SESR), *(2)* post-breakthrough (blue area - SR), and *(3)* the amount of CO_2 desorbed (orange area), cycle after cycle. The results discussed does not interpreted the data before the 3rd for the bad stability measurement, that avoid over-interpration.

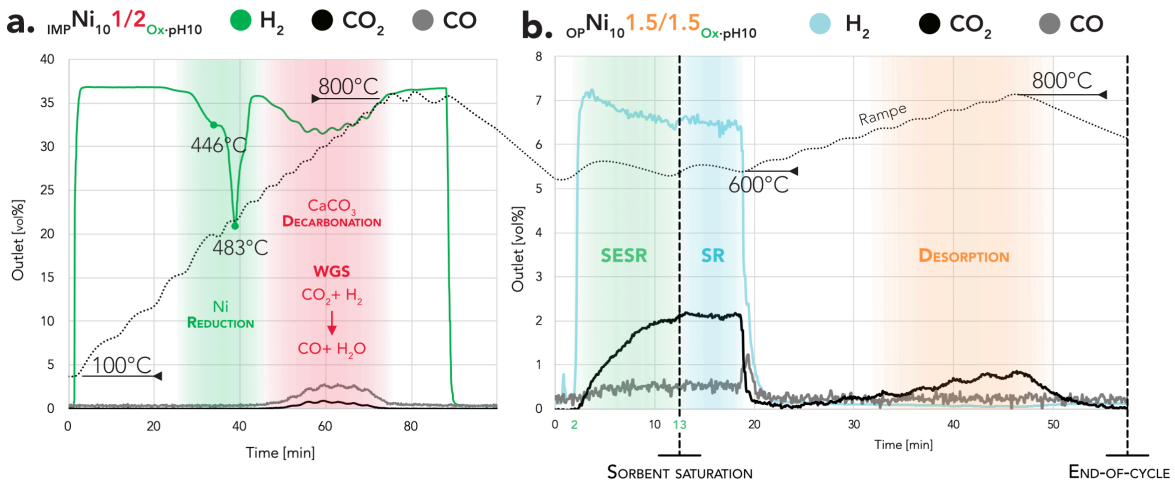

Figure 5.9: H_2, CO_2 and CO outlet flow [$_{vol}$%] composition profiles cyclic-SESR tests of a) reduction step and reverse WGS reacction with $_{IMP}Ni_{10}1/2_{Ox\cdot pH10}$; b) 8th cycle of cyclic-SESR test with $_{OP}Ni_{10}1.5/1.5_{Ox\cdot pH10}$.

The first observation is the temperature of nickel reduction highest pick at 483°C that is much lower than the temperature obtained during all H_2-TPR analyses but it can have a secondary reduction at around 800°C during $CaCO_3$ oxidation. This fact is observed for all three catalysts tested with peaks between 450°C and 500°C. The H_2/N_2 ratio in the gas mixture is probably the cause of this difference. The second decrease in H_2 flow is due to the reverse WGS reaction with CO_2 formed *in situ* by decarbonation. This event is confirmed by the presence of CO.

During the first few minutes of steam reforming, the CO_2 concentration increases until saturation of the sorbent part of the bifunctional sorbent/catalyst material. In the case of $_{OP}Ni_{10}1.5/1.5_{Ox\cdot pH10}$ (Fig. 5.9.b), only 11 min are needed to reach saturation. This time period corresponds to the highest concentration and so H_2 production. The sorption-enhanced advantage is even reduced as saturation is approaching. After the transition period the H_2 and CO_2 fluxes become stable and CO_2 definitively stops being absorbed. As observed in the previous tests, the production of H_2 after breakthrough is stable, thus the desorption step can start.

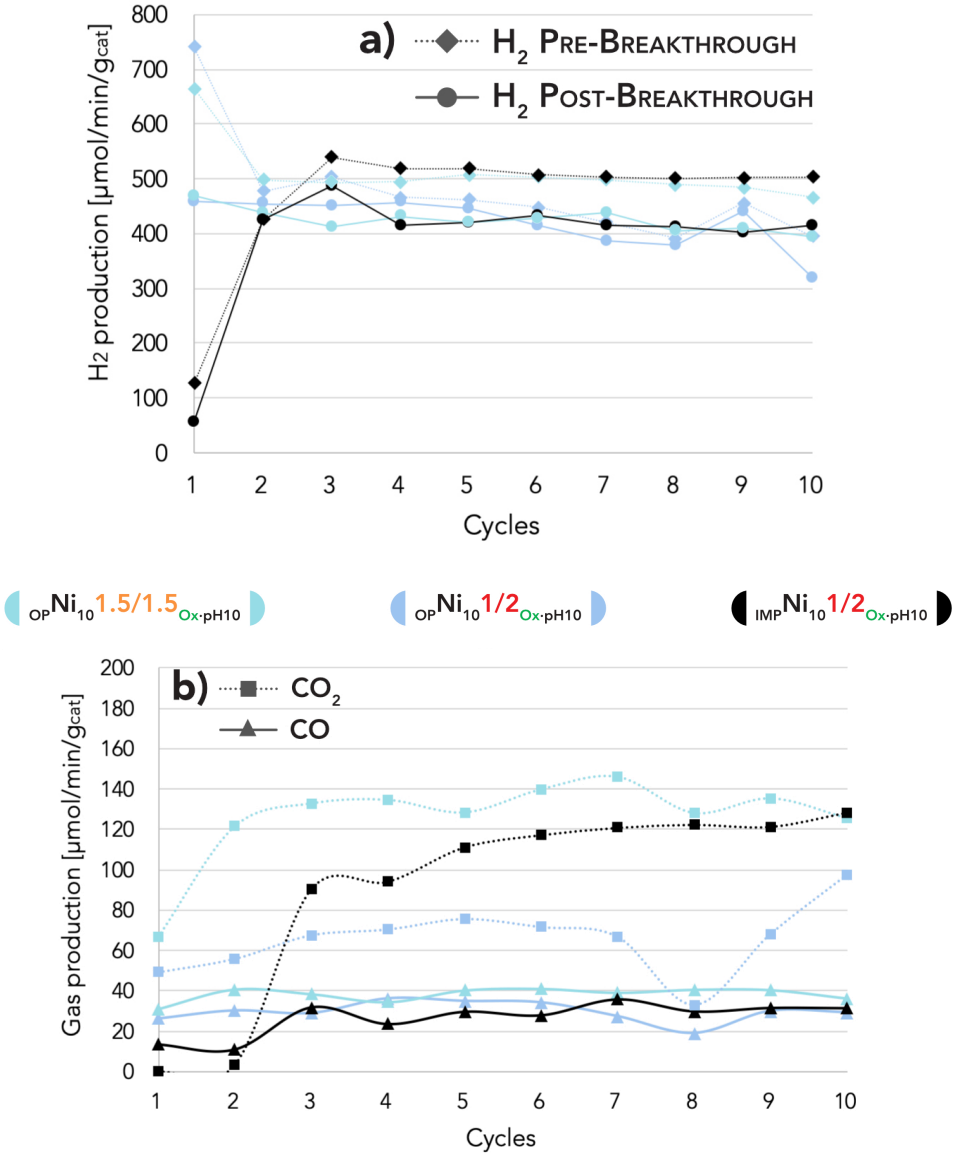

Figure 5.10: a) H_2 production [µmol/min/g_{cat}] pre- and post-breakthrough with ; b) CO_2 and CO production [µmol/min/g_{cat}] post-breakthrough according to cycle.

The data acquisitions allow measuring the evolution of H_2 production pre-breakthrough and post-breakthrough (Fig. 5.10.a) and CO and CO_2 production during post-breakthrough (Fig. 5.10.b) cycle after cycle. The cycle test is performed for ${}_{OP}Ni_{10}1.5/1.5_{Ox\cdot pH10}$, ${}_{OP}Ni_{10}1/2_{Ox\cdot pH10}$ and ${}_{IMP}Ni_{10}1/2_{Ox\cdot pH10}$ to compare the variation of Mg/Ca and the synthesis method (at the same pH and anion).

Inherent to the setup, H_2 production takes one cycle to stabilize itself. In particular, the evolution of ${}_{IMP}Ni_{10}1/2_{Ox\cdot pH10}$ can also be interpreted as a auto-activation of active Ni sites. Thereafter, H_2 productions pre- and post-breakthrough slowly decrease but the gap between them is not growing. The pre-breakthrough values are close and always higher than the post-breakthrough values for all catalysts. The different is more marked for ${}_{OP}Ni_{10}1.5/1.5_{Ox\cdot pH10}$ and ${}_{IMP}Ni_{10}1/2_{Ox\cdot pH10}$. In the best SESR, H_2 production reaches 540 µmol/min/g_{cat} during the third cycle (Table 5.4), with the impregnated catalyst associated with a post-breakthrough production at 487 µmol/min/g_{cat}, in turn, the best post-breakthrough result. After 10 cycles, 504 µmol/min/g_{cat} for ${}_{IMP}Ni_{10}1/2_{Ox\cdot pH10}$ is also the best production associated with a post-breakthrough production at 416 µmol/min/g_{cat}. This means a loss of 15% of the H_2 production.

During the post-breakthrough measurements between cycle 3rd and cycle 10th, the reactivity is maintaining at 95%, 71%, and 85% for ${}_{OP}Ni_{10}1.5/1.5_{Ox\cdot pH10}$ and ${}_{OP}Ni_{10}1/2_{Ox\cdot pH10}$ and ${}_{IMP}Ni_{10}1/2_{Ox\cdot pH10}$ respectively.

As with H_2, the CO_2 and CO outlets stabilize starting from the third cycle. Figure 5.10.b and Table 5.1 demonstrate a constant production of CO_2 and CO according to cycle for ${}_{OP}Ni_{10}1.5/1.5_{Ox\cdot pH10}$ with an $H_2/CO_2/CO$ ratio at 71/23/6 at cycle 3rd as well as cycle 10th. The production of ${}_{OP}Ni_{10}1/2_{Ox\cdot pH10}$ and ${}_{IMP}Ni_{10}1/2_{Ox\cdot pH10}$ catalyst are more in favor of H_2 with higher H_2 content and less CO_2 but the cycles deteriorate the H_2 selectivity to the enhancement of CO_2: definitely, the $H_2/CO_2/CO$ ratio at cycle 10 is the same for the three catalysts.

Regarding the cycle tests, it is recognized that the more stable catalyst is ${}_{IMP}Ni_{10}1/2_{Ox\cdot pH10}$ from the first to the last cycle, but it reaches the same H_2 selectivity. So, the H_2 selectivity stays reactively high but decreases with the cycle as the H_2 production and this is indeed due to the loss of nickel activity.

Table 5.4: a) H_2 production [µmol/min/g_{cat}] pre- and post-breakthrough; b) CO_2 and CO production post-breakthrough; c) conversion and H_2 yield according to the catalyst at the cycles 3rd and 10th.

a) Catalyst	Cycle 3rd			Cycle 10th		
H_2 production µmol/min/g_{cat}	Pre-breakthrough	loss %	Post-breakthrough	Pre-breakthrough	loss %	Post-breakthrough
$_{OP}Ni_{10}1.5/1.5_{Ox\cdot pH10}$	494	-16	413	466	-15	394
$_{OP}Ni_{10}1/2_{Ox\cdot pH10}$	503	-10	452	395	-9	321
$_{IMP}Ni_{10}1/2_{Ox\cdot pH10}$	540	-10	487	504	-17	416

b) Post-breakthrough µmol/min/g_{cat}	Cycle 3rd			Cycle 10th		
	CO_2 production	$H_2/CO_2/CO$	**CO** production	**CO_2** production	$H_2/CO_2/CO$	**CO** production
$_{OP}Ni_{10}1.5/1.5_{Ox\cdot pH10}$	133	71/23/6	38	126	71/23/6	36
$_{OP}Ni_{10}1/2_{Ox\cdot pH10}$	68	82/12/6	29	98	72/22/6	29
$_{IMP}Ni_{10}1/2_{Ox\cdot pH10}$	91	80/15/5	32	128	72/22/6	32

c) Post-breakthrough	Cycle 3rd		Cycle 10th	
%	Conversion	H_2 Yield	Conversion	H_2 Yield
$_{OP}Ni_{10}1.5/1.5_{Ox\cdot pH10}$	80	57	76	54
$_{OP}Ni_{10}1/2_{Ox\cdot pH10}$	75	62	62	44
$_{IMP}Ni_{10}1/2_{Ox\cdot pH10}$	84	67	79	57

Xie et al. [13] deployed a particularly efficient Ni-CaO/mayenite catalyst for steam reforming of toluene with an H_2 concentration of about 100% pre-breackthrough and 70% post-breackthrough. A previous comparison, the chosen temperature at 700°C and brings a better conversion and yield. The second difference resides in the S/C ratio at 12 for a $H_2/CO_2/CO$ selectivity at 70/23/7 post-breackthrough. One finds then a very close selectivity after breackthrough.

To compare the stability, Zhang et al. [3] also operted cyclic reforming with Ni-perovskite/CaO catalysts and optained a highest pre-breakthrough period. The difference of H_2 yield between the pre- and post-breackthrough is -23% wider than $_{OP}Ni_{10}1.5/1.5_{Ox\cdot pH10}$ and other catalysts. But the stability over the cycle is a litle bit better with -5% yield after 5 cycles. The difference is minor, espacially as the temperature is 650°C i.e. a temperature condition different from 50°C more then the experimented SESR cyclic tests.

5.3. Post-SESR analysis

Analyses are made after SESR cycle tests to study the structure and morphology transformation. To measure the variation of material characteristics, XRD, N_2 adsorption, and sorption capacity analysis are compared to previous results correspond to catalysts before SESR tests.

5.3.1. Structure and crystallinity modification

Structure of catalysts tested on cycle conditions present periclase and lime phases (Fig. 5.11). The same phases of the catalysts before the test are thus observed and the structure is not impacted by the reaction. In addition, the NiO phase appears more clearly intense than the initial catalysts. So, there are a Ni oxidation due to the air between test and post-analysis but certainly also due to the excess of water during test at high temperature. This differentiation is common to all three catalysts and neither the Mg/Ca ratio nor IMP method are parameters that stand out by preventing the post-SESR test modifications.

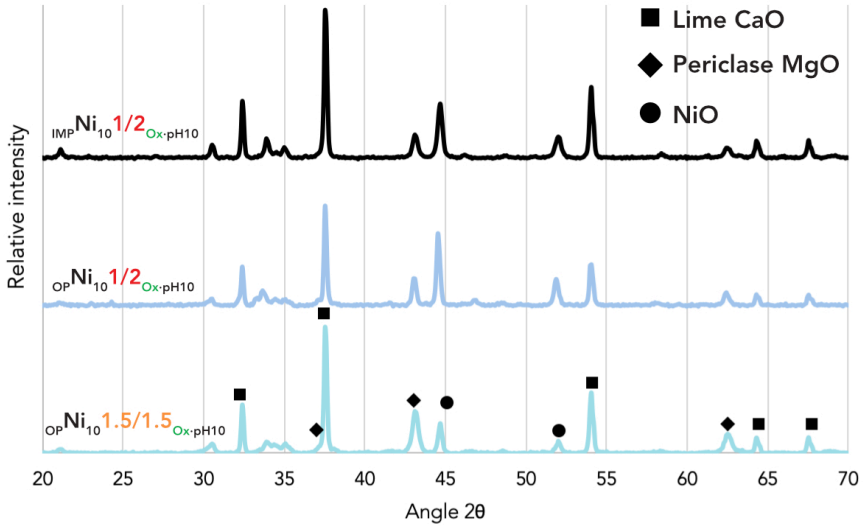

Figure 5.11: X-ray diffractograms of nickel catalysts after cyclic-SESR test.

5.3.2. Surface area and pore volume evolution

New N_2 adsorption analyses are made on catalysts used during short tests, so only after catalytic steps from 600°C until 700°C to compare the effect of different parameters of the syntheses: IMP versus OP, anion, and Mg/Ca ratio. The surface area and pore volume (Fig. 5.12) decrease after the test and in a more pronounced way for the $_{OP}Ni_{10}1.5/1.5_{Ox\cdot10}$. Compare to the same catalyst at Mg/Ca ratio equal to 1/2, the SSA (from 73 to 39 m^2/g) and Pv (from 0.33 to 0.12 cm^3/g) decrease less: the Mg/Ca ratio appears as a better stabilize parameter against reactivity conditions. With much worse starting results, $_{IMP}Ni_{10}1/2_{Ox\cdot10}$ is quiete similar before and after the test (SSA from 20 to 17 m^2/g – Pv from 0.05 to 0.05 cm^3/g) contrary to on homologous OP catalyst which exhibits better properties, despite everything. The evolution of porosity properties does not allow correlated catalytic loss activity. The performance of $_{IMP}Ni_{10}1/2_{CO3\cdot10}$ appears as due to the nickel on surface through the impregnation method better than the porosity. The SR activity does not seems to be affected by the dicreasing of SSA and Pv. Furthermore, the $_{IMP}Ni_{10}1/2_{CO3\cdot10}$ which seems slightly more promising (SSA from 24 to 13 m^2/g – Pv from 0.07 to 0.03 cm^3/g) decreases below $_{IMP}Ni_{10}1/2_{Ox\cdot10}$ properties, making CO_3 anion unfavorable for this purpose. So, that validated one more time the oxalate benefit.

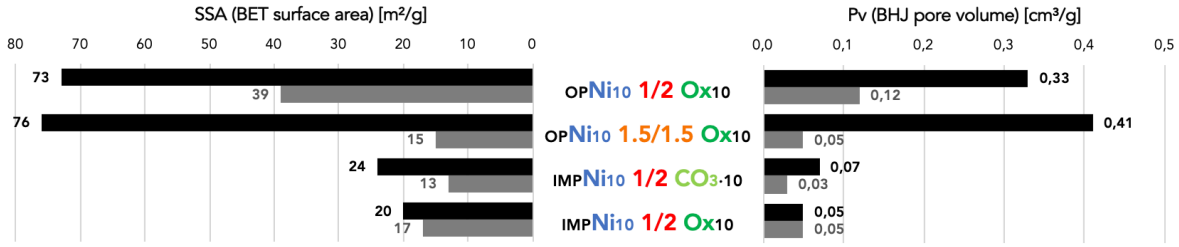

Figure 5.12: SSA and Pv for nickel catalysts pre- (in black) and post-SESR test (in grey).

5.3.3. Sorption capacity decreasing

With the same catalysts used to compare SSA and Pv before and after short tests, CO_2 sorption tests were made to compare sorption capacity and CaO accessibility. As porosity evolution, the sorption capacity and CaO accessibility decrease after SESR tests (Fig. 5.13) in a substantial proportion with a

loss between 45% and 59%. The sorption capacity loss goes along with the CaO accessibility. The difference between OP and IMP conditions is not enough to consider a trend; between carbonate and oxalate, the results are close too. However, a 1/2 Mg/Ca ratio seems once again more appropriated with better initial and final sorption capacity and CaO accessibility but also it shows a lower loss comparing $_{OP}Ni_{10}1/2_{Ox\cdot 10}$ and $_{OP}Ni_{10}1.5/1.5_{Ox\cdot 10}$.

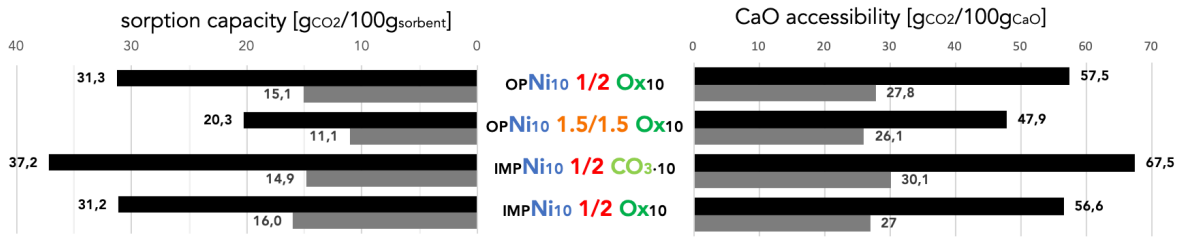

Figure 5.13: Sorption capacity and CaO sites accessibility of different nickel catalysts pre- (in black) and post-SESR (in grey) tests.

5.4.Conclusion

After the catalyst selection, a pre-reduction appears necessary to compare iron and nickel catalysts. The homogeneity of conditions allows to bring to the fore the efficiency of nickel compare to iron catalysts especially at 600°C that was the target temperature to enhanced the SR. Nonetheless, the maximum H_2 production reach 429 µmol/min/g_{cat} at 700°C and 365 µmol/min/g_{cat} at 600°C for the best catalyst: $_{IMP}Ni_{10}1/2_{Ox\cdot10}$. This result has to be related also to the real Fe_{wt}% and Ni_{wt}% (<5_{wt}%) lower than expected during synthesis (§ 4.1). At 600°C, the $H_2/CO_2/CO$ ratio is better than higher temperature and promising for the same catalyst at 95/1/4 with the higher S/C ratio at 6. The Mg/Ca ratio is confirmed it 1/2 as better parameter for reactivity and selectivity reaching for $_{OP}Ni_{10}1/2_{Ox\cdot10}$ 299 µmol/min/g_{cat} and 80/17/3 at 600°C.

Maintained at 6, the S/C ratio is tested during first cycle of cyclic SESR tests and for $_{IMP}Ni_{10}1/2_{Ox\cdot10}$ demonstrates a improvement of the productivity at 540 µmol/min/g_{cat}. Catalysts tested demonstrate a modest sorption enhanced contribution with 10-15% increasing production of H_2 before the breakthrough and over a short period of time (10-15 min). The gap between pre- and post-breakthrough is not pronounced than expected and the SESR step condition should be questioned again notably the inlet flow, high content of hydrocarbons and frequency between each new desorption to optimize the process. In contrast, the stability and selectivity according to cycle is maintaining and is interesting for all the three catalysts tested ($_{OP}Ni_{10}1.5/1.5_{Ox\cdot10}$; $_{OP}Ni_{10}1/2_{Ox\cdot10}$; $_{IMP}Ni_{10}1/2_{Ox\cdot10}$) with a H_2 production reaching 377 µmol/min/g on average after 10 cycle corresponding to 84% of initial efficiency on average of the 3 catalysts. The production drops to around 400 µmol/min/g after the 10^{th} breakthrough for the three Ni catalysts maintaining an H_2 purity at 72%The best H_2 yield is finally optained pre- and post-breakthrough respectively at 67% and 57% with $_{IMP}Ni_{10}1/2_{Ox\cdot10}$ at 600°C, S/C at 6 for a maximal 84% and 79% tar conversion.

After test, the structure stays the same but the loss porosity and sorption capacity observed after one and several cycles are significant. These losses are homogeneous for all catalysts so not determinate by synthesis parameter. Thus, the catalyst choice to optimize SESR is done by the pre-test characterizations.

References

[1] Elaboration et développement d'un catalyseur Ni/Olivine pour la production d'hydrogène par gazéification de la biomasse en lit fluidisé, Dariusz Swierczyński thesis (2004).

[2] Fornasari, G., Gazzano, M., Matteuzzi, D., Trifirò, F.: Structure and reactivity of high-surface-area Ni/Mg/Al mixed oxides, Applied Clay Science, 10, 69-82 (1995).

[3] Zhang, Z., Qin, C., Ou, Z., Xia, H., Ran, J., Wu, C.: Experimental and thermodynamic study on sorption-enhanced steam reforming of toluene for H_2 production using the mixture of Ni/perovskite-CaO, Fuel, 305, 121447 (2021).

[4] Basile, F., Benito, P., Fornasari, G., Vaccari, A.: Hydrotalcite-type precursors of active catalysts for hydrogen production, Applied Clay Science, 48, 250-259 (2010).

[5] Bychkov, V. Tyulenin, P., Firsova, A.A., Shafranovsky, E.A., Gorenberg, A., Korchak, V.N.: Carbonization of nickel catalysts and its effect on methane dry reforming, Applied Catalysis A: General, 453, 71-79 (2013).

[6] Wang, C., Sun, N., Zhao, N., Wei, W., Sun, Y., Sun, C., Liu, H., Snape, C.E.: Coking and deactivation of a mesoporous Ni–CaO–ZrO2 catalyst in dry reforming of methane: A study under different feeding compositions, Fuel, 143, 527-535 (2015).

[7] Tan, R.S., Abdullah, T.A.T., Mahmud, S.A., Zin, R.M., Isa, K.M.: Catalytic steam reforming of complex gasified biomass tar model toward hydrogen over dolomite promoted nickel catalysts, Int. J. Hydrogen Energy, 44, 21303-21314 (2019).

[8] Wu, Y., Liao, Y., Liu, G., Ma, X.: Syngas production by chemical looping gasification of biomass with steam and CaO additive, Int. J. Hydrogen Energy, 43, 19375-19383 (2018)

[9] Hu, Guoxin, Huang, H.: Hydrogen rich fuel gas produciton by gasification of wet biomass using a CO2 sorbent, Biomass & Bioenergy, 33, 899-906 (2009).

[10] Udomsirichakorn, J., Basu, P., Salam, P.A., Acharya, B.: Effect of CaO on tar reforming to hydrogen-enriched gs with in-process CO_2 capture in a bubbling fluidized bed biomass steam gasifier, Int. J. Hydrogen Energy, 38, 14495-14504 (2013).

[11] Jia, Y., Huang, J., Yang, W.: Effects of calcium oxide on the cracking of col tar in the feedboard of a fluidized bed, Energy & Fuels, 18, 1625-1632 (2004).

[12] Wang, X., He Y., Xu, T., Xiao B., Liu, S., Hu, Z., Li, J.: CO2 sorption-enhanced steam reforming of phenol using Ni–M/ T CaO–Ca12Al14O33 (M = Cu, Co, and Ce) as catalytic sorbents, Chem. Eng. J., 393, 124769 (2020).

[13] Xie, Huaqing, Zhang, W., Zhao, X., Chen, H., Yu, Q., Qin, Q.: Sorption-enhanced reforming of tar: influence of the preparation method of CO2 absorbent, Kor. J. Chem. Eng., 35, 2191-2197 (2018).

GENERAL CONCLUSION

Approach and results

The sorption enhanced steam reforming as a tool for purification and production of H_2-rich syngas is an useful approach to valorize the gasification process from biomass sources. The PhD project is integrated into a large and global evolution of the essential energetic transition. The contribution of energy storage and CO_2 capture is a challenge and a pre-requisite for the massive development of sustainable energy. To optimize H_2 purity, the sorption materials base on hydrotalcite then Fe or Ni catalytic materials have been synthesized and analyzed. The steam reforming reaction supported by the WGS and the CO_2 sorption capture can thus increase the reaction efficiency and avoid energy consumption by using a reactor at 600°C and a second one for the regeneration step.

First, the different physic and chemical analyses allow to understand how to optimize the sorbents according to the synthesis method, the pH variation, the anion size, and the aluminum, calcium and magnesium content. The co-precipitation method was promptly selected for the best result and mainly the adaptability of conditions and reactants variation for the next steps. The elementary analysis also provides the co-precipitation efficiency in the real Mg/Ca ratio coherent with the expected composition. The behaviors of Ca-free samples with a hydrotalcite structure appear to be different from Ca-containing samples. The analysis reveals trends indicating that porosity and morphology are overall deteriorated with increasing Ca_{wt}%. The morphology of the *sand roses* observed by SEM confirmed the tends obtained by N_2 adsorption but this morphology could be maintained until the Mg/Ca ratio 1/2 with the carbonate and oxalate anion. The interlayer anion providing the macro-porosity of these anions. The highest SSA and Pv values were optained for the Ca-free samples but are maintained between 79-143 m^2/g and 0.46-0.75 cm^2/g for the 1.5/1.5/1 samples and between 79-107 m^2/g and 0.18-0.41 cm^2/g for the 1/2/1 samples. Evaluation of CO_2 sorption demonstrates a limit of the soption capacity in Ca_{wt}% and accessibility of CaO sites at Mg/Ca = 1/2. The properties optimization between porosity for accessibility and Ca content for sorption amount is found at

Mg/Ca = 1/2 or Mg/Ca = 1.5/1.5 according to anion and pH. The best results were obtained for $1.5/1.5/1_{Ox\cdot pH10}$ (40.6 $g_{CO2}/100g_{sorbent}$ and 69.7 $g_{CO2}/100g_{CaO}$), $1/2/1_{Ox\cdot pH10}$ (41.6 $g_{CO2}/100g_{sorbent}$ and 56.6 $g_{CO2}/100g_{CaO}$), $1/2/1_{CO3\cdot pH10}$ (49.6 $g_{CO2}/100g_{sorbent}$ and 67.5 $g_{CO2}/100g_{CaO}$), and finally for $1/2/1_{CO3\cdot pH8}$ (52.3 $g_{CO2}/100g_{sorbent}$ and 71.1 $g_{CO2}/100g_{CaO}$). The stability tests gave the advantage to the oxalate samples and the Mg/Ca ratio at 1/2. The sorbents cited were the base of catalyst synthesis.

The catalysts were thus synthesized with the previously optimized pH and Mg/Ca ratio. Various iron and nickel contents were added by the OP or IMP method and the characterization presents large differences between these two synthesis methods. Indeed, the porosity and sorption capacity are generally decreasing compared to equivalent sorbents with the exception at the lowest metal contents as ${}_{OP}Fe_{10}1.5/1.5_{CO3\cdot pH10}$ and ${}_{OP}Ni_{5}1/2_{Ox\cdot pH10}$ reached respectively 86 m^2/g and 103 m^2/g and especially for IMP catalysts retained at 30-58 m^2/g for $1.5/1.5_{Ox\cdot pH10}$ and $1/2_{Ox\cdot pH10}$ conditions. SEM analysis shows a partial remaining *sand roses* morphology for the OP catalysts at 1.5/1.5 and 1/2 but at low metal weight percent. On the contrary, the IMP catalysts morphology constitutes collapsing *sand roses* and a massive and bulky shape that refects the porosity values. A loss of CO_2 sorption capacity and CaO sites accessibility results from the addition of metal amount increasing. Iron catalysts are quite equal or often better than nickel equivalents and reach between 19-36 $g_{CO2}/100g_{sorbent}$ and 35-77 $g_{CO2}/100g_{CaO}$ for all OP synthesis conditions tested. These values decline at 4-20 $g_{CO2}/100g_{sorbent}$ and 10-57 $g_{CO2}/100g_{CaO}$ for the IMP samples. These sorption capacity is embedded in the literature values such as Di Giuliano et al. [1] with Ni-CaO-mayenite materials at 14-29 $g_{CO2}/100g_{sorbent}$. At last, cyclic sorption/desorption tests were performed to measure a real improvement of sorption stability compare to sorbent equivalent. The most stable catalysts are ${}_{OP}Ni_{10}1.5/1.5_{Ox\cdot pH10}$ for nickel and ${}_{OP}Fe_{10}1.5/1.5_{CO3\cdot pH10}$ for iron. Finally, ${}_{OP}Ni_{10}1/2_{Ox\cdot pH10}$, ${}_{OP}Ni_{10}1.5/1.5_{Ox\cdot pH10}$ ${}_{IMP}Ni_{10}1/2_{Ox\cdot pH10}$ and ${}_{OP}Ni_{10}1/2_{CO3\cdot pH10}$ are chosen for the nickel part as well as ${}_{OP}Fe_{10}1.5/1.5_{CO3\cdot pH10}$ and ${}_{OP}Fe_{10}1.5/1.5_{Ox\cdot pH10}$ for the iron catalyst to be tested in steam reforming activity.

The reactivity and stability tests were carried out in a continuous fixed-bed apparatus from 600°C to 750°C at various steam/carbon ratios before study the sorption enhanced activity. The best catalyst $_{IMP}Ni_{10}1/2_{Ox\cdot10}$ allows to produce 429 µmol/min/g_{cat} at 700°C and 365 µmol/min/g_{cat} at 600°C of H_2 that is the target temperature to optimize the CO_2 sorption capacity. At this lower temperature, the gas mixture reaches 95% of H_2. This selectivity is obtained at the highest S/C = 4.6 and decreases in productivity with lower S/C values. The Mg/Ca ratio is confirmed equals to 1/2 as a better parameter reaching for the second best catalyst $_{OP}Ni_{10}1/2_{Ox\cdot10}$ 299 µmol/min/g_{cat} and 80/17/3 at 600°C. Indeed, the iron catalysts are very less active and require 700°C to produce 90-100 µmol/min/g_{cat} with a negative impact on the selectivity. The increase of S/C at 6 during the cyclic tests demonstrates a further improvement of the productivity until 540 µmol/min/g_{cat} for $_{IMP}Ni_{10}1/2_{Ox\cdot10}$.

The contribution of sorption enhanced is appropriate between 10-15% increasing H_2 production during the short sorption enhanced reforming period of time (10-15 min) generally below literature which often operated at 650°C and with quiet lower selectivity [2-3]. However, the production and selectivity over the cycles are stable for the nickel catalysts ($_{OP}Ni_{10}1.5/1.5_{Ox\cdot10}$; $_{OP}Ni_{10}1/2_{Ox\cdot10}$; $_{IMP}Ni_{10}1/2_{Ox\cdot10}$). Overall, the obtained results allow to bring an alternative bi-focntional catalysts already studied in the literature with values of absorption, activity and effect of enhancing soption during the competitive SESR. The H_2 production reaches 500 µmol/min/g after 10 cycles i.e. 84% of the initial efficiency on average for the 3 catalysts. The production drops to around 400 µmol/min/g after the 10^{th} breakthrough for the three Ni catalysts maintaining an H_2 purity at 72%. The tar conversions drop from 75-84% at the 3^{rd} cycle to 62-79% in the 10^{th} cycle. So, the loss catalytic activity is thin and the hydrogen yields are also maintained from 67% to 57% in the best condition for $_{IMP}Ni_{10}1/2_{Ox\cdot10}$.

Finally, the production of H_2-rich syngas from a reference gasification mixture could be possible at 600°C by modifying the composition of the layered structure; first with the calcium content to increase the CO_2 sorption temperature and with the addition of nickel sites to proceed steam reforming. The sorption capacity and steam reforming activities are in the line of literature [1-3] and propose a sustainable way to approach biomass valorization.

Ethics and project criticism

This thesis falls within a sustainable chemistry approach. The synthesis, the compounds and elements used, the reaction conditions and the applications aim to respect the concepts of green chemistry for a coherent project. First, the technologies allowing the development of hydrogen production, CO_2 storage and biomass valorization are major advances for the energetic transition, which limits CO_2 emission and avoids fossil fuels utilization and extraction. Alerts about climate change are clear, the mankind will have to let a part of the oil and coal still available under the ground. Global production and consumption more sustainable imples accepting sobriety, relocatization of the production and at least doubtless leave the concept of growth aside, as green as it can be. Thereby, upstream and downstream of this project drifts are to be avoided.

Upstream, gasification biomass can come from different sources, and some of them are unsustainable and undesired. Indeed, biomass gasification processes are adapted to a wide variety of vegetables such as the first generation biofuels that compete with feed production. In addition, the 2nd generation of biofuels can quite come from overexploitation such as gigantic palm monoculture [4] tree farm that causes deforestation, massive use of pesticides problems and loss of biodiversity. A more engaging perspective can be found with local biomass and waste from forest industry [5, 6], current production like empty fruit bunches [7] or rice husk [8]. Furthermore, gasification and pyrolysis of plastic (PP, PE, PS, PET) are possible [9-12] and allow the valorization of plastic waste. The production of plastics comes mainly from oil, so in this case, the concept must not be assimilated to renewable syngas. This is a well solution for the treatment and valorization of plastic wastes, but in no way, warrants the plastic growth industry and the production of single-use plastics. Then, there is the question of the life cycle. Biomass is considered CO_2-neutral [13] but life-cycle assessment (LCA) is an important tool to apprehend the sustainable feature of the biomass industry, notably the time needed to compete the cycle.

Afterward, the SESR reaction converts the mixed gas into H_2-rich syngas and catches CO_2. The different hydrogen production methods are particularly studied from an environment and economic point of view, by Kothari *et al.* who described the steam reforming process as a large GHG emitter [14]. Indeed, 1 mol of CO_2 is produced for 1 mol of H_2, consequently, the reaction has a big impact in large-scale manufacturing exploitation if the CO_2 is not captured. The steam reforming process allows producing syngas from various hydrocarbons such as biomass-derived, light alkanes and ethanol which is well suited to the risk of perpetual oil exploitation. The process requires significant energy consumption (endothermic reaction) to heat the reactor (600°C) and even more (800°C) to desorb CO_2 from the sorbent in the case of this project. The desorption phase is often carried out at 900-1000°C and under high pressure on an industrial scale. This energy cost should typically be found in an LCA which unfortunately is not included in this present study. The use of a nickel catalyst moderates the energy consumption because the metal sites are active at a lower temperature than iron. Sorption and reforming tests were performed in a smaller reactor than the pilot setup. However, this deserves an LCA and economic study (life cycle costs – LCC), even though the study of a larger facility requires further steps at higher technology readiness levels (TRL). Moreover, included in the initial project program, H_2S poisoning tests were not done. Iron and nickel deactivation studies would be essential to envisage scale-up pilot SESR and industrial interest. With a bifunctional sorbent/catalyst as the M-LDO samples, the competitiveness between CO_2 and H_2S adsorption could be decisive for the sorption capacity stability and catalytic site deactivation. A system able to carry out reforming, CO_2 and H_2S sorption in a single reactor will cause less energy consumption and for sure, few intermediary materials to be synthesized.

The composition and synthesis of the catalysts can also be critical. The LDH-based catalysts synthesis respects most green chemistry principle: use of catalyst, of course, nonpolluting auxiliary solvent (water), maximum synthesis in one or two steps, not dangerous, inert product at STP (Standard conditions for Temperature and Pressure – 273.15 K i.e. 0°C and 100 kPa i.e. 1 bar), renewable

resource using and atom economy. In addition, the hydrotalcite synthesis needs low-cost and trivial chemical products. It is also important to consider desorption temperature, facility and long-term stability. In the case of LDOs-derived, the objective is to increase the sorption temperature and thus the desorption temperature inevitably. The SESR process involves a significant energy consumption at 800°C, for the desorption step but allows using only one circulating double beds reactor for the heating. Optimizing the reactor temperature preserves the reactivity of the metal sites. As described in the previous chapters, the catalysts sites are composed of an iron or nickel phase. Iron is abundant on earth and non-toxic contrary to nickel [11]. In detail, nickel content could have been incorporated at a lower content for the SESR and minimalize the environmental impact. Finally, the H_2-rich syngas obtained contains water excess easily separable by condensation which is a very energy-efficient step.

References

[1] Di Giuliano, Girr, J., Massacesi, R., Gallucci, K., Courson, C.: Sorption enhanced steam methane reforming by Ni-CaO materials supported on mayenite, Int. J. Hydrogen Energy, 42, 13661-13680 (2017).

[2] Xie, Huaqing, Zhang, W., Zhao, X., Chen, H., Yu, Q., Qin, Q.: Sorption-enhanced reforming of tar: influence of the preparation method of CO2 absorbent, Kor. J. Chem. Eng., 35, 2191-2197 (2018).

[3] Zhang, Z., Qin, C., Ou, Z., Xia, H., Ran, J., Wu, C.: Experimental and thermodynamic study on sorption-enhanced steam reforming of toluene for H_2 production using the mixture of Ni/perovskite-CaO, Fuel, 305, 121447 (2021).

[4] Khan, Z., Yusup, S., Ahmad, M.M., Chin, B.L.F.: Hydrogen production from palm shell via integrated catalytic adsorption (ICA) steam gasification, Energy Conversion and Management, 87, 1224-1230 (2014).

[5] Sun, Q., Yu, S., Wang, F., Wang, J.: Decomposition and gasification of pyrolysis volatiles pine wood through a bed of hot char, Fuel, 90, 1041-1048 (2011).

[6] Noda, R., Ito, T., Tanaka, N., Horio, M.: Steam gasification of cellulose and wood in a fluidized bed of porous clay particules, J. Chem. Eng. Japan, 42, 490-501 (2009).

[7] Mohd Salleh, M.A., Kisiki, N.H., Yusuf, H.M., Ghani, W.A.: Gasification of biochar from empty fruit bunch in a fluidized bed reactor, Energies, 3, 1344-1352 (2010).

[8] Loha, C., Chattopadhyay, H., Chatterjee, P.K.: Thermodynamic analysis of hydrogen rich synthetic gas generation from fluidized bed gasification of rice husk, Energy, 36, 4063-4071 (2011).

[9] Meng, A., Chen, S., Long Y., Zhou, H., Zhang, Y., Li, Q.: Pyrolysis and gasification of typical components in wastes with macro-TGA,

[10] Kannan, P., Al Shoaibi, A., Srinivasakannan, C.: Energy recovery from co-gasification of waste polyethylene and polyethylene terephthalate blends, Computers & Fluids, 88, 38-42 (2013).

[11] Kumagai, S., Hasegawa, I., Grausea, G., Kameda, T., Yoshioka, T., Thermal decomposition of individual and mixed plastics in the presence of CaO or $Ca(OH)_2$, J. Anal. Appl. Pyrolysis, 113, 584-590 (2015).

[12] Horton, S.R., Woeckener, J., Mohr, R., Zhang, Y., Petrocelli, F., Klein, M.T.: Molecular-level kinetic modeling of the gasification of common plastics, Energy Fuels, 30, 1662-1674 (2016).

[13] Commission decision establishing guidelines for the monitoring and reporting of greenhouse gas emissions pursuant to directive 2003/87/EC of the European Parliament and of the Council, Official Journal of the European Union (2004/156/EC).

[14] Iliuta, M.C.: CO2 Sorbents for Sorption-Enhanced Steam Reforming, Adv. Chem. Eng, 51, ISSN: 0065-2377.

APPENDIX

LIST OF FIGURE

LIST OF TABLES

LIST OF SYMBOLS

Ø	Diameter
θ	angle
°C	Degree Celsius
K	Degree Kelvin
J	Joule
n	Mole
M	Molar weight
m	Meter
L	Liter
g	Gram
sec	Second
min	Minute
h	Hour
Wh	Watt-hour
eq	Equivalent
$t_{CO2 \cdot eq}$	Tone CO_2 equivalent
t	Tone (10^3kg)
k	kilo (10^3)
M	Mega (10^6)
G	Giga (10^9)
T	Tera (10^{12})
m	Milli (10^{-3})
µ	Micro (10^{-6})
n	Nano (10^{-9})
ppm	Parts per million (10^{-6})
yr	Year
ΔH^0_{298K}	Enthalpy standard of reaction
$_{wt}\%$	Weight percent

LIST OF ACRONYMS

COP	Co-precipitation	**SR**	Steam Reforming
HYD	Hydrothermal	**UREA**	Urea hydrolysis
IMP	Impregnation	**WGS**	Water Gas Shift
LDH	Layer Double Hydroxyde	**GHG**	GreenHouse-Gases
LDO	Layer Double Oxide	**NDIR**	Non-Dispersive InfraRed
OP	One-Pot co-precipitation	**EU**	European Union
CO_3	Carbonate	**HHV**	Higher Heating Value
Ox	Oxalate	**LHV**	Lower Heating Value
St	Stearate	**S/C**	Steam/Carbone ratio
Cit	Citrate	**Pv**	pore volume
SMR	Steam Methane Reforming	**SSA**	surface area
XRD	X-Ray Diffraction	**BET**	Brunauer-Emmett-Teller
TGA	Thermo-Gravimetric Analysis	**BJH**	Barrett-Joyner-Halenda
SEM	Scanning Electron Microscopy		
H_2-TPR	Temperature-Programmed Reduction of Hydrogen		
ICP-AES	Inductively Coupled Plasma - Atomic Emission Spectroscopy		
CCUS	Carbon Capture, Utilization and Storage		
SESR	Sorbent Enhanced Steam Reforming		
SE-WGS	Sorbent Enhanced Water Gas Shift		